A Plasticity Model to Predict the Effects of Confinement on Concrete

Thesis by

Julie Wolf

In Partial Fulfillment of the Requirements

for the Degree of

Doctor of Philosophy

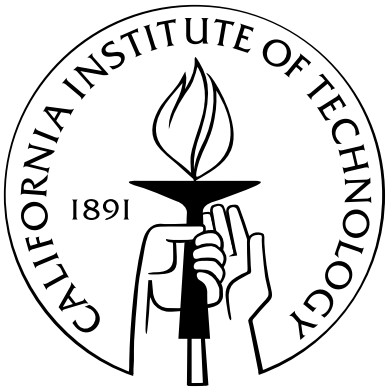

California Institute of Technology

Pasadena, California

2008

(Defended January 9, 2008)

Acknowledgements

I recall, while reading multiple other theses early in the course of my research, wondering why it was that people felt the need to lavishly thank all those around them at the completion of their thesis. I thought to myself, *it's a thesis, not an Academy Award!* But as I arrive (finally!) at the end of my own Ph.D., I now appreciate that this is not a journey one can complete on one's own. Without a strong network of support, I know I would never have finished. And so, I shall launch into my own 'acceptance' speech.

First, and with good reason, my family. Without you, I would never have begun such a bold undertaking and would certainly never have had the disposition, strength, and will to finish. Thanks Mom, Dad, and Lo for making me who I am (in more ways than two!).

Garrett, for putting up with me (the more realistic and less politically correct version of 'support') as I waded through my research project. The world will never know just how crazy I can be, but you always understood. You always recognized what was important to me and did everything in your power to support me in those things. I would never have survived this without you.

John Hall, for putting the idea into my head in the first place, reassuring me that I could and should get a Ph.D., and then convincing me to take on such a difficult subject matter (what was he thinking?). Aren't you glad I'm finally finished?

Anna, for the movie nights, lunches, house shopping as a couple, and general adventures that we embarked on (come on, who wouldn't want to crew for a 25 hour endurance race?). You could always be counted on to understand and sympathize with whatever mess, problem, or predicament I managed to get myself into, and to

jump into whatever harebrained adventure I was trying at the moment. You were always a shoulder to cry on, an ear to vent to, and a pair of eyes to read about the fascinating subject of concrete plasticity. You're probably the only person who is more sick of my thesis than I am!

Laura, for always understanding, never judging, patiently listening, and being one of the best examples I've found of exactly who I want to be.

Patrick, for being the only other person alive (or dead, for that matter) to read every single word of this thesis, the only person willing to debate the use of single versus double quotes into the wee hours of the morning, for teaching me about Oxford commas, semi-colon use, and the glories of the English language (as only an Englishman can do). I thank you for being there at 4 a.m. when the world was on fire, and, just as important, when it wasn't. Oh yeah, and thanks for teaching me how to drive (and we both know what *that* entailed)!

Sue, for being my home away from it all, for showing me a path when I was hopelessly lost and then getting me onto it, and for reminding me that there is a lot more to life than thesis research (shocking, I know). And, of course, teaching me how to not die on a cross country course, and maybe even have a little fun doing it!

Sherpa (your spirit will always be with me in every horse I ride), First Mate, Brushfire, and Cally. Without you all, I would surely have lost my sanity. You have so much to teach us all about how we should live and what's really important (which, as we all know, is carrots!).

Jasmine, because I may be the only person, ever, to dedicate their thesis to a car (have I mentioned the insanity?). As with the horses, you helped keep me sane (well, my version of sane), reminded me of the joys of thinking hard about physics and dynamics (yes, mid-engine cars *are* hard to drive), gave me rewards when I so desperately needed them, and didn't kill me when I messed up (though, clearly, you thought about it).

And last, but not least, I would like to thank the Academy for this award. Oh, wait a minute ...

Abstract

A plasticity model to predict the behavior of confined concrete is developed. The model is designed to implicitly account for the increase in strength and ductility due to confining a concrete member. The concrete model is implemented into a finite element (FE) model. By implicitly including the change in the strength and ductility in the material model, the confining material can be explicitly included in the FE model. Any confining material can be considered, and the effects on the concrete of failure in the confinement material can be modeled. Test data from a wide variety of different concretes utilizing different confinement methods are used to estimate the model parameters. This allows the FE model to capture the generalized behavior of concrete under multiaxial loading. The FE model is used to predict the results of tests on reinforced concrete members confined by steel hoops and fiber reinforced polymer (FRP) jackets. Loading includes pure axial load and axial load-moment combinations. Variability in the test data makes the model predictions difficult to compare but, overall, the FE model is able to capture the effects of confinement on concrete. Finally, the FE model is used to compare the performance of steel hoop to FRP confined sections, and of square to circular cross sections. As expected, circular sections are better able to engage the confining material, leading to higher strengths. However, higher strains are seen in the confining material for the circular sections. This leads to failure at lower axial strain levels in the case of the FRP confined sections. Significant differences are seen in the behavior of FRP confined members and steel hoop confined members. Failure in the FRP members is always determined by rupture in the composite jacket. As a result, the FRP members continue to take load up to failure. In contrast, the steel hoop confined sections exhibit extensive strain

softening before failure. This comparison illustrates the usefulness of the concrete model as a tool for designers. Overall, the concrete model provides a flexible and powerful method to predict the performance of confined concrete.

Contents

List of Figures

List of Tables

Table of Variables

Variable	Definition	Location
$a_{0,peak}$, $a_{1,peak}$, $a_{2,peak}$, $a_{3,peak}$	parameters defining the peak tensile meridian	Equation 3.1
$b_{0,peak}$, $b_{1,peak}$, $b_{2,peak}$, $b_{3,peak}$	parameters defining the peak compressive meridian	Equation 3.1
$a_{0,residual}$, $a_{1,residual}$, $a_{2,residual}$, $a_{3,residual}$	parameters defining the residual tensile meridian	Equation 3.1
$b_{0,residual}$, $b_{1,residual}$, $b_{2,residual}$, $b_{3,residual}$	parameters defining the residual compressive meridian	Equation 3.1
c	parameter defining the yield tensile meridian	Equation 3.2
D^e_{ijkl}	material elastic modulus tensor	Section 2.3
D^p_{ijkl}	material plastic modulus tensor	Equation 3.14
$D^{tangent}_{ijkl}$	material tangent modulus tensor	Equation 3.13
d	parameter defining the yield compressive meridian	Equation 3.2
$d\epsilon_{ij}$	total strain increment	Equation 2.14
$d\epsilon^p_{ij}$	plastic strain increment	Equation 2.14
$\overline{d\epsilon^p}$	effective plastic strain increment	Equation 2.17

$d\lambda$	positive scalar factor of proportionality, used for plastic flow definition	Equation 3.12
$d\sigma_{ij}$	elastic stress increment	Equation 3.10
$d\psi$	damage increment	Equation 3.5
E	modulus of elasticity	Section 3.4
F	failure surface	Section 2.2
F_{peak}	peak loading surface	Equation 3.4
$F_{residual}$	residual loading surface	Equation 3.4
F_{yield}	yield loading surface	Equation 3.4
f'_c	unconfined concrete compressive strength	Section 3.1.1
I_1, I_2, I_3	first, second, and third invariants of the stress tensor	Equations 2.5 through 2.7
J_2, J_3	second and third invariants of the deviatoric stress tensor	Equation 2.8 and 2.9
Q	potential surface	Section 3.3
$R_{peak}(\xi, \theta)$	cross section of the peak loading surface in the deviatoric plane	Equation 3.3
$R_{residual}(\xi, \theta)$	cross section of the residual loading surface in the deviatoric plane	Equation 3.3
$R_{yield}(\xi, \theta)$	cross section of the yield loading surface in the deviatoric plane	Equation 3.3
r	deviatoric length invariant	Equation 2.11
$r_{c,peak}$	compression meridian of the peak loading surface	Equation 3.1
$r_{c,residual}$	compression meridian of the residual loading surface	Equation 3.1
$r_{c,yield}$	compression meridian of the yield loading surface	Equation 3.2
$r_{t,peak}$	tensile meridian of the peak loading surface	Equation 3.1
$r_{t,residual}$	tensile meridian of the residual loading surface	Equation 3.1

$r_{t,yield}$	tensile meridian of the yield loading surface	Equation 3.2
s_{ij}	deviatoric stress tensor	Equation 2.3
α, γ	parameters controlling the effect of confinement on damage accumulation	Equation 3.5
β	defines the location of the failure surface relative to the loading surface	Equation 3.7
ϵ^e_{ij}	total elastic strain	Equation 2.16
ϵ_{ij}	total strain	Equation 2.15
ϵ^p_{ij}	total plastic strain	Section 2.3
θ	Lode angle or angle of similarity	Equation 2.12
κ	parameter controlling the rate of travel of the failure surface from one loading surface to the next	Equation 3.7
ν	Poisson's ratio	Section 3.4
ξ	hydrostatic length invariant	Equation 2.10
σ_{ij}	stress tensor	Equation 2.1
$\sigma_1, \sigma_2, \sigma_3$	principal stress invariants	Section 2.1
ϕ	parameter controlling damage accumulation at low stress levels	Equation 3.5
ψ	current damage level	Section 3.2
ψ_{peak}	damage level corresponding to the peak stress state	Section 3.2
ω	parameter controlling the amount of plastic volume change	Figure 3.6

Chapter 1

Introduction

Concrete is the most prevalent construction material in the world (Craig et al., 1996). It has been used in widely varying structural applications from the dome of the Pantheon to Hoover Dam to the Guggenheim Museum. Much has been learned about concrete behavior through its varied and historical use. One of the most recent lessons came from the February 9, 1971 magnitude 6.6 San Fernando earthquake. Damage to reinforced concrete structures, even some recently built to the latest building code, was extensive. Engineers discovered that the buildings of the time were non-ductile and that the design of future concrete structures would require more ductility to withstand seismic loading. While the idea of confinement was not a new one, the level of confinement demanded in seismic zones, and the details of its implementation, required new understanding. Special details for ductile response were implemented into the building code as a result of the lessons learned in the San Fernando earthquake. The January 17, 1994 magnitude 6.7 Northridge earthquake provided a reminder of the danger presented by the existing non-ductile reinforced concrete structures, built before the change in the building code. Today, the design of new reinforced concrete structures in active seismic zones and the problem of existing non-ductile reinforced concrete structures are both important challenges. This thesis seeks to aid engineers by providing a design tool to evaluate the ductility and strength of confined reinforced concrete members.

Concrete shows a significant change in strength and ductility due to confinement. Confinement can come in many forms. The traditional method is to wrap the concrete

member with hoops or spirals of steel rebar. Many new forms of confinement have arisen to be used in the retrofit of existing non-ductile concrete structures. Steel jackets, welded wire fabric, and fiber reinforced polymer (FRP) composites are some of the many confinement strategies employed in retrofits. Methods to evaluate the performance of concrete members under different forms of confinement are required to evaluate and compare different retrofit strategies. Of importance to designers is the increase in the peak stress, the strain at peak stress, and the post-peak behavior of the concrete. This thesis provides a tool to predict these important quantities.

Due to the extensive use of concrete, experimental test data for concrete is abundant. However, reviews of test data in this thesis show that concrete behavior can be inconsistent. The inconsistencies are likely due to the fact that concrete is an amalgamation of various different materials. Something as fundamental as the concrete compressive strength, f'_c, will be quite different among specimens from the same mixture of concrete. Further, the behavior of concrete can be rather complex, changing drastically with different load configurations and histories. The combination of the inconsistency and complexity make it extremely difficult to accurately model. However, since the use of concrete is widespread and extensive, attempts to model this material are necessary. The inconsistency and complexity of the material must be kept in mind when defining any concrete model. The goal of the model is to capture the overall trends seen in the behavior, not specific details observed in a particular test.

Many models currently exist for reinforced concrete. Several different approaches have been considered. Some models perform simple curve fits to confined tests and use these fits to predict the behavior of a similarly confined section. Others use nonlinear elasticity or plasticity models to capture the more complicated effects and predict the behavior of concrete in a general sense. Somewhat more recently, attempts have been made to create endochronic models for concrete. Each approach has its strengths, complexity level, and complications. The intended use of any particular concrete model may dictate which approach is best suited. For a more in-depth discussion of the different types of concrete models, see Chen (1982).

This thesis presents a new model to represent the confined behavior of concrete. It predicts the change in the behavior of concrete when confined. The model utilizes plasticity theory to represent the behavior of concrete under multiaxial loading. Relevant plasticity theory is reviewed in Chapter 2. The changes in the stress and strain behavior of confined concrete due to the current three-dimensional load state are implicitly taken into account. The concrete model is defined and discussed in Chapter 3.

In Chapter 4, a large set of experimental data is compiled consisting of tests on a variety of concretes which have a wide range of different properties. Test data from concrete with different compressive strengths, aggregate sizes and properties, water-cement ratios, saturation values, ages, additives, and many other variables are utilized to estimate the model parameters. Including a large variety of concrete variables allows the model to represent a more generalized behavior of concrete.

The new material model for concrete is implemented into a finite element (FE) program, described in Chapter 5, for use in representing reinforced concrete structural members. By implicitly including the multiaxial behavior in the concrete model, the confining material can be explicitly included in the FE model. This allows for any type of confinement to be considered. As new retrofit strategies are considered and new confining materials are created, the FE model can be used to predict and evaluate the behavior of the concrete due to the retrofit.

The FE model is utilized to predict the behavior of confined reinforced concrete member laboratory tests in Chapter 6. Different load types and confinement configurations are considered. The predictions of the FE model are then compared to the experimental data to evaluate the performance of the FE model. In Chapter 7, the FE model is used to perform a comparison of the behavior of circular versus square cross sections, as well as a comparison of the performance of members with steel rebar confinement versus FRP confinement. The confined concrete members are compared under both axial load and moment. The performance results of the different members are discussed.

Chapter 8 discusses the conclusions drawn from this thesis. While discrepancies

in the experimental data led to some differences between test results and FE model predictions, the FE model did not exhibit any obvious or clear errors. The model was able to capture the general behavior of concrete under confinement. Use of the FE model to compare square to circular cross sections, and steel hoop to FRP confinement, emphasized the effects of cross sectional shape and confinement material on concrete behavior. Significantly different behaviors were exhibited by sections confined by FRP versus steel hoops. While both sections withstand large strains, the FRP confined sections fail at their peak stress while the steel confined sections exhibit strain softening post-peak. This raises the question of how to define ductility for this type of section. Thus, designers must determine exactly what type of performance they want out of the member. With that behavior in mind, the model defined in this thesis serves as an excellent tool to predict concrete behavior for the different configurations being considered.

Chapter 2

Plasticity Review

The creation of the concrete model in this thesis required extensive use of current plasticity theory. In order for the reader to understand the model, a brief review of relevant plasticity theory is presented here. First, Section 2.1 defines the stress invariants used for the definition of this model and discusses their physical significance. Second, the definition and requirements of a failure surface are reviewed in Section 2.2. Third, the definitions for plastic flow and effective plastic strain are discussed in Section 2.3. Finally, the consistency condition, used for determining the tangent material matrix, is outlined in Section 2.4. For a complete discussion of plasticity theory and its application to concrete, see Chen (1982).

2.1 Stress Invariants

For a concrete model to be most useful, the model itself should be defined independent of the coordinate system attached to the material. Thus, it is necessary to define the model in terms of stress invariants which are, by definition, independent of the coordinate system selected. The three-dimensional stress state of the material is traditionally defined by the stress tensor, which can be represented relative to a

chosen coordinate system by a matrix:

$$\sigma_{ij} = \begin{bmatrix} \sigma_x & \tau_{xy} & \tau_{xz} \\ \tau_{xy} & \sigma_y & \tau_{yz} \\ \tau_{xz} & \tau_{yz} & \sigma_z \end{bmatrix} \tag{2.1}$$

This stress tensor is often decomposed into two parts: a purely hydrostatic stress, σ_m, defined in Equation 2.2, and the deviatoric stress tensor, s_{ij}, defined in Equation 2.3.

$$\sigma_m = \frac{1}{3}\left(\sigma_x + \sigma_y + \sigma_z\right) \tag{2.2}$$

$$s_{ij} = \begin{bmatrix} \sigma_x - \sigma_m & \tau_{xy} & \tau_{xz} \\ \tau_{xy} & \sigma_y - \sigma_m & \tau_{yz} \\ \tau_{xz} & \tau_{yz} & \sigma_z - \sigma_m \end{bmatrix} \tag{2.3}$$

A common set of stress invariants are the three principal stress invariants. The principal stress coordinate system is the coordinate system in which shear stresses vanish, leaving only normal stresses. This requirement of zero shear stresses leads to the characteristic equation:

$$\sigma^3 - I_1\sigma^2 + I_2\sigma - I_3 = 0 \tag{2.4}$$

The first, second, and third invariant of the stress tensor, I_1, I_2, and I_3 are defined in the following equations:

$$I_1 = \sigma_x + \sigma_y + \sigma_z \tag{2.5}$$

$$I_2 = (\sigma_x\sigma_y + \sigma_y\sigma_z + \sigma_z\sigma_x) - \tau_{xy}^2 - \tau_{yz}^2 - \tau_{zx}^2 \tag{2.6}$$

$$I_3 = \begin{vmatrix} \sigma_x & \tau_{xy} & \tau_{xz} \\ \tau_{yx} & \sigma_y & \tau_{yz} \\ \tau_{zx} & \tau_{zy} & \sigma_z \end{vmatrix} \tag{2.7}$$

The three roots of Equation 2.4 are the three principal stress invariants, also called the three principal stresses. They are ordered so that $\sigma_1 > \sigma_2 > \sigma_3$.

The three principal stresses, as well as most other stress invariants, can be rewritten in terms of three core invariants: the first invariant of the stress tensor, I_1, and the second and third invariants of the deviatoric stress tensor, J_2 and J_3. The first invariant of the stress tensor, I_1, was previously defined in Equation 2.5. The second and third invariants of the deviatoric stress tensor are defined as:

$$J_2 = \frac{1}{6}[(\sigma_x - \sigma_y)^2 + (\sigma_y - \sigma_z)^2 + (\sigma_z - \sigma_x)^2] + \tau_{xy}^2 + \tau_{yz}^2 + \tau_{zx}^2 \tag{2.8}$$

$$J_3 = \frac{1}{3}s_{ij}s_{jk}s_{ki} = \begin{vmatrix} \sigma_x - \frac{1}{3}I_1 & \tau_{xy} & \tau_{xz} \\ \tau_{yx} & \sigma_y - \frac{1}{3}I_1 & \tau_{yz} \\ \tau_{zx} & \tau_{zy} & \sigma_z - \frac{1}{3}I_1 \end{vmatrix} \tag{2.9}$$

Clearly, a large variety of stress invariants were available to use in defining the model. The three stress invariants ξ, r, and θ were chosen to define the components of the concrete model:

$$\xi = \frac{1}{\sqrt{3}}I_1 = \frac{1}{\sqrt{3}}(\sigma_1 + \sigma_2 + \sigma_3) \tag{2.10}$$

$$r = \sqrt{2J_2} = \sqrt{\frac{1}{3}[(\sigma_1 - \sigma_2)^2 + (\sigma_2 - \sigma_3)^2 + (\sigma_3 - \sigma_1)^2]} \tag{2.11}$$

$$cos(3\theta) = \frac{3\sqrt{3}}{2}\frac{J_3}{J_2^{3/2}} \tag{2.12}$$

They have a direct physical interpretation which makes it easier to understand the physical implications of the model. To understand the physical significance of each of these invariants, it is helpful to look at them in the principal stress coordinate system $(\sigma_1, \sigma_2, \sigma_3)$. Recall that the principal stress coordinate system corresponds to the orientation in which the material has no shear stresses. A diagram of this coordinate system is shown in Figure 2.1. Consider the case of purely hydrostatic loading with magnitude equal to σ_h. For this load case, $\sigma_1 = \sigma_2 = \sigma_3 = \sigma_h$. Thus, the load path travels along the ξ axis. The magnitude of the hydrostatic load, σ_h, is equal to the stress invariant ξ. Therefore, it is clear that the invariant ξ represents the hydrostatic component of the current stress state. Now we consider the planes that lie

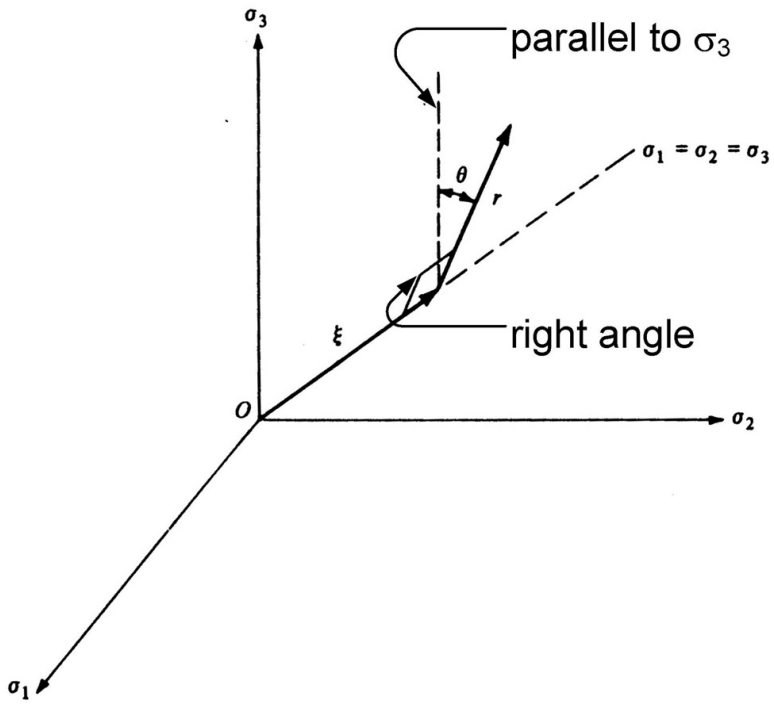

Figure 2.1: Graphical interpretation of stress invariants (ξ, r, θ) in the principal stress space. Modified from Chen (1982).

perpendicular to this hydrostatic axis. For any given stress state lying in one of these planes, the distance between the point representing the stress state in the principal stress coordinate system and the hydrostatic axis is related to the deviatoric stress. The magnitude of this distance is equal to the invariant r. Thus, r represents the stress invariant measure of the deviatoric stress. This leaves only the third invariant, θ, also known as the Lode angle. The invariant θ is controlled by the relationship of the intermediate principal stress to the major and minor principal stresses. When the intermediate principal stress, σ_2, is equal to the minor principal stress, σ_3, the value for θ becomes 60°. When the intermediate principal stress, σ_2, is equal to the major principal stress, σ_1, the value for θ becomes 0°. Thus, θ is an indication of the magnitude of the intermediate principal stress in relation to the minor and major principal stresses.

2.2 Failure Surface

An important component of a concrete plasticity model is the *failure surface*. In traditional plasticity theory, this surface is alternately referred to as the yield or loading surface. In this thesis, to prevent confusion, this surface will be known exclusively as the failure surface, which defines the boundary of elastic behavior. (The concepts of the yield surface and the loading surface will be introduced in Chapter 3 to refer to surfaces which do not follow the rules required of the failure surface.) When the current stress state of the material lies within the failure surface, the material behaves purely elastically. The definition of the failure surface will clearly depend on stress variables, but can also depend upon other variables, such as the plastic strain, or constant parameters, often called hardening parameters. Detailed discussions of the variables on which this surface can depend can be found in other texts [(Chen, 1982), (Lubliner, 1990), (Khan and Huang, 1995)]. The failure surface defined in this thesis is a function of stress variables, through the invariants discussed in Section 2.1, and the effective plastic strain, $\overline{\epsilon^p}$, which will be defined in Section 2.3. Thus, the surface can be expressed as:

$$F = F(\sigma_{ij}, \overline{\epsilon^p}) = 0 \tag{2.13}$$

The failure surface is defined such that, for load states where $F < 0$, the material behaves elastically. Once the load path intersects the failure surface, unloading is defined as returning to a stress state where $F < 0$. While loading continues, the stress state must stay on the failure surface with F = 0, although this surface can move and change shape as $\overline{\epsilon^p}$ varies.

There are well documented behaviors of concrete that affect the definition of the failure surface. Details of the experimental behavior of concrete will be given in Sections 4.2 through 4.5. From these experiments, it is known that the failure surface for concrete should be smooth. Further, consider the failure surface in the (ξ, r) plane, also known as the meridian plane. The shape of the failure surface in this plane describes how the deviatoric stress, r, that can be supported by the concrete will change with the current hydrostatic stress, ξ. Recall that the value for the Lode

angle, θ, varies only between 0° and 60°. The two meridian planes corresponding to these two extreme values of the Lode angle are called the tensile and compressive meridians, respectively. The tensile meridian is so named because uniaxial tension is one of the load cases which corresponds to a Lode angle of 0°. The compressive meridian is given that name because uniaxial compression corresponds to a Lode angle of 60°. It is known that, in general, concrete can withstand higher deviatoric stresses when subjected to confinement. There are two forms of confinement: active and passive. Active confinement is a lateral pressure applied to the concrete. Passive confinement consists of wrapping a concrete member in a material such as steel rebar, steel jackets, or fiber reinforced polymer (FRP) jackets, to create a lateral pressure through restraining the expansion of the concrete under axial loading. Confining the concrete results in an increase in apparent strength. In addition, when subjected to loading with θ values near 60°, it will withstand higher deviatoric stresses than when loading occurs near a θ value of 0°. Also, experimental results imply that these meridians should be convex and curved. Thus, in the model's meridian planes: the deviatoric stress increases with ξ; the compressive meridian lies outside the tensile meridian; and the intersection of the surface in all meridian planes is convex. This is exemplified later in Figure 3.2. Experiments have shown that concrete does not fail under purely hydrostatic loading. Therefore, the failure surface should not cross the hydrostatic axis.

It is also useful to consider experimental results in the (r,θ), or deviatoric, plane. The failure surface in this plane exhibits a three-fold symmetry. This is due to the fact that concrete typically behaves as an isotropic material. For small values of ξ, the failure surface is nearly triangular. As ξ increases, the cross section becomes more circular. Physically, this means that the dependence on the intermediate principal stress decreases with increasing confinement.

As previously mentioned, experimental results show that the meridians of the failure surface should be convex. Theory also supports this requirement, since Drucker's stability postulate [(Drucker, 1951), (Drucker, 1960)] requires that the failure surface itself be convex.

2.3 Plastic Flow

To properly model concrete, it is necessary to incorporate the phenomenon called *hardening* into the model. This allows the failure surface to expand and change shape as the concrete is plastically loaded. This requires that the failure surface depend on the plastic strain. Determining the amount of plastic strain that has occurred requires a concept in plasticity known as *plastic flow*.

As previously stated, the failure surface defines the boundary of elastic deformation. When the stress state reaches the failure surface, further loading induces plastic flow. While, by definition of a failure surface, the stress state must stay on the failure surface, due to the presence of hardening in the model, the failure surface can move or change shape due to the plastic flow. However, rules must be established to determine the behavior of this plastic flow. Similar to the failure surface in stress space, a plastic potential function, Q, is defined in strain space. While the potential function is considered to lie in the strain space, the stress and strain variables are commonly thought of as being interchangeable. First, the plastic strain increment is defined:

$$d\epsilon_{ij}^{p} = d\lambda \frac{\partial Q}{\partial \sigma_{ij}} \tag{2.14}$$

The scalar $d\lambda$ represents a proportionality coefficient that can change with loading. The total plastic strain is used to determine the total strain:

$$\epsilon_{ij} = \epsilon_{ij}^{e} + \epsilon_{ij}^{p} \tag{2.15}$$

The elastic strain, ϵ_{ij}^{e}, is determined in the traditional fashion using a generalized Hooke's Law:

$$\sigma_{ij} = D_{ijkl}^{e} \epsilon_{kl}^{e} \tag{2.16}$$

The variable D_{ijkl}^{e} represents the elastic modulus tensor of the material.

A common approach, known as associated plasticity, is to define the plastic potential function to have the same shape as the current failure surface. As will be

discussed in Section 3.3, associated plasticity does not correctly predict the behavior of concrete and, therefore, this thesis will use non-associated plasticity with the plastic potential function having a different shape than the current failure surface.

The loading history of the material should affect the location of the failure surface. Within this thesis, this is accomplished through the use of the effective plastic strain increment. The movement of the failure surface will be directly controlled by the effective plastic strain increment:

$$\overline{d\epsilon^p} = \sqrt{\frac{2}{3} d\epsilon^p_{ij} d\epsilon^p_{ij}} \tag{2.17}$$

The introduction of the $\frac{2}{3}$ multiplier comes from requiring a von Mises type material model to satisfy the uniaxial compressive stress test. While the model presented in this thesis shows little resemblance to a von Mises model, this particular definition for effective plastic strain is often used and was, therefore, selected for use here. The effective plastic strain increment is used to control the hardening behavior of the failure surface, as discussed in Section 3.2.

2.4 Consistency Condition

The consistency condition is a mathematical expression of the requirement that the stress state stay on the failure surface as long as loading continues, even though the failure surface itself will be moving and changing shape due to hardening.

$$F + dF = 0 \tag{2.18}$$

However, recall that the failure surface is defined such that $F = 0$ is the onset of plastic flow. Thus, the above equation can be simplified:

$$dF = 0 \tag{2.19}$$

The failure surface in this thesis is written as a function of the stress and the effective plastic strain. Thus, the above condition can be rewritten a final time:

$$dF = \frac{\partial F}{\partial \sigma_{ij}} d\sigma_{ij} + \frac{\partial F}{\partial \overline{\epsilon^p}} d\overline{\epsilon^p} = 0 \tag{2.20}$$

This condition will be used in Section 3.5 to determine the tangent modulus tensor. The tangent modulus tensor is necessary to define the relationship between the stress and strain increments, as will be discussed in Section 3.5.

Chapter 3

Model Definition

This model was designed to take into account the change in strength and ductility of concrete due to confinement. Ductility is a measure of the failure strain relative to the yield or peak strain. Previous researchers have utilized two different approaches when modeling these effects. The "effective confinement" approach [(Mander et al., 1988b), (Ahmad and Shah, 1982), (Sheikh and Uzumeri, 1982)] estimates the amount of confining pressure that the confinement applies on the concrete. This is typically done by estimating the stress in the confining material, the effectiveness of the confinement over the cross section, and other cross sectional properties. It is assumed that this confining pressure will be constant throughout the loading. The increase in concrete strength is then determined by considering experimental results of concrete at an equivalent confining pressure. Therefore, any change in the concrete behavior due to a change in the confinement pressure cannot be captured with this method. The "effective confinement" method cannot explicitly include the variation in the stress throughout the cross section or the change in confinement pressure with loading or changing confinement material properties. The second approach, which was chosen for this thesis, is to implicitly model the effect of concrete confinement by including it in the concrete plasticity theory. In this method, the confinement mechanism is modeled explicitly in the finite element (FE) model. By explicitly including the confining material, this method allows any form of confinement (active or passive) and any confining material (for example, rebar, steel jackets, or fiber reinforced polymer (FRP) sheets) to be modeled. Interaction between the concrete and the confining

mechanism is properly accounted for. For example, fracture of a stirrup in a column, and the subsequent drastic change in the confinement level of the concrete, leading to a change in the behavior of the concrete itself, can be modeled. Even the effect of the variable confinement over the cross section of a tied column can be modeled.

The ability to accurately represent the three-dimensional behavior of concrete is fundamental to the approach taken in this thesis. Once the failure surface is reached, the current three-dimensional load state of the concrete directly affects the failure surface location and rate of damage accumulation. Through this approach, confinement can come not only from the traditional forms of rebar or FRP jackets, but also from loading in perpendicular directions. By understanding and modeling the actual three-dimensional behavior of the concrete under true triaxial loading conditions, the model is more flexible than the "effective confinement" models. It can be applied to more diverse structures instead of being limited to simple columns with designated types of confinement.

It is not the intention that all aspects of concrete behavior be included in the model defined in this thesis. Creep, fracture, shear sliding, strain rate effects, and cyclic loading behaviors are not built into the present model. Tension strength is also not included. The specimen is assumed to be pre-cracked, thus the initial tension strength is set to zero. At a later date, this model could be incorporated into an existing framework that includes these behaviors [for example, ABAQUS ABAQUS (Inc.) or ADINA ADINA R&D (Inc.)] to create a complete, versatile concrete model. However, the scope of this thesis is limited to monotonic compression or bending to create the backbone curves of concrete. The backbone curve presents the boundary of the stress versus strain behavior for the concrete. If the specimen were cyclically loaded, unloading would fall away from the backbone curve, but loading would eventually cause a return to the backbone curve.

This chapter details the equations defining the concrete model. The plasticity model presented in Malvar et al. (1994) and improved upon in Malvar et al. (1996) was used as a starting point for the creation of the model defined in this thesis. Section 3.1 shows the three loading surfaces that underlie this model. Within this

thesis, the term *loading surface* describes a surface that is fixed in the invariant space. The loading surfaces are a tool to define the location of the *failure surface*. The failure surface defines the boundary between elastic and plastic loading, as discussed in Section 2.2. Section 3.2 defines the current failure surface, which moves between the three fixed loading surfaces. Section 3.3 discusses the final component of the concrete model, the flow rule. Section 3.4 summarizes the input parameters required to utilize the model. Section 3.5 derives the tangent modulus tensor.

3.1 Loading Surfaces

The backbone of the model is three loading surfaces corresponding to the yield, peak, and residual stress states of the concrete, following Malvar et al. (1994). The loading surfaces are three-dimensional and are fixed in the (ξ, r, θ) invariant space. For a specimen compressed in only one direction and free in the other two orthogonal directions (uniaxial compressive loading), the surfaces correspond to the yield, peak, and residual points as shown in Figure 3.1. The current failure surface travels be-

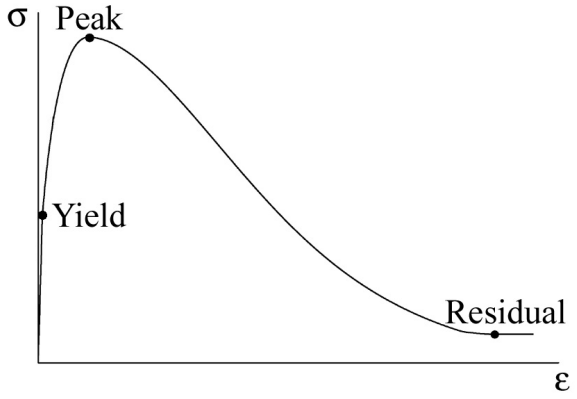

Figure 3.1: Loading surface locations.

tween these three fixed surfaces based on a damage parameter defined in Section 3.2. The equations defining the peak and residual loading surfaces are identical, while the yield loading surface is given a different shape. Values for the parameters controlling these equations are determined from experimental data for each of the three surfaces. The shape of each loading surface can be best understood by examining its shape in

two separate planes, as previously discussed in Section 2.2. The first is the meridian plane, which is the (ξ, r) plane, and represents lines of constant θ. The second is the deviatoric plane, which is the (r, θ) plane, and defines the cross section of the failure surface for constant values of ξ. By examining the behavior in these two planes, the full three-dimensional shape of the surface can be easily visualized.

The peak and residual loading surfaces are assigned a hyperbolic shape in the meridian plane as described in Section 3.1.1. This particular shape was chosen because it presented the best fit to the test data over the largest range of confinement. The shape of the test data in the meridian plane can be seen in Figures 4.3 and 4.4 for the peak surface and Figure 4.18 for the residual surface. The yield loading surface has a different shape in the meridian plane, which will be discussed in Section 3.1.1. The cross section for all three loading surfaces in the deviatoric plane is defined by an elliptic interpolation between the two meridians, as introduced by William and Warnke (1975). This is the most common approach for the deviatoric plane, as it meets all the requirements for a concrete failure surface discussed in Chapter 2. It also produces the best fit to the test data shown in Figure 4.11. Section 3.1.2 shows the equations defining this elliptic shape.

3.1.1 Meridians

The peak and residual loading surfaces are controlled by two hyperbolic meridians in the (ξ, r), or meridian, plane. They are denoted as the tensile and compressive meridians based on the value of the Lode angle for that meridian. Recall from Section 2.2 that the tensile and compressive meridians correspond to Lode angles of 0° and 60°, respectively. For the peak and residual surfaces, these two meridians have a hyperbolic shape as described by Equation 3.1 and seen in Figure 3.2.

$$\begin{aligned} \frac{r_{t,i}}{f'_c} &= -\tfrac{1}{2}a_{3,i} + \sqrt{a_{0,i} + a_{1,i}\frac{\xi}{f'_c} + a_{2,i}\left(\frac{\xi}{f'_c}\right)^2 + \tfrac{1}{4}a_{3,i}^2} \qquad \theta = 0^\circ \\ \frac{r_{c,i}}{f'_c} &= -\tfrac{1}{2}b_{3,i} + \sqrt{b_{0,i} + b_{1,i}\frac{\xi}{f'_c} + b_{2,i}\left(\frac{\xi}{f'_c}\right)^2 + \tfrac{1}{4}b_{3,i}^2} \qquad \theta = 60^\circ \end{aligned} \qquad i = \text{peak, residual} \tag{3.1}$$

The concrete compressive strength, f'_c, is defined in the accepted fashion as the compressive strength at 28 days of a uniaxially loaded cylinder, with a height equal to twice the width (ACI Committee 318, 2000). Note that values of ξ are negative for

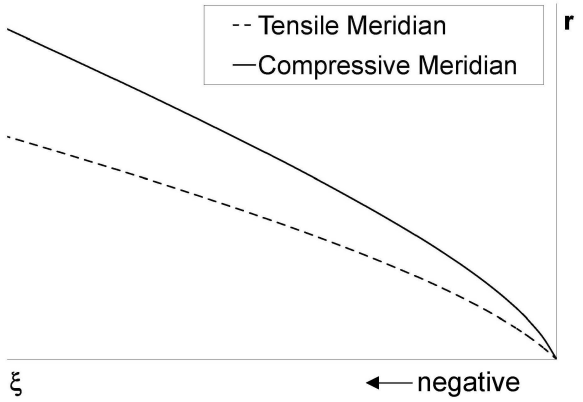

Figure 3.2: Shape of the peak and residual tensile and compressive meridians in the (ξ, r) space. Note that values of ξ are negative for compression.

compression. The invariants ξ and θ are defined in Equations 2.10 and 2.12, respectively. Values of the parameters a_0 through a_3 and b_0 through b_3 are determined from test data in Section 4.2.3 for the peak surface and Section 4.3.3 for the residual loading surface.

The yield loading surface is not based on hyperbolic meridians. It is well known that the yield point for concrete is not precisely defined due to the gradual onset of yielding. However, a single yield surface is designated at the initiation of yielding, rather than using multiple surfaces to define a yield region. The region of yielding will be accounted for through the transition of the failure surface from the yield surface to the peak surface, wherein damage is accumulating but strain softening has not yet initiated. Strain softening is defined as the region in which the stress in the material is actually decreasing with an increase in strain. The location of the yield surface is somewhat arbitrary but should be close to the initial onset of yielding. The test data show that the peak and residual stresses increase more significantly with confinement than the yield stress. Whereas the peak and residual stresses increase hyperbolically with confinement, the yield stress approaches a constant. Thus, the

following equation is chosen to define the meridians for the yield loading surface:

$$\begin{array}{rclcrcl} \frac{r_{t,yield}}{f'_c} & = & -c\frac{\xi}{f'_c}\left(1-\frac{\xi}{f'_c}\right)^{-1} & & \theta & = & 0^\circ \\ \frac{r_{c,yield}}{f'_c} & = & -d\frac{\xi}{f'_c}\left(1-\frac{\xi}{f'_c}\right)^{-1} & & \theta & = & 60^\circ \end{array} \tag{3.2}$$

The shape of the yield tensile and compressive meridians is shown in Figure 3.3.

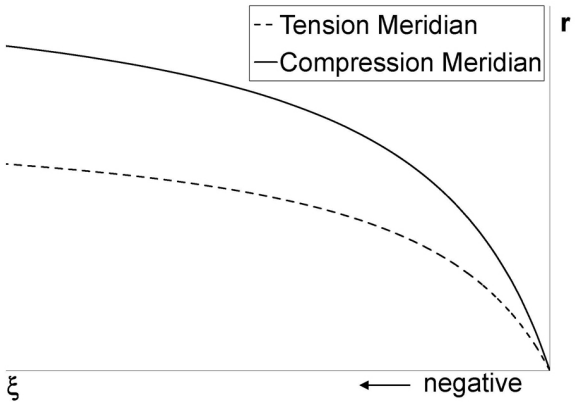

Figure 3.3: Shape of the yield tensile and compressive meridians in the (ξ, r) space. Note that values of ξ are negative for compression.

There are eighteen parameters (the a and b series for the peak and residual surfaces, and c and d for the yield surface) that control the increase in the failure deviatoric stress due to confinement. For all three loading surfaces, the difference between the a and b series of parameters (or c and d for the yield loading surface) accounts for the change in deviatoric stress caused by the Lode angle passing from 0° to 60°. It can be seen from test data that the deviatoric stress at yield, peak, or residual is lower at a Lode angle of 0° then at 60°. Thus, the tensile meridian will always have a smaller magnitude than the compressive meridian as seen in Figure 3.2. Equations 3.1 and 3.2 account for the increase in the strength of concrete as a result of confinement. The magnitude of ξ increases with increasing confinement. Through Equations 3.1 and 3.2, higher magnitudes of ξ lead to higher values for r before the failure surface is reached. The increase in the magnitudes of both ξ and r equate to larger stresses being supported by the concrete under confinement.

3.1.2 Elliptic Fit

The shape of the loading surface in the deviatoric plane is chosen as an elliptic curve, shown in Figure 3.4, defined by a method introduced in William and Warnke (1975). By using an ellipse, all the conditions of smoothness, symmetry, and convexity dis-

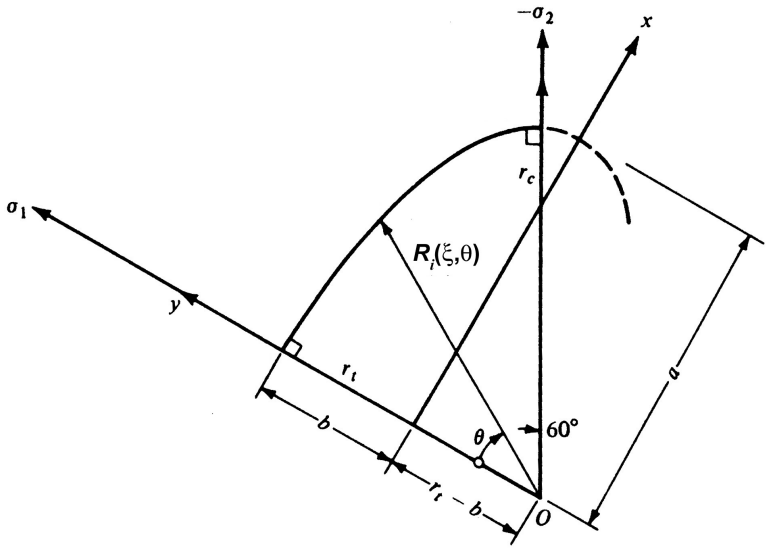

Figure 3.4: Elliptic trace of the failure surface for $0° \leq \theta \leq 60°$. Based on Chen (1982).

cussed in Chapter 2 are met. The elliptic curve between the two meridians is defined by Equation 3.3. The resulting full cross section of the loading surface in the deviatoric plane can be seen in Figure 3.5. Note that in Figure 3.5, the ξ axis is normal to the cross section plane, which is also the plane of the page, and passes through the origin.

$$R_i(\xi,\theta) = \frac{2r_{c,i}(r_{c,i}^2-r_{t,i}^2)cos\theta+r_{c,i}(2r_{t,i}-r_{c,i})\sqrt{4(r_{c,i}^2-r_{t,i}^2)cos^2\theta+5r_{t,i}^2-4r_{t,i}r_{c,i}}}{4(r_{c,i}^2-r_{t,i}^2)cos^2\theta+(r_{c,i}-2r_{t,i})^2} \tag{3.3}$$

$i =$ yield, peak, residual

Thus, each of the three loading surfaces is defined:

$$F_i = r - R_i(\xi,\theta) = 0 \qquad i = \text{yield, peak, residual} \tag{3.4}$$

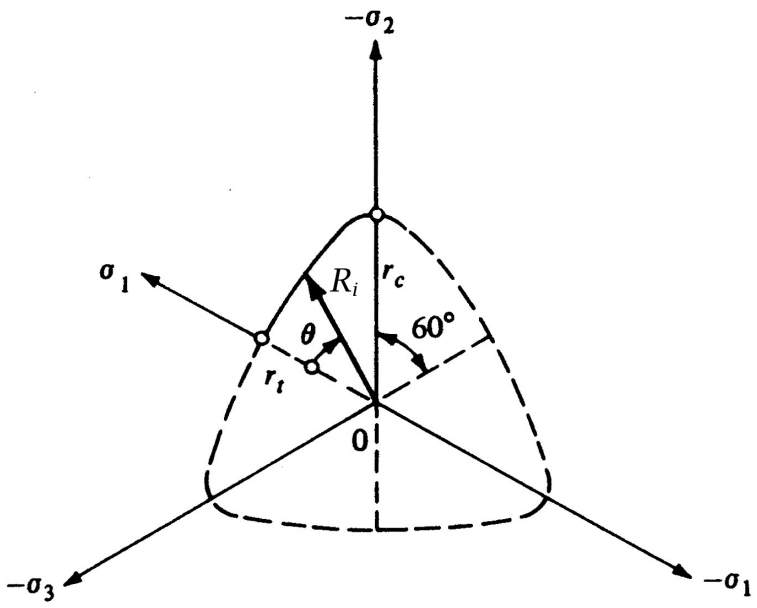

Figure 3.5: Deviatoric section of the failure surface. Modified from Chen (1982).

The invariant r is defined in Equation 2.11. The value for $R_i(\xi, \theta)$ is given by Equation 3.3 with the corresponding set of parameters for that loading surface (i.e., yield, peak, or residual).

3.2 Failure Surface

Recall that all three of these loading surfaces are fixed in the (ξ, r, θ) invariant space. The current failure surface is a linear combination of two of the three surfaces based on the current damage level, ψ. The value for ψ is integrated along the loading path of the material in order to represent the current total damage level. The incremental damage for a given load step is defined by:

$$d\psi = \frac{\overline{d\epsilon^p}}{\phi + \alpha(|\frac{\xi}{f'_c}|^\gamma)} \tag{3.5}$$

The effective plastic strain increment, $\overline{d\epsilon^p}$, was previously defined in Equation 2.17 and is restated here:

$$\overline{d\epsilon^p} = \sqrt{\frac{2}{3} d\epsilon^p_{ij} d\epsilon^p_{ij}} \tag{3.6}$$

The parameter, ϕ, defines how damage is accumulated at very low levels of stress. The invariant ξ must be located in the denominator so that large values of confinement, which result in large values for ξ, result in a decrease in the rate at which damage is accumulated. The parameters α and γ control how the damage accumulation rate is affected by confinement. Equation 3.5 is used to account for the increase in ductility seen in concrete due to increasing levels of confinement. The form of this equation is based on Malvar et al. (1994); changes were made in order to simplify the model and to better match the test data.

The location of the current failure surface based on the damage level is controlled by the variable β:

$$\beta = \left(\frac{\psi}{\psi_{peak}}\right)^{\kappa} e^{1-\left(\frac{\psi}{\psi_{peak}}\right)^{\kappa}} \tag{3.7}$$

The parameter, ψ_{peak}, defines the damage level at which the peak surface is reached. The parameter, κ, controls the rate at which the failure surface travels from one loading surface to the next. This functional form of β is based on a form derived by Smith and Young (1955) to represent the shape of the stress versus strain relationship for uniaxial compression loading shown in Figure 3.1. The value of β is zero until the load path intersects the yield loading surface. It then passes from zero to one as the current failure surface travels from the yield to the peak loading surfaces. The value of β then decreases from one back to zero as the current failure surface travels from the peak to the residual loading surface. The current failure surface can now be found by:

$$F = 0 = r - \begin{cases} \beta\left(R_{peak}(\xi,\theta) - R_{yield}(\xi,\theta)\right) + R_{yield}(\xi,\theta) & \psi \leq \psi_{peak} \\ \beta\left(R_{peak}(\xi,\theta) - R_{residual}(\xi,\theta)\right) + R_{residual}(\xi,\theta) & \psi > \psi_{peak} \end{cases} \tag{3.8}$$

The invariant r is defined in Equation 2.11. $R_{yield}(\xi,\theta)$, $R_{peak}(\xi,\theta)$, and $R_{residual}(\xi,\theta)$ are defined in Equation 3.3.

3.3 Flow Rule

Based on Malvar et al. (1996), a blend of two common flow rules was utilized which led to good agreement with test data. An associated flow rule for this model results in plastic volume expansion in excess of that indicated by test data. However, using a Prandtl-Reuss flow rule (Chen, 1982) does not allow for any plastic volume expansion, which is also not correct for concrete. Thus, a combination of the two rules is used, resulting in a nonassociated flow rule for the model.

The potential surface, Q, is therefore defined as the interpolation of two surfaces. The first surface is equal to the failure surface, as would be defined for associative flow. The second surface represents a circular cylinder passing through the failure surface at the point representing the current stress state whose axis lies along the ξ axis. This definition for Q is implemented into Equation 2.14 to determine the plastic strain increment. The parameter, ω, controls the amount of plastic volume change seen in the material. The effect of ω on the direction of plastic flow can be seen in Figure 3.6.

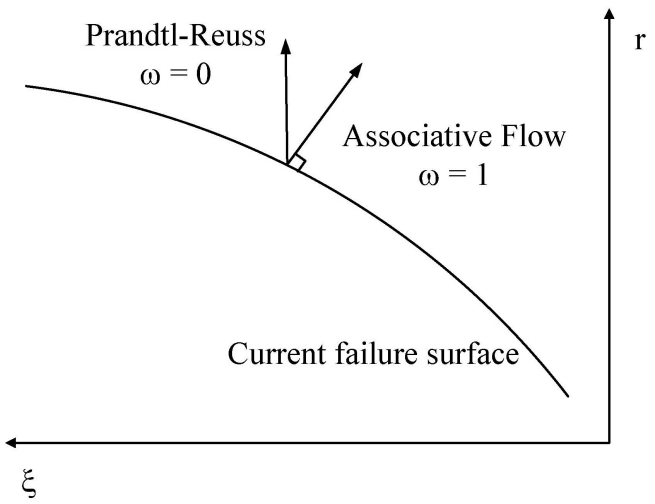

Figure 3.6: Graphical representation of the direction of plastic flow depending on ω based on Noble et al. (2005). Note that values of ξ are negative for compression.

3.4 Model Parameters

The model contains a total of twenty-four parameters that control its behavior. The values for these parameters are determined using test data in Chapter 4. A summary of these parameters and their significance is shown in Table 3.1. These twenty-four

Table 3.1: Summary of model parameters.

Name	Behavior Controlled	Total
a_0, a_1, a_2, a_3 x 2 surfaces	shape of the hyperbolic tensile meridian for the peak and residual loading surfaces	8
b_0, b_1, b_2, b_3 x 2 surfaces	shape of the hyperbolic compressive meridian for the peak and residual loading surfaces	8
c	shape of the tensile meridian for the yield loading surface	1
d	shape of the compressive meridian for the yield loading surface	1
ϕ	accumulation of damage at low stress levels	1
α, γ	accumulation of damage as a function of confinement	2
ψ_{peak}	amount of damage corresponding to the peak stress level of the concrete	1
κ	rate at which the current loading surface passes between each of the fixed surfaces	1
ω	ratio of associated plastic flow to Prandtl-Reuss plastic flow	1
Total		24

parameters can be fit to the test data for all types of concrete and defined permanently. Thus, a user of the model does not need to specially tune these parameters to the individual specimen of concrete being analyzed. However, if the user is intending to model a specific concrete mix, or a specific type of concrete, the parameters could be fit using a subset of data matching the concrete that is to be modeled. The model also requires three input parameters that are specific to the concrete specimen being modeled: the modulus of elasticity, E; Poisson's ratio, ν; and the unconfined compressive strength, f'_c, of the concrete.

3.5 Tangent Modulus Tensor

Once the plasticity model is completely defined, the consistency condition is used to derive the tangent modulus tensor, which defines the relationship between the incremental stress and strain. The consistency condition as derived in Section 2.4 and given in Equation 2.20 is:

$$dF = \frac{\partial F}{\partial \sigma_{ij}} d\sigma_{ij} + \frac{\partial F}{\partial \overline{\epsilon^p}} d\overline{\epsilon^p} = 0 \tag{3.9}$$

where $d\overline{\epsilon^p}$ is given by Equation 3.6 and the elastic stress increment, $d\sigma_{ij}$, is given by:

$$d\sigma_{ij} = D^e_{ijkl} \left(d\epsilon_{kl} - d\epsilon^p_{kl} \right) \tag{3.10}$$

D^e_{ijkl} is the elastic modulus tensor, $d\epsilon_{kl}$ the total strain increment, and $d\epsilon^p_{kl}$ the plastic strain increment as defined in Section 2.3. The definition of the plastic strain increment, as given in Equation 2.14, is restated here:

$$d\epsilon^p_{ij} = d\lambda \frac{\partial Q}{\partial \sigma_{ij}} \tag{3.11}$$

where Q is defined as discussed in Section 3.3. Substituting Equations 3.10 and 3.11 into Equation 3.9, combined with Equation 3.6 for $\overline{d\epsilon^p}$, yields an equation that can be solved for $d\lambda$:

$$d\lambda = \frac{\frac{\partial F}{\partial \sigma_{ij}} D^e_{ijkl} d\epsilon_{kl}}{\frac{\partial F}{\partial \sigma_{mn}} D^e_{mnpq} \frac{\partial Q}{\partial \sigma_{pq}} - \frac{\partial F}{\partial \overline{\epsilon^p}} \sqrt{\frac{2}{3} \frac{\partial Q}{\partial \sigma_{ij}} \frac{\partial Q}{\partial \sigma_{ij}}}} \tag{3.12}$$

Using Equation 3.12 for $d\lambda$ with Equation 3.11 yields an expression for $d\epsilon^p_{ij}$ which can be combined with Equation 3.10 to define the tangent modulus tensor.

$$d\sigma_{ij} = D^{tangent}_{ijkl} d\epsilon_{kl} = \left(D^e_{ijkl} + D^p_{ijkl} \right) d\epsilon_{kl} \tag{3.13}$$

where the plastic modulus tensor is given by:

$$D^p_{ijkl} = -\frac{D^e_{ijtu}\left(\frac{\partial Q}{\partial \sigma_{tu}}\right)\left(\frac{\partial F}{\partial \sigma_{rs}}\right)D^e_{rskl}}{\frac{\partial F}{\partial \sigma_{mn}}D^e_{mnpq}\frac{\partial Q}{\partial \sigma_{pq}} - \frac{\partial F}{\partial \overline{\epsilon^p}}\sqrt{\frac{2}{3}\frac{\partial Q}{\partial \sigma_{ij}}\frac{\partial Q}{\partial \sigma_{ij}}}} \tag{3.14}$$

A detailed derivation of this equation can be found in Section 8.5 of Chen (1982). Expressions for the partial derivatives in Equation 3.14 can be derived from the equations found in this chapter and are given in Appendix A. The tangent modulus tensor will be implemented into finite element code in order to utilize the material model for predicting the behavior of concrete.

Chapter 4

Model Identification

The twenty-four parameters that define the concrete model must be determined using test data and common assumptions about concrete behaviors. If the model is to be used for a specific analysis, the ideal approach would be to fit the model using test data from the actual concrete being analyzed. However, if the model is to be used for predictive analysis, the exact behavior of the concrete will likely not be known before the analysis is performed. For this type of use, the parameters should be determined for some average concrete behavior that is able to represent typical concretes used in construction. Thus, a large quantity of test data with different types of confinement methods, concrete strengths, aggregate sizes, saturation levels, cross-sectional shapes, loading configurations, age, etc., were used to choose the values for the parameters. While it is clear that some of these variables will affect the strength and ductility of concrete, in many cases the values for these variables are not known at the time the analysis is performed. For example, the aggregate type used in the mix may not be known at the time of design, but would be known once the structure was constructed. Another example is the age of concrete, because the designer cannot know when the concrete will experience an extreme loading event. Therefore, it is necessary to obtain data with a wide range of values for these variables.

In typical structural applications, it is common to assume that the concrete is pre-cracked. Thus, for simplicity of the model as defined in this thesis, the pre-cracked assumption is used. This means that the yield, peak, and residual surfaces must all pass through the origin in the (ξ, r, θ) invariant space. The yield surface meridians

are defined such that this criteria is already met. For the peak and residual surfaces, the pre-cracked assumption is used to define two of the parameters. In the case of all three surfaces, tension strength could easily be added at a later time, were it required.

This chapter describes how the values of the twenty-four parameters given in Table 3.1 were determined. The process for obtaining the parameters c and d, which define the yield surface, is discussed in Section 4.1. Determining the parameters for the peak surface—and the extensive test data used in that process—is discussed in Section 4.2. Similarly, the method for determining the residual surface is outlined in Section 4.3. The relationship used to define the damage increment, $d\psi$, and the determination of the value for γ, are discussed in Section 4.4. Finally, the determination of the parameters relating to the flow rule and the location of the failure surface are discussed in Section 4.5.

4.1 Yield Surface Definition

The equations that define the yield surface have only two parameters. As discussed in Section 3.1.1, the precise location of the yield surface is not critical since the onset of concrete yielding occurs gradually. Thus, the parameter d was determined by assuming that the yield point of uniaxially loaded concrete is 45% of the peak stress. This assumed yield point for concrete is commonly used [for example, Malvar et al. (1994)]. The stress state at uniaxial yield is given by:

$$\left.\begin{aligned} \sigma_x &= \sigma_y = 0 \\ \sigma_z &= (-0.45) f'_c \end{aligned}\right\} \text{at uniaxial yield} \tag{4.1}$$

Equation 4.1 corresponds to the invariant values:

$$\left.\begin{aligned} \xi &= -\tfrac{0.45 f'_c}{\sqrt{3}} \\ r &= 0.45\sqrt{\tfrac{2}{3}} f'_c \\ \theta &= 60^\circ \end{aligned}\right\} \text{at uniaxial yield} \tag{4.2}$$

Implementing this stress state into Equation 3.4 for the yield surface gives a value for the parameter d:

$$d = 0.45\sqrt{\frac{2}{3}}\left(1 + \frac{\sqrt{3}}{0.45}\right) \simeq 1.78 \tag{4.3}$$

Similarly, data from Kupfer et al. (1969) indicate that biaxial loading of concrete results in a 16% increase in concrete stress when a specimen is loaded biaxially. Thus, it is assumed that a specimen loaded biaxially will yield at 45% of a peak stress increased by 16%. This corresponds to the stress state given by:

$$\left.\begin{aligned} \sigma_x &= 0 \\ \sigma_y = \sigma_z &= -(0.45)(1.16)f'_c \end{aligned}\right\} \text{at biaxial yield} \tag{4.4}$$

Equation 4.4 corresponds to the invariant values:

$$\left.\begin{aligned} \xi &= -\tfrac{(2)(0.45)(1.16)f'_c}{\sqrt{3}} \\ r &= (0.45)(1.16)\sqrt{\tfrac{2}{3}}f'_c \\ \theta &= 0^\circ \end{aligned}\right\} \text{at biaxial yield} \tag{4.5}$$

Implementing this stress state into Equation 3.4 for the yield surface gives a value for the parameter c:

$$c = (0.45)(1.16)\sqrt{\frac{2}{3}}\left(1 + \frac{\sqrt{3}}{(2)(0.45)(1.16)}\right) \simeq 1.13 \tag{4.6}$$

The parameters c and d uniquely define the yield surface. These values for the parameters, defined in Equations 4.3 and 4.6, respectively, were used to validate the model (Chapter 6) and predict concrete behavior (Chapter 7).

In summary, a simplified approach was taken to define the yield surface since it is not critical in predicting the effect of confinement on concrete. The remaining components of the model capture the important behaviors of concrete under confinement. Parameters pertaining to those components will be determined in a more rigorous fashion in the following sections.

4.2 Peak Surface Correlation

A total of twenty-one data sets, published in twenty-seven papers, were obtained to estimate the parameters defining the peak surface. The tests performed in each of the published studies were intended to study the effects of confinement on the behavior of concrete. Several of the authors designed their experiments to test the effects of certain variables on confined concrete behavior. Other papers only test a single concrete mix at different confinement levels, but can be compared to similar papers to understand the effect of different concrete variables. With the compilation of all twenty-one data sets, a large number of concrete variables were taken into consideration.

Several concrete mix variations were tested in the different papers. The concrete age at testing varied from 10 to 200 days. Water-cement ratios of 0.26 to 1.25 were used. Several different additives were considered, including fly ash, silica fume, superplasticizers, air-entraining agents, and water-reducing agents. The type, weight, surface roughness, and size of the aggregates varied widely throughout the studies. A maximum coarse aggregate size range of 0.375 to 1.5 inches (9.5 to 38 mm) was seen throughout the papers, and some mixes did not include any coarse aggregate, only sand. The proportions of water/cement/sand/aggregate were varied over a large range. The saturation level was varied from oven dried to 100% saturated and immersed in fluid at the time of testing. The final concrete compressive strength in the tests varied from 1.1 to 19.1 ksi (7.5 to 132 MPa)

Test setup details created other variables within the tests. Specimen sizes and shapes ranged from 2.125 x 4.25 inch (54 x 108 mm) cylinders, 5 x 5 x 0.5 inch (125 x 125 x 12.5 mm) plates, and 2.25 x 2.25 x 2.25 inch (57.2 x 57.2 x 57.2 mm) cubes up to 12 x 14 inch (305 x 350 mm) cylinders, 7.9 x 7.9 x 2 inch (200 x 200 x 50 mm) plates, and 4 x 4 x 4 inch (100 x 100 x 100 mm) cubes. The load paths varied over Lode angles from 0° to 60°, and failure was approached from multiple different directions. Two papers detailed experiments with different friction reducing boundary conditions including dry steel platens, one or two 0.08 in (2 mm) thick resin sheets

both ungreased and greased, teflon greased teflon pads, and polyester film greased aluminum pads.

The method of testing was varied utilizing different methods of lateral load application including active and passive confinement and biaxial and triaxial loading. Passive tests included several different types of confining materials including steel rebar and glass and carbon fiber reinforced polymer (FRP). The number and strength of the FRP wraps was varied as well as the diameter, spacing, and yield strength of the steel rebar.

The compilation of the data represents a wide range of a large number of important concrete variables, which is critical to representing a wide variety of different concrete and loading conditions. Details of each paper contributing data used for the peak surface are discussed in Section 4.2.1. The compilation of the data is shown and discussed in Section 4.2.2. Finally, the fit for the peak loading surface is discussed in Section 4.2.3.

4.2.1 Peak Surface Papers

Table B.1 gives a summary of the twenty-one data sets. Discussion of the papers is divided based on the loading configuration. Though the papers are discussed and separated by loading configuration, all data were used together for estimating the parameters. The other variables tested will be highlighted in the discussion of each individual paper.

Twelve of the data sets used a triaxial pressure vessel, or Hoek cell, for loading. Details of this type of machine are discussed extensively elsewhere [for example, MTS Systems Corporation (2004), Hoek and Franklin (1968), and Blanks and McHenry (1945)]. To summarize, the specimen to be tested is placed in a traditional universal testing machine for the axial loading. However, the cylinder is enclosed by a fluid-filled pressure chamber and sheathed in rubber, neoprene, plastic, or similar casing to prevent the fluid from penetrating the specimen. In this way, the specimen has a constant, controlled lateral pressure throughout the duration of the loading. In these

types of tests, hydrostatic pressure means that equal loads are applied axially (by the universal testing machine) and laterally (by the fluid). A typical example of this type of machine is shown in Figure 4.1. Use of this type of machine proves an ideal

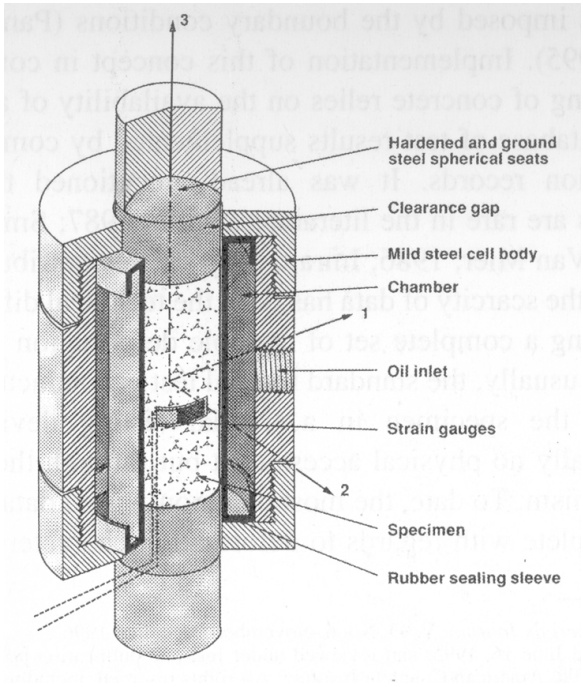

Figure 4.1: Example of a triaxial pressure vessel. Reproduced from Imran and Pantazopoulou (1996).

way to test the effect of confinement on different types of concrete. For this reason, the majority of the data sets chosen used this method. These papers are discussed in Section 4.2.1.1. The limitation of this setup is the inability to have intermediate values for the Lode angle. The Lode angle is either 0° or 60°, based on whether the fluid pressure exceeds the axial load being applied.

Four papers were chosen that tested concrete cubes under true triaxial loading, allowing for the full range of Lode angles to be tested. These researchers utilized a triaxial device that had the ability to apply loads along each of the three axes independently. The four true triaxial papers are detailed in Section 4.2.1.2. The machine utilized for each set of experiments is discussed in the individual papers. The typical setup was to use three independent hydraulic rams to apply loads in the three orthogonal directions of the cubic specimen. An example of this type of

machine is shown in Figure 4.2. The challenge with this type of loading is to ensure the

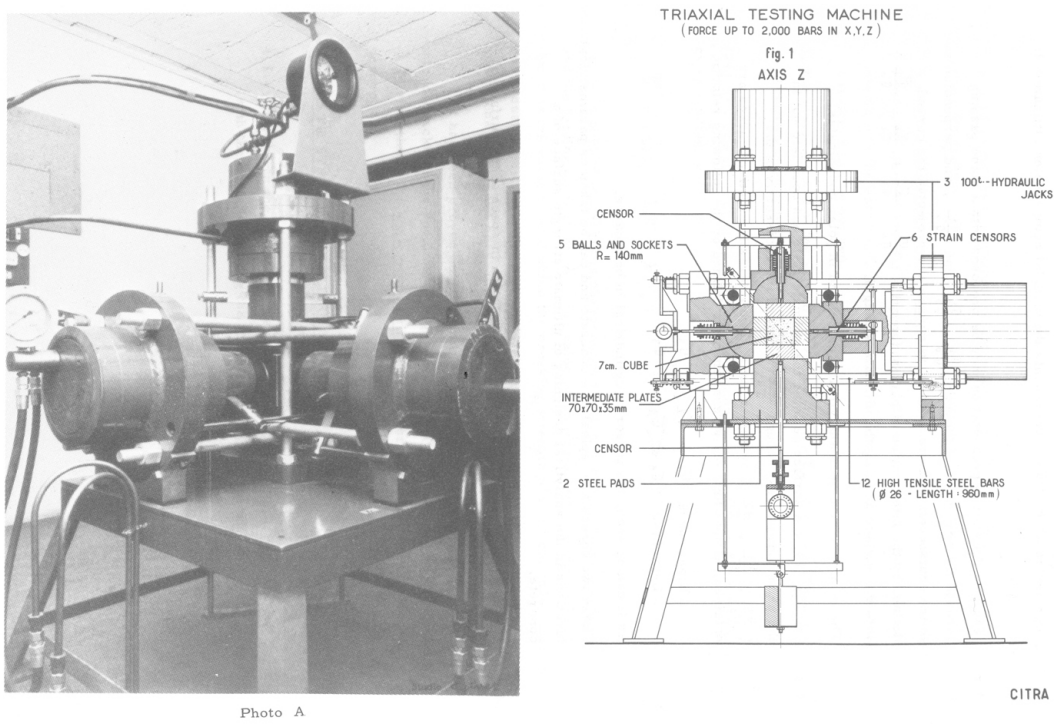

Figure 4.2: Example of a true triaxial testing machine. Reproduced from Launay and Gachon (1972a).

proper friction reducing boundary condition. The approach to avoid these boundary condition effects is discussed in each individual paper.

Three papers were chosen that used passive confinement. Two of these utilized steel rebar or wire, the third used fiber reinforced composite sheets. Equations were presented in each paper to estimate lateral pressure as a function of the confinement configuration. Those equations were used in this thesis when calculating the lateral pressure on the specimen at peak stress. The papers are summarized in Section 4.2.1.3.

Finally, two papers were selected that performed traditional biaxial tests. Biaxial testing has the same challenges as true triaxial loading in regards to minimizing the effects of the boundary conditions. Biaxial papers are discussed in Section 4.2.1.4.

4.2.1.1 Peak Surface Papers Utilizing a Triaxial Pressure Vessel

A set of papers were published by Q. Li and F. Ansari detailing their experiments [(Ansari and Li, 1998), (Li and Ansari, 1999), (Li and Ansari, 2000)]. A modern triaxial pressure vessel (MTS Systems Corporation, 2004) was used for these tests. Concrete cylinders were enclosed in a rubber membrane for testing. The confinement effect of this membrane, leading to an average 7% increase in axial strength, was taken into account in the results. Three high strength mixes with f'_c values of 6.9, 10.3, and 15.6 ksi (47.7, 71.1, and 107.3 MPa) were tested in Ansari and Li (1998) and Li and Ansari (1999), while only the two higher strength mixes were tested in Li and Ansari (2000). A comparison of specimen sizes was performed by using 4 x 8 inch (100 x 200 mm) cylinders in Ansari and Li (1998) and Li and Ansari (1999), while 3 x 6 inch (76 x 152 mm) cylinders were used in Li and Ansari (2000). Specimens in Ansari and Li (1998) and Li and Ansari (1999) were tested at an age of 40 $\pm$ 7 days. Specimens in Li and Ansari (2000) were tested at an age of 35 $\pm$ 7 days. In both cases, the specimens were moist cured until the day before testing. Specimens were hydrostatically loaded to the desired lateral confining pressure, then the axial load was increased to failure. Confinement pressures ranging from $0.18f'_c$ to $0.93f'_c$ were applied. The authors concluded that the influence of confining pressure on the failure strength of high strength concrete is not as pronounced as with normal strength concrete. However, there is a large and distinct increase in the failure strain of high strength concrete due to confinement. Results of the final paper were used to conclude that high strength concrete has a minor size effect, but it is not necessary to take it into account when modeling failure surfaces.

Attard and Setunge (1994) and Attard and Setunge (1996) used five different concrete mixes with three different coarse aggregate types leading to eleven different cylinder strengths, with f'_c values ranging from 8.4 to 19.1 ksi (58 to 132 MPa). The 4 x 8 inch (100 x 200 mm) cylindrical specimens were moist cured at 100% humidity until 7 days before testing, then air dried to reduce the influence of pore water pressure on the results. Most of the specimens were tested at 90 days after casting. Confining

pressures ranging from 72.5 to 2900 psi (0.5 to 20 MPa) were applied to the cylinders through the pressurized fluid. The authors concluded that the type of aggregate used had a significant influence on the elastic modulus, strain at peak stress, and ductility.

Balmer (1949) used the then recently constructed triaxial pressure vessel (Blanks and McHenry, 1945) for his experiments. The 6 x 12 inch (152 x 305 mm) cylindrical specimens were all cast from the same mix, fog-cured for 28 or 90 days, then oven dried for 7 days. The 28 and 90 day specimens had unconfined strengths of 3.6 and 4.0 ksi (25 and 28 MPa), respectively. Confining pressures from 1 to 25 ksi (7 to 172 MPa) were applied through the use of pressurized kerosene. The specimens were encased in rubber jackets. The author concluded that the increase in strength with confinement was nonlinear.

Bellamy (1961) used both solid and hollow cylinders in his testing. The cylinders were 6 x 12 inches (152 x 305 mm) in size, and the hollow cylinders had an inner diameter of 2.95 inches (74.9 mm). Specimens were fog cured at 100% humidity for 7 days and then stored at 80% humidity until testing at an approximate age of 200 days. The solid cylinders were tested to determine the increase in strength and strain at failure due to triaxial loading. The hollow cylinders were used to investigate biaxial loading. Failure always initiated at the inside face of the hollow cylinders where the concrete was in a biaxial stress state. Both types of cylinders were hydrostatically loaded to the desired lateral pressure, then the axial load was increased to failure. The comparison of the two different loading types was used to draw some conclusions about the effect of the Lode angle. The author concluded that the intermediate principal stress increased the major principal stress at failure by a minimum of 75%.

Tests performed by Candappa, Setunge, and Sanjayan investigated the complete stress versus strain curves of high strength concrete [(Candappa et al., 1999), (Candappa et al., 2001)]. The 4 x 8 inch (100 x 200 mm) cylinders were placed in a thin polyurethane membrane, and the lateral confining pressure was applied through the use of oil. Three high strength mixes and one normal strength mix were tested. Cylinders were cured for 28 days in standard bath conditions, then allowed to air dry for at least 28 days before testing. At the time of testing, cylinder strengths

(f'_c) of the four mixes were 6.1, 8.8, 10.6, and 15.0 ksi (41.9, 60.6, 73.1, and 103.3 MPa). Confining pressures of 0.6, 1.2, and 1.7 ksi (4, 8, and 12 MPa) were tested. Specimens were loaded laterally to the desired confinement level and then the axial load was increased to failure. The authors concluded that the axial strain at peak stress showed a linear relationship with confinement. They also noted that the effect of confinement on strains at peak stress appears less for high strength concrete under higher confinement levels.

Chinn and Zimmerman (1965) used the same triaxial pressure vessel as Balmer (1949), but specimens were loaded to much higher confining pressures. Four different loading paths were tested. Type one loading, similar to other papers, was to load the specimen hydrostatically to the desired confining pressure, then increase the axial load to failure. Confining pressures for this load type varied from $0.5f'_c$ to $17.1f'_c$. Type two was to load the specimens hydrostatically to the desired axial pressure and then increase the confining pressure to failure. Axial loads ranged from 0.0 to $3.7f'_c$, while final lateral pressures ranged from $1.4f'_c$ to $11.5f'_c$. These two loading types were performed to examine the effect of the two extreme values for the Lode angle at various confinement levels. Type three was pure hydrostatic loading to the capacity of the testing machine. Type four was to increase lateral stresses as a constant proportion of the axial stress until the specimen failed. Final confining pressures for this loading varied from $2.2f'_c$ to $12.2f'_c$. During testing, the 6 x 12 inch (152 x 305 mm) cylinders were encased in either a neoprene or polyvinylchloride sheath. Three concrete mixes were arbitrarily selected with target compressive strengths of 4, 7, and 10 ksi (28, 48, and 69 MPa). Due to variations in the mixture and casting methods, the actual f'_c values varied from 3.4 to 10.3 ksi (23 to 71 MPa). Specimens were cured for 7 days and then oven dried for 24 hours. Due to issues with the testing machine, the specimens were then stored in the lab for 1 to 10 days before being tested. Both type one and type two loading showed a linear increase in strength with confinement. However, the slope of this line was 1.0 for type one and 2.1 for type two. By comparing type four loading with type one, it was noted that the load path did not affect the final stress state of the specimen at failure.

Cordon and Gillespie (1963) undertook an extensive investigation of the effects of different aggregates and cements on the strength of concrete. Eighteen different concrete mixes were made for triaxial testing with water-cement ratios of 0.40, 0.55, and 0.70 with 0.75 and 1.5 inch (19 and 38 mm) maximum coarse aggregate sizes. Final f'_c values ranged from 5.7 to 6.6 ksi (39 to 46 MPa), with slumps ranging from 1 to 8 inches (25 to 200 mm). The 6 x 12 inch (152 x 305 mm) cylinders were encased in thin plastic bags and tested at confinement pressures ranging from $0.05f'_c$ to $1.13f'_c$. The authors concluded that water-cement ratio is not the sole important variable in establishing the strength of the concrete; the maximum size, surface texture, and shape of the aggregate are also important.

Duke and Davis (1944) studied the effect of saturation on the creep and triaxial strength of concrete. Saturated specimens were moist cured for 28 days before testing and were in direct contact with the water used to apply the lateral loads during testing. Partially-dry specimens were moist cured for 21 days, moved to 50% humidity for 5 days, and then coated with a heavy moisture-resistance lacquer for testing. Saturated specimens had a compressive strength, f'_c, of 5.7 ksi (39 MPa), while the partially-dry specimens had a compressive strength, f'_c, of 6.6 ksi (46 MPa). Lateral pressures of 0 to 900 psi (0 to 6 MPa) were applied to the 3 x 6 inch (76 x 152 mm) cylinders. Test results indicated that while the strength of the saturated specimens was lower, the strength increase due to lateral confinement was the same for saturated and partially-dry specimens.

Imran and Pantazopoulou (1996) investigated the effects of saturation, water-cement ratio, and load path on the triaxial behavior of concrete. Cylinders were encased in a urethane rubber membrane for testing in the triaxial pressure vessel. Lateral stresses of $0.05f'_c$, $0.10f'_c$, $0.20f'_c$, $0.40f'_c$, $0.70f'_c$, and $1.0f'_c$ were applied to the 2.125 x 4.25 inch (54 x 108 mm) cylinders. Water-cement ratios of 0.40, 0.55, and 0.75 were used. Saturated specimens were moist cured for approximately 3.5 months before testing, leading to concrete strengths of 3.1, 6.3, and 9.4 ksi (21.2, 43.5, and 64.7 MPa). Dry specimens were also moist cured for approximately 3.5 months, but then dried at 140°F (60°C) for 72 hours before testing. Final concrete strengths of the

dry specimens at testing were 4.2, 6.9, and 10.6 ksi (28.6, 47.4, and 73.4 MPa). Four load paths were considered. Type A loading applied the desired confining pressure while the axial load remained zero and then increased the axial load to failure. Type B loading alternated between increasing the confining pressure and the axial load in increments until failure was reached. Type C loading applied a specified confining pressure and then decreased the confining pressure and increased the axial load in increments until failure was reached. Type D loading applied the lateral pressure then cycled the axial load. The authors made several important conclusions. Failure of the concrete specimens tested triaxially was defined by the initiation of volumetric expansion. Saturated concrete specimens exhibited lower strength than comparable dry specimens. This weakening was more pronounced for concretes with a higher water-cement ratio. Concrete loaded cyclically exhibited a degradation in elastic modulus which led to some path dependence of the deformation behavior. Cyclically loaded specimens also exhibited higher volumetric expansion at the same level of axial deformation. However, the peak strength of the concrete was observed to be path independent.

Richart, Brandtzaeg, and Brown performed the pioneering work in the study of the triaxial behavior of concrete in their two papers, Richart et al. (1928) and Richart et al. (1929). The latter paper tested passively confined columns and will be discussed in Section 4.2.1.3. The former paper studied the effect of confinement on the strength and ductility of concrete through the use of a triaxial pressure vessel. Three different mixes were tested triaxially. The three mixes, with water-cement ratios of 0.64, 0.88, and 1.25, yielded final f'_c values of 1.1, 2.6, and 3.7 ksi (7.6, 18, and 26 MPa). The 4 x 8 inch (100 x 200 mm) and 4 x 22 inch (100 x 560 mm) cylinders were moist cured for approximately 27 days, then were typically allowed to air dry about one day before testing. Lateral confining pressure ranged from $0.07f'_c$ to $5.71f'_c$. Due to many problems with the testing equipment, the authors were only able to conclude that the strength of concrete is significantly raised through confinement. However, the variation with Lode angle was uncertain.

Rosenthal and Glucklich (1970) studied the biaxial behavior of concrete using

hollow cylinders in a triaxial pressure vessel. The 12 x 14 inch (305 x 350 mm) cylinders had an inner diameter of 9.8 inches (250 mm). Two concrete mixes, with water-cement ratios of 0.63 and 0.94, yielded compressive strengths at testing ranging from 2.8 to 6.9 ksi (20 to 48 MPa). The specimens were stored for 7 days under water, then for another 75 days at 65% humidity. Testing took place at an age of 90 days. The authors concluded that the initiation of failure in the concrete is through the initiation of internal cracking. They noted that by increasing the mean stress, the concrete was able to delay the onset of internal cracking to a higher load.

Sfer et al. (2002) studied the effect of age on the behavior of concrete under triaxial compression. One mix of concrete was used with a water-cement ratio of 0.57. The 6 x 12 inch (150 x 300 mm) cylinders were moist cured until tested. The cylinders were placed in a butyl sleeve, with a neoprene sleeve fitted over it, before being placed in the pressure vessel. One series of tests was performed at an age of 60 $\pm$ 9 days with a concrete compressive strength at testing of 4.8 ksi (32.8 MPa). The second series of tests, identical to the first, was performed at an age of 100 $\pm$ 15 days with a concrete compressive strength at testing of 5.6 ksi (38.8 MPa). Lateral pressures ranging from $0.04f'_c$ to $1.83f'_c$ were tested. By comparing the results with other tests, the authors concluded that the results were independent of specimen size. They also noted that by increasing the confining pressure, the failure of the specimens transitioned from a brittle to a ductile failure.

4.2.1.2 Peak Surface Papers Utilizing a True Triaxial Testing Machine

Chuan-zhi et al. (1987) studied the effects of different friction reducing boundary conditions on true triaxial testing. Four different friction-reducing pads were compared in the testing. Two mixes with two different coarse aggregates were used to cast the 4 x 4 x 4 inch (100 x 100 x 100 mm) cubes with concrete strengths ranging from 1.1 to 2.1 ksi (7.5 to 14.3 MPa) . Specimens were tested both biaxially and triaxially, with lateral confinement pressures ranging from $0.06f'_c$ to $3.43f'_c$ for the biaxial loading and $0.10f'_c$ to $4.20f'_c$ for the triaxial testing. The authors concluded that the Lode angle significantly affects the peak strength of the triaxially loaded specimens.

Lan and Guo (1997) investigated the effect of the load path on the multiaxial behavior of concrete. One concrete mix was used with a water-cement ratio of 0.71. The specimens were cast in four batches with f_c' values ranging from 2.2 to 3.8 ksi (15.0 to 26.5 MPa). The 2.78 x 2.78 x 2.78 inch (70.7 x 70.7 x 70.7 mm) cubes were moist cured for 28 days, then placed in air until testing. Four biaxial and two triaxial loading paths were considered. Details of the biaxial load paths can be found in the cited paper. The first triaxial load path was to hydrostatically load the cube and then decrease the axial load to failure. The second triaxial load path was to apply the two lateral loads to the desired value and then increase the axial load to failure. The authors concluded that, in practice, the biaxial strength of concrete is independent of the load path. By comparing the triaxial results of these experiments with triaxial results of other papers which utilized a different load path, the authors concluded that the triaxial strength of concrete is also load independent.

Launay and Gachon (1972a) and Launay and Gachon (1972b) performed triaxial tests on a concrete intended for use in a nuclear reactor. The mix for this concrete used a water-cement ratio of 0.53, creating a final compressive strength of 5.2 ksi (36 MPa). Cubes 2.76 x 2.76 x 2.76 inches (70 x 70 x 70 mm) were cured under water for 7 days and were then stored in a tight polyethylene sack until testing at 28 days. Specimens were tested at lateral pressures ranging from $0.20f_c'$ to $5.64f_c'$. The results included a fairly wide range of both the Lode angle and confinement levels.

Mills and Zimmerman (1970) also studied different friction reducing boundary conditions under uniaxial testing then utilized the best boundary pads to investigate the multiaxial behavior of concrete. Three different mixes with water-cement ratios of 0.49, 0.58, and 0.66 were used to cast the 2.25 x 2.25 x 2.25 inch (57.2 x 57.2 x 57.2 mm) cubes. Final compressive strengths of 3.3, 3.9, and 5.2 ksi (23, 27, and 36 MPa) were reached in the concrete. The cubes were moist cured for 28 days, then allowed to dry for approximately one month before testing. All stresses were applied hydrostatically until a particular direction had reached the desired level, at which point only the other directions continued to increase. This continued until failure of the specimen. Lateral stresses ranging from $0.02f_c'$ to $3.14f_c'$ were applied

to the cubes. A wide range of Lode angles was tested. The authors noted that the failure planes appeared in the plane or planes of the minimum principal stress. They also noted that the effect of the Lode angle was significant and should be taken into account when creating failure criteria.

4.2.1.3 Peak Surface Papers Utilizing Passive Confinement

Ahmad and Shah (1982) tested spirally-reinforced concrete cylinders. Seven series of tests were utilized: five with normal weight concrete, all of the same mix; two with lightweight concrete, each with its own mix. Cylindrical specimens 3 x 6 inches (75 x 150 mm) in size were stored at 100% humidity until 1 to 2 days before testing, when conditions were changed to 50% humidity. The age of the specimens at testing was varied from 28 to 200 days so as to have a variety of compressive strengths ranging from 3.8 to 9.5 ksi (26 to 65 MPa). The spiral pitch, diameter, and yield strength were varied for the eight different series. The authors concluded that an increase in compressive strength or use of lightweight aggregate decreases the effectiveness of confinement.

Toutanji (1999) studied the behavior of concrete columns wrapped in varying levels of FRP composite sheets. The 3 x 12 inch (76 x 305 mm) cylindrical specimens were all cast from the same mix, having a water-cement ratio of 0.5. The final compressive strength of the plain cylinders was 4.5 ksi (30.9 MPa). The cylinders were confined with two wraps of a unidirectional FRP sheet. Three types of fibers were used for the sheets, two carbon and one glass, which were bonded with the same type of epoxy system. The confined cylinders were then loaded in uniaxial compression to failure. The authors concluded that the compressive strength, maximum strain, and ductility were all significantly increased through the use of FRP confinement. The increase in strength of the specimens confined with carbon fiber was higher due to the higher lateral stresses supported by the carbon fiber, which had a higher elastic modulus and tensile strength.

Richart et al. (1929) tested concrete passively confined by steel wire or bar. Only one mix was tested, with a water-cement ratio of 0.87, and all specimens were 10 x

40 inch (254 x 1016 mm) cylinders. Cylinders were stored in the lab in wet burlap for 24 days to cure. Two days before testing, the burlap was removed and the cylinders were prepared for testing. Testing variables included only the amount and kind of spiral reinforcement. Two different sized mild steel drawn wires, three different sized mild steel rolled bars, and one high strength cable steel stock were used for reinforcement. Only one pitch was tested for each size of each steel type. Thus, six different reinforcement ratios were tested. The authors concluded that, within the range of confinement found by steel spirals, the increase in the strength of concrete was linear with confinement pressure.

4.2.1.4 Peak Surface Papers Utilizing Biaxial Loading

Calixto (2002) performed biaxial tension-compression loading. Specimens were 5 x 5 x 0.5 inch (125 x 125 x 12.5 mm) plates cast from the same high strength mix. The plates were cured at 100% humidity for 56 days, then removed and prepared for testing. The compressive strength of the plates at testing was 8.6 ksi (59.6 MPa), while comparable cylinder tests showed a compressive strength of 10.8 ksi (74.4 MPa). This difference was attributed to the lack of confinement existing in the plate specimens. The author noted that the shape of the strength envelope for high strength concrete is much more linear than that obtained for normal strength concrete. Further, the decrease in the compressive strength under biaxial tension-compression is lower for normal strength concrete than for high strength concrete.

Kupfer et al. (1969) and Kupfer and Gerstle (1973) performed a series of biaxial tests. Three concrete mixes with water-cement ratios of 0.43, 0.90, and 1.20 were used. Specimens were moist cured for 7 days, then stored at 65% humidity for 21 days. Final compressive strengths, f'_c values, of 2.77, 4.51, and 8.62 ksi (19.1, 31.1, and 59.4 MPa) were reached by the concrete. The 7.9 x 7.9 x 2.0 inch (200 x 200 x 50 mm) plates were tested at four different stress ratios: biaxial tension, tension-compression, and two biaxial compression states. The authors noted an average increase in strength of 16% when the specimens were loaded with equal compressive stresses in two principal directions.

4.2.2 Peak Surface Data

Figures 4.3 and 4.4 show all test data for Lode angles of 0° and 60° which correspond to the peak tensile and compressive meridians, respectively. Note that compression is defined as negative. Plots for each individual set of experiments are shown in Appendix C.

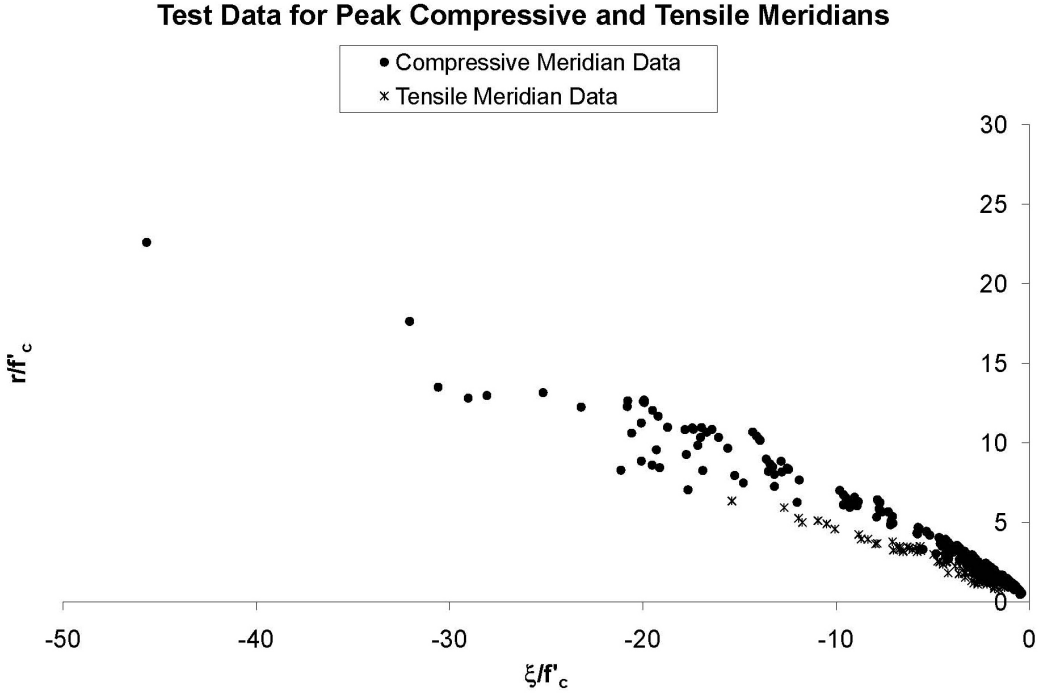

Figure 4.3: Test data for peak compressive and tensile meridians.

It is observed that some of the data at a Lode angle of 60° actually overlap with data for a Lode angle of 0°. The multiaxial loading configuration that corresponds to the strongest state for a concrete specimen is a Lode angle of 60°. If there exists some problem within the test setup, the concrete will soften prematurely, and the experimentally determined peak stress state will lie below the true peak stress state of the concrete. From all data sets, it is apparent that a Lode angle of 0° corresponds to a lower deviatoric stress, r, for the same hydrostatic stress, ξ. Authors that investigated the effect of the Lode angle on concrete behavior previously noted this from individual tests. Thus, a problem with the test setup could cause some data points for a Lode angle of 60° to be smaller and in the range of data for a Lode angle

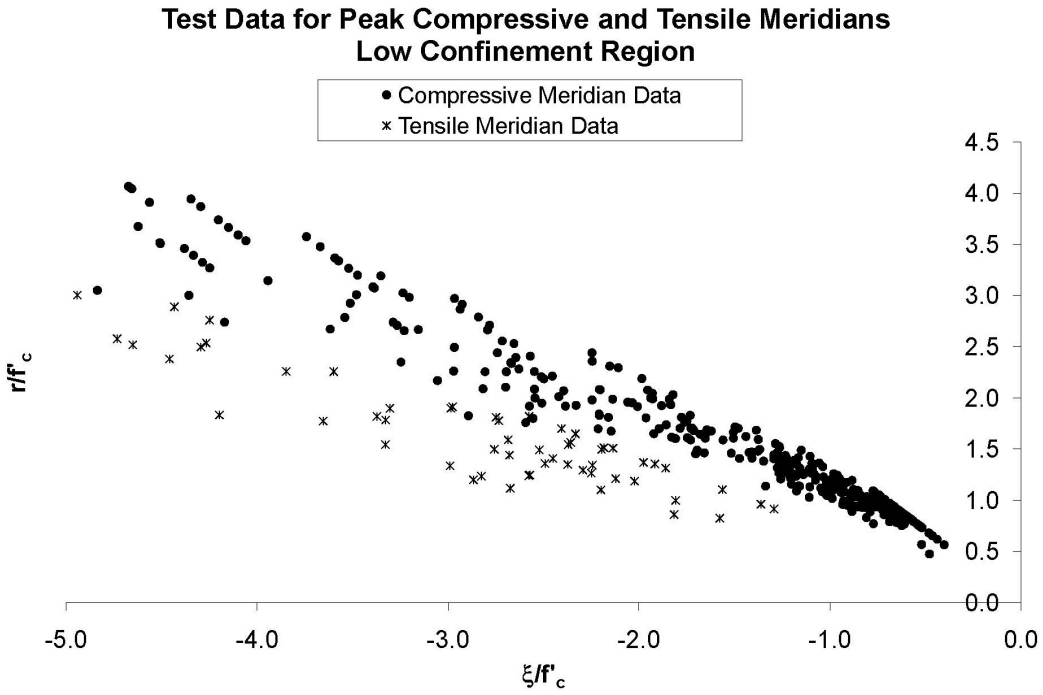

Figure 4.4: Test data for peak compressive and tensile meridians: low confinement region.

of 0°.

There are several ways in which testing problems can lead to premature concrete failure. For example, for concrete specimens loaded in a triaxial pressure vessel, failure often led to puncturing of the protective sheath and penetration of the fluid. However, there is no way to be certain that the sheath was not ruptured prematurely, leading to penetration of the fluid. The dramatic increase in pore pressure due to penetration of the fluid into the pores of the specimen would alter the stress state in the concrete, similar to the effective stress concept in soils. This penetration of the fluid could cause premature failure of the specimen. Thus, there may be some ambiguity as to whether the true peak strength of the concrete was reached. Similarly, for true triaxial testing, if the boundary conditions are not frictionless, additional stresses introduced at the boundary could affect failure of the specimen. For these reasons, it is understood why there exists some data points corresponding to a Lode angle of 60° which may lie somewhat below the compressive meridian. Problems with the testing conditions will typically cause the specimen to fail at a stress state less than the true peak. This

is an important point in understanding the scatter seen in the data.

As previously mentioned, it was the intent to gather data with a large variation in concrete and testing variables. Bringing this large quantity of data together allows for the investigation into the effects of these variables on concrete behavior. The effects of the concrete compressive strength, the confinement method, the specimen size, and the year of testing are explored in the following figures.

Figures 4.5 and 4.6 show the spread in the peak compressive meridian data due to the value of f'_c for that concrete specimen. It is widely accepted that concrete

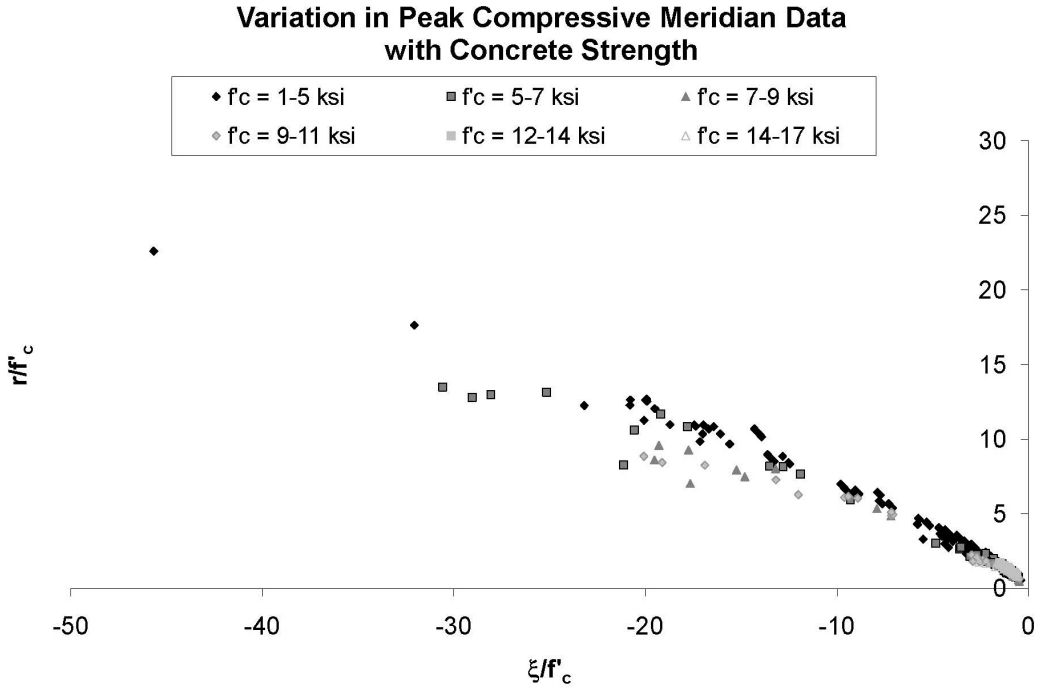

Figure 4.5: Change in the effectiveness of confinement with concrete compressive strength.

uniaxial compressive strength has an influence on the strength increase of concrete due to confinement. Higher strength concretes supposedly do not have as great of an increase in strength with confinement as lower strength concretes. This conclusion is not obvious from the test data compiled for this thesis. For confinement levels with ξ/f'_c between -2 and 0, the effect of concrete compressive strength is indistinguishable. At higher confinement levels, it becomes possible to observe some effect of the concrete compressive strength. However, the effect of concrete compressive strength is small

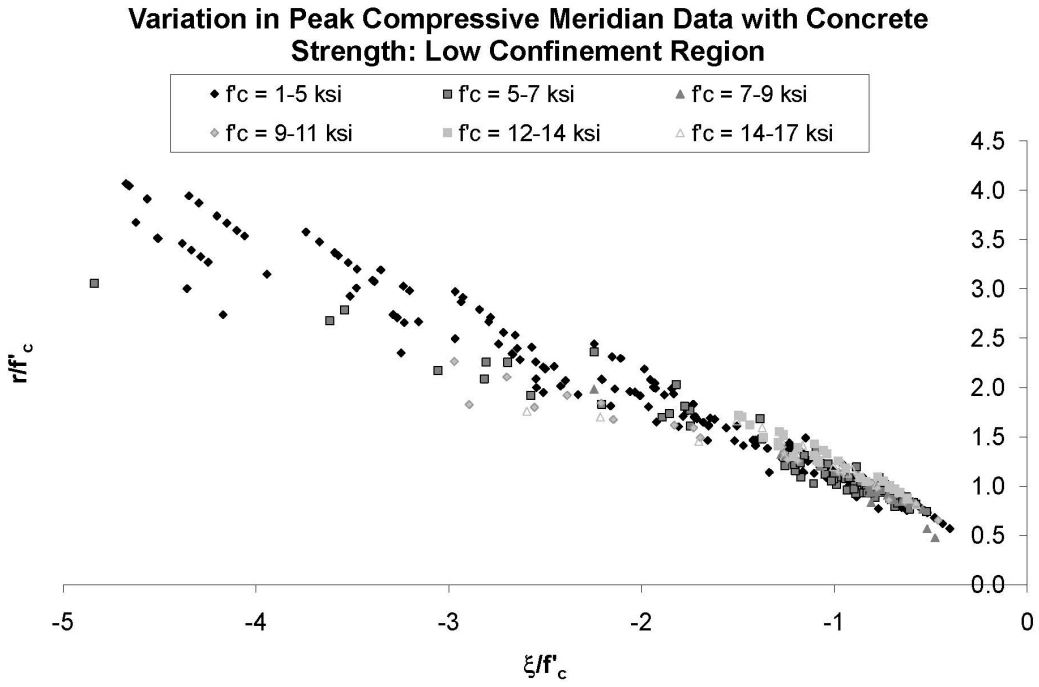

Figure 4.6: Change in the effectiveness of confinement with concrete compressive strength: low confinement region.

relative to the scatter in the data. For this reason, as well as the fact that the intention of this thesis is to model the conditions of passive confinement—which corresponds to the lower confinement range—the change in the effectiveness of confinement with concrete strength was not taken into account in the model presented herein.

Figure 4.7 shows the effect of the type of confinement on the peak compressive meridian data. The only type of tests that yielded results where ξ/f'_c was less than -5 were tests utilizing a triaxial pressure vessel. Thus, only the lower confinement range is shown for this testing variable. There appears to be a small influence of the testing method that leads to higher strength values in the true triaxial tests than the other testing methods. This topic has been extensively studied elsewhere [for example, Gerstle et al. (1980) and Schickert and Winkler (1977)], and this author will defer to those results as it is outside the scope of this thesis.

Figure 4.8 shows the effect of specimen size on the peak compressive meridian data. All but six of the data points with ξ/f'_c less than -5 were 6 x 12 inch (152 x 305 mm) cylinders, so the figure is limited to ξ/f'_c between -5 and 0. The size of the

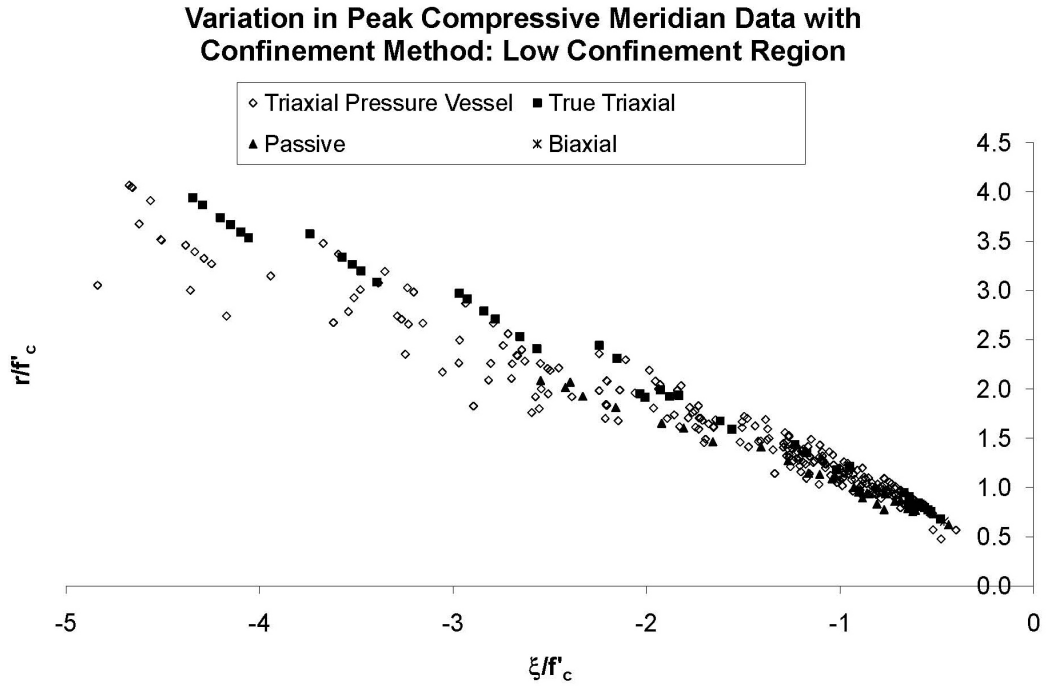

Figure 4.7: Change in the effectiveness of confinement with the confinement method: low confinement region.

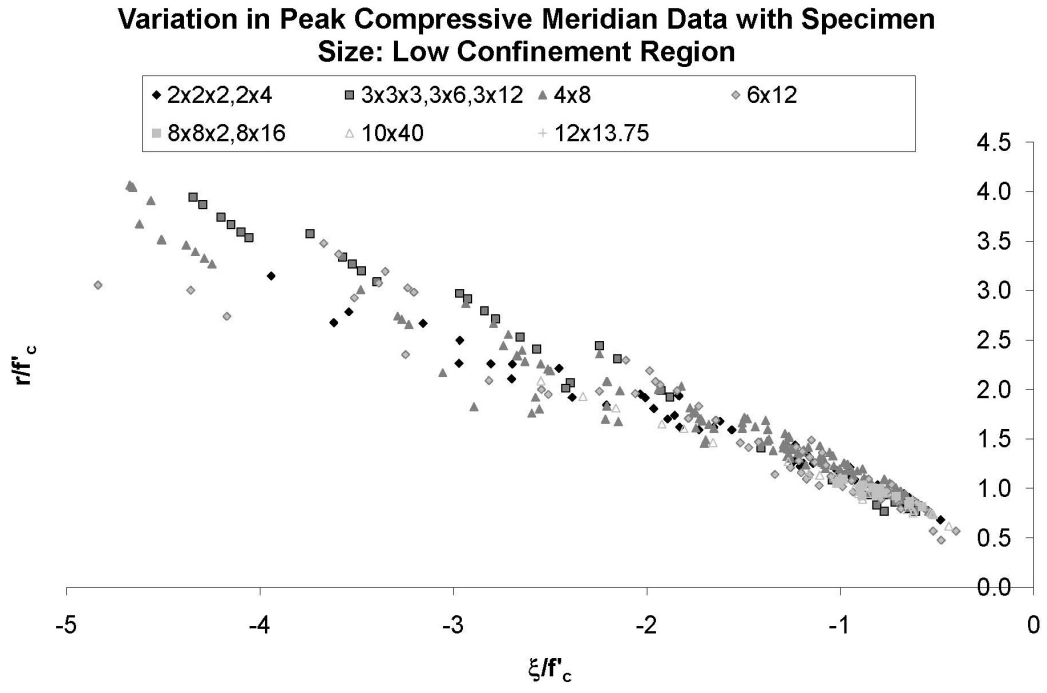

Figure 4.8: Change in the effectiveness of confinement with specimen size: low confinement region.

specimen does not appear to alter the effectiveness of confinement on the strength of the concrete.

An interesting result of bringing this large collection of data together is to consider the generation in which the experiments were performed. Clearly, the technology of concrete testing has advanced considerably from the time of the first published paper in this set of data (Richart et al., 1928). Thus, the data were grouped by the year in which the tests were published in order to determine if this advance in technology has changed the apparent behavior of the concrete. Figures 4.9 and 4.10 show the variation in the results with their year of publication. While the papers published

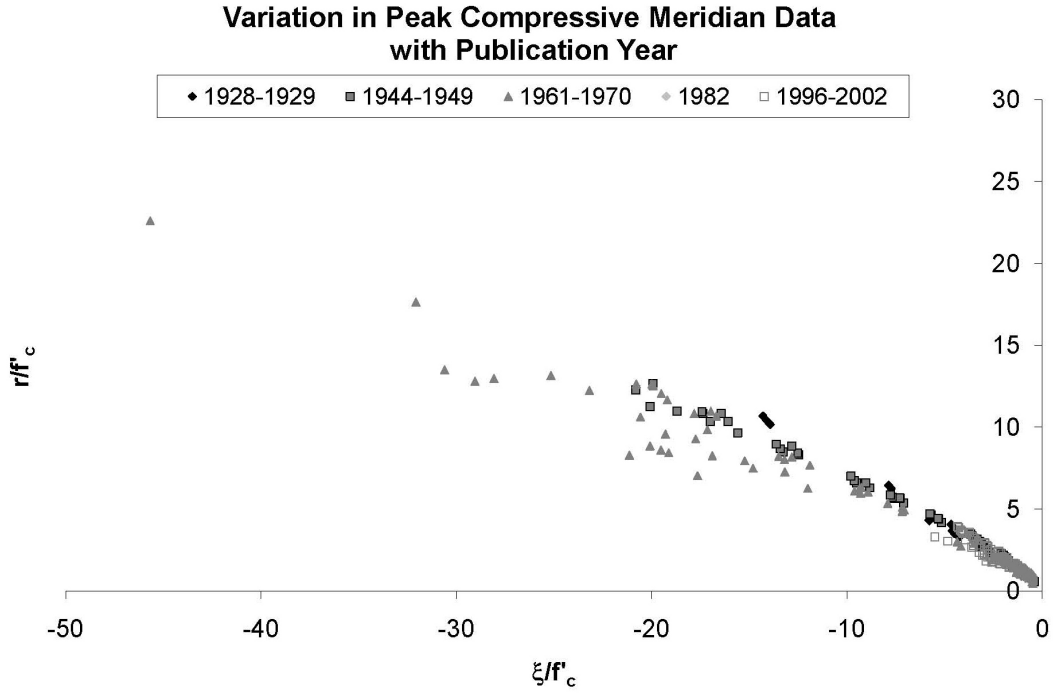

Figure 4.9: Change in the effectiveness of confinement with year of experiment.

from 1961 to 1970 appear to have the largest scatter, there is no distinguishable trend in the data. Thus, it is interesting to note that the now primitive techniques utilized in the 1920s appear to yield quite similar results to tests performed with far more advanced equipment. Regardless, there is clearly no reason to disregard data due to the use of antiquated testing techniques.

Plotting the data in the (r, θ) plane requires some data modification due to the fact that the data for a range of Lode angles are never all in the same ξ plane. Thus,

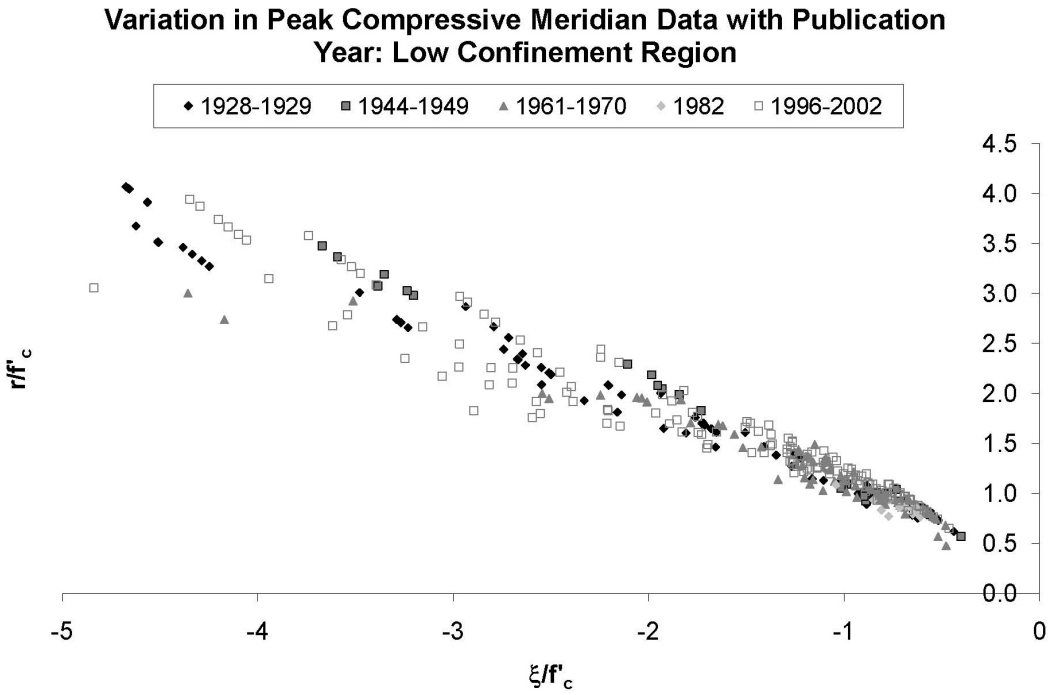

Figure 4.10: Change in the effectiveness of confinement with era of experiment: low confinement region.

to assist in visualizing the shape of the test data, a parabolic fit was performed for 5°-10° increments in the Lode angle, based on the quantity of test data obtained for that Lode angle range. The fit was then evaluated at a specific value for ξ. In this way, the general shape of the test data can be understood. Figure 4.11 shows the shape of the test data in the (r, θ) plane for various levels of ξ. Recall that values of the Lode angle may only range from 0° to 60°. For the sake of illustration, this range is copied and reflected to the full 360° using the three-fold symmetry of concrete.

4.2.3 Peak Surface Fit

As discussed at the beginning of this chapter, the concrete is assumed to be pre-cracked. Thus, two of the parameters for the peak loading surface, a_0 and b_0, are set to zero. Also, due to the manner in which the loading surface is defined, it is possible to eliminate a third parameter. Consider the unconfined axial loading of a cylindrical specimen. The model must be defined so that the peak surface is reached at a stress state corresponding to the defined compressive strength of the specimen. For this

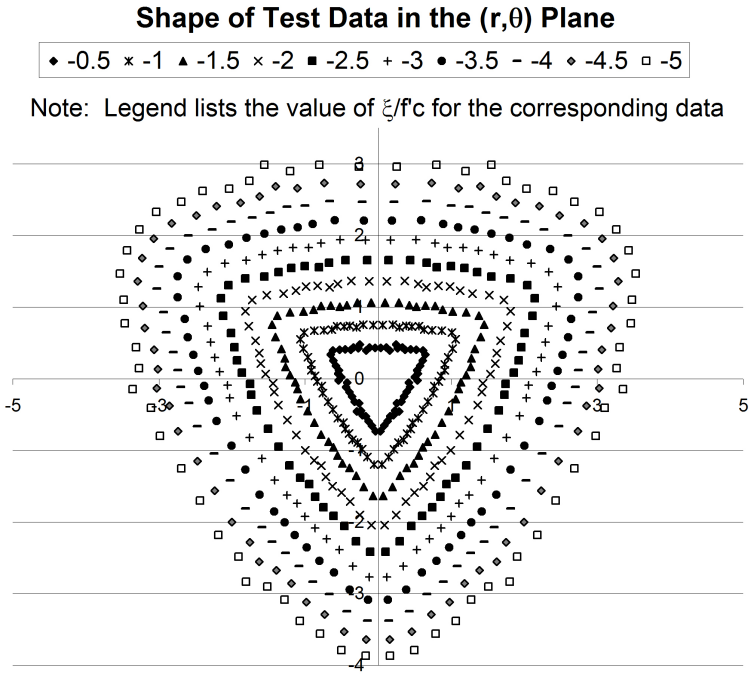

Figure 4.11: Shape of the test data in the (r, θ) plane.

case, the triaxial stress state can be defined:

$$\left.\begin{aligned} \sigma_x = \sigma_y &= 0 \\ \sigma_z &= -f'_c \end{aligned}\right\} \text{at uniaxial peak} \tag{4.7}$$

This corresponds to invariant values:

$$\left.\begin{aligned} \xi &= -\tfrac{f'_c}{\sqrt{3}} \\ r &= \sqrt{\tfrac{2}{3}} f'_c \\ \theta &= 60^\circ \end{aligned}\right\} \text{at uniaxial peak} \tag{4.8}$$

Implementing this stress state into Equation 3.4 for the peak surface gives parameter b_1 in terms of b_2 and b_3, the remaining compressive meridian parameters:

$$b_1 = \frac{b_2}{\sqrt{3}} - \frac{2}{\sqrt{3}} - b_3\sqrt{\frac{2}{9}} \tag{4.9}$$

This leaves only five parameters for the peak surface that must be determined using the test data: a_1, a_2, a_3, b_2, and b_3.

A least squares fit of the data was performed to estimate the remaining parameters for the peak tensile and compressive meridians. Equation 3.4 defines the peak surface. Since the stress state is on the peak surface when the value of F_{peak} is zero, the error between each data point and the model is defined using the same equation. Thus, the parameters a_1, a_2, a_3, b_2, and b_3 for the peak surface were adjusted to minimize the error, defined as:

$$error = \sum_{i=1}^{n} [r_i - R_{peak}(\xi_i, \theta_i)]^2 \tag{4.10}$$

Using the entire data set, the peak surface parameter values shown in Table 4.1 were obtained. The fit for these parameters is shown with the test data in Figures 4.12

Table 4.1: Peak surface parameters.

Parameter	Value	Parameter	Value
$a_{0,peak}$	0.0	$b_{0,peak}$	0.0
$a_{1,peak}$	-1.3419	$b_{1,peak}$	-3.6425
$a_{2,peak}$	0.1327	$b_{2,peak}$	0.1761
$a_{3,peak}$	0.8889	$b_{3,peak}$	1.8310

and 4.13.

Note that Equation 4.9 requires that the peak compressive meridian pass through the uniaxial peak compression point $(-\sqrt{\frac{1}{3}}, \sqrt{\frac{2}{3}})$=$(-0.58, 0.82)$ in (ξ, r) space. The scatter in the data near that point is due to the fact that the compressive strength of concrete often varies from specimen to specimen. While the compressive strength of the batch is given at a certain value, different specimens will fail at a different point than defined in Equation 4.8 because of this variation in f'_c.

It can be seen from the fit that peak compressive meridian data at lower confinement are being somewhat overestimated in this fit. There are only two parameters used to fit the peak compressive meridian: b_2 and b_3. Thus, it may be the case that the data at higher confinement levels are responsible for the fit being poorer at lower confinement levels. Since the scope of this thesis involves modeling the behavior of passively confined columns, a second fit to the test data was made to obtain better

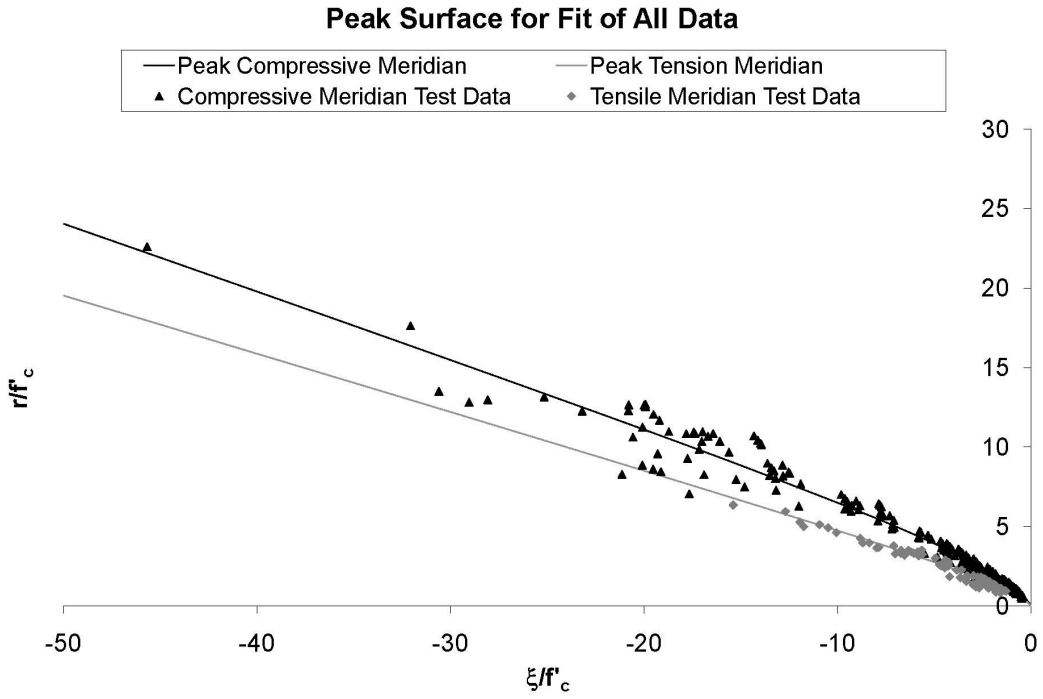

Figure 4.12: Peak compressive and tensile meridians for fit of all data.

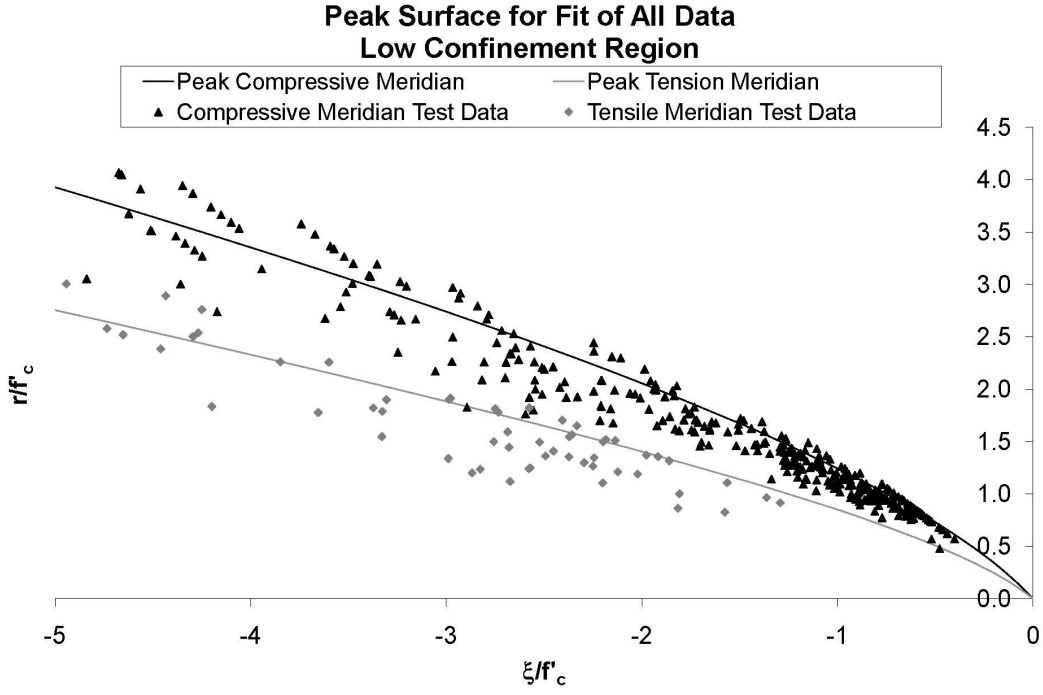

Figure 4.13: Peak compressive and tensile meridians for fit of all data: low confinement region.

correlation in the lower confinement range. However, if the intent is to model the complete triaxial load range of concrete, this first fit represents the best choice of parameters.

For the second fit, the data were limited to the subset having a ξ/f'_c value between -3.5 and 0.0. This range was chosen as it represents the largest range of values for steel or composite confined columns commonly used for civil engineering applications. All types of loading were used in this fit, not just passive confinement data. The reason for this is due to the physical mechanism being represented. True triaxial loading and triaxial pressure vessels both have a more even stress distribution in the specimen. These testing methods directly measure the lateral stress on the specimen. The passive confinement data uses an assumed formula (given in each individual paper) to calculate an effective lateral stress created by the confinement. However, it is understood that this lateral stress distribution is not evenly distributed over the height of the cylinder due to the fact that the confinement (in the case of steel rebar, for example) is not evenly distributed. Thus, non-passive test data more accurately represent the physical mechanism causing the strength increase through confinement. The finite element model itself will handle the unevenness in the lateral stress distribution. For this reason, the entire set of data for low confinement was utilized for this second fit.

Parameter estimates resulting from the second fit are defined in Table 4.2. These values for the parameters were used to validate the model (Chapter 6) and predict concrete behavior (Chapter 7). A comparison of the peak tensile and compressive

Table 4.2: Peak surface parameters for low confinement range.

Parameter	Value	Parameter	Value
$a_{0,peak}$	0.0	$b_{0,peak}$	0.0
$a_{1,peak}$	-1.4344	$b_{1,peak}$	-1.9711
$a_{2,peak}$	0.0924	$b_{2,peak}$	0.3103
$a_{3,peak}$	1.1005	$b_{3,peak}$	0.7039

meridians for both fits is shown in Figures 4.14 and 4.15. The second fit reduces the overestimation of the data in the low confinement range. However, the peak

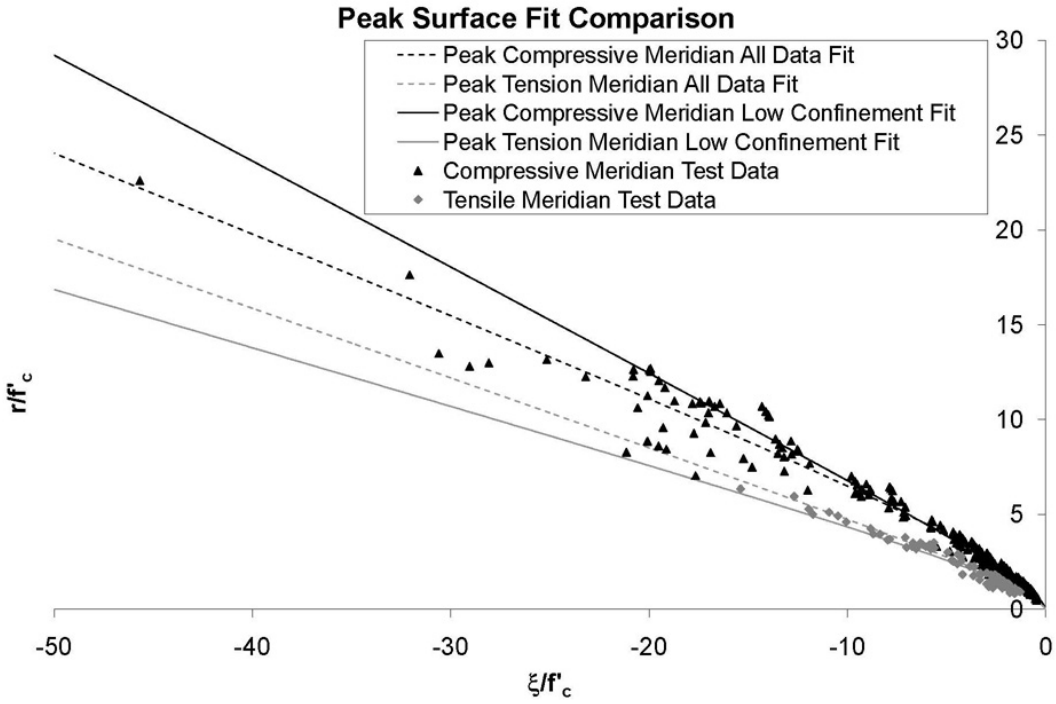

Figure 4.14: Comparison of peak compressive and tensile meridians for two different fits.

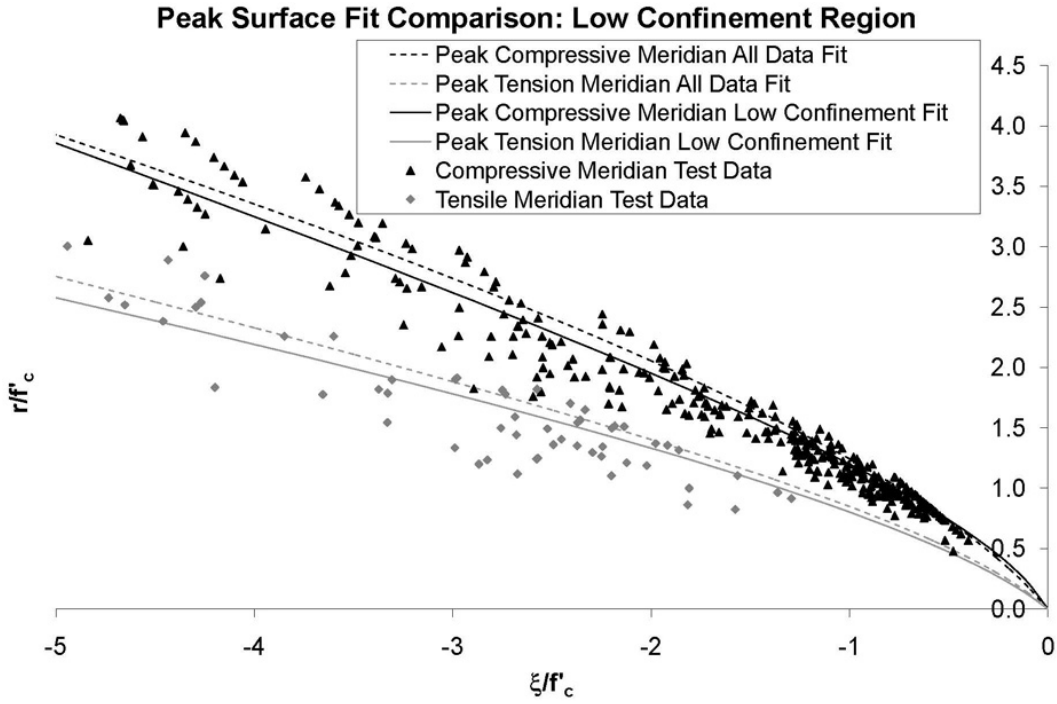

Figure 4.15: Comparison of peak compressive and tensile meridians for two different fits: low confinement region.

compressive meridian still does not lie near the middle of the data. One reason is the requirement that the peak compressive meridian pass through the uniaxial peak point $(-0.58, 0.82)$ as previously discussed. This is, however, a valid requirement to enforce. Also, the model assumed a hyperbolic shape of the meridian with only two remaining parameters to fit to the data. However, the fact that the peak compressive meridian does not pass through the middle of the data is not considered a problem for this case. As discussed in Section 4.2.2, peak compressive meridian data points that lie close to, or within, the peak tensile meridian data points are clearly suspect since they may be due to problems with the test setup. For these reasons, a slight overestimation of the peak compressive meridian data is considered acceptable.

The peak compressive meridians for the two different fits are compared to two existing models in Figures 4.16 and 4.17. One of the two existing models is discussed in Malvar et al. (1994) and Malvar et al. (1996) and the other in ANATECH Corp. (1998). It is clear that a hyperbola represents the better fit to data when considering both high and low confinement ranges. Although a separate fit was utilized in this thesis to better fit the lower confinement range, a hyperbolic shape is still a superior choice to the two models shown.

4.3 Residual Surface Correlation

Papers showing the full stress versus strain behavior of multiaxially loaded concrete are somewhat rare. Few papers extend to a large enough strain to be useable in determining the residual stress of the concrete. Thus, only five sets of experiments were found to determine the parameters defining the residual surface. Test data from Ansari and Li (1998), Attard and Setunge (1994), and Attard and Setunge (1996), used for the peak surface, were also able to be utilized for determining the residual surface parameters. Details of those papers are discussed in Section 4.2.1.1. An additional three data sets were obtained from Jamet et al. (1984), van Mier (1984), and Xie et al. (1995) to be used in determining the residual surface parameters. These three papers will be discussed in Section 4.3.1. The compilation of the residual

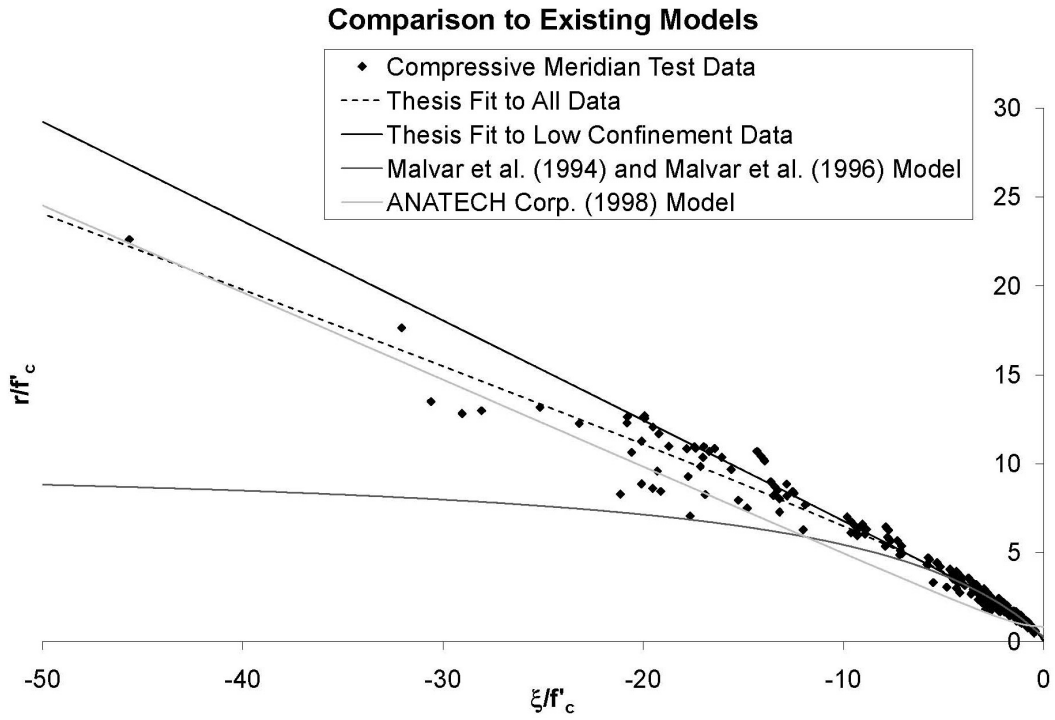

Figure 4.16: Comparison of peak compressive meridian to existing models.

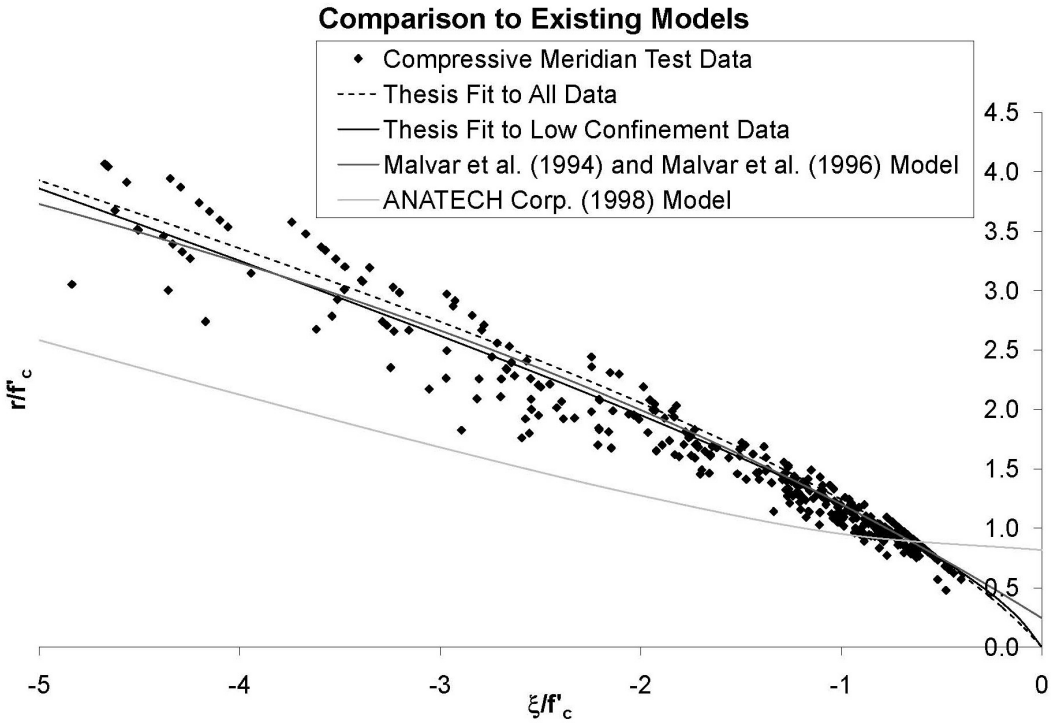

Figure 4.17: Comparison of peak compressive meridian to existing models: low confinement region.

surface data is shown and discussed in Section 4.3.2. Last, the method for choosing the parameters defining the residual surface is discussed in Section 4.3.3.

4.3.1 Residual Surface Papers

Four of the five experiments used a triaxial pressure vessel as previously described in Section 4.2.1. The fifth used a true triaxial setup, also described in Section 4.2.1. Thus, only one of these experiments had test data for a Lode angle other than 60°. However, a fairly large range of some important variables was obtained in the limited number of papers found. Concrete compressive strengths from 4.2 to 19.1 ksi (29 to 132 MPa) were tested. Cylinder sizes from 2.19 x 4.33 inches (55.5 x 110 mm) to 4 x 8 inches (100 x 200 mm) and cubes of 4 x 4 x 4 inches (100 x 100 x 100 mm) were all considered in the tests. While the variable range was not nearly as great as that of the peak surface data, a reasonable amount of variation in the testing variables was seen in the five sets utilized for the residual surface. A summary of these five sets of test data can be found in Table D.1.

Jamet et al. (1984) performed a limited set of experiments up to strain levels of 10%, with the focus on measuring the axial and lateral deformation patterns. One mix of normal strength concrete, with a water-cement ratio of 0.53, was used to create the specimens. The final concrete compressive strength of the 4.33 x 8.66 inch (110 x 220 mm) cylinders was 4.2 ksi (29 MPa). Specimens were sealed and stored in the molds for 48 hours, then removed and stored for 30 days at 65% relative humidity. At this point, some amount of grinding was performed to ensure true parallelism between all faces. Finally, the cylinders were again stored at 65% relative humidity for 180 more days before being removed for testing. A triaxial pressure vessel was utilized to apply confining pressures of 0.4, 1.5, 3.6, 7.3, and 14.5 ksi (3, 10, 25, 50, and 100 MPa). Unfortunately, tests employing confining pressures of 7.3 and 14.5 ksi (50 and 100 MPa) were terminated before the residual stress was reached and so could not be used for determining the residual surface parameters. During testing, the cylinders were jacketed in rubber sleeves to prevent penetration of the confining

fluid. Specimens were first loaded hydrostatically until the desired confining pressure was reached. The axial load was then increased to a total axial strain of 10%. The authors concluded that, as confining pressures are increased, concrete transitions from drastic strain softening behavior to that of classical ductility. It was also determined that the lateral strains achieved by the cylinders were strongly dependent upon the magnitude of the confining pressure.

van Mier (1984) studied the strain softening behavior of concrete under multiaxial loading conditions. A triaxial testing machine was constructed for this purpose. Details of this machine can be found in the cited paper. The machine allowed for independent loading of the specimens in three orthogonal directions. One mix of concrete with a water-cement ratio of 0.50 was used to create all of the 4 inch (100 mm) cubes. Specimens were cast in 28 x 5 x 5 inch (700 x 135 x 135 mm) prisms. The prisms were stored under water for 28 days and then removed and cut into 4.1 inch (104 mm) cubes. These cubes were then ground flat to the desired size to ensure that all faces were parallel. The final specimens were then stored in plastic bags at room temperature until testing. The age at testing ranged from 71 to 252 days, leading to a range of concrete compressive strengths of 5.8 to 7.4 ksi (39.9 to 51.0 MPa). Specimens were tested in a variety of loading paths: uniaxial, biaxial, triaxial, constant stress-ratio, constant strain-ratio, etc. The author found that the casting direction of the concrete had a significant effect on the ductility of the specimen under uniaxial loading. Casting direction refers to whether the axially loaded direction was horizontal or vertical when the specimen was originally cast. Two different failure mechanisms were observed for Lode angles near 60° and near 0°. For Lode angles near 60°, corresponding to the compressive meridian, fracture occurred in a large number of inclined planes. This type of failure corresponded to a more ductile strain softening behavior. Lode angles near 0°, corresponding to the tensile meridian, showed a planar fracture with failure occurring mainly in one direction. This type of failure showed a more brittle strain softening behavior. The author noted that failure along the compressive meridian showed a significant increase in ductility with confining pressure, while failures along the tensile meridian were not as significantly influenced

by an increase in confining pressure.

Xie et al. (1995) studied the triaxial behavior of high strength concretes. Three different concrete mixes were used with water-cement ratios of 0.321, 0.283, and 0.216 for compressive strengths at testing of 8.7, 13.4, and 17.3 ksi (60.2, 92.2, and 119 MPa) which were tested at 29, 35, and 39 days, respectively. The 2.19 x 4.33 inch (55.5 x 110 mm) cylinders were encased in a polyurethane membrane for testing in a modified Hoek cell. Eleven different confining pressures were tested for each concrete strength ranging from $0.01 f_c'$ to $0.50 f_c'$. The authors concluded that high strength concrete is less ductile than normal strength concrete. However, like normal strength, increasing confinement leads to an increase in the maximum and residual compressive strengths and improves the ductility.

4.3.2 Residual Surface Data

Similar to the yield stress, the residual stress is a somewhat ambiguous quantity. Following the definition laid out in Xie et al. (1995), the residual stress was defined as the point at which the magnitude of the descending slope of the stress-strain curve is less than 2% of the initial elastic slope of the curve. This definition resulted in much of the test data being thrown out. Specifically, all data for Lode angles other than 60° (found only in van Mier (1984)) did not meet this requirement. Figure 4.18 shows the remaining test data, all of which lie on the compressive meridian. It is difficult to see the effect of different variables with such a small set of data. It is interesting to note that the data from van Mier (1984), Ansari and Li (1998), and Jamet et al. (1984) appear to lie on the same curve, while Xie et al. (1995), Attard and Setunge (1994), and Attard and Setunge (1996) appear to lie on a different curve. There is nothing obvious to differentiate these two sets of experimental data that would lead to a different behavior from each other. It is clear that more testing is necessary to determine the effect of different variables on the residual stress of concrete.

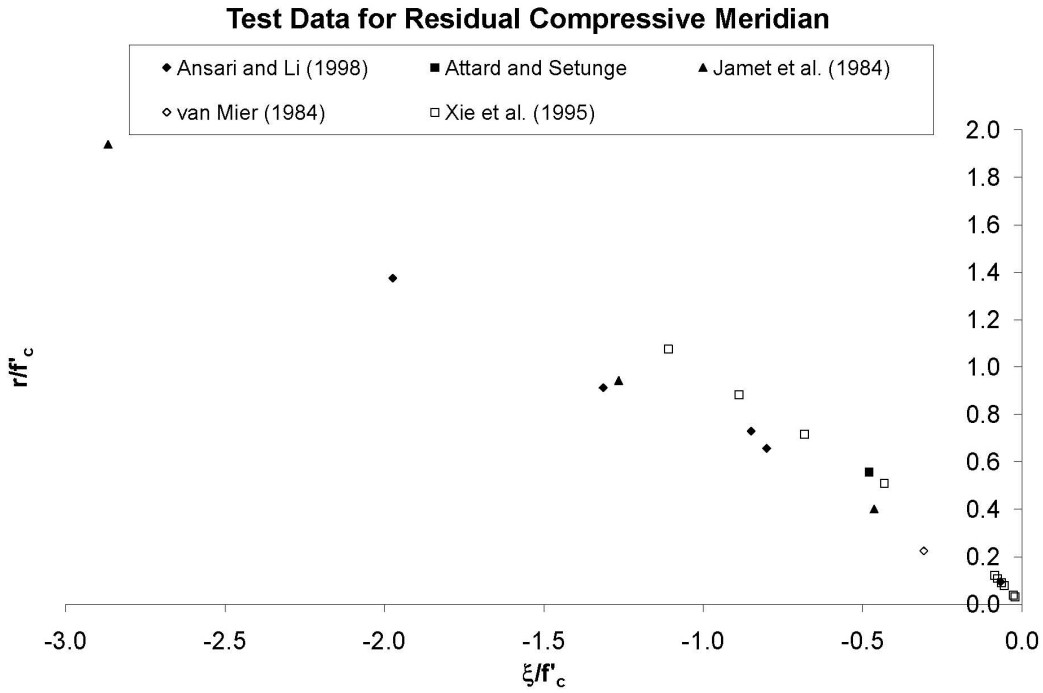

Figure 4.18: Test data for residual compressive meridian.

4.3.3 Residual Surface Fit

As discussed at the beginning of this chapter, due to the concrete being defined as pre-cracked, parameters a_0 and b_0 for the residual surface are set to zero. Due to lack of data for Lode angles other than 60°, the ratios of the tensile meridian parameters to the compressive meridian parameters for the residual surface were set equal to that of the peak surface. Thus, it was only necessary to determine the parameters for the compressive meridian.

The parameters defining the compressive meridian of the residual surface were determined by performing a least squares fit to the previously discussed test data. Similar to Equation 4.10, the least squares error minimized for the residual compressive meridian is defined by:

$$error = \sum_{i=1}^{n} [r_i - r_{c,residual}]^2 \tag{4.11}$$

The definition of $r_{c,residual}$ is given by Equation 3.1.

Determining the parameters using only this fit created a residual surface that intersects the uniaxial load path in the (ξ, r) space at two locations, as shown in Figure 4.19. This is physically incorrect. Under uniaxial loading, the specimen will

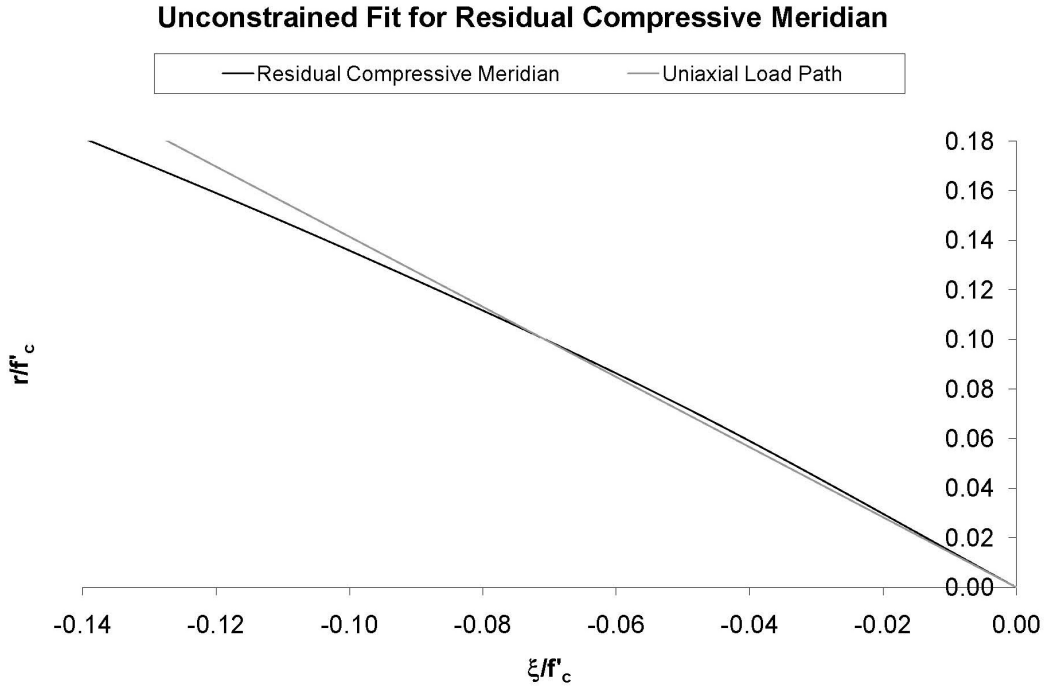

Figure 4.19: Fit for residual compressive meridian with no constraints on the parameters.

soften until the load path intersects the residual surface. For this loading case, it should be possible for the specimen to soften down to a zero stress state. However, the model is defined such that the stress state stops changing when the residual surface is reached. Thus, the residual surface must only intersect the uniaxial load path at the origin. Therefore, it was necessary to introduce a constraint that the slope of the residual surface be tangent to the uniaxial load path at the origin of the (ξ, r) space. From Equation 4.8, it can be seen that the slope of the uniaxial load path (which is a line in (ξ, r) space) is:

$$r = -\xi\sqrt{2} \tag{4.12}$$

By taking the derivative of Equation 3.1 and setting the derivative equal to $-\sqrt{2}$ at

$\xi = 0$, we can eliminate the parameter b_3.

$$b_3 = -\frac{b_1}{\sqrt{2}} \tag{4.13}$$

Using this constraint, the parameters defining the residual compressive meridian were determined through a least squares fit. With the ratio of the tensile to compressive meridian parameters determined by the peak surface parameters given in Table 4.2, the parameters for the tensile meridian of the residual surface were calculated. The

Table 4.3: Residual surface parameters.

Parameter	Value	Parameter	Value
$a_{0,residual}$	0.0	$b_{0,residual}$	0.0
$a_{1,residual}$	-0.9764	$b_{1,residual}$	-1.3417
$a_{2,residual}$	0.0565	$b_{2,residual}$	0.1898
$a_{3,residual}$	1.4833	$b_{3,residual}$	0.9847

values for the parameters, defined in Table 4.3, were used to validate the model (Chapter 6) and predict concrete behavior (Chapter 7). The compressive meridian for the residual surface is shown along with the test data in Figure 4.20.

4.4 Determination of the Equation for the Damage Increment

The intent of this thesis is to model the increase in the strength and ductility of concrete due to confinement. The effect on strength is handled by the shape of the loading surfaces discussed in Sections 4.1, 4.2, and 4.3. The variable that affects ductility in the model is the damage parameter, ψ. The damage parameter defines the location of the failure surface as a function of the strain state. However, the damage parameter is simply the sum of the damage increments, $d\psi$, over the load path. Thus, ductility will be controlled by the definition of the damage increment, $d\psi$.

The magnitude of the damage increment, $d\psi$, (for a given load increment) as a

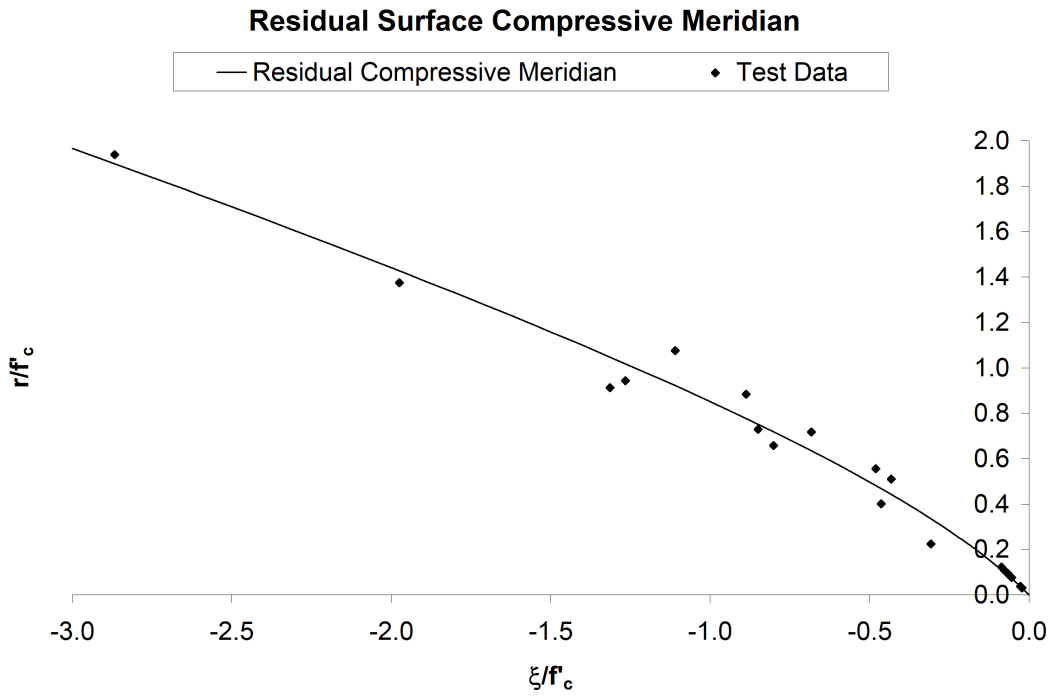

Figure 4.20: Final fit for the residual surface compressive meridian.

function of confinement, accounts for the increase in ductility due to confinement. The invariant ξ, defined in Equation 2.10, is representative of the amount of confinement present in the material, as it is a measure of the hydrostatic state of stress. Therefore, it is desirable to determine the nature of the relationship between the increment in damage, $d\psi$, and the invariant ξ.

The functional relationship between ξ and $d\psi$ cannot be seen directly from test data. Since the damage level is an artificially created quantity, it cannot be measured by concrete testing. Thus, it is necessary to find a state where the damage level is a known value and a related, measurable quantity is also at a known value. This occurs at the peak stress of the concrete. At the peak stress, as previously defined in Equation 3.8, ψ is equal to ψ_{peak}, and the strain at peak stress, ϵ_{peak}, can be easily determined from the test data. It is also necessary that ψ_{peak} and ϵ_{peak} be related if the assumption is to be made that they vary with ξ in a similar way. The model has been defined (following traditional plasticity theory) such that the increment in damage, $d\psi$, is directly proportional to the normalized plastic strain increment, $\overline{d\epsilon_p}$ (through a relationship that involves ξ, see Equation 3.5). Thus, $d\psi$ is going to be a

function of the strain at peak stress, since ϵ_{peak} contributes to $\overline{d\epsilon_p}$. A variable that affects ϵ_{peak} will affect $d\psi$ in the same way. Therefore, to determine the relationship between the damage increment and the stress invariant ξ, the variation of ϵ_{peak} will be examined for different confinement levels and concrete compressive strengths. The functional form of the relationship between $d\psi$ and ξ is chosen as the same form between ϵ_{peak} and ξ.

The relationship between the damage increment, $d\psi$, and the plastic strain increment, $d\epsilon_{ij}^p$, will be determined by observing the relationship between the strain at peak stress and the confinement level. Data from Attard and Setunge (1994), Attard and Setunge (1996), Candappa et al. (1999), Candappa et al. (2001), Smith et al. (1989), and Xie et al. (1995) were utilized to explore this relationship. All of the data were used for previous parameter determination except Smith et al. (1989). Discussion of the other papers can be found in Sections 4.2.1.1 and 4.3.1. Details of the experiments performed by Smith et al. (1989) will be discussed in Section 4.4.1. This collection of data will be explored in Section 4.4.2, and the final relationship for $d\psi$ and determination for the value of γ will also be discussed.

4.4.1 Papers Used to Determine the Equation for the Damage Increment

Details of the experiments from Attard and Setunge (1994), Attard and Setunge (1996), Candappa et al. (1999), and Candappa et al. (2001) are discussed in Section 4.2.1.1. Discussion of the experiments performed in Xie et al. (1995) is in Section 4.3.1.

Smith et al. (1989) performed a set of experiments to determine the post-peak behavior of concrete under triaxial loading. A triaxial pressure vessel was used to apply lateral confinement to the 2.125 x 4.250 inch (54 x 108 mm) cylinders. The specimens were encased in a polyurethane membrane during testing. One mix of concrete was created to cast thirty-five of the specimens. A water-cement ratio of 0.83 was used for a final compressive strength of 5.0 ksi (34.5 MPa). Blocks of concrete

6 x 6 x 10 inch (152 x 152 x 254 mm) were cast and aged for eight months. At that time, the blocks were removed and the cylinders cored out and used for testing. An additional sixteen specimens were furnished by the Waterways Experiment Station that had a final compressive strength of 6.4 ksi (44.1 MPa). However, the results from the testing of these specimens were not used in this thesis for the determination of failure surface and flow rule parameters due to the fact that they were cyclically loaded. The 5.0 ksi (34.5 MPa) specimens were loaded laterally up to the desired confining pressure. The axial load was then increased to an axial strain level of 5%. The authors concluded that increasing confining pressure leads to a transition from brittle to ductile post-peak behavior. They further concluded that the plastic strain increments at peak were not compatible with an associated flow rule. The volume dilatation was somewhat less than an associated flow rule would predict. Last, the general stress versus strain behavior of different strength concretes is similar, but with a trend of increasing brittleness with increasing strength.

4.4.2 Discussion of Test Data Used to Determine the Equation for the Damage Increment

Several authors noted that the change in ductility with confinement is different for normal- versus high-strength concrete. This was discussed in Sections 4.2.1, 4.3.1, and 4.4.1. Therefore, the effect of the concrete compressive strength on the axial strain at peak stress must also be explored if its effect is to be taken into account in the model. It is necessary to understand how both the concrete compressive strength and the confinement level change the strain at peak stress.

The way in which the concrete compressive strength changes the behavior of the strain at peak stress is examined by considering the unconfined loading case. Figure 4.21 shows the axial strain at peak unconfined stress plotted against the concrete compressive strength. No correlation appears between these two quantities. Thus, it is assumed that the concrete compressive strength only affects how confinement changes the strain at peak stress, but it does not directly affect the strain at peak

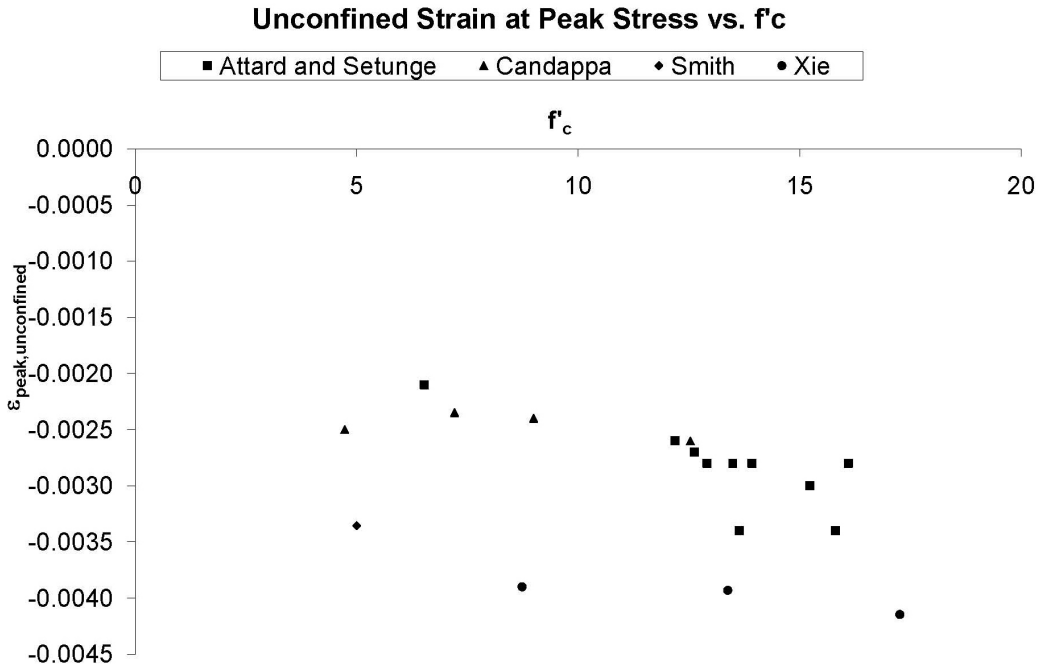

Figure 4.21: Variation of strain at unconfined peak stress with concrete compressive strength, f'_c.

stress itself. In order to examine this effect, it is necessary to explore the *change* in strain at peak confined stress for various confinement levels and concrete compressive strength.

It is clear from Figure 4.21 that different concretes have a different strain at unconfined peak stress. To study only the change in strain at peak stress with confinement, the ratio of the strain at peak stress for the confined case to the strain at peak stress for the unconfined case is observed. This allows the variation in the unconfined strain at peak stress to be normalized out of the behavior.

Figure 4.22 shows the ratio of the confined to unconfined strain at peak stress plotted against the invariant ξ. It can be seen that a roughly linear relationship between the strain ratio and ξ exists. The slope of this line appears to vary with the compressive strength of the concrete.

Malvar et al. (1994) proposed that the relationship between the damage parameter

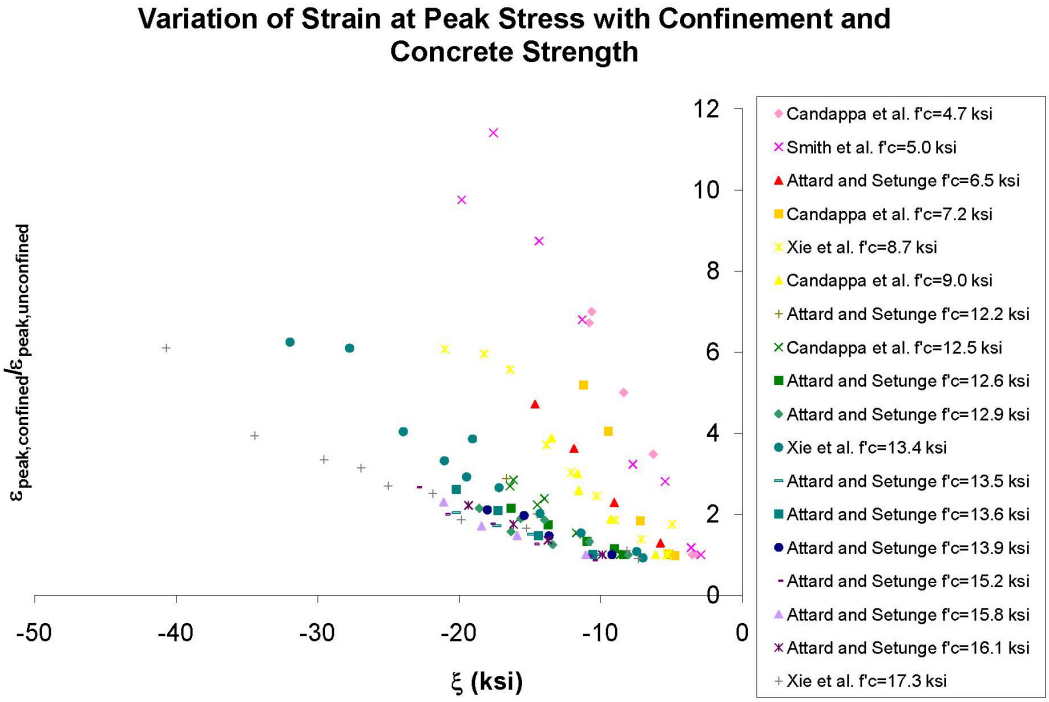

Figure 4.22: Ratio of confined strain to unconfined strain at peak stress plotted versus ξ.

and confinement be defined by:

$$d\psi = \frac{\overline{d\epsilon^p}}{r_f \left(1 + |\frac{p}{f_t}|\right)^b} \tag{4.14}$$

The form of this equation was used as a starting point for the relationship for $d\psi$. The parameters r_f and b were to be estimated for their model. This thesis replaces the quantity represented by the hydrostatic pressure, p, with the invariant ξ. Further, the tension strength of concrete, f_t, is known to vary as the square root of the concrete compressive strength f'_c (Nilson, 1997). Thus, it is implied that by normalizing the invariant ξ with the square root of the concrete compressive strength, the variation with f'_c should disappear.

Figure 4.23 shows the ratio of confined to unconfined strain at peak stress plotted against the ratio of ξ to the square root of the concrete compressive strength. Scatter still exists within the data due to the concrete compressive strength. Thus, this relationship is not adequate to determine how the peak strain should vary with both

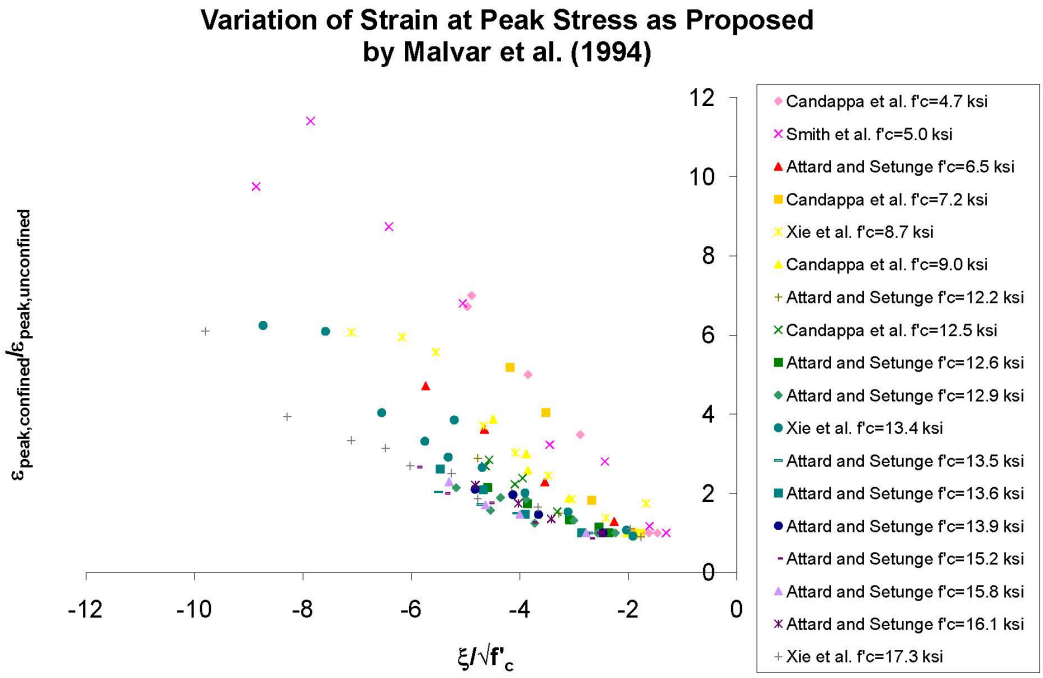

Figure 4.23: Ratio of confined strain to unconfined strain at peak stress plotted versus $\xi/\sqrt{f'_c}$.

the invariant ξ and f'_c.

The equations for the loading surfaces of this model predict that the shape of the surface will scale with the ratio of ξ to the concrete compressive strength itself. Further, the linear relationship shown in Figure 4.22, with only the slope of the line varying with f'_c, implies that the increase in strain at peak stress should scale with ξ/f'_c. Thus, the ratio of confined to unconfined strain at peak stress was plotted against the ratio of ξ to the concrete compressive strength in Figure 4.24. While scatter still exists in the data, there is no longer a distinguishable trend in this scatter based on the concrete compressive strength. Thus, it is defined that the damage level will vary with the ratio of ξ to f'_c.

By comparing Figure 4.22 to Figure 4.24, the behavior no longer appears linear. A power law was chosen to represent this relationship. A least squares fit of the power law is shown with the data in Figure 4.25. The Smith et al. (1989) data point plotted at the extreme left of all the data points may appear to call into question the validity of the power law fit. However, examining this data point relative to the others in

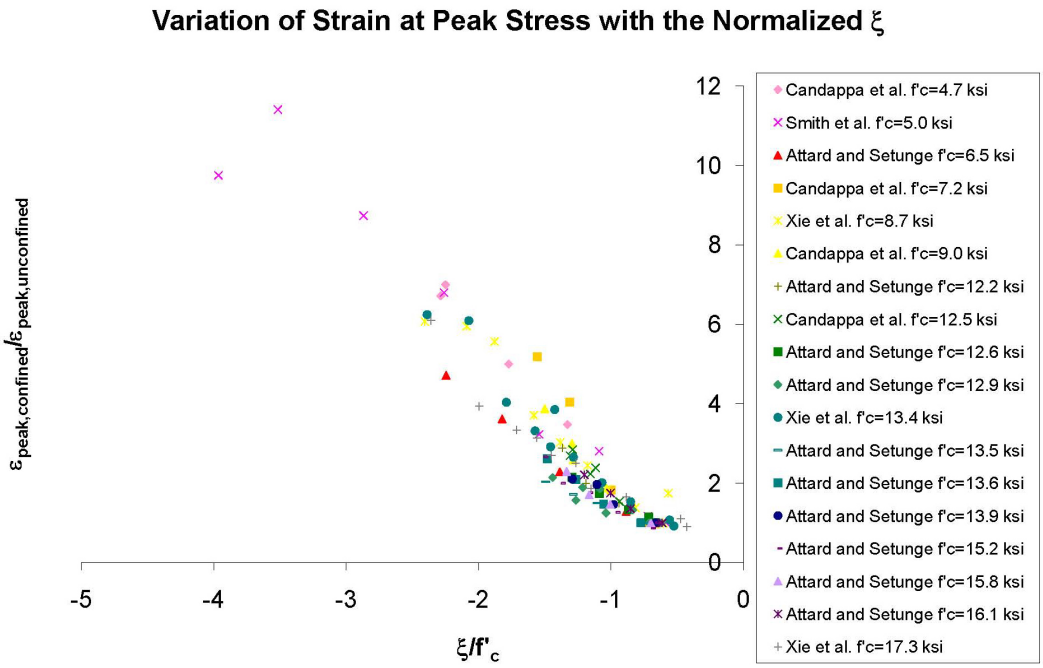

Figure 4.24: Ratio of confined strain to unconfined strain at peak stress plotted versus ξ/f'_c.

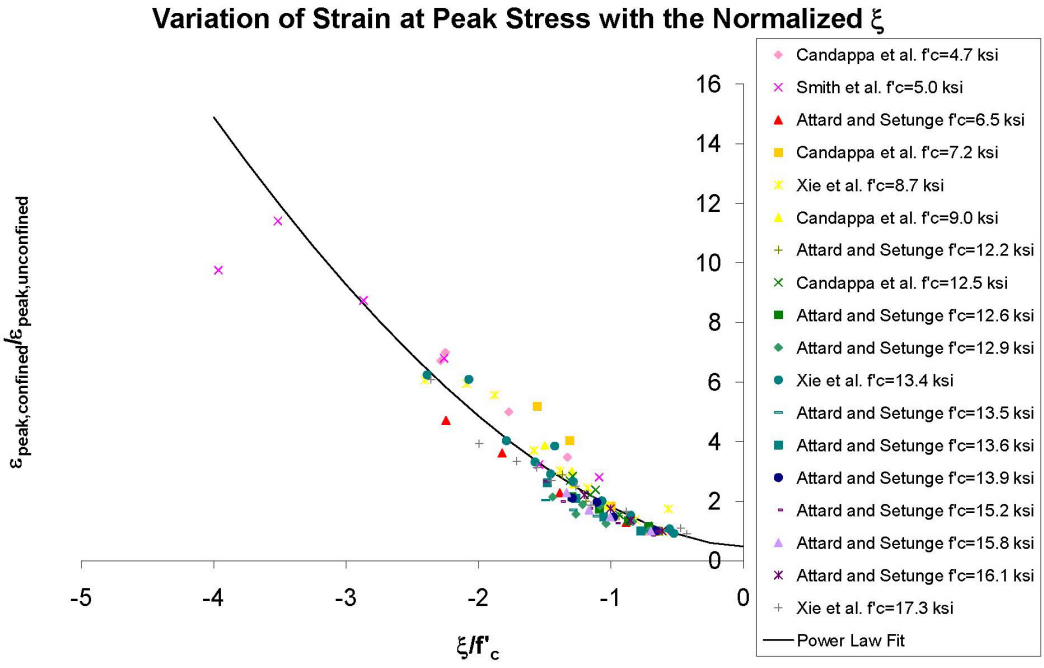

Figure 4.25: Power law fit for ratio of confined strain to unconfined strain at peak stress versus ξ/f'_c.

his experiments, it very quickly becomes apparent that this is an anomalously low value for the strain at peak stress. Consider the raw data for the eight data points from Smith et al. (1989) shown in Table 4.4. From the trend in the ϵ_{peak} values, it is

Table 4.4: Smith et al. (1989) raw data points.

$\sigma_{confining}$ (ksi)	σ_{peak} (ksi)	ϵ_{peak}
0.0	-5.0	-0.003
-0.1	-6.0	-0.004
-0.5	-8.4	-0.009
-1.0	-11.4	-0.011
-2.0	-15.6	-0.023
-3.0	-18.8	-0.029
-4.0	-22.4	-0.038
-5.0	-24.3	-0.033

expected that the strain at peak stress for the final load point would be near -0.047, which corresponds to a ratio of confined to unconfined strain at peak stress of 15.7. The power law fit predicts a ratio of 14.7. Thus, while this data point appears to call into question the power law fit, it can be disregarded.

The equation describing the power law as fit to the data is given by:

$$\frac{\epsilon_{peak,confined}}{\epsilon_{peak,unconfined}} = 1.3276 \left(\frac{|\xi|}{f'_c} \right)^{1.7199} + \left(1 - (1.3276) 3^{-\frac{1.7199}{2}} \right) \tag{4.15}$$

The constant term ensures that, for the uniaxial case, the strain ratio takes the value of one. The important parts of this equation are the power law relationship and the value of the power determined from the fit. The constants will not carry over to the relationship between $d\psi$ and ξ / f'_c; ψ_{peak} is the integral of $d\psi$ up to the peak stress, whereas the axial strain at peak stress is the integral of the axial strain. Thus, the constants will be combined with other coefficients in the integration of $\overline{d\epsilon_p}$ when calculating the relationship between $d\psi$ and ξ / f'_c. These coefficients are represented by the introduction of the parameters ϕ and α. The final equation for $d\psi$, given by Equation 3.5, is also shown in Equation 4.16. The power law functional form was used to determine the form of Equation 3.5, and the value of the power in Equation 4.15 is an estimate of γ in Equation 3.5. This value for γ was used to validate the model

(Chapter 6) and predict concrete behavior (Chapter 7).

$$d\psi = \frac{\overline{d\epsilon^p}}{\phi + \alpha(|\frac{\xi}{f_c'}|^\gamma)} \tag{4.16}$$

4.5 Correlation of the Failure Surface and Flow Rule Parameters

Four of the five remaining parameters, ϕ, α, ψ_{peak}, and κ, relate to the definition of the failure surface. The final parameter, ω, is used in the definition of the flow rule. Due to the nature of these parameters, it is not possible to directly measure them through test data. To further complicate the estimation of these parameters, their values are inter-related. More than one parameter can affect a particular concrete behavior in a similar way, and the nature of this behavior can change with the values of other parameters.

The process chosen to determine values for these parameters was to observe their effect on the shape of the stress versus strain curve of the concrete under different loadings, and visually determine the best choices for these parameters. Due to the somewhat subjective and iterative nature of this process, a limited set of test data representative of typical concrete behavior was chosen to estimate these parameters. The experiments published in Smith et al. (1989), Candappa et al. (1999), and Candappa et al. (2001) were utilized for the selection of the remaining five parameters. Test data from Candappa et al. (1999) and Candappa et al. (2001) were discussed in Section 4.2.1; Smith et al. (1989) were discussed in Section 4.4.1.

These two sets were chosen primarily because of the large strain values to which the experiments were run, and the recording of both axial and lateral strains throughout all experiments. Both sets contained lateral loading magnitudes in the range expected from modern passive confinement methods. While testing was performed outside of the expected range, only data with confinement pressures that could be reached by passive confinement were used.

An additional reason these two sets were chosen was the values of their concrete compressive strengths. As mentioned in Sections 4.2.1, 4.3.1, and 4.4.1, test data show that the increase in the ductility and strength of concrete brought about by confinement is different for normal- versus high-strength concrete. The current model does not explicitly take this effect into account. Thus, it was decided that these parameters would be chosen to best represent normal-strength concrete due to it being most prevalent in modern construction. If modeling of high-strength concrete is desirable, these parameters could instead be determined using high-strength concrete, or the model could be altered to include the effects of high- versus normal-strength concrete at a later time. However, within this thesis, the parameters were chosen based on the results of Smith et al. (1989) for concrete with a compressive strength of 5.0 ksi (34.5 MPa) and the results of Candappa et al. (1999) and Candappa et al. (2001) for concrete with a compressive strength of 6.1 ksi (41.9 MPa). Test data to large strains containing both axial and lateral strains for concrete strengths of 3.0 to 4.0 ksi (21 to 28 MPa) could not be found, so these two were selected as the closest available data to normal-strength concrete.

Results of the 5.0 ksi (34.5 MPa) concrete tested in Smith et al. (1989) are shown in Figure 4.26. Results of the 6.1 ksi (41.9 MPa) concrete tested in Candappa et al. (1999) and Candappa et al. (2001) are shown in Figure 4.27. Note that neither of these data sets were used in determining the residual surface. This is due to the fact that, with one exception, none of the curves extended to the point where the final slope was less than 2% of the initial slope of the curve. However, due to the fact that the parameters being determined in this section affect the entire stress versus strain curve, not simply the post-peak behavior, it is not critical that the residual stress be reached in order to properly estimate these five parameters.

The curves that actually met the residual surface criterion are the curves from Smith et al. (1989) for a confining pressure of 1000 psi (6.9 MPa). From Figure 4.26, it can be seen that those particular curves are actually exhibiting strain hardening at their final behavior, which is not expected or typically seen for concrete in that area of the curve. Thus, the residual stress may not have actually been reached, as

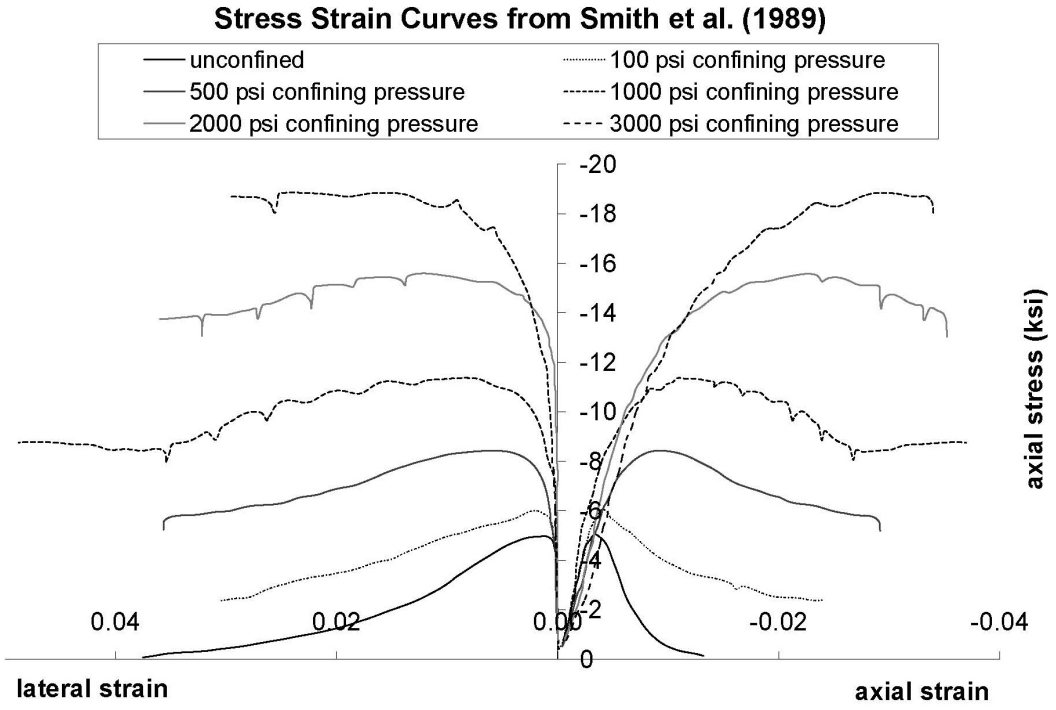

Figure 4.26: Test data for 5.0 ksi (34.5 MPa) concrete from Smith et al. (1989).

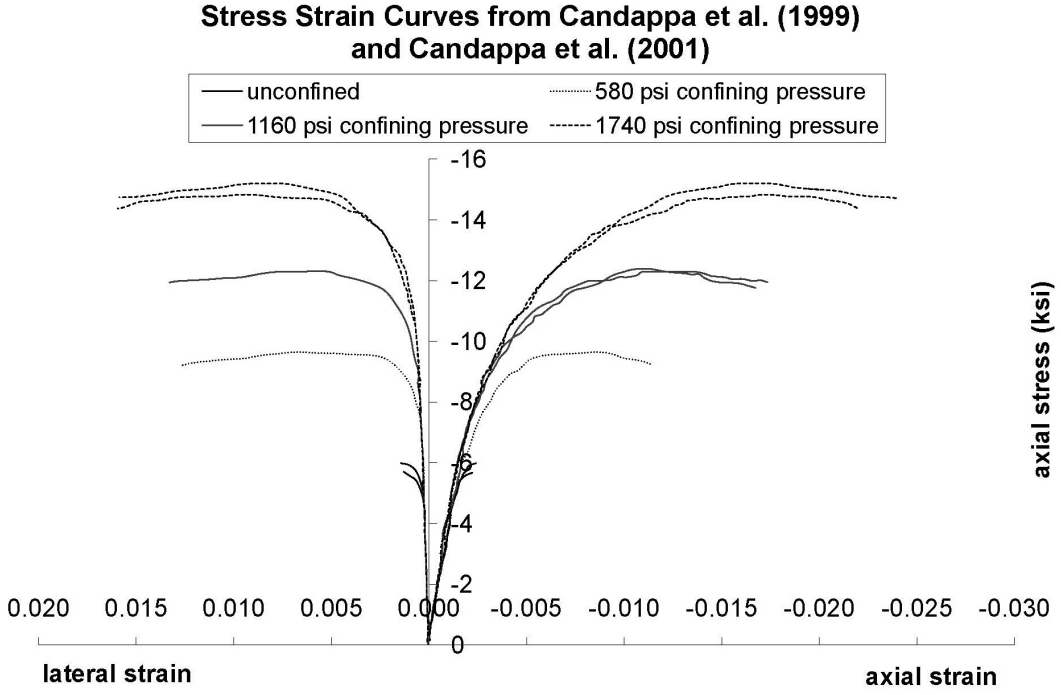

Figure 4.27: Test data for 6.1 ksi (41.9 MPa) concrete from Candappa et al. (1999) and Candappa et al. (2001).

there may be some problem with that particular specimen. Regardless, the general trend of both of these sets of data fall well in line with the majority of concrete data. Therefore, it is acceptable to choose these as being representative of the change in the stress versus strain curve with confinement.

The stress versus strain curves predicted by the model were generated using a special case of the procedure detailed in Chapter 5. A single solid element was used, with the prescribed pressure applied laterally to the element. The axial displacement was then monotonically increased until the axial strain reached that of the corresponding data.

Using the two data sets, the final five parameters were determined by visually matching the model to the data. The values for these last five parameters are given in Table 4.5. The precision of these variables is limited due to the method by which

Table 4.5: Summary of failure surface and flow rule parameter values.

Parameter	Value	Parameter	Value
ϕ	0.5	α	10.
ψ_{peak}	0.6×10^{-3}	κ	0.6
ω	0.5		

they were estimated. A comparison of the finalized model to the Smith et al. (1989) data is shown in Figure 4.28. Similarly, Candappa et al. (1999) and Candappa et al. (2001) data are compared to the final model in Figure 4.29.

The model appears to predict reasonably well results at low confining pressures. At very low levels of confinement [below 500 psi (3.4 MPa) for Smith et al. (1989)], strain softening may be a bit too rapid, but at slightly higher levels, the model follows the data more closely. The model is quite successful at predicting the data from Candappa et al. (1999) and Candappa et al. (2001). The results for Smith et al. (1989) are not as close. However, the model does well in the lower confinement range. The ratio of lateral strain to axial strain appears to be working well in the model, which is an important component if passive confinement is to be correctly modeled. Overall, the model is able to predict the behavior of confined concrete throughout the entire loading history.

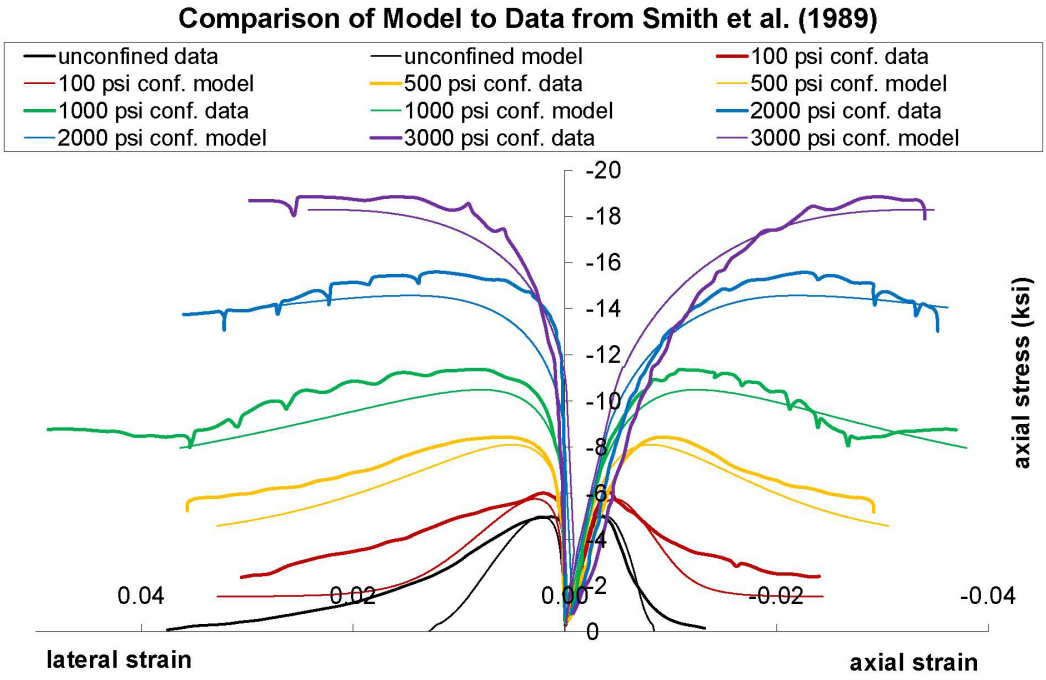

Figure 4.28: Comparison of model to data from Smith et al. (1989).

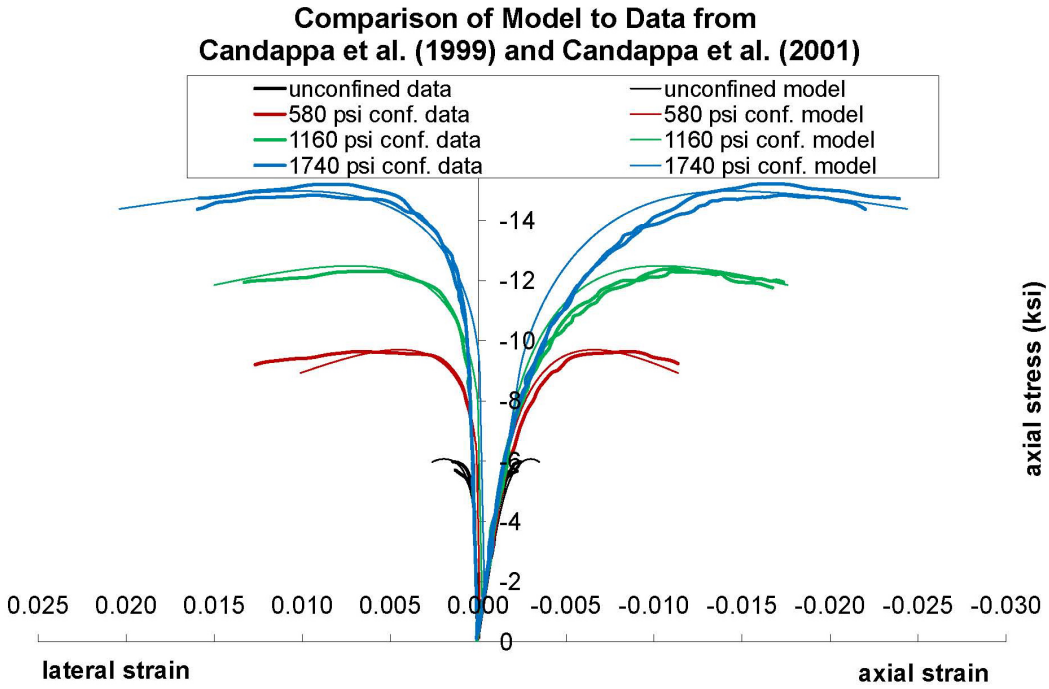

Figure 4.29: Comparison of model to data from Candappa et al. (1999) and Candappa et al. (2001).

4.6 Summary of Parameters

Table 4.6 shows the final values for the twenty-four parameters of the concrete plasticity model. These values were implemented into a finite element program to predict the behavior of confined concrete.

Table 4.6: Summary of model parameter values.

Parameter	Value	Parameter	Value
c	1.1333	d	1.7816
$a_{0,peak}$	0.0	$b_{0,peak}$	0.0
$a_{1,peak}$	-1.4344	$b_{1,peak}$	-1.9711
$a_{2,peak}$	0.0924	$b_{2,peak}$	0.3103
$a_{3,peak}$	1.1005	$b_{3,peak}$	0.7039
$a_{0,residual}$	0.0	$b_{0,residual}$	0.0
$a_{1,residual}$	-0.9764	$b_{1,residual}$	-1.3417
$a_{2,residual}$	0.0565	$b_{2,residual}$	0.1898
$a_{3,residual}$	1.4833	$b_{3,residual}$	0.9847
γ	1.7199	ϕ	0.5
α	10.	ψ_{peak}	0.6×10^{-3}
κ	0.6	ω	0.5

Chapter 5

Finite Element Program

An existing finite element (FE) program, written by John F. Hall, is adapted for use with this model. The original program was a linearly elastic, static analysis FE program for solid and structural mechanics. It was designed to solve the equation [K]{x} = {f} for {x} given a linear elastic stiffness matrix and constant force values. It contained only linear springs and four node isotropic plane stress or strain elements.

Modifications of the program are necessary to model reinforced concrete columns. The first step is to add or modify elements to be used for representing reinforced concrete columns confined by steel rebar or fiber reinforced polymer (FRP) sheets. Capabilities for six node tetrahedral and eight node rectangular brick elements are added to the existing program; both using an eight point integration scheme. Each node of the solid element has three translational degrees of freedom. The solid elements are to be used for modeling the concrete. The material model defined in this thesis is implemented into the newly added solid elements. Three material parameters need to be provided as input to these solid elements: the modulus of elasticity, E; Poisson's ratio, ν; and the unconfined compressive strength, f'_c. Further, the linear spring element is modified to be bilinear elastic. The loading behavior of the spring element is bilinear, and the unloading behavior is along the current stiffness value, not the initial stiffness value. Four input quantities are required for the spring elements: the initial modulus of elasticity, E; area, A; yield stress, f_y; and the yield ratio, defined as the ratio of the post yield stiffness to the initial elastic stiffness. The solid and spring elements are used to model a reinforced concrete column with two

different types of confinement materials in subsequent chapters.

Nonlinear solution capabilities and coordinate updating are also added to the program. The applied load is divided into smaller steps so that the full stress versus strain behavior of the material can be mapped. For each small load increment, the program iterates using the elastic stiffness matrix until convergence is achieved. For each iteration, the current difference between the applied load and the internal resisting load is calculated. This force residual is used in conjunction with the elastic stiffness matrix to calculate a new increment in displacement. This increment is added to the previous increments determined during iteration on the current load step and then applied to the previously converged step for calculation of the current internal load. At the end of each converged load increment, the coordinates are updated. The full Fortran code is shown in Appendix E.

To reduce the problem size, only a horizontal slice of the column is considered. Figure 5.1 shows a slice of a typical cylindrical column. The slice is meshed by one

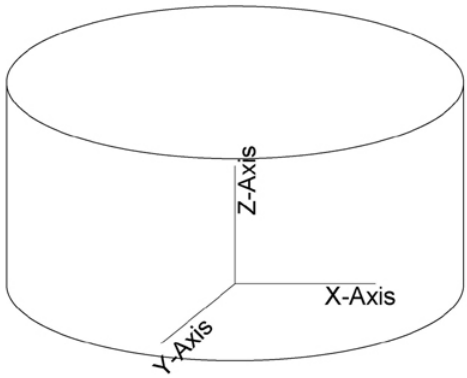

Figure 5.1: Typical slice of column used for FE model.

layer of solid elements. The height of the slice should be equal to half of the hoop spacing or spiral pitch for the case of a steel rebar confined section. Where adequate symmetry exists in the cross sectional shape and rebar layout, only a fraction of the cross section is modeled. For the case of pure axial loading, only one quarter of the slice is typically modeled. When moments are applied to the section, one half of the section is modeled. In both load cases, symmetric boundary conditions are applied. For circular cross sections, the centermost elements of the section are six node solid

elements. All other elements in the section are eight node elements. A typical mesh used for a load case including moments about the x-axis is shown in Figure 5.2. The

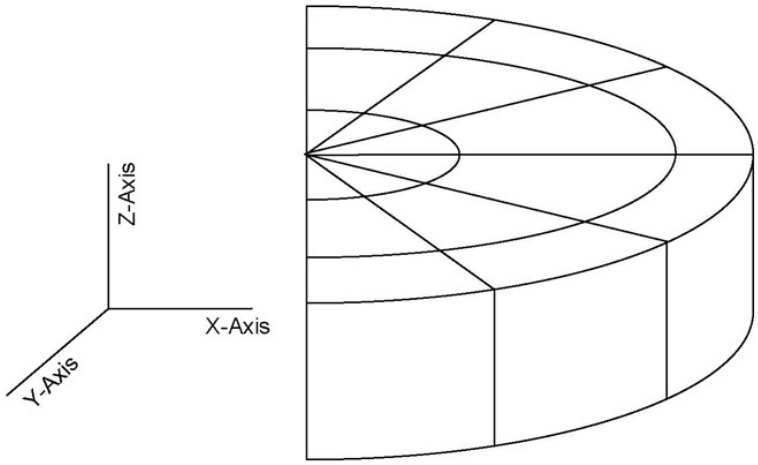

Figure 5.2: Typical mesh used for circular cross sections.

nodes on the left hand face would be restrained in the x-direction. For the case of a square cross section, only eight node solid elements are used and the section is meshed with a simple grid.

The assumption that plane sections remain plane is designed into the program. The nodes in the bottom plane are fixed in the vertical degree of freedom; this vertical direction is labeled as the z-axis in Figures 5.1 and 5.2. The top plane of nodes is defined to move as a plane having three degrees of freedom, representing a vertical displacement and two rotations. In the figures, all nodes in the top plane would share one z degree of freedom, one rotation about the x-axis, and one rotation about the y-axis as a plane. Each top plane node is free to move within the plane that has its orientation defined by the three shared degrees of freedom. These conditions constrain the top and bottom planes to remain planar, a typical assumption for columns.

Since the confinement material is to be explicitly included, a method for modeling steel rebar and FRP sheets must be defined. For steel rebar, spring elements are defined within the bottom layer of nodes to represent the steel hoops. Spirals are modeled in an identical fashion, ignoring the fact that the rebar would change over the height of the given section. No attempt is made to account for the difference in

behavior between a hoop and a spiral. The slice is defined with a height equal to half of the hoop spacing or spiral pitch. Longitudinal rebar is also modeled using bilinear spring elements. In both cases, the post-yield stiffness of the rebar is set to zero. Thus, strain hardening in the rebar is not modeled. For the case of FRP confinement, springs are defined around the top and bottom layers of perimeter nodes to represent the FRP sheet. In this case, the slice height is typically set equal to the height of the steel confined column to which the FRP confined column is being compared. The FRP sheets are represented as purely elastic. Thus, the yield ratio is defined as one. For comparisons between the FE model and experimental results performed in this thesis, the yield stress, f_y, is defined as the rupture stress of the FRP, and the program is terminated if any FRP element reaches its f_y value. The area of the spring element is defined as the thickness of the sheet multiplied by half the slice height. This is the area of the FRP sheet being represented by the individual spring element.

Comparable steel hoop and FRP confined meshes are shown in Figure 5.3. This mesh would be used for axial load, as it represents only one quarter of the cross sectional slice. Thick lines indicate the presence of spring elements in the mesh. All

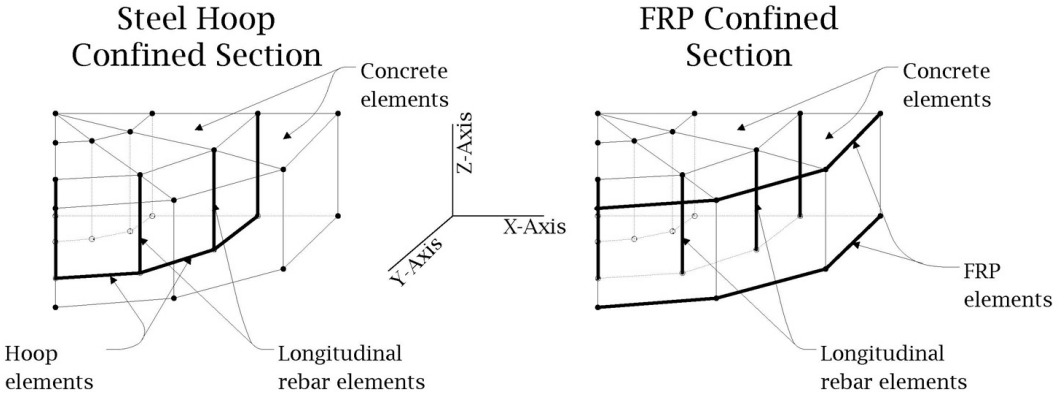

Figure 5.3: Comparable meshes with steel hoops versus FRP confinement.

finite element meshes used for Chapters 6 and 7 are shown in Appendices G and H, respectively.

In the scope of this thesis, several different load configurations are considered. Finite element theory allows for the application of loads in many different ways.

Thus, some details are necessary about how the loads are applied. Axial loads are applied by a force on the z degree of freedom of the top plane. Moments are applied to the x or y rotational degrees of freedom of the top plane. For the case of combined axial load and moment, the member is loaded to the specified axial load, and then the moment is increased to failure. When active confinement is modeled (for example, a cylinder immersed in a pressurized fluid), radial forces are applied to the external nodes in proportion to the area represented by that node. This is not the only way of applying these load cases, but simply the manner chosen for this thesis. For all cases, when the concrete stress is given, this stress is calculated as the weighted average over all integration points lying within the confined area of the section. The weights are given by the product of the Gauss-Legendre weight and the determinant of the Jacobian calculated at that integration point.

Chapter 6

Comparisons to Tests on Reinforced Concrete Members

Finite element (FE) model predictions of laboratory test results of reinforced concrete members with various confinement methods are presented in this chapter. Five different papers were obtained (none of which were used for the correlations in Chapter 4) that reported tests of confined concrete members. These papers tested a variety of confinement configurations, materials, and cross sectional geometries, since the concrete plasticity model is intended to be used for many different applications. The papers are discussed individually in Section 6.1. The FE model predictions are compared to the test results in Section 6.2. A discussion of the overall performance of the FE model is in Section 6.3.

6.1 Test Data

Test data for confined concrete members are quite abundant; thus, it was possible to select test data similar to that which this FE model is intended to predict. A fairly broad spectrum was considered in the five papers. Both steel rebar and fiber reinforced polymer (FRP) confinement, as well as circular, square, and rectangular cross-sections, were included. Four of the papers presented results from axially loaded confined concrete members, while the fifth presented an axial load-moment strength interaction diagram. The set of papers is considered typical of what the FE model is designed to predict.

Chaallal and Shahawy (2000) studied the combined effects of axial and flexural loads on confined concrete members. The intent of the paper was to study the enhancement in strength by wrapping a lightly confined section in carbon fiber reinforced polymer (CFRP). The concrete was purchased from a commercial supplier with an experimentally determined compressive strength of 3.7 ksi (25.0 MPa) and a water-cement ratio of 0.68. The members tested were 8 x 14 x 84 inch (200 x 350 x 2100 mm) rectangular sections with 1 inch (25 mm) radius corners. Four Grade 60 number 6 bars ran longitudinally through the section. The hoops consisted of Grade 60 number 3 bars at 4 inches (100 mm). A cross section of the steel confined member, along with the material properties, is shown in Figure 6.1. The second member was identical to the first, but was wrapped with 2 plies of a bi-directional CFRP. Unfortunately, due to lack of information about the CFRP material and layout, the CFRP confined section could not be modeled. Hence, only the results for the hoop confined members are employed here. Pure axial load and pure moment were considered along with four intermediate axial load-moment combinations.

Harries and Carey (2003) observed the effect of cross sectional shape on performance. Two members with square cross sections, each with a different corner radius, and one member with a circular cross section were tested. The circular columns were 6 x 12 inch (152 x 305 mm) specimens, while the square columns were 6 x 6 x 12 inch (152 x 152 x 305 mm) specimens with either a 0.43 or 0.98 inch (11 or 25 mm) radius applied to the corners. The concrete had a compressive strength at testing of 4.6 ksi (31.8 MPa) for the cylindrical specimens, 4.1 ksi (28.6 MPa) for the square specimens with a 0.43 inch (11 mm) corner radius, and 4.7 ksi (32.4 MPa) for the square specimens with a 0.98 inch (25 mm) corner radius. All specimens were confined by three or six plies of E-glass FRP. The FRP had an experimentally-determined strength of 428 lb per inch per ply (75 N per mm per ply) and an elastic modulus of 28 kips per inch per ply (4.9 kN per mm per ply). The authors performed axial load tests on the specimens both with the FRP bonded to the member using epoxy as well as unbonded by covering the member with a kitchen-type plastic wrap before applying the FRP. Typical applications of composite confinement are bonded to the column,

so the unbonded tests were not used here.

Harries and Kharel (2003) investigated the effects of varying amounts and type of FRP confinement on axial behavior of confined columns. All specimens were 6 x 12 inch (152 x 305 mm) cylinders. The concrete had a compressive strength at testing of 4.7 ksi (32.1 MPa). Two different composite materials were used to create the FRP: a carbon fiber and an E-Glass fiber. The carbon fiber had an experimentally-determined strength of 994 lb per inch per ply (174 N per mm per ply) with an elastic modulus of 90 kips per inch per ply (15.7 kN per mm per ply). The E-Glass fiber had an experimentally-determined strength of 428 lb per inch per ply (75 N per mm per ply) and an elastic modulus of 28 kips per inch per ply (4.9 kN per mm per ply). The carbon FRP confined columns were tested with 1, 2, or 3 plies for confinement. The E-Glass FRP confined columns were tested with 1, 2, 3, 6, 9, 12, or 15 plies for confinement.

Mander et al. (1988a) tested the effect of steel rebar confinement on columns and walls. The columns were circular in cross section with dimensions of 19.7 x 59.1 inches (500 x 1500 mm), while the rectangular walls were 5.9 x 27.6 x 47.2 inches (150 x 700 x 1200 mm). All columns used in this comparison were loaded axially at a strain rate of 0.013 sec^{-1}. This strain rate was utilized to simulate the rate of seismic loading. The unconfined compressive strength, determined at the 0.013 sec^{-1} strain rate, was 4.1 ksi (28 MPa). Mander et al. (1988b) states that loading at this strain rate will result in an increase in the stiffness, peak strength, and strain at peak stress. Thus, the unconfined compressive strength measured at this same strain rate of 0.013 sec^{-1} was designated as f'_c in the FE model. All walls used in this comparison were loaded axially at a strain rate of 0.00001 sec^{-1} and had a measured compressive strength, at that strain rate, of 3.8 ksi (26 MPa). All steel rebar used for longitudinal and confining steel was Grade 275. Scott et al. (1982) experimentally tested different rebar sizes, and the yield strength of the bars was found to vary with the size of the bar. These measured yield strengths were used in the FE model. Four columns were chosen for comparison. The columns all had twelve 0.63 inch (16 mm) diameter deformed longitudinal bars. Three were confined with spirals of 0.47 inch (12 mm)

diameter round bars at pitches of 1.61 to 4.06 inches (41 to 103 mm). The fourth was confined by a spiral of 0.39 inch (10 mm) diameter round bar at 4.69 inch (119 mm) pitch. Three different walls were used for comparison. All walls had sixteen 0.47 inch (12 mm) diameter deformed longitudinal bars. Transverse steel configurations were different for each of the three walls. All three consisted of hoops formed by 0.24 inch (6 mm) diameter round bars at either 0.98 or 1.97 inch (25 or 50 mm) spacing. The rebar configuration and material strengths for all columns and walls considered are shown in Figures 6.9 and 6.13.

Scott et al. (1982) studied square columns confined by steel rebar. All columns tested were 17.7 x 17.7 x 47.2 inches (450 x 450 x 1200 mm). Normal weight concrete was used. The concrete had a maximum aggregate size of 0.79 inches (20 mm) and a slump of 3 inches (75 mm). The cylinders were cured for 7 days at 68°F (20°C) and 100% humidity. They were then stripped and left standing in the laboratory for approximately five weeks before testing. Two confined columns were chosen for comparison which had a compressive strength, f'_c, for the concrete of 3.16 ksi (21.8 MPa). One column had twelve 0.79 inch (20 mm) diameter longitudinal bars with a yield strength, f_y, of 62.9 ksi (434 MPa). The other column had eight 0.94 inch (24 mm) diameter longitudinal bars with a yield strength, f_y, of 57.1 ksi (394 MPa). Both columns used 0.39 inch (10 mm) double hoops at a spacing of 2.84 inches (72 mm) having a yield strength of 44.8 ksi (309 MPa). The hoop configurations were different for the two columns. The cross sections and material properties are shown in Figure 6.16. Both columns were loaded axially at a strain rate of 0.0000033 $\sec^{-1}$. Stress versus strain curves for various sizes of steel bars were determined in the paper and used for defining the yield strength of the rebar.

6.2 Comparison Results

6.2.1 Chaallal and Shahawy (2000)

The FE model was used to predict the axial load-moment interaction diagram of a hoop confined section, as tested in Chaallal and Shahawy (2000). The finite element mesh used to represent the section is shown in Appendix Section G.1. The comparison of the test results to the FE model prediction, along with the member cross section, is shown in Figure 6.1. At both the pure axial and balanced point loadings, the FE

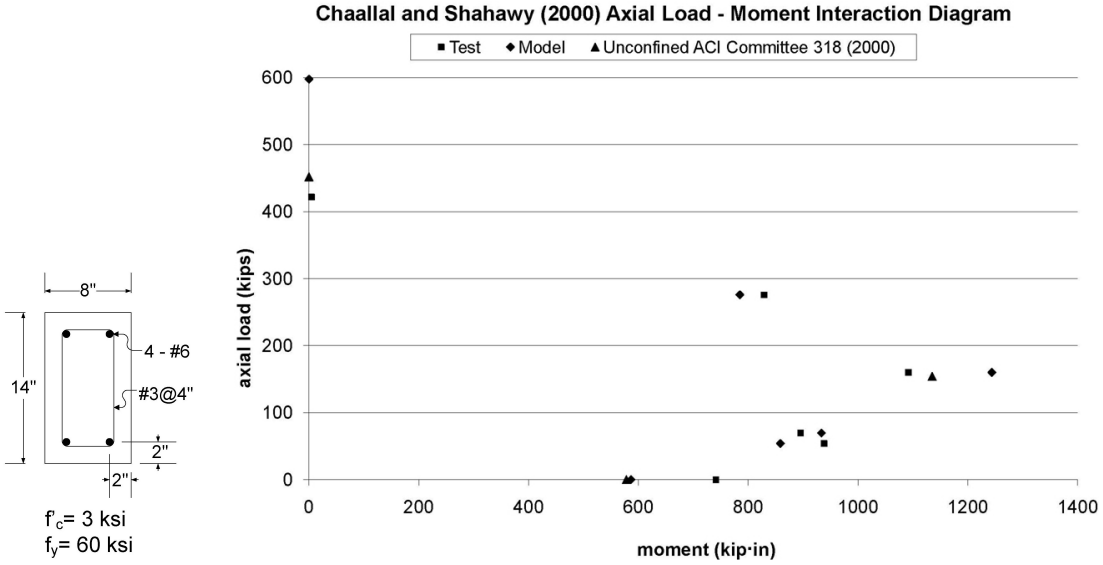

Figure 6.1: Comparison of model to test data from Chaallal and Shahawy (2000).

model appears to overestimate the experimental results. The balanced load point is defined as the point where the steel yields in tension at the same curvature that the concrete crushes under the compression. This balanced point will have the highest moment capacity of any axial load-moment combination. Assuming unconfined concrete and using equations from ACI Committee 318 (2000), the pure axial load supported by this column would be 452 kips (2012 kN), and the balanced moment would be 1135 kip·in (128.2 kN·m) at an axial load of 154 kips (685 kN). The experimental points lie below even this unconfined assumption. Thus, the experimental results at these points are not considered reliable. The opposite is observed at the pure moment point. For this case, the FE model is underestimating the experimen-

tal data. Again, assuming unconfined concrete and equations from ACI Committee 318 (2000), the pure moment that this section can withstand would be 578 kip·in (65.3 kN·m). The FE model prediction is 586 kip·in (66.2 kN·m). The FE model is predicting that the confinement is not effective under pure moment, which may be a reasonable assumption since the section will be partially cracked and the axial stress will vary over the uncracked portion. It is not clear what can be concluded from this comparison due to large discrepancies in the test results. The FE model may be overestimating the increase in strength for a lightly confined section. However, the test data clearly has some discrepancies, so the problems may not lie with the FE model.

6.2.2 Harries and Carey (2003)

Results from the testing of E-Glass FRP confined columns performed by Harries and Carey (2003) were compared to predictions from the FE model. The comparisons for the circular column and the two square columns are shown in Figures 6.2 through 6.4. The finite element meshes used to perform these predictions are shown in Appendix Section G.2. In Figure 6.4, the mismatch in the peak stress of the 0 ply column between the FE model and the test is due to the fact that the 0 ply column strength did not match the f'_c value specified in the paper.

The FE model predicts exceptionally well the behavior of the circular column. For the square columns, the experimental data suggest that there is sometimes slack in the loading mechanism. This type of variability in loading will not be accounted for in the FE model. However, the FE model does predict the peak stress of the specimen reasonably well. The square sections show a concave upward type behavior after the peak stress is reached. This behavior is not seen in the FE model, nor is it seen in the circular column. The physical mechanism leading to this abrupt drop is not discussed in the paper. Therefore, it is difficult to know whether there is a problem with the concrete plasticity model, a problem with the FE model, or a problem with the experimental results. There may be some features of the behavior

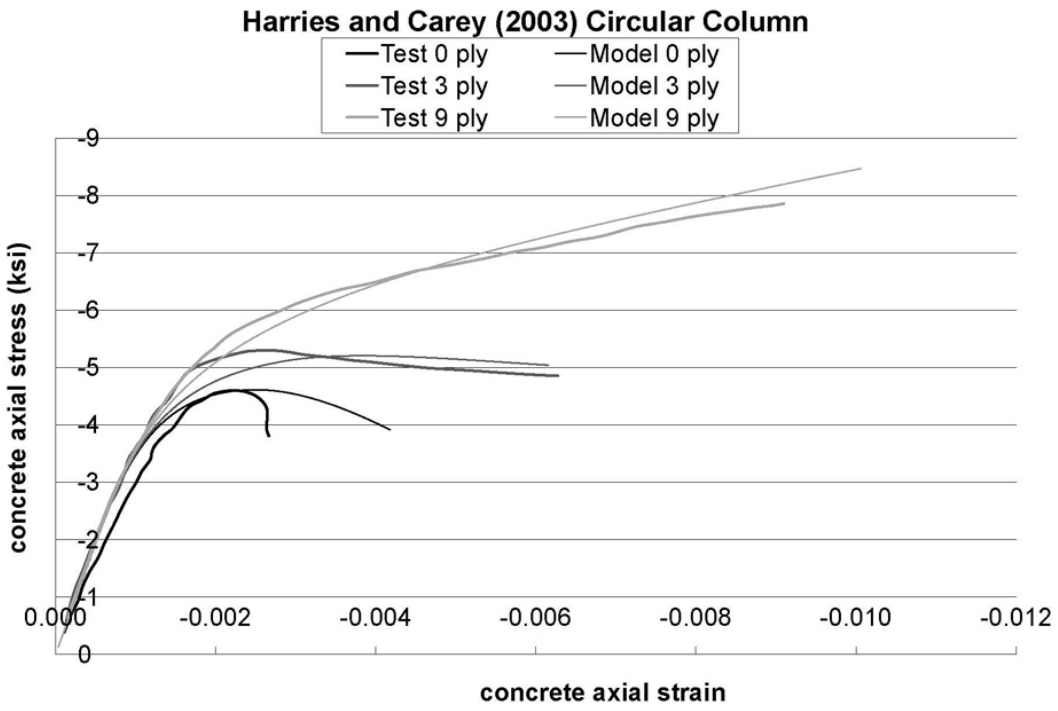

Figure 6.2: Comparison of model to test data from Harries and Carey (2003) for circular column.

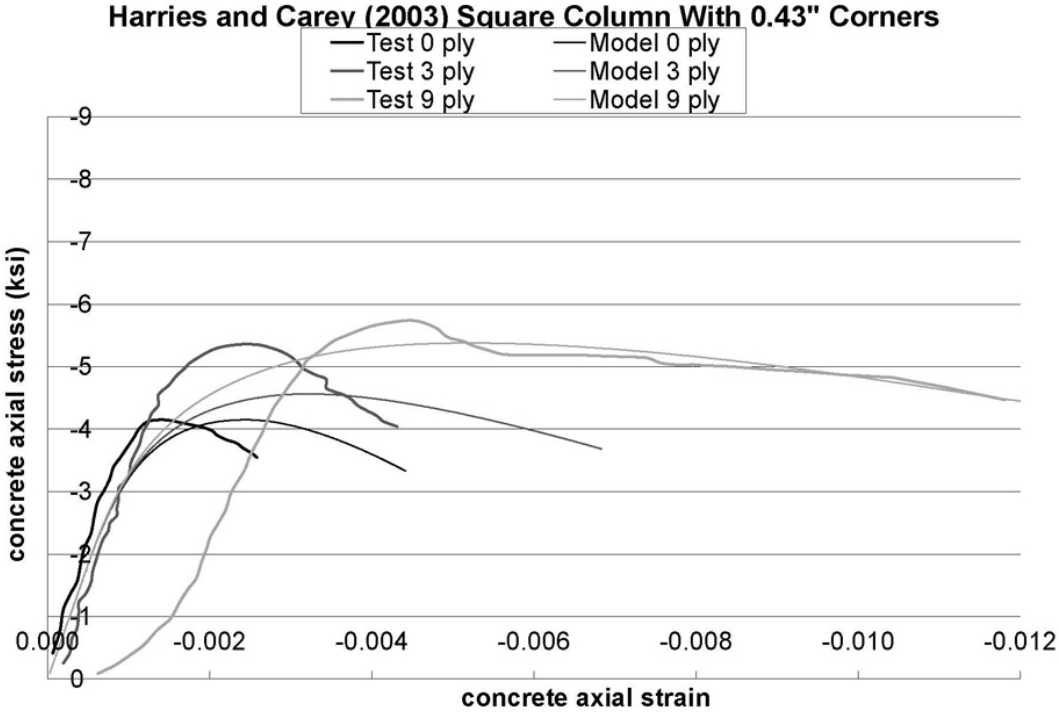

Figure 6.3: Comparison of model to test data from Harries and Carey (2003) for square column with 0.43 inch (11 mm) corner radius.

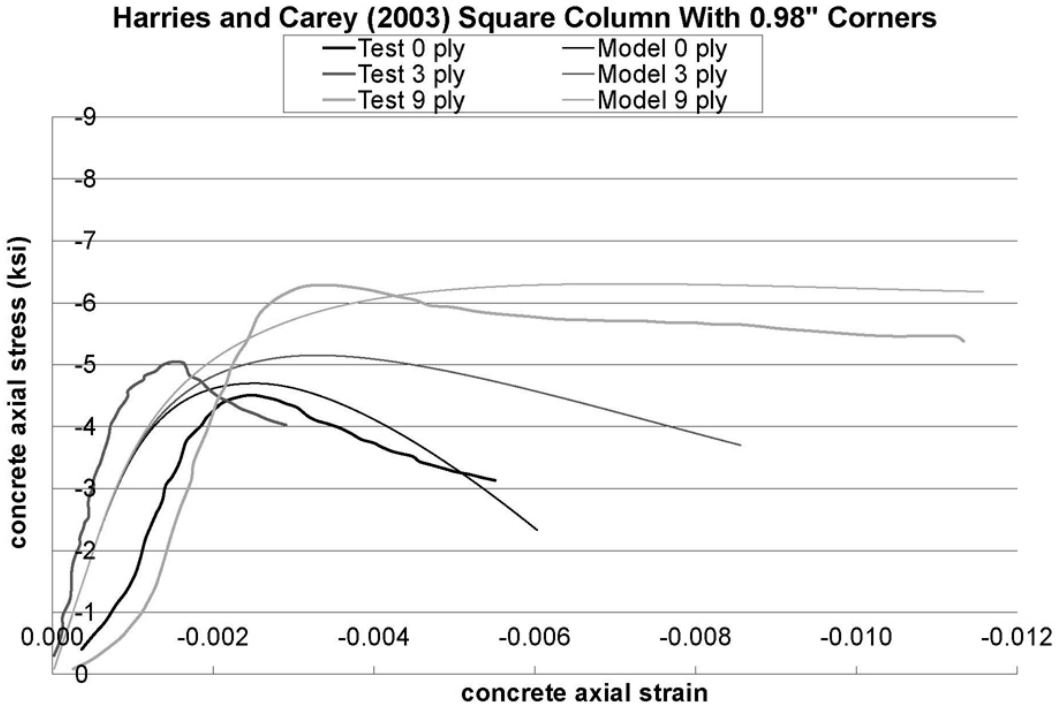

Figure 6.4: Comparison of model to test data from Harries and Carey (2003) for square column with 0.98 inch (25 mm) corner radius.

of square columns which are not captured by the FE model. However, since these shapes were again compared for steel confined sections, this issue will be discussed in conjunction with the results presented in Section 6.2.4.

6.2.3 Harries and Kharel (2003)

Experimental data for circular columns confined by two types of composites was given in Harries and Kharel (2003). In addition to the typical concrete axial stress versus strain data, the authors provided the dilation ratio of the column. The dilation ratio is defined as the ratio of the transverse strain to the axial strain. In order to compare transverse strains, the FE model was loaded to the point at which it reached the same axial strain as the experiment. In some cases, the FE model predicted composite rupture before it reached the final experimental axial strain. These cases are denoted by an asterisk (*) in the figures. Comparison of the carbon FRP confined columns is shown in Figures 6.5 and 6.6. Results of the E-glass FRP confined columns are

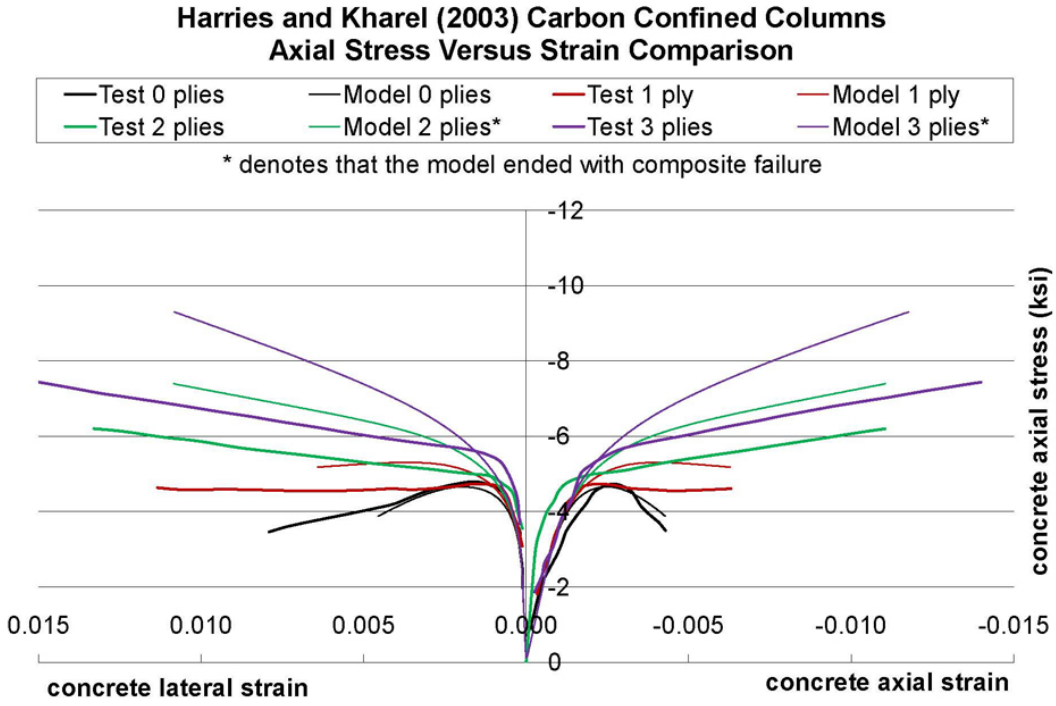

Figure 6.5: Axial stress versus strain comparison of model to test data from Harries and Kharel (2003) for columns confined by carbon FRP.

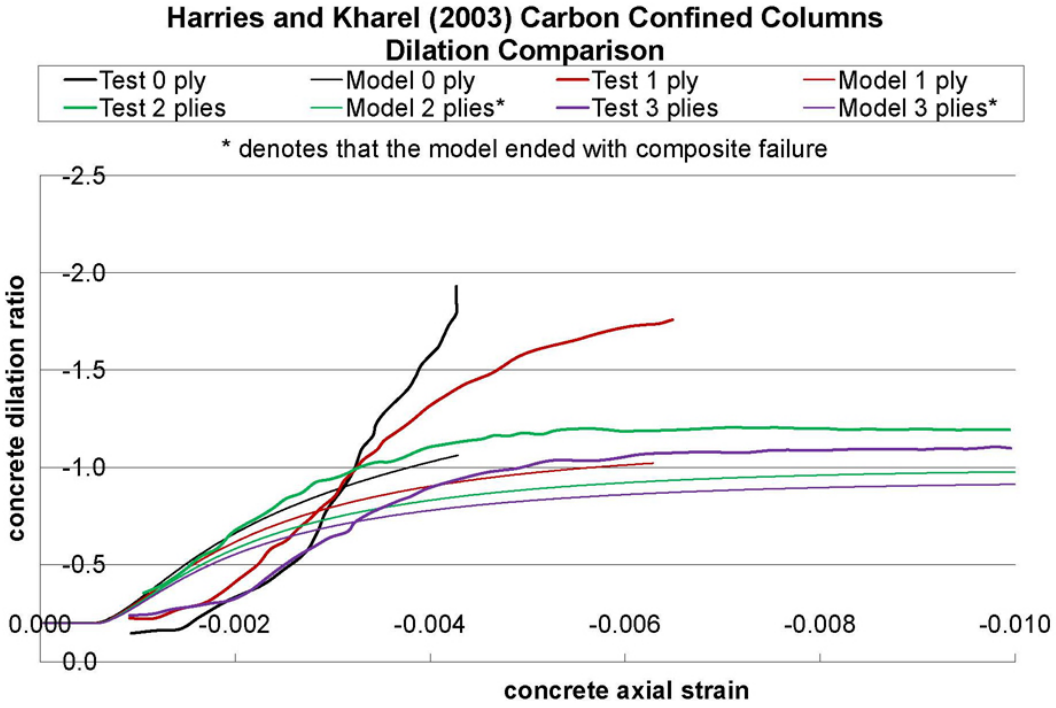

Figure 6.6: Dilation ratio comparison of model to test data from Harries and Kharel (2003) for columns confined by carbon FRP.

compared in Figures 6.7 and 6.8. The mesh used to generate the FE results is shown

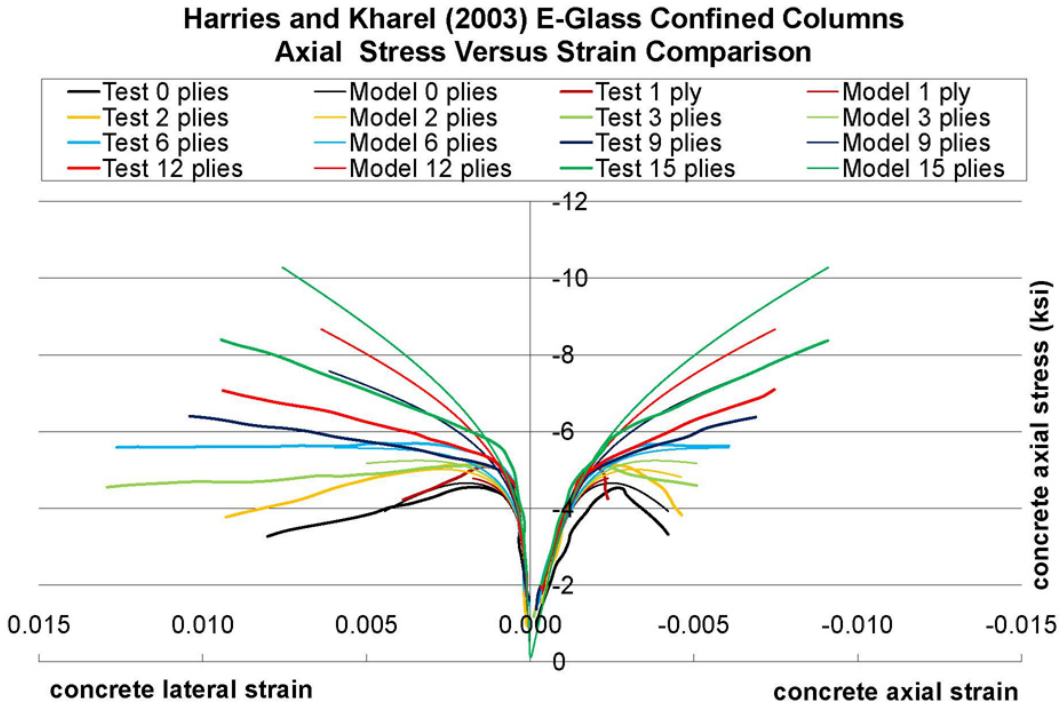

Figure 6.7: Axial stress versus strain comparison of model to test data from Harries and Kharel (2003) for columns confined by E-glass FRP.

in Appendix Section G.3.

For the carbon FRP confined columns, the FE model appears to consistently overestimate the increase in strength with confinement. However, it also underestimates the amount of transverse strain that the column should exhibit. It would be expected that if the FE model were underestimating the transverse strains of the specimen, it would also underestimate the strains in the confining material and, thus, underestimate the strength increase. The fact that the FE model underestimates the transverse strain but overestimates the strength implies that the stiffness of the confining material provided by the paper is too large. This idea is reinforced by the fact that for lower levels of E-glass confinement (where the confining material behavior will not affect the results as significantly), the strength increase in the FE model is somewhat closer to that predicted by the experiment. However, it must also be noted that the overestimate of the strength and underestimate of the transverse strains are consistent between the two different confining materials found in the paper. Thus, while it

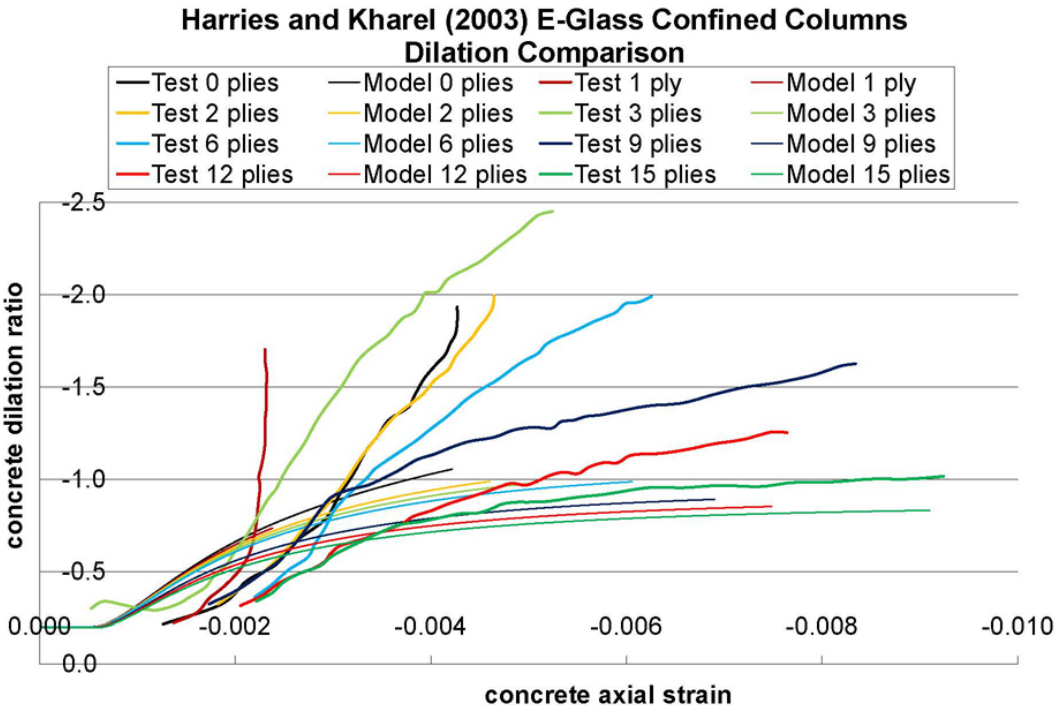

Figure 6.8: Dilation ratio comparison of model to test data from Harries and Kharel (2003) for columns confined by E-glass FRP.

may still be the case that the manufacturer overestimated the composite properties for both types of fiber, it may also be the case that the FE model is not predicting the behavior of this concrete mix very well. Examining the FE model prediction for the unconfined columns shows that it is also underestimating the transverse strains for that unconfined case.

This paper and Harries and Carey (2003) used the same E-glass FRP for confinement. The FE model performed exceptionally well at predicting the behavior of the circular columns confined by the E-glass FRP in Harries and Carey (2003). Thus, it would seem that the composite properties are well defined for that case. It may be the case, physically, that the ply effectiveness is decreased with an increasing number of plies due to the increase in the final thickness of the FRP. This would mean that the strength increase from one ply to two plies would be more significant than the strength increase from, for example, 12 plies to 13 plies. Unfortunately, the data at lower confinement levels exhibit some discrepancies. In the case of the Carbon FRP, no strength increase is exhibited by the addition of the first ply. In the case of the

E-Glass FRP, the 1, 2, and 3 ply results exhibit the same peak stress, which is higher than the unconfined peak stress. Due to these inconsistencies in the test data at lower confinement levels, it is difficult to see the increase in strength with each ply. However, if it is a valid assumption that the ply effectiveness is decreased with an increasing number of plies, this effect is not accounted for in the FE model and could lead to the fact that the strength overestimation is more severe at higher ply counts.

The FE model does reasonably well predicting the data, particularly considering that the data is not consistent for low ply counts. Thus, it is considered that the errors seen between the FE model and the experiments are not significantly larger than the errors that can be seen in the experiments themselves.

6.2.4 Mander et al. (1988a)

Both circular columns and rectangular walls were tested by Mander et al. (1988a). The FE model was used to predict four different columns and three different walls. The FE meshes used are shown in Appendix Section G.4. The cross section and rebar configuration for the four circular columns is shown in Figure 6.9. It should be

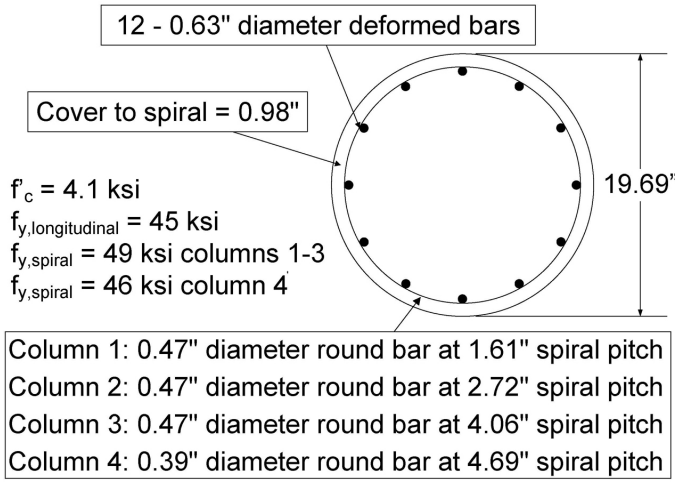

Figure 6.9: Details of circular columns tested in Mander et al. (1988a) and predicted using the current model.

noted that a difference between the FRP tests and the steel rebar confined tests is the presence of cover concrete. It is expected that the concrete external to the steel

hoops or spirals will spall off and become ineffective at strains higher than the axial concrete strain at peak uniaxial stress. The model should properly account for this effect. A comparison of the FE model prediction to the experimental data is shown in Figure 6.10. The FE model predictions do not extend to the same axial strain as

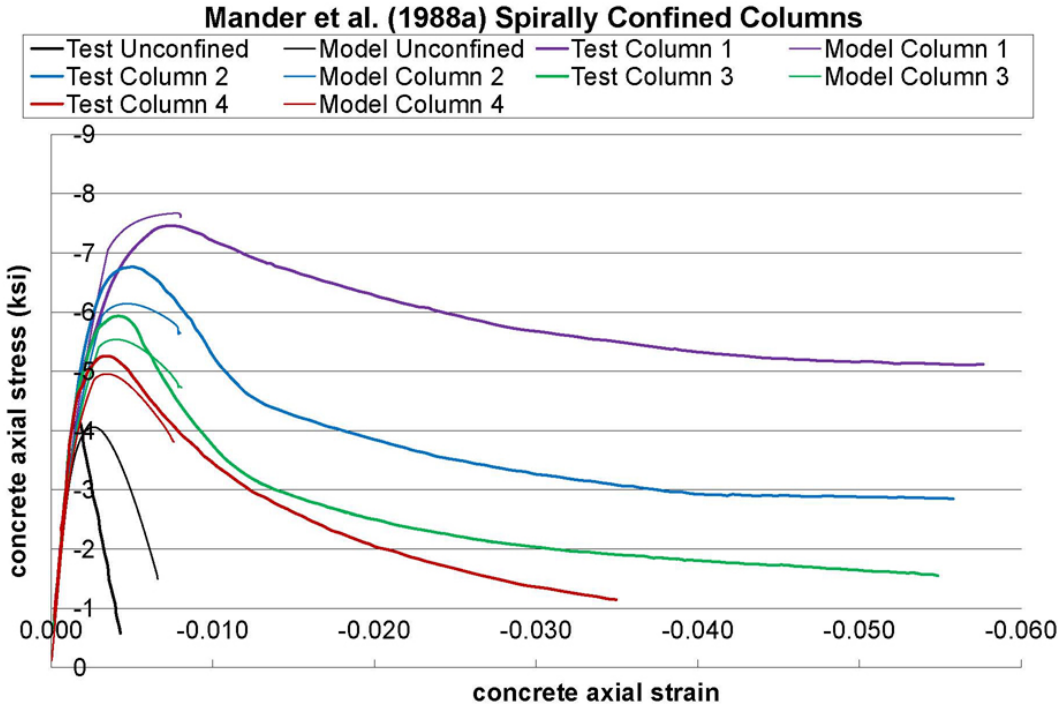

Figure 6.10: Comparison of model to test data from Mander et al. (1988a) for circular columns.

the test data. While the FE model successfully predicted strain softening in the case of the FRP confined sections, it stops converging not long after the peak stress in the steel rebar confined case. However, it was discovered that if the tensile meridian of the residual surface was set to be equal to that of the compression meridian, the FE model would continue on to the desired strain levels. It is not apparent why this change fixes the convergence problem. Fundamentally, a nonlinear problem with strain softening is extremely sensitive and finding a reliable iteration method can be extremely difficult. Further, recall from Section 4.3, no data was found for the tensile meridian of the residual surface. An assumption was made that the ratio of the parameters for the compressive and tensile meridians between the peak and residual surface would be the same. There is no physical basis for that particular assumption.

Therefore, there is also no data to refute the assumption that the residual surface is round. Thus, the concrete model, altered to have a round residual surface, was implemented into the FE model and used to predict the column data. Results for this case are shown in Figure 6.11. The spiral strains were given for column 4 and

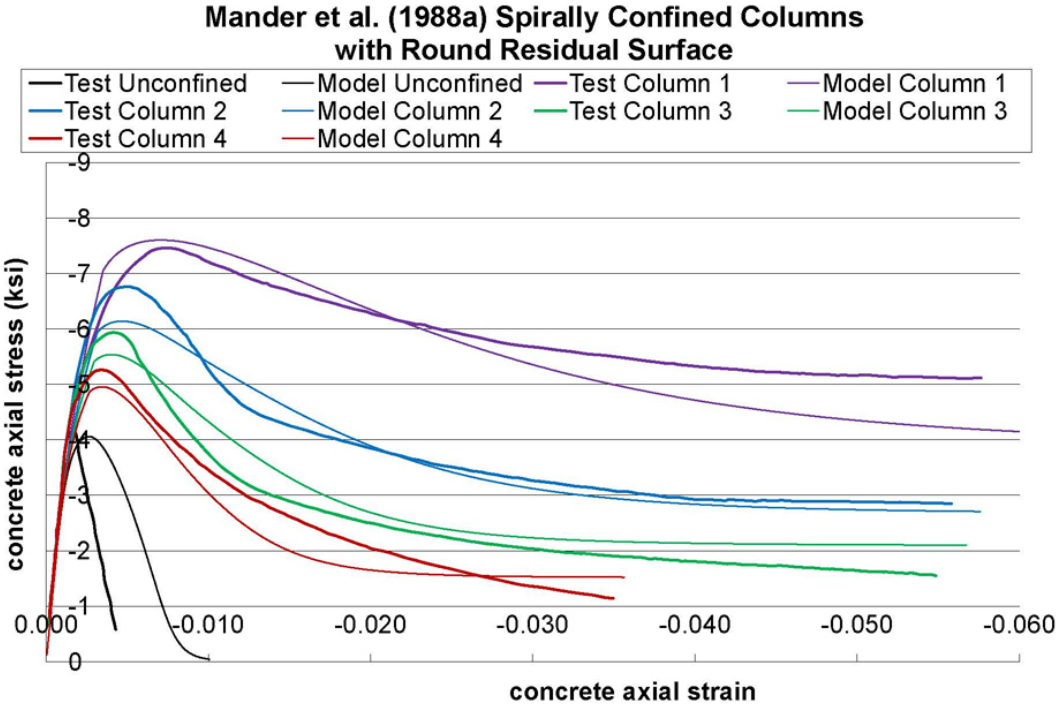

Figure 6.11: Comparison of model with round residual surface to test data from Mander et al. (1988a) for circular columns.

are compared to FE model predictions in Figure 6.12. Up to the peak stress of the concrete, the results will be identical for the two different residual surfaces. Use of a round residual surface is expected to overestimate the residual strength of the concrete for cases where the Lode angle is less than 60°. However, for circular columns, the theoretical Lode angle will be close to 60° throughout the specimen because the two lateral in-plane stresses are roughly equal. Thus, it is not expected that the concrete model with a round residual surface will differ much in prediction from the concrete model originally defined in Chapter 3.

The FE model does quite well at predicting the strain at peak stress. However, it underestimates the peak stress increase due to confinement for the circular columns except for the case with highest confinement. This may be due to the strain rate

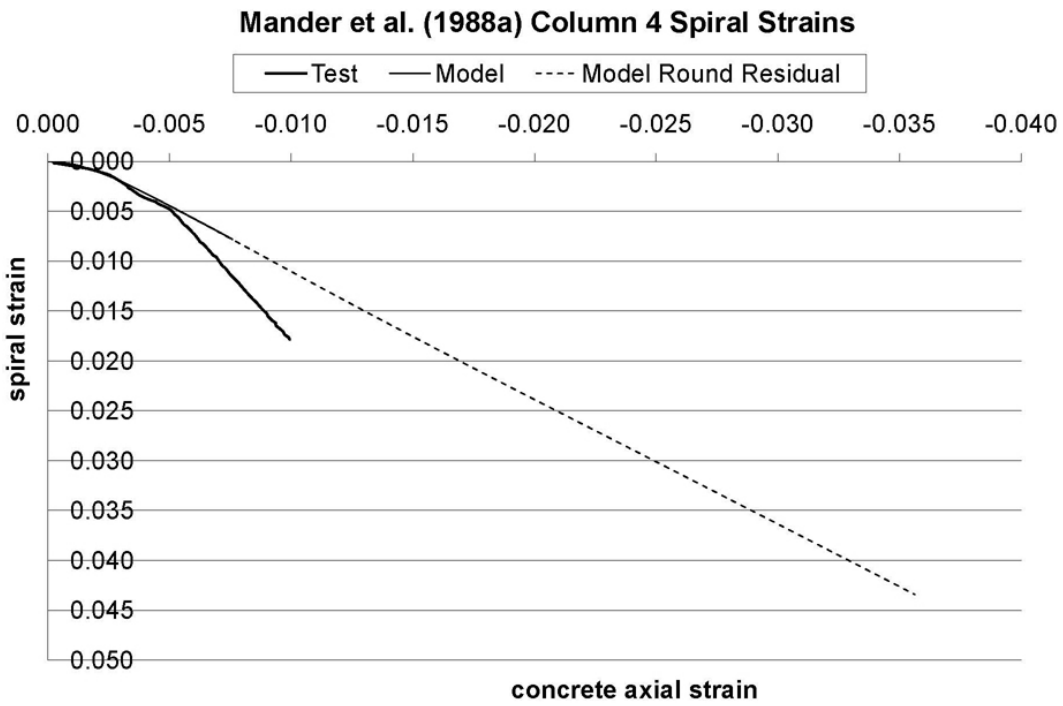

Figure 6.12: Comparison of FE model to test data from Mander et al. (1988a) for column 4.

of 0.013 $\sec^{-1}$ at which the columns were tested. As mentioned in Section 6.1, the concrete stiffness, peak strength, and strain at peak stress are increased when loading at a strain rate of 0.013 $\sec^{-1}$. This higher value for f'_c was used for the FE model. However, it appears that how the peak strength increases with confinement may also be affected by rapid loading, which is not accounted for in the FE model. Scott et al. (1982) measured a larger strength increase due to confinement at a strain rate of 0.0167 $\sec^{-1}$ than the strength increase at a strain rate of 0.0000033 $\sec^{-1}$. Thus, it is this dynamic loading effect which is most likely leading to the discrepancy in peak stress, as the concrete model presented in this thesis does not account for strain rate effects.

The FE model does exceptionally well at predicting the spiral strains up to the peak stress of the concrete. In the strain softening portion, the FE model appears to be underestimating the spiral strains. The concrete axial strain at peak stress is approximately 0.0034. Thus, it would appear that the FE model is underestimating the post-peak volumetric expansion for this column.

The cross section and rebar configuration for the three different walls are shown in Figure 6.13. The experimental results are compared to the FE model predictions

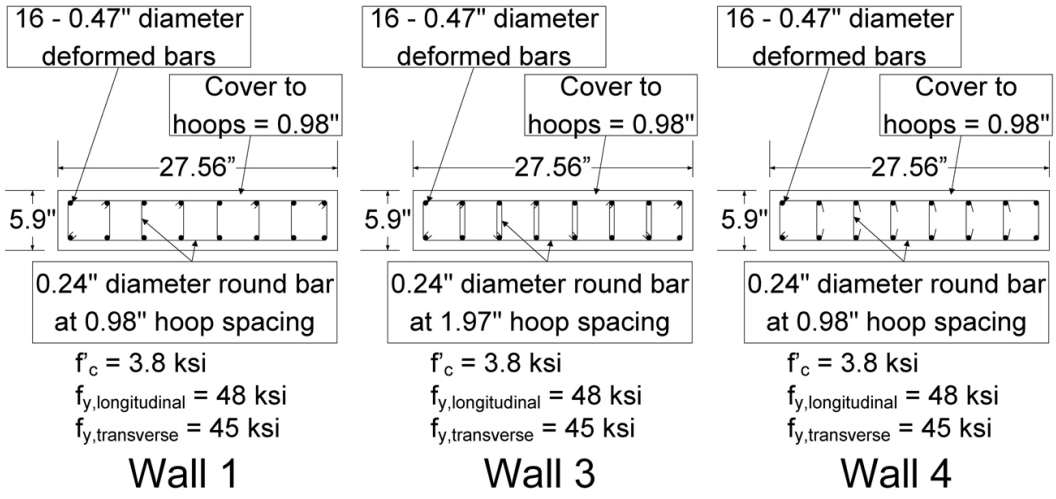

Figure 6.13: Details of rectangular walls tested in Mander et al. (1988a) and predicted using the current model.

for the walls in Figure 6.14. Note that wall 8 was one of four unconfined walls tested by Mander et al. (1988a). This wall had no longitudinal or transverse steel. As with the circular columns, the identical problem was encountered with the walls: the FE model was not able to predict the post-peak behavior of the rectangular walls. The concrete model was again modified to have a round residual surface, and the FE model was then able to successfully predict the strain softening behavior of the walls. However, for the rectangular walls, it is expected that the Lode angle will be different than 60°, as was the case for the circular columns. Therefore, it is expected that the residual strength of the walls will be slightly overestimated by using a round residual surface compared to the residual surface laid out in Chapter 3. However, recall that there is no data for a Lode angle of 0°, so it is not known which residual surface more closely represents concrete.

The FE model prediction with the round residual surface is compared to experimental results in Figure 6.15. The FE model is not as successful at predicting the behavior of the walls as it was with the circular columns. However, a review of the experimental data may reveal the cause of some of the discrepancies. Wall 3 had

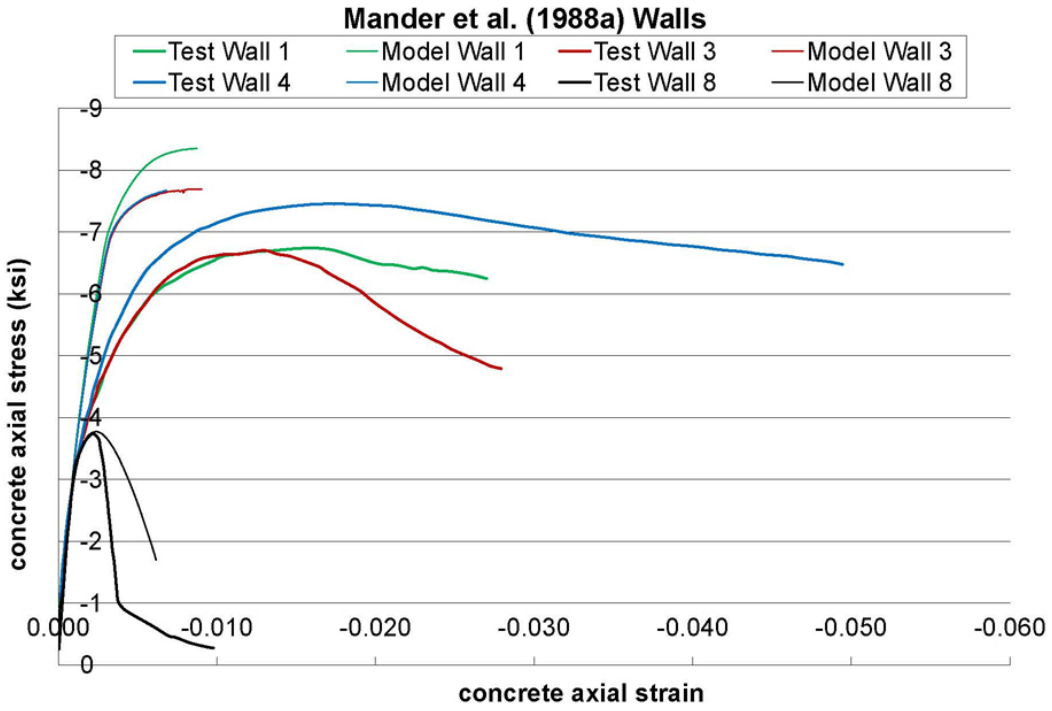

Figure 6.14: Comparison of model to test data from Mander et al. (1988a) for rectangular walls.

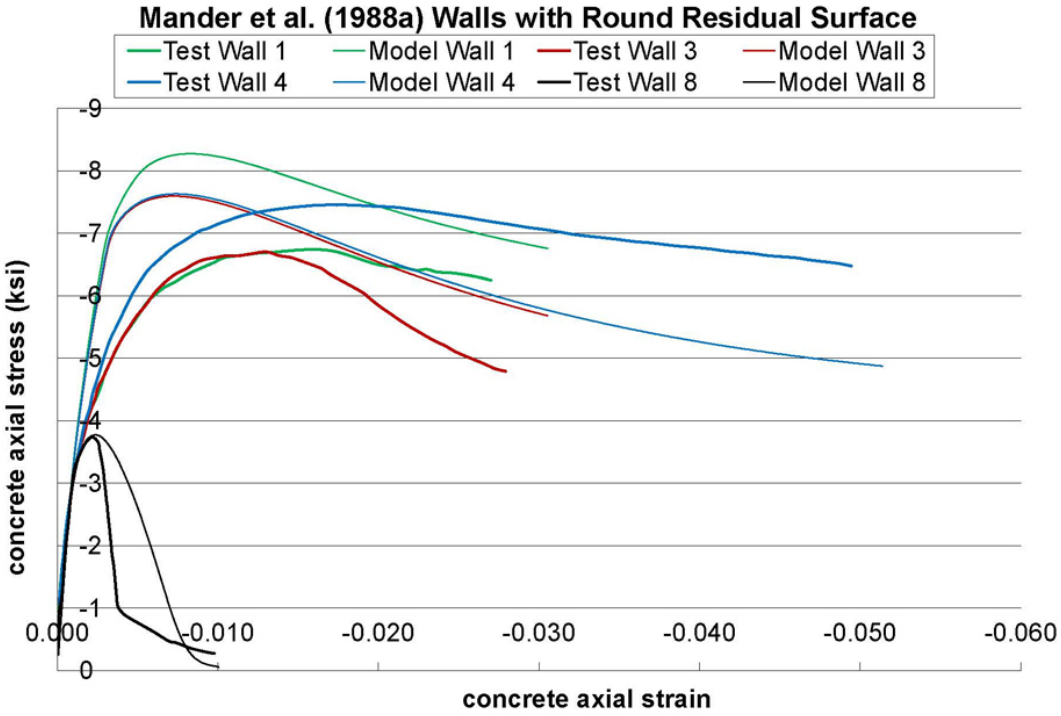

Figure 6.15: Comparison of model with round residual surface to test data from Mander et al. (1988a) for rectangular walls.

twice as much transverse steel as wall 4, but with twice the hoop spacing. Thus, it is expected that their behaviors may be similar. Wall 1 had more transverse steel than wall 4, but with the identical hoop spacing. Therefore, it is expected that wall 1 will support a higher concrete stress then wall 4. However, these results are not seen in the experimental testing. Mander et al. (1988a) noted that an unexpected issue with wall buckling likely led to the premature failure of wall 1. Thus, similar testing issues may have lead to the discrepancies seen in predicting the peak stress. It is clear that the FE model is also underestimating the strain at peak stress for all of these walls. The FE model also appears to soften more rapidly than the experiments. This is likely due to the absence of strain hardening in the steel model. The effects of not modeling strain hardening in the rebar will be illustrated further in Section 6.2.5.

6.2.5 Scott et al. (1982)

Two square columns tested by Scott et al. (1982) were compared to predictions made by the FE model, using the FE meshes shown in Appendix Section G.5. The cross section and rebar details for these two columns are shown in Figure 6.16. A compar-

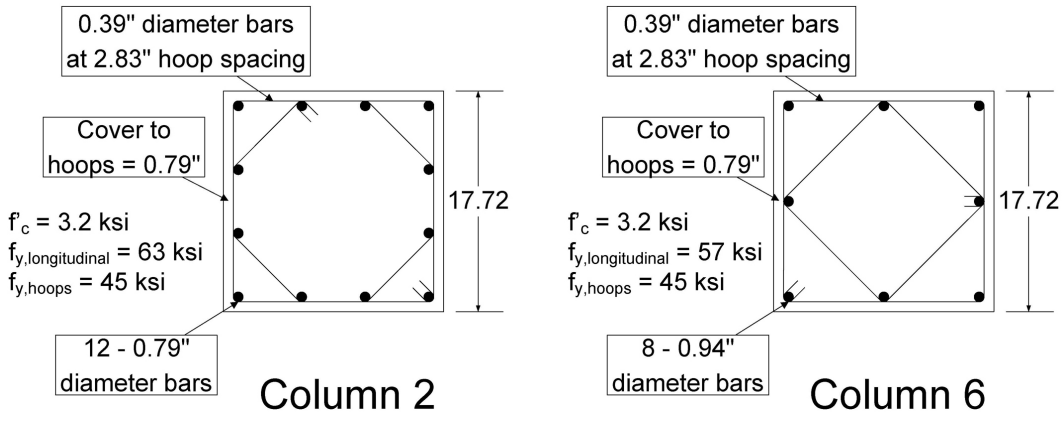

Figure 6.16: Details of square columns tested in Scott et al. (1982) and predicted using the current model.

ison of the experimental results to the FE model predictions is shown in Figure 6.17. Note that column 1 was an unconfined specimen and, therefore, had no longitudinal or transverse steel. The same problem discussed in Section 6.2.4 was encountered

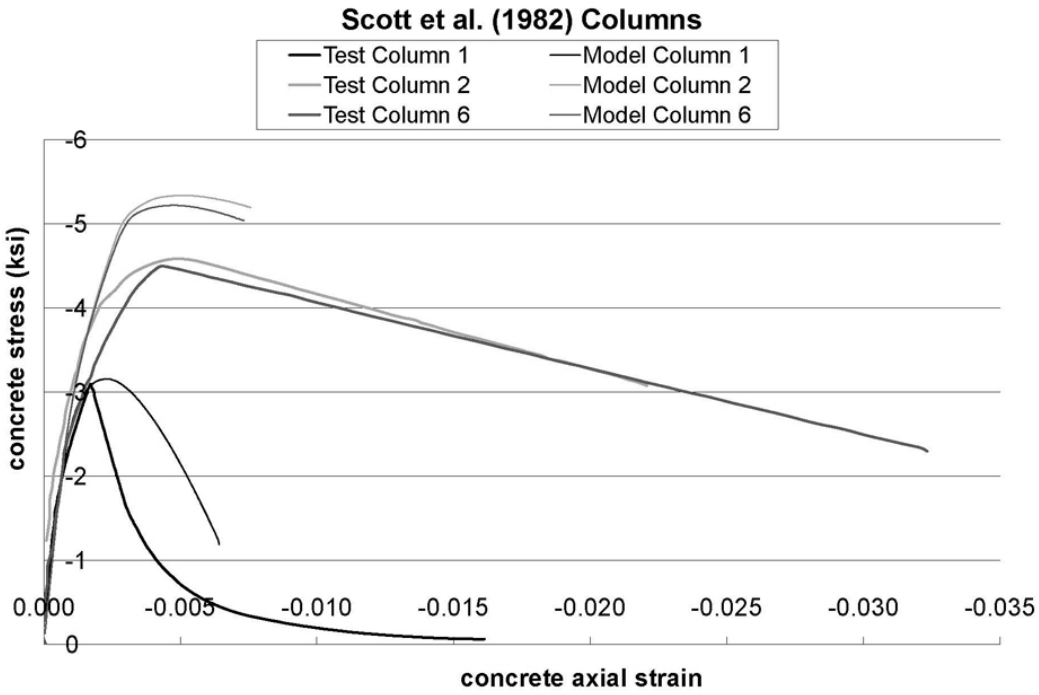

Figure 6.17: Comparison of model to test data from Scott et al. (1982) for square columns.

with this data: the FE model is not able to predict the strain softening region. The concrete model was again altered to have a round residual surface, and the results are compared in Figure 6.18. While the strength is overestimated for both columns, the FE model does an excellent job at predicting the difference in strength due to the different transverse rebar configurations. While the performance difference is small, the ability of the FE model to accurately capture it shows that the FE model is able to predict the way in which confinement affects the strength and ductility of the concrete, which was its core purpose.

Scott et al. (1982) also provided plots of the concrete and longitudinal steel forces as well as the average hoop stresses for each of these two columns. These are compared to the FE model predictions in Figures 6.19 through 6.22. Here, it is apparent how well the FE model is able to predict the concrete expansion which engages and loads the steel rebar. The strain softening appears to occur too quickly in the FE model, but this is likely due to the absence of strain hardening in the steel model. The strains at which steel strain hardening begins to take place in the experiment is where the

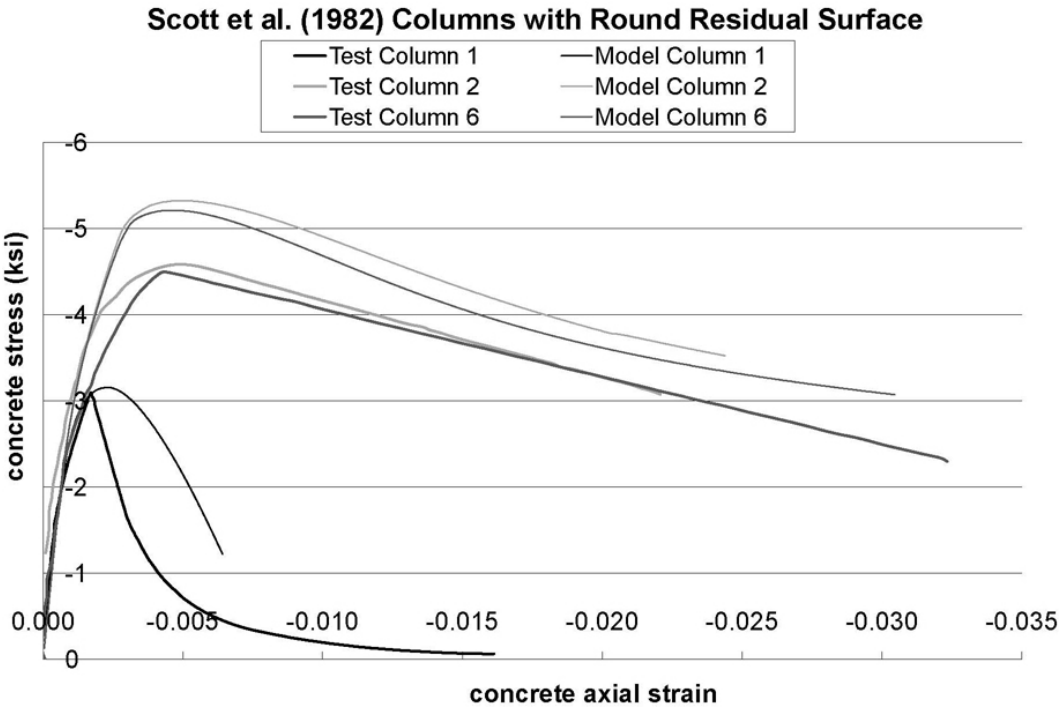

Figure 6.18: Comparison of model with round residual surface to test data from Scott et al. (1982) for square columns.

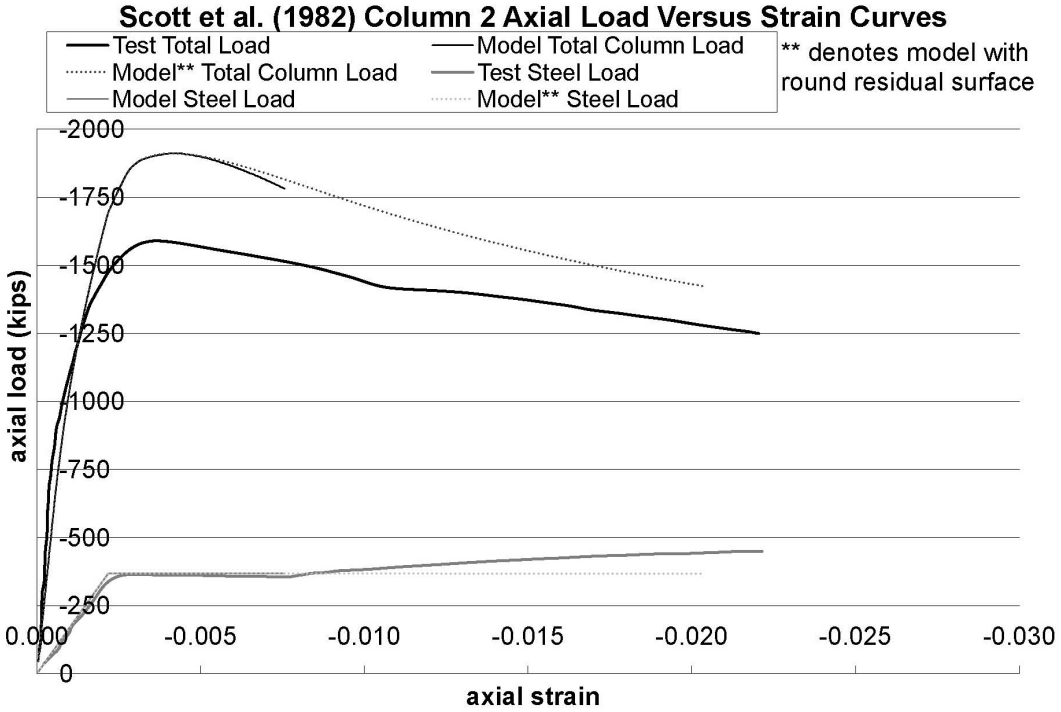

Figure 6.19: Comparison of model to test data from Scott et al. (1982) for column 2 concrete and steel forces.

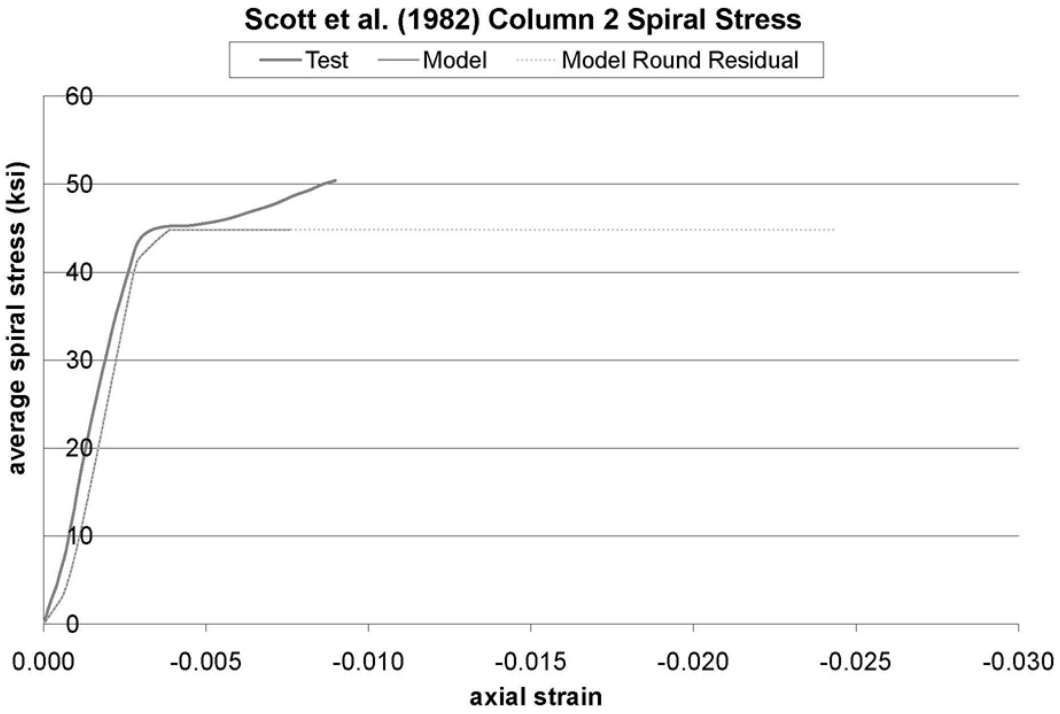

Figure 6.20: Comparison of model to test data from Scott et al. (1982) for column 2 hoop stresses.

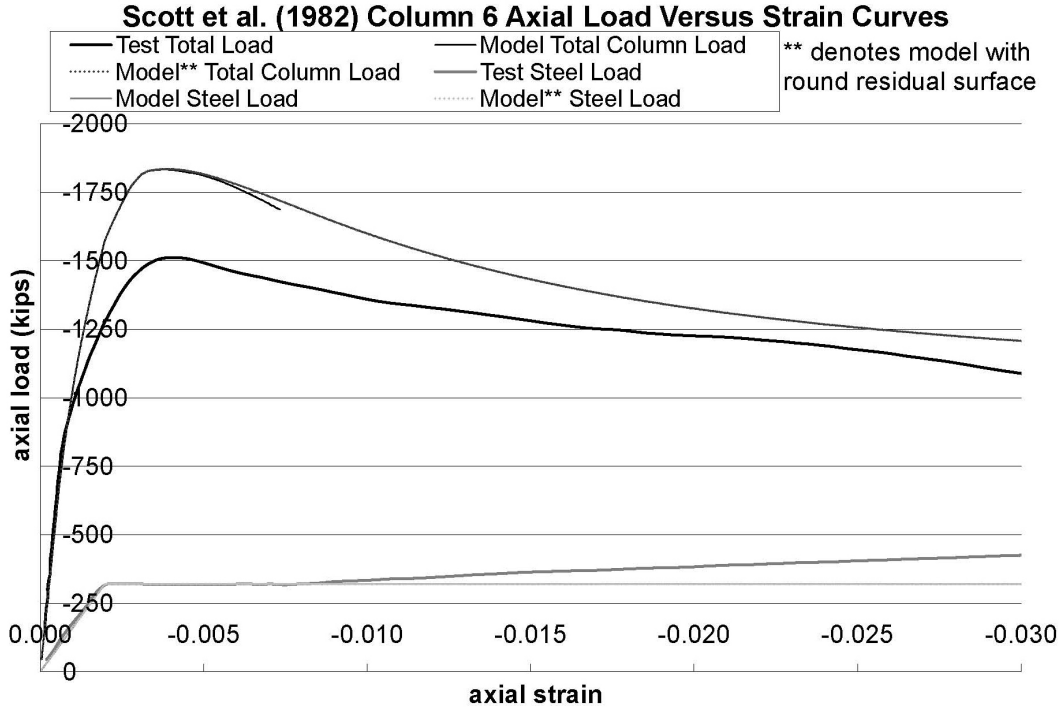

Figure 6.21: Comparison of model to test data from Scott et al. (1982) for column 6 concrete and steel forces.

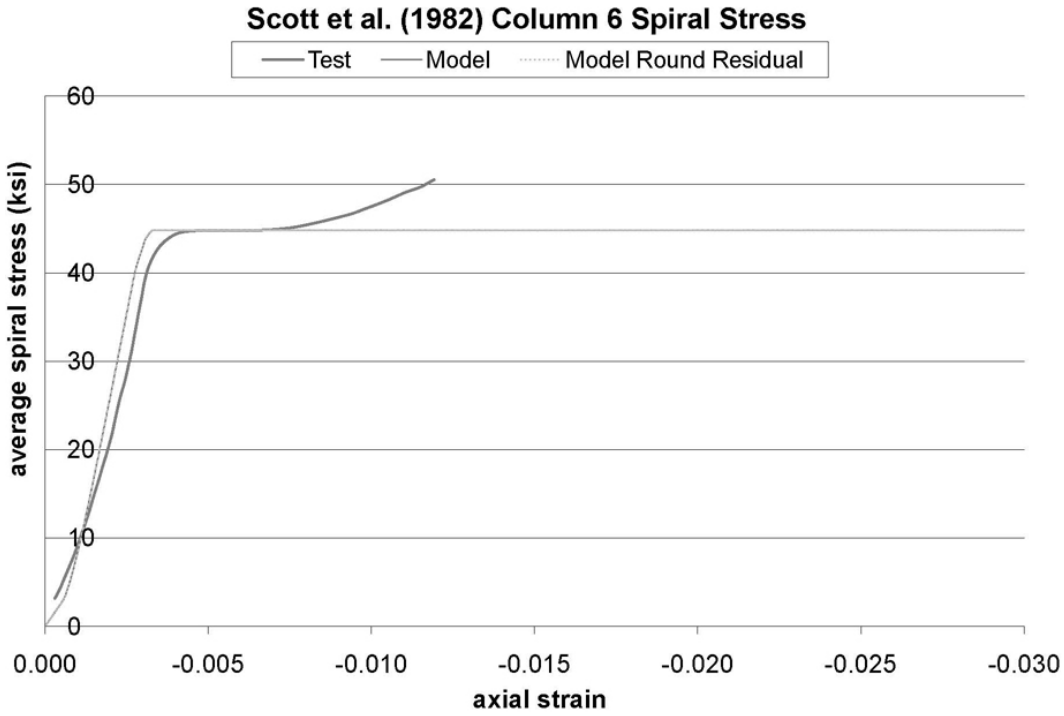

Figure 6.22: Comparison of model to test data from Scott et al. (1982) for column 6 hoop stresses.

FE model continues to soften more rapidly than seen in the experiments. If strain hardening were to be introduced into the steel model, the FE model predictions may fall at nearly the same rate as the experiments show. Thus, although the FE model over-predicts the strength for this case, all other behaviors are predicted extremely well by the concrete model.

6.3 Conclusions from the Comparisons

It is well established that variability in the behavior of concrete can be quite substantial (Nilson, 1997). Due to the variability within each material used to create the mix, the process by which it is created, the change in the concrete with age and loading, and the fact that concrete is a congeries of different materials, the strength, stiffness, and other overall properties of concrete will vary. For these reasons, it is difficult to consistently predict the behavior of concrete when the material itself does not behave consistently. For most modeling comparisons, the ideal is to have the prediction lie

within a few percent of the tests; this is not possible for concrete. Several experiments performed identically on the same batch of concrete specimens typically will not lie within a few percent of each other [for example, Bresler and Pister (1958), Duke and Davis (1944), and Hurlbut (1985)]. This must be appreciated when comparing a computer model to the somewhat erratic experimental data for concrete.

The FE model is able to predict concrete behavior under a wide range of loading and confinement types. There is no consistent error observed in any predicted quantity; an overestimate in a particular quantity on one set of data will be an underestimate on a different set. With the FRP confined circular columns, the FE model shows an overestimation of the observed strength, whereas for the circular steel confined columns, the FE model underestimates the observed strength. The FE model prediction of the square FRP confined columns tends to overestimate the experimental strain at peak strength, while the prediction for the steel confined walls underestimates this quantity. The remaining experiments showed close agreement in the experimental strain at peak stress. Thus, the FE model does not appear to be flawed in some fundamental way that would lead to a consistent difference between experiments and model predictions.

More significantly, the FE model is able to capture the changes in concrete behavior brought about by changes in shape, confining material, steel confinement configuration, and other experimental variables. While the FE model prediction of the square FRP confined columns of Section 6.2.2 shows a difference in the shape of the axial stress versus strain curves, the FE model predicts the curves for the square rebar confined columns of Section 6.2.5 reasonably well. Also, the FE model is able to predict the behavior of circular columns quite well. Thus, it is shown that the FE model can successfully predict concrete behavior for both square and circular cross sections. Further, the FE model is able to represent the concrete behavior with both FRP confinement and steel rebar confinement. The circular cross sections in Section 6.2.3 show a transition from post-peak strain softening to strain hardening. This transition is predicted by the FE model. The small increase in peak stress with a change in transverse steel configuration in Section 6.2.5 is also seen in the FE model

predictions. Thus, the FE model is able to predict concrete behavior confined by two quite different confinement materials.

The experimental data in Section 6.2.1 proved to have some obvious discrepancies. The unconfined ACI equations were able to predict the behavior better than the FE model. While the section was lightly confined, some effect of confinement would be expected. However, none was seen in the experimental results. Thus, issues with the data made it impossible to draw any conclusions about the accuracy of the FE model predictions. More data of this type is needed for comparison before the FE model can be considered accurate in predicting axial load-moment strength interaction diagrams.

The FE model was designed to account for a variety of different loading configurations (confinement material, geometry, loading type, etc.) so that the behavior of concrete under these conditions could be studied. While it is unfortunate that the original concrete model has an unknown issue that prevents prediction of the full strain softening region for steel confinement, use of the round residual surface appears to be a satisfactory substitute until the issue can be resolved. Overall, the FE model is considered to perform adequately for predicting the axial load behavior of confined sections.

Chapter 7

Effects of Cross Sectional Shape and Confining Material

The finite element (FE) model is utilized to compare the performance of square versus circular cross sections, as well as fiber reinforced polymer (FRP) versus steel hoop confined sections. A series of concrete axial stress versus strain curves are generated with different confinement levels for each confining material. An axial load-moment strength interaction diagram is created for the highest confinement level for each cross sectional shape and confining material. Using these analyses, a comparison is performed to examine how cross sectional shape and confining material affect the strength and ductility of the section. The cross sections and loading details are described in Section 7.1. The results of this comparison are discussed in Section 7.2.

This comparison can be used to highlight the different advantages and disadvantages of the different section shapes and confining materials. Designers face many decisions when laying out the details of a section. For each specific application, a slightly different performance standard may be applied. By understanding the effects of these two design variables, the designer is able to choose the shape or confining material that exhibit more optimal performance for the specific application.

7.1 Discussion of Sections Used for Performance Comparison

A square and a circular cross section, both confined by steel hoops, are designed in order to examine the effects of cross sectional shape. To more easily facilitate the comparison, the two sections are designed to have an identical confined area. It is important that the two cross sections have the same confined area because it is expected that the cover concrete will spall off and become ineffective. Details of the two cross sections are shown in Figure 7.1. For both sections, hoop spacings of 3, 6,

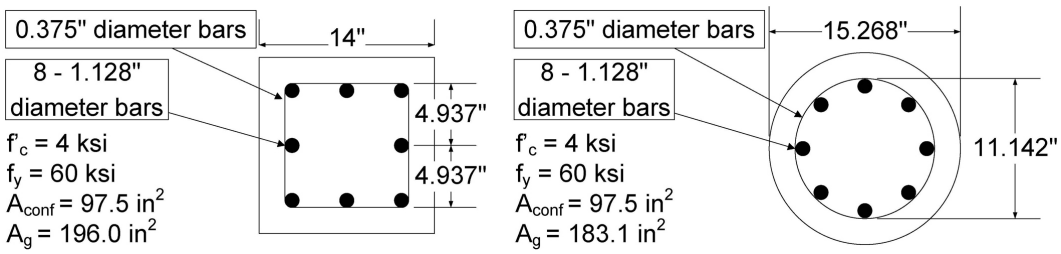

Figure 7.1: Details of square and circular cross sections confined by steel hoops.

10, and 14 inches (76, 152, 254, and 356 mm) are employed. A concrete axial stress versus strain curve is computed for each cross section and hoop spacing. The FE meshes used to represent these cross sections are shown in Appendix H. As discussed in Sections 6.2.4 and 6.2.5, it is necessary to modify the concrete model to have a round residual surface in order to predict the behavior to sufficiently large compressive strain levels. This is only necessary for axial loading of the steel confined sections. Recall that use of the round residual surface is expected to slightly overstimate the residual stress for loading which is not close to a Lode angle of 60°. All other analyses are performed with the original concrete model as described in Chapter 4. An axial load-moment interaction diagram was created for both cross sections with the 3 inch (76 mm) hoop spacing only.

A similar configuration is then considered with an alternative confining material. The steel hoops are removed from the FE model and replaced with an E-glass FRP around the outside of each section. In this configuration, the confined area is no

longer identical for the square and the circular cross sections. The confined area of the square cross section is 196.0 square inches (1265 square centimeters), whereas the confined area for the circular cross section is 183.1 square inches (1181 square centimeters). The E-glass FRP used for confinement has a strength of 428 lb per inch per ply (75 N per mm per ply) and an elastic modulus of 28 kips per inch per ply (4.9 kN per mm per ply). The FE meshes used to predict the behavior of these sections are shown in Appendix H. Concrete axial stress versus strain curves are generated for a confinement of 10 and 30 plies of the E-glass FRP. An axial load-moment interaction diagram is then generated for the two cross sections confined by 30 plies of E-glass FRP. Note that four of the axial load-moment cases required a refined mesh, shown in Figure H.5.

It is difficult to define what a comparable amount of confinement for steel hoops and E-Glass FRP is. In order to evaluate the confinement amounts for these two disparate materials, the elastic stiffness of each particular confinement configuration was evaluated. Table 7.1 shows the configuration of steel hoops that equates to the same confinement stiffness as a given ply count of E-Glass FRP.

Table 7.1: Confinement equivalence by elastic stiffness.

Number of E-Glass Plies	Equivalent Hoop Spacing (in)	Steel Hoop Bar Number	Steel Hoop Bar Area (in^2)
10	11.4	#3	0.11
10	20.7	#4	0.20
30	3.8	#3	0.11
30	6.9	#4	0.20
30	10.7	#5	0.31

7.2 Results of Comparison

The performance comparison for purely axial loads is presented in Section 7.2.1. Results of the axial load-moment interaction diagram are discussed in Section 7.2.2. In considering the performance of columns, axial load and moment capacity are the typical metrics used to determine the capability of the section to perform as required.

Thus, these quantities are used to explore the effects of section shape and confining material on the behavior of the column.

7.2.1 Axial Load Performance Comparison

As discussed in Sections 6.2.4 and 6.2.5, the analysis terminates prematurely when steel hoops are used for confinement. Thus, for the pure axial load cases of the steel confined sections only, the residual surface is round with the tensile meridian changed to match the compression meridian. For the E-glass FRP confined sections, the residual surface defined in Section 4.3 is used.

Concrete axial stress versus strain curves for the steel confined sections are shown in Figure 7.2, and for the E-glass FRP confined sections in Figure 7.3. The uncon-

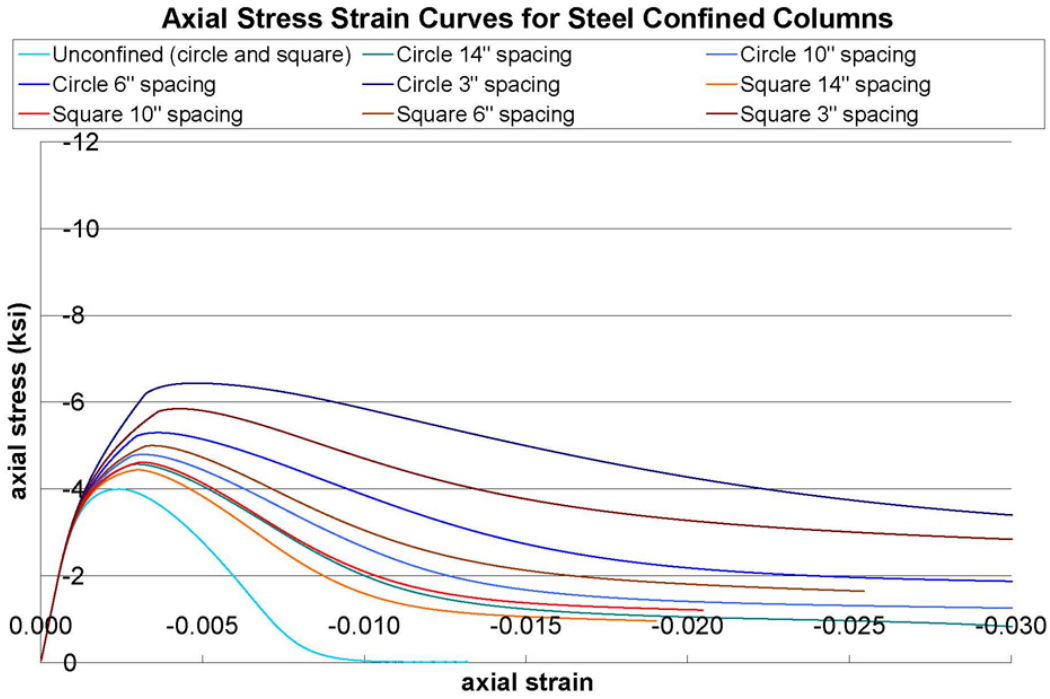

Figure 7.2: Comparison of the axial performance of steel confined sections.

fined square and circular sections have identical axial stress versus strain curves as predicted by the FE model. For the E-glass FRP confined cases, all modeled sections terminated with failure of the E-glass FRP (meaning that failure was defined by rupture of the fibers in the FRP).

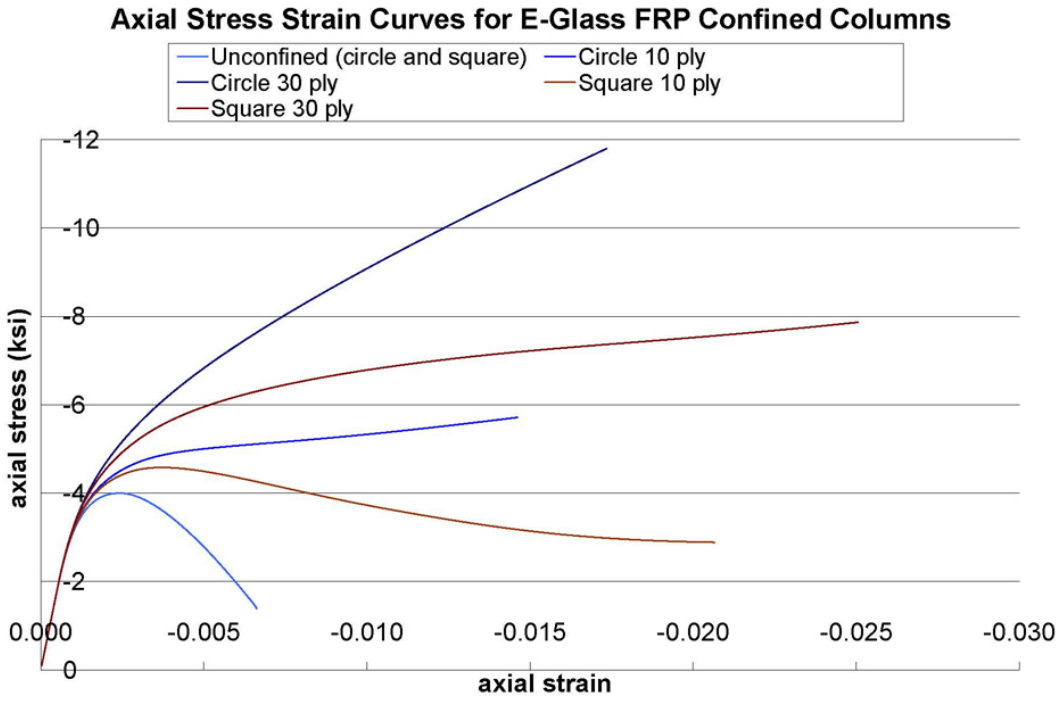

Figure 7.3: Comparison of the axial performance of E-glass confined sections.

For both types of confining materials, higher concrete stresses are supported by the circular sections than the comparable square sections, as expected due to the fact that confinement is more effective in circular sections. It is difficult to discern from Figure 7.2 how the two steel confined cross sections compare in ductility. Thus, Table 7.2 compares the strains at peak stress to those when the stress falls to 50% of the peak stress. The strain ratio is defined as the strain at 50% of peak stress divided by the strain at peak stress. It is clear that the ductility of the circular cross sections exceeds that of the square cross sections for the case of steel confinement. However, this is achieved through more effective use of the confinement, which leads to higher strains in the confining material for the circular sections (as shown by the last column of Table 7.2). The higher strains in the confinement for circular sections is more readily seen in the E-glass FRP results, since rupture of the FRP dictates the axial strain at failure. While the strength increase is much higher in the circular sections, the final axial strain of the square cross sections is higher because the FRP is not as highly stressed for this case. This lower stress in the FRP means that rupture of the FRP will occur at a higher axial strain. Thus, if a designer

Table 7.2: Strength and ductility comparison of square versus circular steel confined sections.

Cross Section Shape	Hoop Spacing (in)	Peak Stress (ksi)	Peak Stress $/f'_c$	Strain at Peak Stress	Strain at 50% of Peak Stress	Strain Ratio	Confinement Plastic Strain at 50% of Peak Stress
Circle	14	-4.574	1.143	-0.0030	-0.0092	3.084	0.0081
Circle	10	-4.799	1.200	-0.0032	-0.0109	3.404	0.0100
Circle	6	-5.302	1.326	-0.0036	-0.0155	4.270	0.0151
Circle	3	-6.441	1.610	-0.0048	-0.0341	7.079	0.0343
Square	14	-4.448	1.112	-0.0030	-0.0082	2.734	0.0054
Square	10	-4.620	1.155	-0.0031	-0.0093	3.009	0.0063
Square	6	-5.000	1.250	-0.0034	-0.0123	3.580	0.0087
Square	3	-5.851	1.463	-0.0043	-0.0274	6.405	0.0211

was concerned more about the axial strain of the section at confinement rupture, the square cross section would outperform the circular cross section. However, if the greater concern is the load carrying capacity of the column, the circular cross sections consistently outperform the square cross sections. With structural design, the designer often requires a ductile failure mode. These results raise the question of what exactly represents a ductile failure. If it is desirable that the specimens exhibit some form of softening as a warning of the onset of failure, only the square cross section confined by 10 layers of FRP would be considered to exhibit ductile failure. All other sections reach their peak stress simultaneously with the failure of the E-glass FRP. This may be considered a brittle failure mode, as the onset of failure is not preceded by softening and redistribution of the load. Examples of this brittle failure can be found in the literature (Pulido et al., 2004). However, all FRP confined sections are still reaching large strain values. Reaching large strains may also be considered ductile. The difference is that those three specimens are continuing to take load right up to the failure point, which may be a useful behavior, depending upon the individual structure being considered. This type of behavior is not typically seen in reinforced concrete members. The designer must think about what ductility means and its purpose for the individual structure being considered. Thus, when designing a section using FRP confinement, it is important to correctly design the

number of plies so that the section will exhibit the behavior desired by the designer. The FE model can be used for this purpose.

7.2.2 Axial Load-Moment Performance Comparison

No convergence problems are experienced when moments are applied to steel confined sections. Thus, the residual surface as defined in Chapter 3 is used for all FE model predictions in this section (with the exception of the steel confined pure axial load cases, as discussed in Section 7.1). The axial load-moment interaction diagrams for the two cross-sections confined by either 30 plies of E-glass FRP or steel hoops at 3 inch (76 mm) spacing are shown in Figure 7.4. For reference, ACI Committee

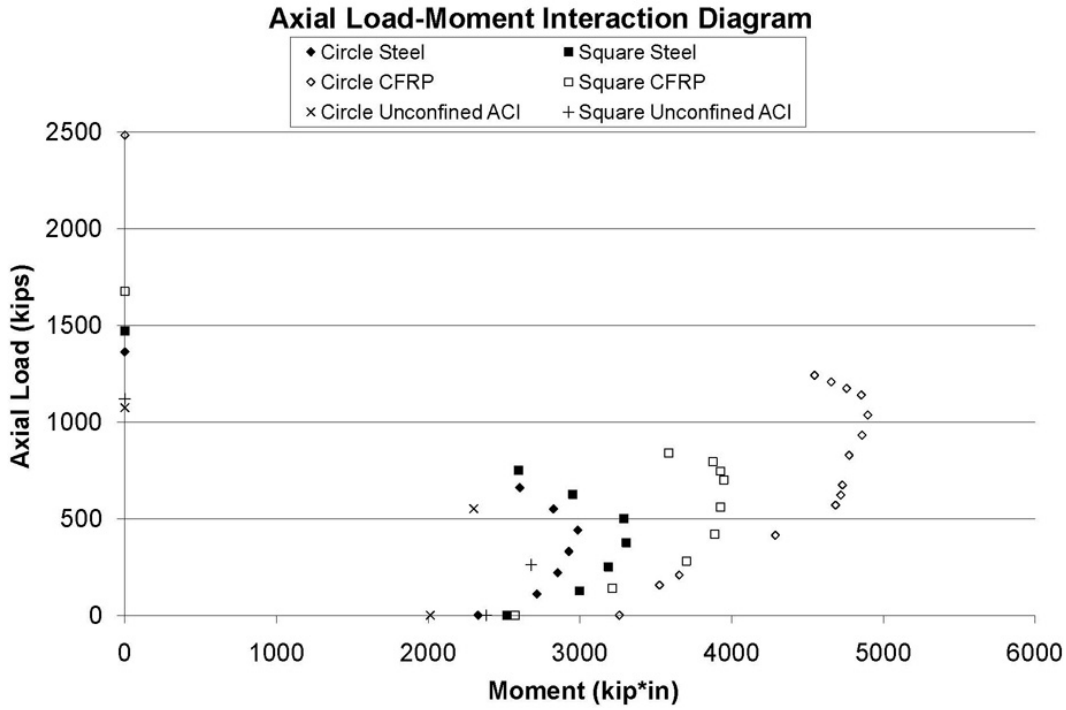

Figure 7.4: Axial load-moment interaction diagram for all four different sections.

318 (2000) equations were used with the assumption of unconfined concrete to make the predictions labeled as unconfined ACI. As with the axial loadings, the circular cross section confined by the E-glass FRP terminated with failure of the confining material. However, the square cross sections confined by E-glass FRP did not reach their peak moments at composite failure, but were instead limited by the strength

of the concrete. For the steel confined case, the square cross section withstands higher moments than the circular. This is likely due to the fact that the square cross section has a higher gross area than the circular section, and the fact that more of the area is distributed away from the neutral axis, thereby yielding a higher moment capacity. The pattern is reversed for the E-glass confined sections, with the circular cross section sustaining higher loads than the square. This is an unexpected result due to the fact that many consider confinement to be ineffective at increasing moment capacity, which may not be correct. A possible explanation is that the less effective confinement of the square section is not able to prevent degradation of the concrete, whereas in the circular section, the confinement is able to prevent the concrete from softening. Thus, confinement effectiveness comes into play with the FRP sections. This would not be the case for the steel confined sections because the concrete that is supporting the compression side of the moment couple is outside the steel hoops. For the FRP confined sections, all concrete is confined.

In order to more easily compare the increase in moment capacity with axial load, the axial load is normalized by the pure axial load capacity of the section, and the moment is normalized by the pure moment capacity of the section. This normalized axial load-moment interaction diagram is shown in Figure 7.5. For both types of confinement, the square section actually has a larger increase in moment capacity with the addition of axial load than the circular section. Since no unconfined sections were modeled, it is difficult to know if this is an effect of the shape or the effectiveness of the confinement. From Section 7.2.1, it is seen that in the case of pure axial loading, the circular sections showed a greater increase in axial load carrying capacity with confinement than the square sections. Therefore, it is likely that the square sections' outperformance of the circular sections' is due to the shape, not the effectiveness of the confinement. Clearly, the E-glass FRP shows a greater increase in moment capacity with the addition of load than the comparable steel confined section. As with pure axial loading, the E-glass FRP creates a stronger section than a comparable steel confined section. From Table 7.1, the stiffness of 30 plies of E-Glass FRP is equivalent to #3 bars at approximately 4 inch (100 mm) hoop spacing. Yet the 30 ply E-Glass

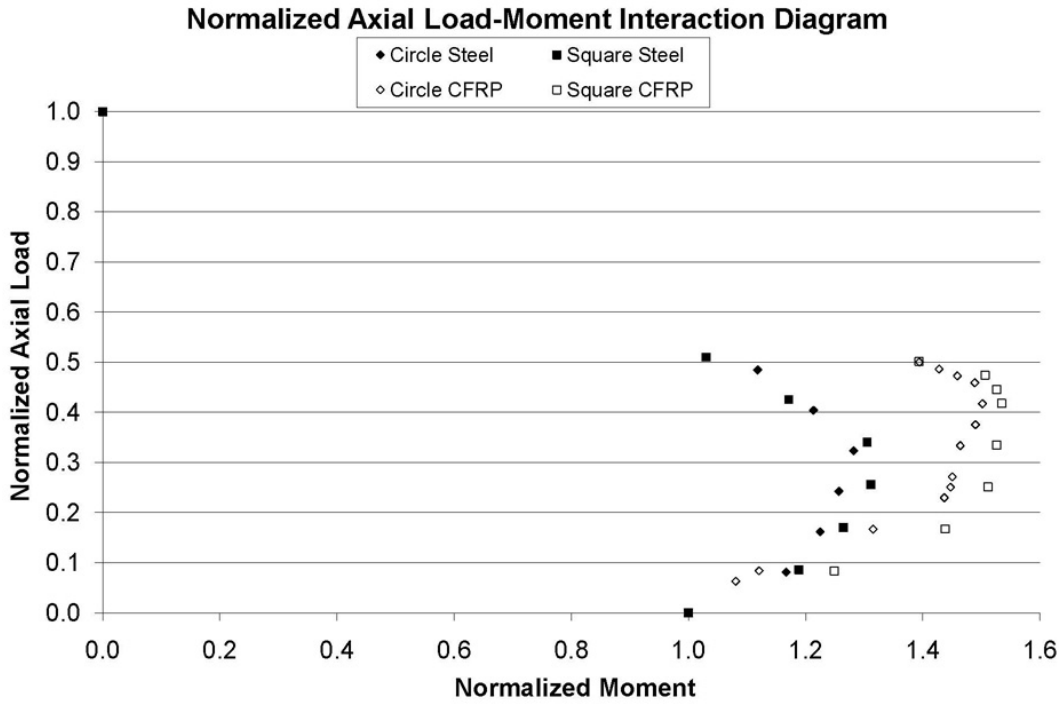

Figure 7.5: Normalized axial load-moment interaction diagram for all four different sections.

FRP confined section shows a greater increase in strength than the section confined by #3 bars at 3 inches (76 mm). However, this strength increase again comes at the cost of a loss of ductility, as will be seen in the following figures.

Figures 7.6 through 7.9 show the moment-curvature curves for all points computed for the axial load-moment interaction diagrams. Several moment-curvature curves show a small drop due to the occasional convergence problem. However, the solution always returns to the correct path. It is in these plots that the performance of the E-glass FRP confined circular section stands out. The curvature values for that section are significantly higher at failure than any other section modeled. However, as previously mentioned, failure is caused by rupture of the composite, which may not be considered a ductile failure mode. Thus, this section may not be desirable to designers seeking to create a ductile structure, depending upon that designer's definition of ductility. However, if fewer plies of the E-glass FRP were used, the section would return to a more ductile failure mode, albeit at a lower strength. This may be more useful for structural design purposes. The three other sections showed

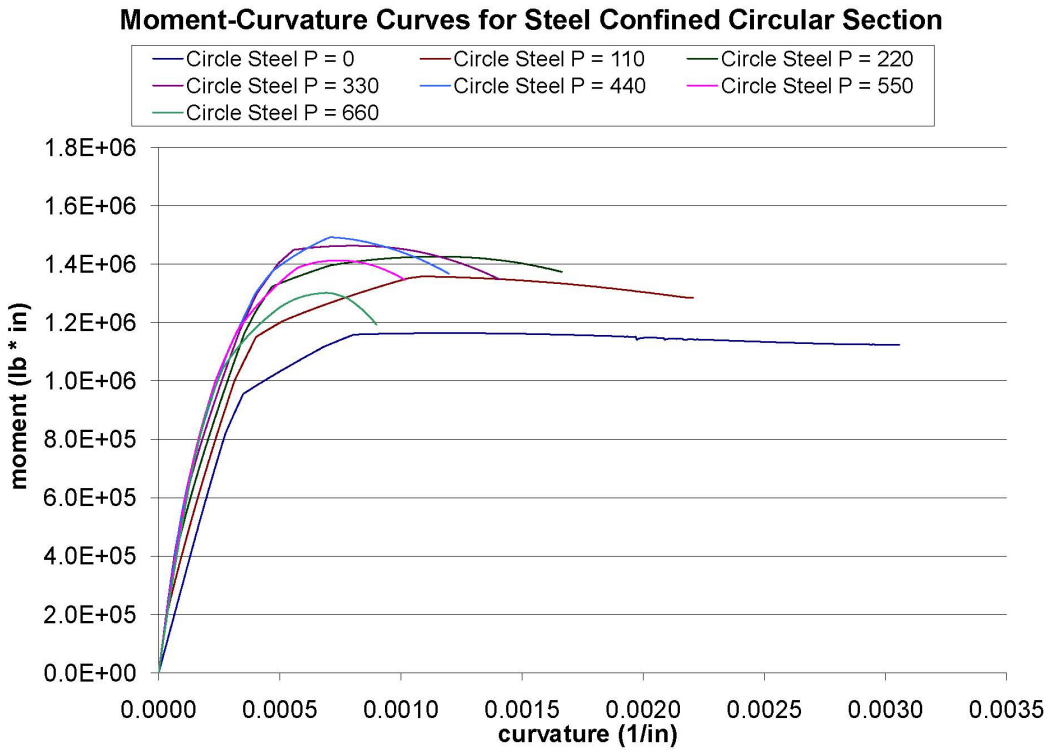

Figure 7.6: Moment versus curvature curves for the steel confined circular cross section.

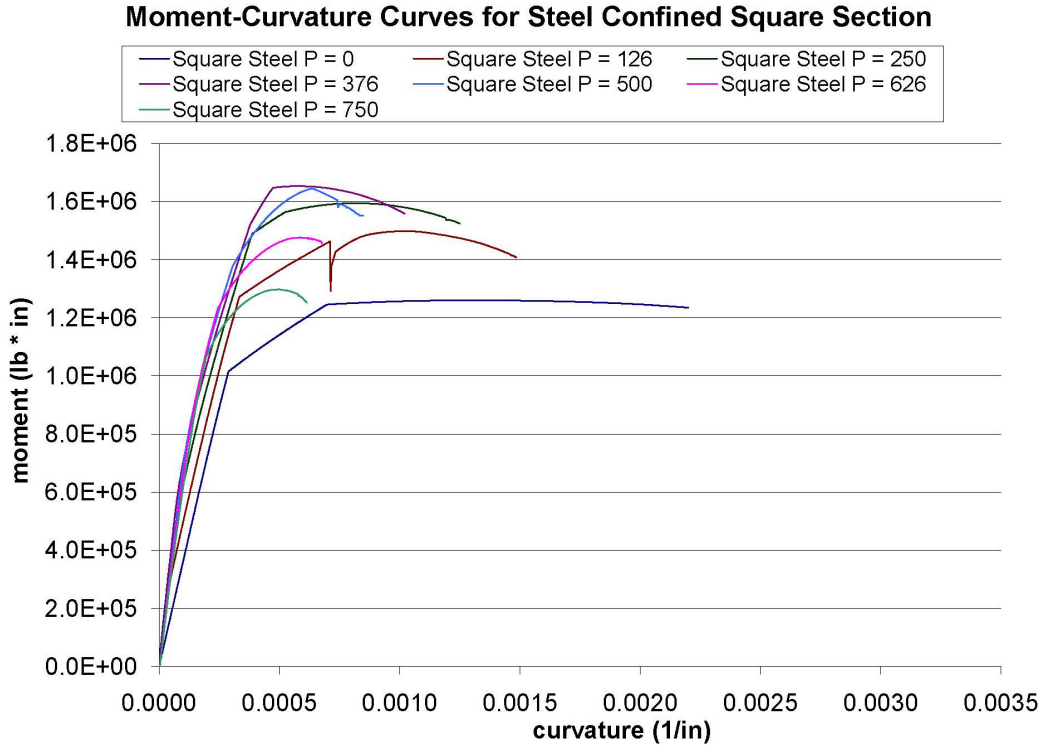

Figure 7.7: Moment versus curvature curves for the steel confined square cross section.

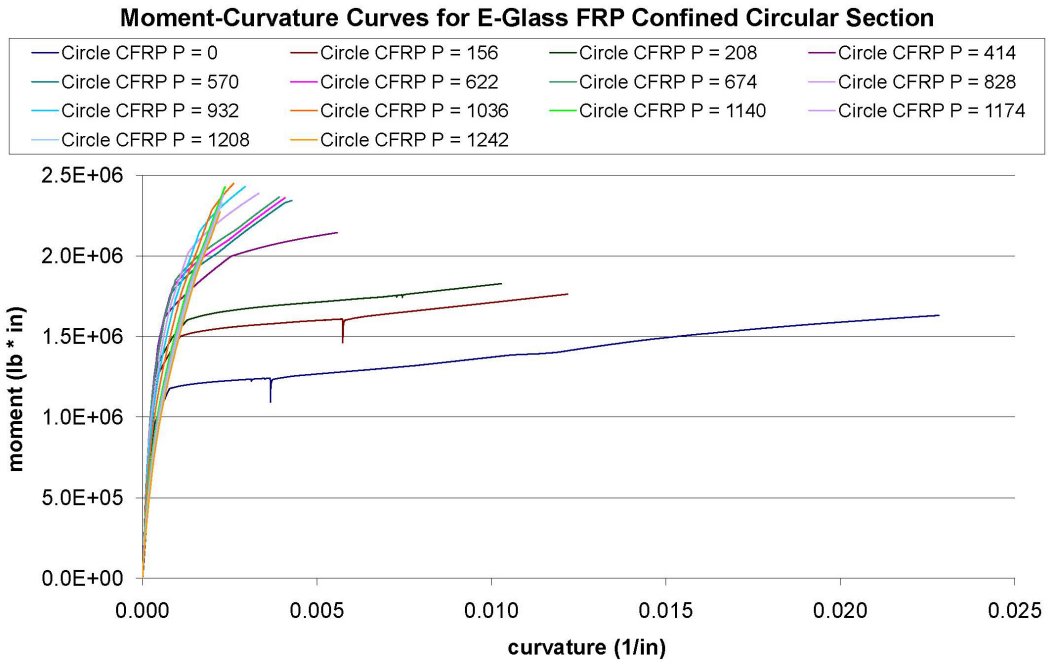

Figure 7.8: Moment versus curvature curves for the E-glass FRP confined circular cross section.

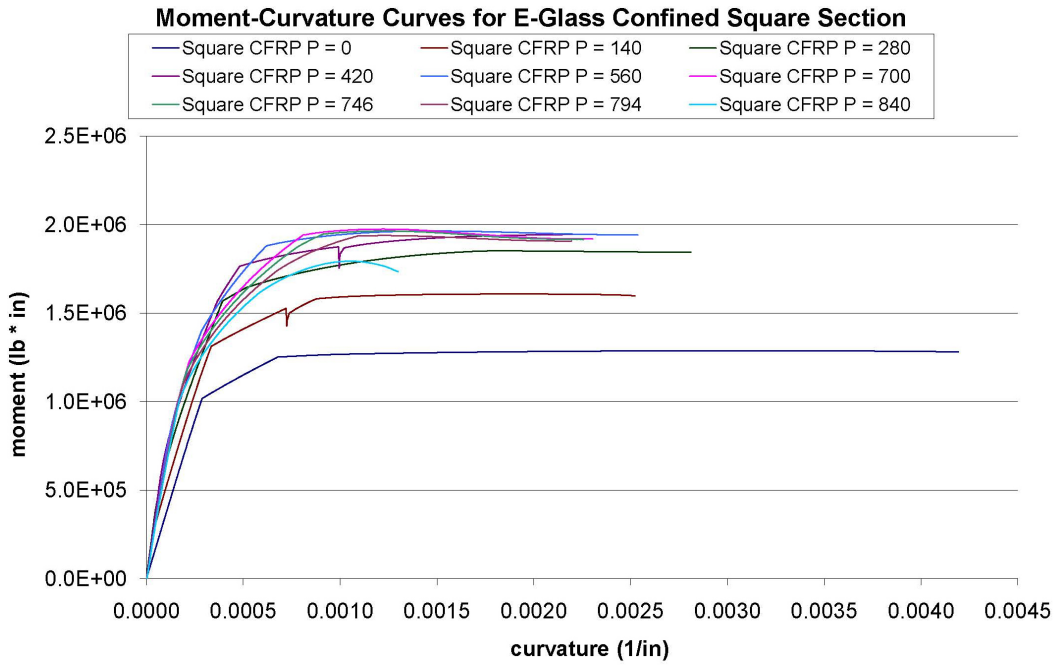

Figure 7.9: Moment versus curvature curves for the E-glass FRP confined square cross section.

somewhat less strength and significantly less curvature at failure. However, failure for the lower axial load levels was preceded by strain softening.

Clearly, when choosing the confining material and section geometry, many different factors come into play. These analyses are designed to highlight the tradeoff between strength and ductility that is seen for the FRP versus steel confinement, and for square versus circular cross sections. It is important for the designer to keep this trade off in mind when choosing the right confining material and geometry.

Chapter 8

Conclusions

Concrete is a material that exhibits complex behaviors, including a strong dependence on its multiaxial load state. It has long been recognized that it is necessary to confine concrete in order to have the required strength and ductility for structural use. However, due to its heterogeneous composition, even the most basic properties of concrete, such as its compressive strength, can vary widely from specimen to specimen. This combination of complex behavior and varying properties makes concrete a difficult material to accurately model. Despite these challenges, this thesis seeks to model the multiaxial behavior of concrete. The concrete model defined in this thesis defines the backbone monotonic loading curves for concrete. It can then be combined with existing finite element codes that account for other concrete behaviors, including cracking, shear sliding, and creep, to fully model this complex material.

Current plasticity theory provides an ideal framework to model concrete. Basic ideas of failure surfaces and plastic flow are adapted to represent the behaviors exhibited by concrete. A complex, work hardening failure surface is defined in the stress invariant space. This failure surface is composed of three fixed loading surfaces that correspond to the uniaxial yield, peak, and residual stresses. The current failure surface travels between these three fixed loading surfaces based on the accrual of damage in the material. The damage level is related to the amount of plastic strain accumulated in the specimen. The plastic strain is determined through the use of a non-associated flow rule. The full plasticity model is then coupled to finite element theory to create a computer program capable of predicting the behavior of concrete.

The full plasticity model contains twenty-four parameters, which must be defined using experimental concrete data and knowledge of fundamental concrete behavior. For this purpose, twenty-five experimental data sets were obtained from published works. These data sets included results from tests on a wide variety of concrete mixes and strengths, specimen shapes, confinement configurations, and load paths. Some of these variables are explicitly taken into account by the concrete model, while others deemed to be less significant are not accounted for. The concrete model parameters were then fit to the data. In the scope of this thesis, the data utilized for the fit are consistent with the loading of confined concrete columns. If a different use is required of the program, these parameters can be fit to data more closely representative of the problem being considered.

The finite element (FE) model is utilized to predict the experimental results of concrete. Five experimental data sets were obtained representing the variety of problems that this model is designed to solve. Four data sets are results of axial loading of confined columns. Two utilized steel rebar as a confinement material, and two used a fiber reinforced polymer (FRP) for confinement. The fifth data set tested a steel confined column under combined axial load and moment. When these data sets were initially modeled, a problem with the residual surface led to premature termination of the program for steel confined sections. It is desirable to determine the issue with this model that leads to the problem. However, a simple workaround was utilized by defining the tensile meridian to be equal to the compressive meridian, creating a round residual surface. The FE model predictions, using a round residual surface for steel confined sections only, are compared to the results obtained from the experiments. While the data contains large scatter, the program exhibited no consistent or systematic error in predicting the experimental results. Overall, the FE model was quite successful at accounting for a wide variety of testing variables, including shape, confining material, and confinement layout.

A concrete model of this type can be utilized as both a design and analysis tool. A study is performed to determine the effects of confining material and cross sectional shape. Concrete confined by FRP is shown to be capable of much greater increases

in strength. However, this increase in strength can be accompanied by a significant decrease in the ductility of the failure mode. This is a significant point for designers to consider when using this confining material. In general, circular shaped cross sections show a larger increase in strength and ductility than comparable square sections. This performance increase comes at the cost of higher stresses in the confining material. This exploration of these two design variables is useful information when designing structures.

In this thesis, a detailed concrete model is designed, its parameters are estimated using test data, the identified model is validated, and then it is used to explore certain aspects of concrete behavior. Comparisons to test data are shown to be favorable, making the predictive results of this model useful for understanding how concrete will perform under a particular loading configuration. The potential uses of such a program are quite extensive. It can be applied as a simple design tool for use in capacity calculations. New confining materials can be explored, and the resulting concrete behavior compared to existing confinement techniques. A deeper understanding of concrete behavior can be gained through careful examination of the stress distribution in the material in many different types of loading configurations. Implementing this model into existing code that would account for cyclic loading effects (including cracking, shear sliding, etc.) would allow a complete time history analysis of a concrete structure undergoing dynamic loading such as an earthquake. The concrete model presented in this thesis presents a powerful and flexible tool for the future analysis of concrete behavior under loads.

Bibliography

ABAQUS, Inc. (2006). *ABAQUS Analysis User's Manual*. 166 Valley Street, Providence, RI 02909.

ACI Committee 318 (2000). Building code requirements for structural concrete (318-99) and commentary (318R-99). Technical Report ACI 318-99, American Concrete Institute, PO Box 9094, Farmington Hills, Michigan, 48333-9094. Second Printing.

ADINA R&D, Inc. (2006). *ADINA Users Manual*. 71 Elton Avenue, Watertown, MA.

Ahmad, S. H. and Shah, S. P. (1982). Stress-strain curves of concrete confined by spiral reinforcement. *ACI Journal*, 79(6):484–490.

ANATECH Corp. (1998). *ANACAP-U/ANAMAT Theory Manual Version 2.5*. 5435 Oberlin Drive, San Diego, CA 92121. ANA-QA-145.

Ansari, F. and Li, Q. (1998). High-strength concrete subjected to triaxial compression. *ACI Materials Journal*, 95(6):747–755.

Attard, M. M. and Setunge, S. (1994). The stress-strain relationship of confined and unconfined normal and high strength concretes. UNICIV Report R-341, The University of New South Wales, School of Civil Engineering.

Attard, M. M. and Setunge, S. (1996). Stress-strain relationship of confined and unconfined concrete. *ACI Materials Journal*, 93(5):432–442.

Balmer, G. G. (1949). Shearing strength of concrete under high triaxial stress –

computation of Mohr's envelope as a curve. Structural Research Laboratory Report SP-23, Bureau of Reclamation, Research and Geology Division, Denver, Colorado.

Bellamy, C. J. (1961). Strength of concrete under combined stress. *Journal of the American Concrete Institute*, 58(4):367–380.

Blanks and McHenry (1945). Large triaxial testing machine built by bureau of reclamation. *Engineering News-Record*, 135:171–173.

Bresler, B. and Pister, K. S. (1958). Strength of concrete under combined stresses. *Journal of the American Concrete Institute*, 55(20):321–345.

Calixto, J. M. (2002). Behavior of high-performance concrete subjected to biaxial tension-compression stresses. In *Third International Conference on High Performance Concrete: Performance and Quality of Concrete Structures*, volume Special Publication 201, pages 1–14, Brazil. ACI.

Candappa, D. C., Sanjayan, J. G., and Setunge, S. (2001). Complete triaxial stress-strain curves of high-strength concrete. *Journal of Materials in Civil Engineering*, 13(3):209–215.

Candappa, D. P., Setunge, S., and Sanjayan, J. G. (1999). Stress versus strain relationship of high strength concrete under high lateral confinement. *Cement and Concrete Research*, 29(12):1977–1982.

Chaallal, O. and Shahawy, M. (2000). Performance of fiber-reinforced polymer-wrapped reinforced concrete column under combined axial-flexural loading. *ACI Structural Journal*, 97(4):659–668.

Chen, W.-F. (1982). *Plasticity in Reinforced Concrete*. McGraw-Hill Book Company.

Chinn, J. and Zimmerman, R. M. (1965). Behavior of plain concrete under various triaxial compression loading conditions. Technical Report WL TR 64-163, Air Force Weapons Laboratory, University of Colorado, Boulder.

Chuan-zhi, W., Zhen-hai, G., and Xiu-qin, Z. (1987). Experimental investigation of biaxial and triaxial compressive concrete strength. *ACI Materials Journal*, 84(2):92–100.

Cordon, W. A. and Gillespie, H. A. (1963). Variables in concrete aggregates and portland cement paste which influence the strength of concrete. *Journal of the American Concrete Institute*, 60(8):1029–1050.

Craig, J. R., Vaughan, D. J., and Skinner, B. J. (1996). *Resources of the Earth: Origin, Use and Environmental Impact*. Prentice Hall, Upper Saddle River, NJ, second edition.

Drucker, D. C. (1951). A more fundamental approach to plastic stress-strain relations. In *Proceedings of the First U. S. National Congress of Applied Mechanics*, pages 487–491, Chicago. ASME.

Drucker, D. C. (1960). Extension of the stability postulate with emphasis on temperature changes. In *Plasticity - Proceedings of the Second Symposium on Naval Structural Mechanics*, pages 170–184, New York. Pergamon Press.

Duke, C. M. and Davis, H. E. (1944). Some properties of concrete under sustained combined stresses. *Proceedings - American Society for Testing and Materials*, 44:888–896.

Gerstle, K. H., Aschl, H., Bellotti, R., Bertacchi, P., Kotsovos, M. D., Ko, H.-Y., Linse, D., Newman, J. B., Rossi, P., Schickert, G., Taylor, M. A., Traina, L. A., Winkler, H., and Zimmerman, R. M. (1980). Behavior of concrete under multiaxial stress states. *Journal of the Engineering Mechanics Division*, 106(EM6):1383–1403.

Harries, K. A. and Carey, S. A. (2003). Shape and "gap" effects on the behavior of variably confined concrete. *Cement and Concrete Research*, 33(6):881–890.

Harries, K. A. and Kharel, G. (2003). Experimental investigation of the behavior of variably confined concrete. *Cement and Concrete Research*, 33(6):873–880.

Hoek, E. and Franklin, J. A. (1968). Simple triaxial cell for field or laboratory testing of rock. *Transactions of the Institution of Mining and Metallurgy*, 77:A22–A26.

Hurlbut, B. J. (1985). Experimental and computational investigation of strain-softening in concrete. Master's thesis, University of Colorado.

Imran, I. and Pantazopoulou, S. J. (1996). Experimental study of plain concrete under triaxial stress. *ACI Materials Journal*, 93(6):589–601.

Jamet, P., Millard, A., and Nahas, G. (1984). Triaxial behaviour of a micro-concrete complete stress-strain curves for confining pressures ranging from 0 to 100 MPa. In *Proceedings of International Conference on Concrete under Multiaxial Conditions*, volume 1, pages 133–140, Toulouse, France. RILEM-CEB-CNRS, Presses de'l Université Paul Sabatier.

Khan, A. S. and Huang, S. (1995). *Continuum Theory of Plasticity*. Wiley.

Kupfer, H., Hilsdorf, H. K., and Rusch, H. (1969). Behavior of concrete under biaxial stresses. *ACI Journal*, 66(8):656–666.

Kupfer, H. B. and Gerstle, K. H. (1973). Behavior of concrete under biaxial stresses. *Journal of the Engineering Mechanics Division*, 99(EM4):853–866.

Lan, S. and Guo, Z. (1997). Experimental investigation of multiaxial compressive strength of concrete under different stress paths. *ACI Materials Journal*, 94(5):427–434.

Launay, P. and Gachon, H. (1972a). Strain and ultimate strength of concrete under triaxial stress. *Concrete for Nuclear Reactors*, pages 269–282. Proceedings of an international seminar held at the Bundesanstalt für Materialprüfung in Berlin, October 5-9, 1970, sponsored by the American Concrete Institute and the Bundesanstalt für Materialprüfung.

Launay, P. and Gachon, H. (1972b). Strain and ultimate strength of concrete under triaxial stress. In Jaeger, T. A., editor, *Proceedings of the First International*

Conference on Structural Mechanics in Reactor Technology, Berlin, Germany, 20-24 September 1971, volume 4H 1/3, pages 23–34, Brussels. Commission of the European Communities.

Li, Q. and Ansari, F. (1999). Mechanics of damage and constitutive relationships for high-strength concrete in triaxial compression. *Journal of Engineering Mechanics*, 125(1):1–10.

Li, Q. and Ansari, F. (2000). High-strength concrete in triaxial compression by different sizes of specimens. *ACI Materials Journal*, 97(6):684–689.

Lubliner, J. (1990). *Plasticity Theory*. Macmillan Publishing.

Malvar, L. J., Crawford, J. E., Wesevich, J. W., and Simons, D. (1994). A new concrete material model for DYNA3D. Technical Report TR-94-14.3, Karagozian & Case.

Malvar, L. J., Crawford, J. E., Wesevich, J. W., and Simons, D. (1996). A new concrete material model for DYNA3D release II: Shear dilation and directional rate enhancements. Technical Report TR-96-2.2, Karagozian & Case.

Mander, J. B., Priestley, M. J. N., and Park, R. (1988a). Observed stress-strain behavior of confined concrete. *Journal of Structural Engineering*, 114(8):1827–1849.

Mander, J. B., Priestley, M. J. N., and Park, R. (1988b). Theoretical stress-strain model for confined concrete. *Journal of Structural Engineering*, 114(8):1804–1826.

Mills, L. L. and Zimmerman, R. M. (1970). Compressive strength of plain concrete under multiaxial loading conditions. *ACI Journal*, 67(10):802–807.

MTS Systems Corporation (2004). *MTS Rock and Concrete Mechanics Testing Systems*. Eden Prairie, Minnesota.

Nilson, A. H. (1997). *Design of Concrete Structures*. WCB/McGraw-Hill.

Noble, C., Kokko, E., Darnell, I., Dunn, T., Hagler, L., and Leininger, L. (2005). Concrete model descriptions and summary of benchmark studies for blast effects simulations. Technical Report UCRL-TR-215024, U. S. Department of Energy Lawrence Livermore National Laboratory.

Pulido, C. M., Saiidi, D., Sanders, A. I., and El-Azazy, S. (2004). Seismic performance of two-column bents, part i retrofit with cfrp. *ACI Structural Journal*, 101(4):558–568.

Richart, F. E., Brandtzaeg, A., and Brown, R. L. (1928). A study of the failure of concrete under combined compressive stresses. Technical Report Bulletin No. 185, Engineering Experiment Station, University of Illinois, Urbana.

Richart, F. E., Brandtzaeg, A., and Brown, R. L. (1929). The failure of plain and spirally reinforced concrete in compression. Technical Report Bulletin No. 190, Engineering Experiment Station, University of Illinois, Urbana.

Rosenthal, I. and Glucklich, J. (1970). Strength of plain concrete under biaxial stress. *ACI Journal*, 67(11):903–914.

Schickert, G. and Winkler, H. (1977). Results of tests concerning strength and strain of concrete subjected to multiaxial compressive stresses. *Deutscher Ausschuss für Stahlbeton*, 277. Berlin, W. Germany.

Scott, B. D., Park, R., and Priestley, M. J. N. (1982). Stress-strain behavior of concrete confined by overlapping hoops at low and high strain rates. *ACI Journal*, 79(1):13–27.

Sfer, D., Carol, I., Gettu, R., and Etse, G. (2002). Study of the behavior of concrete under triaxial compression. *Journal of Engineering Mechanics*, 128(2):156–163.

Sheikh, S. A. and Uzumeri, S. M. (1982). Analytical model for concrete confinement in tied columns. *Journal of the Structural Division*, 108(12):2703–2722.

Smith, G. M. and Young, L. E. (1955). Ultimate theory in flexure by exponential function. *Journal of the American Concrete Institute*, 52(11):349–359.

Smith, S. S., William, K. J., Gerstle, K. H., and Sture, S. (1989). Concrete over the top, or: Is there life after peak? *ACI Materials Journal*, 86(5):491–497.

Toutanji, H. A. (1999). Stress-strain characteristics of concrete columns externally confined with advanced fiber composite sheets. *ACI Materials Journal*, 96(3):397–404.

van Mier, J. G. M. (1984). *Strain-Softening of Concrete Under Multiaxial Loading Conditions*. PhD thesis, Eindhoven University of Technology, The Netherlands.

William, K. J. and Warnke, E. P. (1975). Constitutive model for the triaxial behaviour of concrete. In *Proceedings of the International Association for Bridge and Structural Engineering: Seminar on Concrete Structures Subjected to Triaxial Stress*, volume 19, pages 174–186, Bergamo, Italy. ISMES.

Xie, J., Elwi, A. E., and MacGregor, J. G. (1995). Mechanical properties of three high-strength concretes containing silica fume. *ACI Materials Journal*, 92(2):135–145.

Appendix A

Partial Derivatives Required for Equation 3.14

This appendix consists of the partial derivatives necessary for calculating the tangent modulus tensor as laid out in Section 3.5 and Equation 3.14. The equations from which these derivatives are determined are all given in Chapter 3.

$$\frac{\partial Q}{\partial \sigma_{ij}} = \omega \frac{\partial F}{d\sigma_{ij}} + (1-\omega)\frac{\partial r}{\partial \sigma_{ij}} \tag{A.1}$$

$$\frac{\partial F}{\partial \sigma_{ij}} = \frac{\partial F}{\partial r}\frac{\partial r}{\partial \sigma_{ij}} + \frac{\partial F}{\partial \xi}\frac{\partial \xi}{\partial \sigma_{ij}} + \frac{\partial F}{\partial \theta}\frac{\partial \theta}{\partial \sigma_{ij}} \tag{A.2}$$

$$\frac{\partial F}{\partial \overline{\epsilon^p}} = \frac{\partial F}{\partial \beta}\frac{\partial \beta}{\partial \psi}\frac{\partial \psi}{\partial \overline{\epsilon^p}} \tag{A.3}$$

$$\frac{\partial F}{\partial r} = 1 \tag{A.4}$$

$$\frac{\partial F}{\partial \xi} = -\begin{cases} \beta\left(\frac{\partial R_{peak}(\xi,\theta)}{\partial \xi} - \frac{\partial R_{yield}(\xi,\theta)}{\partial \xi}\right) + \frac{\partial R_{yield}(\xi,\theta)}{\partial \xi} & \psi \leq \psi_{peak} \\ \beta\left(\frac{\partial R_{peak}(\xi,\theta)}{\partial \xi} - \frac{\partial R_{residual}(\xi,\theta)}{\partial \xi}\right) + \frac{\partial R_{residual}(\xi,\theta)}{\partial \xi} & \psi > \psi_{peak} \end{cases} \tag{A.5}$$

$$\frac{\partial F}{\partial \theta} = -\begin{cases} \beta\left(\frac{\partial R_{peak}(\xi,\theta)}{\partial \theta} - \frac{\partial R_{yield}(\xi,\theta)}{\partial \theta}\right) + \frac{\partial R_{yield}(\xi,\theta)}{\partial \theta} & \psi \leq \psi_{peak} \\ \beta\left(\frac{\partial R_{peak}(\xi,\theta)}{\partial \theta} - \frac{\partial R_{residual}(\xi,\theta)}{\partial \theta}\right) + \frac{\partial R_{residual}(\xi,\theta)}{\partial \theta} & \psi > \psi_{peak} \end{cases} \tag{A.6}$$

$$\frac{\partial F}{\partial \beta} = -\begin{cases} R_{peak}(\xi,\theta) - R_{yield}(\xi,\theta) & \psi \leq \psi_{peak} \\ R_{peak}(\xi,\theta) - R_{residual}(\xi,\theta) & \psi > \psi_{peak} \end{cases} \tag{A.7}$$

$$\frac{\partial \beta}{\partial \psi} = \frac{\kappa e^{1-\left(\frac{\psi}{\psi_{peak}}\right)^{\kappa}}\left[1-\left(\frac{\psi}{\psi_{peak}}\right)^{\kappa}\right]}{\psi_{peak}\left(\frac{\psi}{\psi_{peak}}\right)^{1-\kappa}} \tag{A.8}$$

$$\frac{\partial \psi}{\partial \overline{\epsilon^p}} = \frac{1}{\phi + \alpha(|\frac{\xi}{f_c'}|^{\gamma})} \tag{A.9}$$

$$
\begin{aligned}
\frac{\partial R_i(\xi,\theta)}{\partial \xi} = & \frac{1}{4(r_{c,i}^2 - r_{t,i}^2)cos^2(\theta) + (r_{c,i} - 2r_{t,i})^2} \Bigg\{ 2\frac{dr_{c,i}}{d\xi}(r_{c,i}^2 - r_{t,i}^2)cos(\theta) \\
& + 2r_{c,i}(2r_{c,i}\frac{dr_{c,i}}{d\xi} - 2r_{t,i}\frac{dr_{t,i}}{d\xi})cos(\theta) \\
& + \frac{dr_{c,i}}{d\xi}(2r_{t,i} - r_{c,i})\sqrt{4(r_{c,i}^2 - r_{t,i}^2)cos^2(\theta) + 5r_{t,i}^2 - 4r_{t,i}r_{c,i}} \\
& + r_{c,i}(2\frac{dr_{t,i}}{d\xi} - \frac{dr_{c,i}}{d\xi})\sqrt{4(r_{c,i}^2 - r_{t,i}^2)cos^2(\theta) + 5r_{t,i}^2 - 4r_{t,i}r_{c,i}} \\
& + \frac{1}{2\sqrt{4(r_{c,i}^2 - r_{t,i}^2)cos^2(\theta) + 5r_{t,i}^2 - 4r_{t,i}r_{c,i}}} \\
& \Big[r_{c,i}(2r_{t,i} - r_{c,i})(4(2r_{c,i}\frac{dr_{c,i}}{d\xi} - 2r_{t,i}\frac{dr_{t,i}}{d\xi})cos^2(\theta) \\
& + 10r_{t,i}\frac{dr_{t,i}}{d\xi} - 4\frac{dr_{t,i}}{d\xi}r_{c,i} - 4r_{t,i}\frac{dr_{c,i}}{d\xi}) \Big] \Bigg\} \\
& - \frac{1}{\Big[4(r_{c,i}^2 - r_{t,i}^2)cos^2(\theta) + (r_{c,i} - 2r_{t,i})^2\Big]^2} \Bigg\{ \Big[2r_{c,i}(r_{c,i}^2 - r_{t,i}^2)cos(\theta) \\
& + r_{c,i}(2r_{t,i} - r_{c,i})\sqrt{4(r_{c,i}^2 - r_{t,i}^2)cos^2(\theta) + 5r_{t,i}^2 - 4r_{t,i}r_{c,i}} \Big] \\
& \Big[4(2r_{c,i}\frac{dr_{c,i}}{d\xi} - 2r_{t,i}\frac{dr_{t,i}}{d\xi})cos^2(\theta) + 2(r_{c,i} - 2r_{t,i})(\frac{dr_{c,i}}{d\xi} - 2\frac{dr_{t,i}}{d\xi}) \Big] \Bigg\}
\end{aligned}
\tag{A.10}
$$

$i =$ yield, peak, residual

$$\frac{\partial R_i(\xi,\theta)}{\partial\theta} = \frac{1}{4(r_{c,i}^2 - r_{t,i}^2)cos^2(\theta) + (r_{c,i} - 2r_{t,i})^2}\Bigg\{-2r_{c,i}(r_{c,i}^2 - r_{t,i}^2)sin(\theta) - \frac{1}{\sqrt{4(r_{c,i}^2 - r_{t,i}^2)cos^2(\theta) + 5r_{t,i}^2 - 4r_{t,i}r_{c,i}}} \Big[4r_{t,i}(2r_{t,i} - r_{c,i})(r_{c,i}^2 - r_{t,i}^2)sin(\theta)cos(\theta)\Big]\Bigg\} + \frac{1}{\Big[4(r_{c,i}^2 - r_{t,i}^2)cos^2(\theta) + (r_{c,i} - 2r_{t,i})^2\Big]^2} \Bigg\{8\Big[2r_{c,i}(r_{c,i}^2 - r_{t,i}^2)cos(\theta) + r_{c,i}(2r_{t,i} - r_{c,i}) \sqrt{4(r_{c,i}^2 - r_{t,i}^2)cos^2(\theta) + 5r_{t,i}^2 - 4r_{t,i}r_{c,i}}\Big](r_{c,i}^2 - r_{t,i}^2)sin(\theta)cos(\theta)\Bigg\} \tag{A.11}$$

$i =$ yield, peak, residual

$$\frac{dr_{t,i}}{d\xi} = \frac{\frac{1}{2}a_{1,i} + a_{2,i}\frac{\xi}{f_c'}}{\sqrt{a_{0,i} + a_{1,i}\frac{\xi}{f_c'} + a_{2,i}\Big(\frac{\xi}{f_c'}\Big)^2 + \frac{1}{4}a_{3,i}^2}} \qquad i = \text{peak, residual} \tag{A.12}$$

$$\frac{dr_{c,i}}{d\xi} = \frac{\frac{1}{2}b_{1,i} + b_{2,i}\frac{\xi}{f_c'}}{\sqrt{b_{0,i} + b_{1,i}\frac{\xi}{f_c'} + b_{2,i}\Big(\frac{\xi}{f_c'}\Big)^2 + \frac{1}{4}b_{3,i}^2}} \qquad i = \text{peak, residual} \tag{A.13}$$

$$\frac{dr_{t,yield}}{d\xi} = -\frac{c}{\Big(1 - \frac{\xi}{f_c'}\Big)^2} \tag{A.14}$$

$$\frac{dr_{c,yield}}{d\xi} = -\frac{d}{\Big(1 - \frac{\xi}{f_c'}\Big)^2} \tag{A.15}$$

$$\frac{\partial r}{\partial\sigma_{ij}} = \frac{1}{\sqrt{2J_2}}\frac{\partial J_2}{\partial\sigma_{ij}} \tag{A.16}$$

$$\frac{\partial \xi}{\partial \sigma_x} = \frac{\partial \xi}{\partial \sigma_y} = \frac{\partial \xi}{\partial \sigma_z} = \frac{1}{\sqrt{3}} \tag{A.17}$$

$$\frac{\partial \xi}{\partial \tau_{xy}} = \frac{\partial \xi}{\partial \tau_{yz}} = \frac{\partial \xi}{\partial \tau_{xz}} = 0 \tag{A.18}$$

$$\frac{\partial \theta}{\partial \sigma_{ij}} = \frac{\partial \theta}{\partial J_2}\frac{\partial J_2}{\partial \sigma_{ij}} + \frac{\partial \theta}{\partial J_3}\frac{\partial J_3}{\partial \sigma_{ij}} \tag{A.19}$$

$$\frac{\partial \theta}{\partial J_2} = \frac{3\sqrt{3}}{4}\frac{J_3}{J_2^{\frac{5}{2}} sin\,(3\theta)} \tag{A.20}$$

$$\frac{\partial \theta}{\partial J_3} = -\frac{\sqrt{3}}{2}\frac{1}{J_2^{\frac{3}{2}} sin\,(3\theta)} \tag{A.21}$$

$$\frac{\partial J_2}{\partial \sigma_x} = \frac{1}{3}\left(2\sigma_{xx} - \sigma_{yy} - \sigma_{zz}\right) \tag{A.22}$$

$$\frac{\partial J_2}{\partial \sigma_y} = \frac{1}{3}\left(-\sigma_{xx} + 2\sigma_{yy} - \sigma_{zz}\right) \tag{A.23}$$

$$\frac{\partial J_2}{\partial \sigma_z} = \frac{1}{3}\left(-\sigma_{xx} - \sigma_{yy} + 2\sigma_{zz}\right) \tag{A.24}$$

$$\frac{\partial J_2}{\partial \tau_{xy}} = 2\tau_{xy} \tag{A.25}$$

$$\frac{\partial J_2}{\partial \tau_{yz}} = 2\tau_{yz} \tag{A.26}$$

$$\frac{\partial J_2}{\partial \tau_{xz}} = 2\tau_{xz} \tag{A.27}$$

$$\frac{\partial J_3}{\partial \sigma_x} = \frac{1}{9}\left[4\sigma_y\sigma_z - 2\sigma_x\left(-\sigma_x + \sigma_y + \sigma_z\right) - \left(\sigma_y^2 + \sigma_z^2\right)\right] - \frac{1}{3}\left[2\tau_{yz}^2 - \left(\tau_{xy}^2 + \tau_{xz}^2\right)\right] \tag{A.28}$$

$$\frac{\partial J_3}{\partial \sigma_y} = \frac{1}{9}\left[4\sigma_x\sigma_z - 2\sigma_y\left(\sigma_x - \sigma_y + \sigma_z\right) - \left(\sigma_x^2 + \sigma_z^2\right)\right] - \frac{1}{3}\left[2\tau_{xz}^2 - \left(\tau_{xy}^2 + \tau_{yz}^2\right)\right] \quad \text{(A.29)}$$

$$\frac{\partial J_3}{\partial \sigma_z} = \frac{1}{9}\left[4\sigma_x\sigma_y - 2\sigma_z\left(\sigma_x + \sigma_y - \sigma_z\right) - \left(\sigma_x^2 + \sigma_y^2\right)\right] - \frac{1}{3}\left[2\tau_{xy}^2 - \left(\tau_{xz}^2 + \tau_{yz}^2\right)\right] \quad \text{(A.30)}$$

$$\frac{\partial J_3}{\partial \tau_{xy}} = 2\tau_{xz}\tau_{yz} + \frac{2}{3}\tau_{xy}\left(\sigma_x + \sigma_y - 2\sigma_z\right) \quad \text{(A.31)}$$

$$\frac{\partial J_3}{\partial \tau_{yz}} = 2\tau_{xy}\tau_{xz} + \frac{2}{3}\tau_{yz}\left(-2\sigma_x + \sigma_y + \sigma_z\right) \quad \text{(A.32)}$$

$$\frac{\partial J_3}{\partial \tau_{xz}} = 2\tau_{xy}\tau_{yz} + \frac{2}{3}\tau_{xz}\left(\sigma_x - 2\sigma_y + \sigma_z\right) \quad \text{(A.33)}$$

Note that as $\theta \to 60^\circ$, $\frac{\partial R_i(\xi,\theta)}{\partial \theta} \to 0$ while $\frac{\partial \theta}{\partial J_2} \to \infty$ and $\frac{\partial \theta}{\partial J_3} \to \infty$. Therefore, the product $\frac{\partial R_i(\xi,\theta)}{\partial \theta}\frac{\partial \theta}{\partial J_{2,3}}$ should go to zero. However, due to numerical roundoff, this isn't guaranteed. Therefore, for $\theta \simeq 60^\circ$, a linearization is used for this product.

For $\theta \simeq 60^\circ$:

$$\frac{\partial R_i(\xi,\theta)}{\partial \theta}\frac{\partial \theta}{\partial J_2} = \frac{3\sqrt{3}r_c\left(r_c^2 - r_t^2\right)}{4\left(2r_t - r_c\right)^2}\frac{J_3}{J_2^{\frac{5}{2}}} \quad \text{(A.34)}$$

$$\frac{\partial R_i(\xi,\theta)}{\partial \theta}\frac{\partial \theta}{\partial J_3} = -\frac{\sqrt{3}r_c\left(r_c^2 - r_t^2\right)}{2\left(2r_t - r_c\right)^2 J_2^{\frac{3}{2}}} \quad \text{(A.35)}$$

Appendix B

Summary of Papers Used for Determining Peak Surface Parameters

Table B.1: Summary of papers used for determining peak surface parameters.

Paper	Triaxial Loading Type	Lateral Loading Magnitude (as % of f'_c)	Concrete Strength (ksi)	Specimen Shape	Specimen Size (inches)	Water-Cement Ratio	Notes
Ahmad and Shah (1982)	Passive Confinement (Steel rebar/wire)	0.1% - 1%	3.8 - 9.5	Cylinder	3 x 6	0.45 - 0.60	included mixes: two lightweight, one normal weight
Ansari and Li (1998), Li and Ansari (1999), Li and Ansari (2000)	Triaxial pressure vessel	18% - 93%	6.9 - 15.6	Cylinder	3 x 6, 4 x 8	0.26 - 0.46	included mixes: two high strength, one normal strength
Attard and Setunge (1996), Attard and Setunge (1994)	Triaxial pressure vessel	0.4% - 25%	8.4 - 19.1	Cylinder	4 x 8	0.26 - 0.45	included mixes: four high strength, one normal strength; three different coarse aggregates
Balmer (1949)	Triaxial pressure vessel	25% - 700%	3.6 - 4.0	Cylinder	6 x 12	0.58	one mix tested at 35 and 97 days
Bellamy (1961)	Triaxial pressure vessel	28% - 129%	3.8 - 4.9	Cylinders (solid and hollow)	6 x 12	0.55	hollow cylinders failed at inner surface, thus a biaxial failure state

Continued on next page

Table B.1: Summary of papers used for determining peak surface parameters.

Paper	Triaxial Loading Type	Lateral Loading Magnitude (as % of f'_c)	Concrete Strength (ksi)	Specimen Shape	Specimen Size (inches)	Water-Cement Ratio	Notes
Calixto (2002)	Biaxial	5% - 30%	10.8	Plate	5 x 5 x 0.5	0.28	
Candappa et al. (2001), Candappa et al. (1999)	Triaxial pressure vessel	4% - 30%	6.1 - 15.0	Cylinder	4 x 8	0.30 - 0.63	included mixes: three high strength, one normal strength
Chinn and Zimmerman (1965)	Triaxial pressure vessel	49% - 1714%	3.4 - 10.3	Cylinder	6 x 12	0.30 - 0.53	included mixes: two high strength, one normal strength
Chuan-zhi et al. (1987)	True triaxial	6% - 343%	1.1 - 2.1	Cube	4 x 4 x 4	0.72	two different coarse aggregates
Cordon and Gillespie (1963)	Triaxial pressure vessel	5% - 113%	1.8 - 7.4	Cylinder	6 x 12	0.40 - 0.70	two different maximum aggregate sizes for each water-cement ratio
Duke and Davis (1944)	Triaxial pressure vessel	2% - 26%	5.7 - 6.6	Cylinder	8 x 16	0.48	comparison of saturated to partially dry specimens

Continued on next page

Table B.1: Summary of papers used for determining peak surface parameters.

Paper	Triaxial Loading Type	Lateral Loading Magnitude (as % of f'_c)	Concrete Strength (ksi)	Specimen Shape	Specimen Size (inches)	Water-Cement Ratio	Notes
Imran and Pantazopoulou (1996)	Triaxial pressure vessel	4% - 91%	4.2 - 10.6	Cylinder	2.125 x 4.25	0.40 - 0.75	comparison of saturated to oven dried specimens, and of various load paths
Kupfer et al. (1969), Kupfer and Gerstle (1973)	Biaxial	26% - 118%	2.8 - 8.6	Plate	7.9 x 7.9 x 2.0	0.43 - 1.20	
Lan and Guo (1997)	True triaxial	8% - 350%	2.2 - 3.8	Cube	2.78 x 2.78 x 2.78	0.71	comparison of different triaxial load paths
Launay and Gachon (1972a), Launay and Gachon (1972b)	True triaxial	20% - 564%	5.2	Cube	2.76 x 2.76 x 2.76	0.53	
Mills and Zimmerman (1970)	True triaxial	2% - 314%	3.3 - 5.2	Cube	2.25 x 2.25 x 2.25	0.49 - 0.66	
Richart et al. (1928)	Triaxial pressure vessel	7% - 571%	1.1 - 3.7	Cylinder	4 x 8, 4 x 22	0.64 - 1.25	

Continued on next page

Table B.1: Summary of papers used for determining peak surface parameters.

Paper	Triaxial Loading Type	Lateral Loading Magnitude (as % of f'_c)	Concrete Strength (ksi)	Specimen Shape	Specimen Size (inches)	Water-Cement Ratio	Notes
Richart et al. (1929)	Passive (Steel rebar/wire)	6% - 71%	2.1	Cylinder	10 x 40	0.87	
Rosenthal and Glucklich (1970)	Triaxial pressure vessel	31% - 222%	2.8 - 6.9	Cylinder (hollow)	12 x 14	0.63 - 0.94	hollow cylinders failed at inner surface, thus a biaxial failure state
Sfer et al. (2002)	Triaxial pressure vessel	4% - 183%	4.8 - 5.6	Cylinder	6 x 12	0.57	
Toutanji (1999)	Passive (Fiber composite sheets)	24% - 57%	4.5	Cylinder	3 x 12	0.5	

Appendix C

Figures Showing Individual Data Sets for Papers Used to Determine Peak Surface

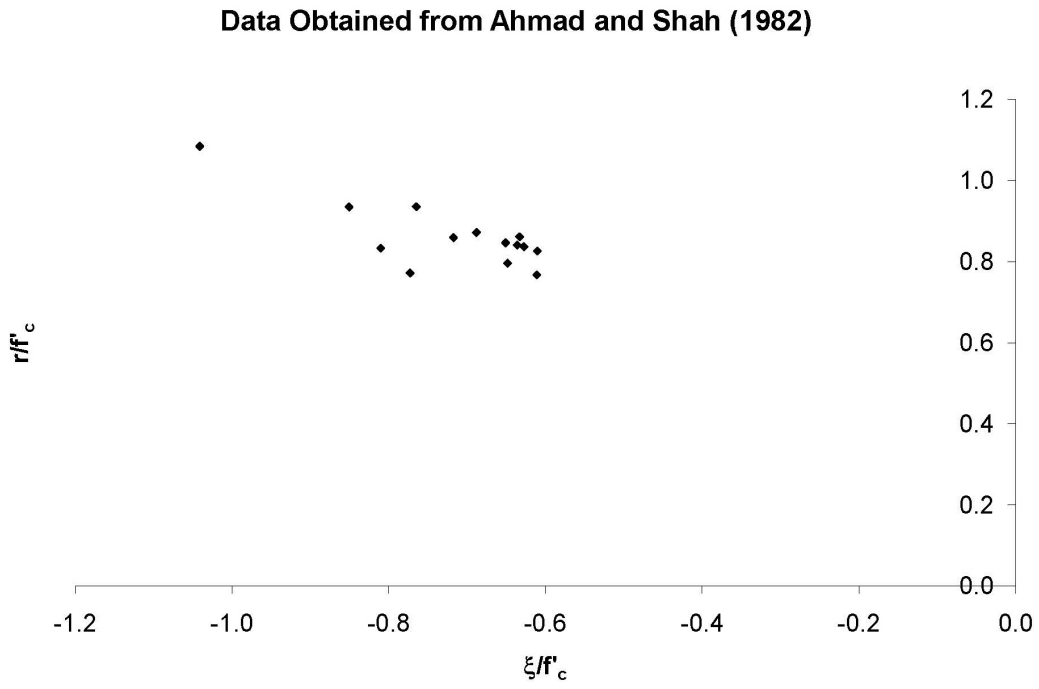

Figure C.1: Test data from Ahmad and Shah (1982).

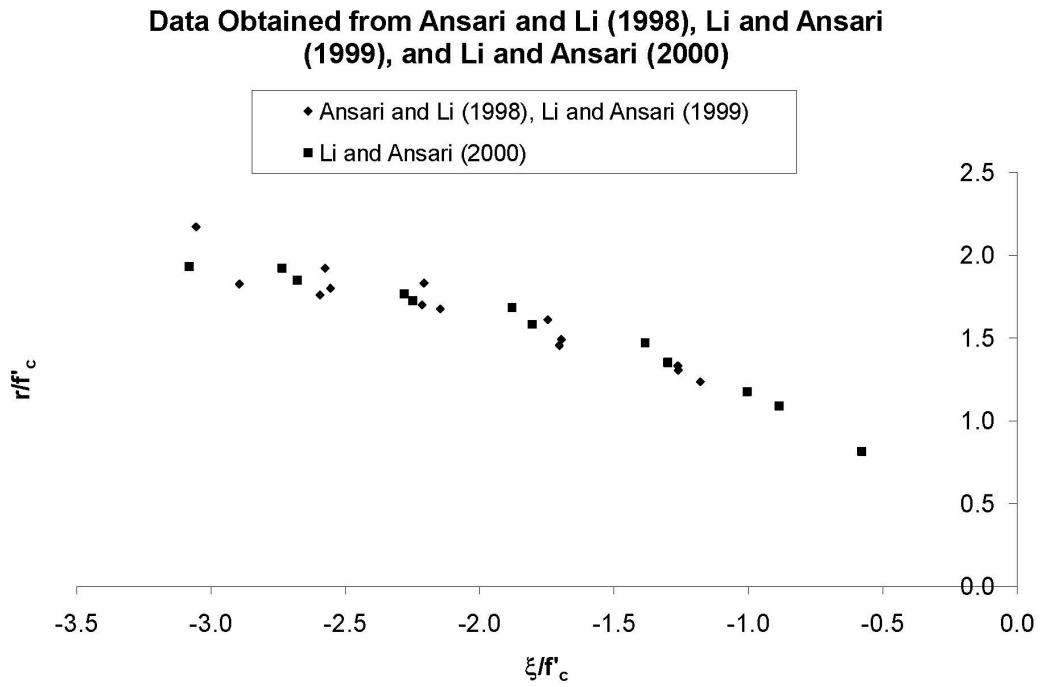

Figure C.2: Test data from Ansari and Li (1998), Li and Ansari (1999), and Li and Ansari (2000).

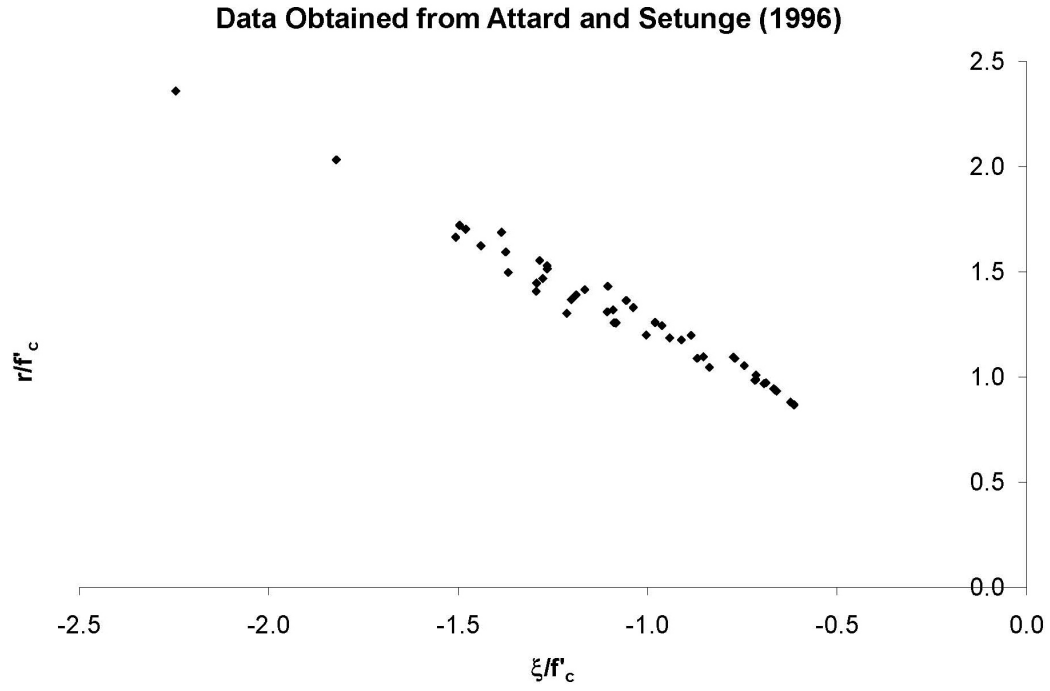

Figure C.3: Test data from Attard and Setunge (1996).

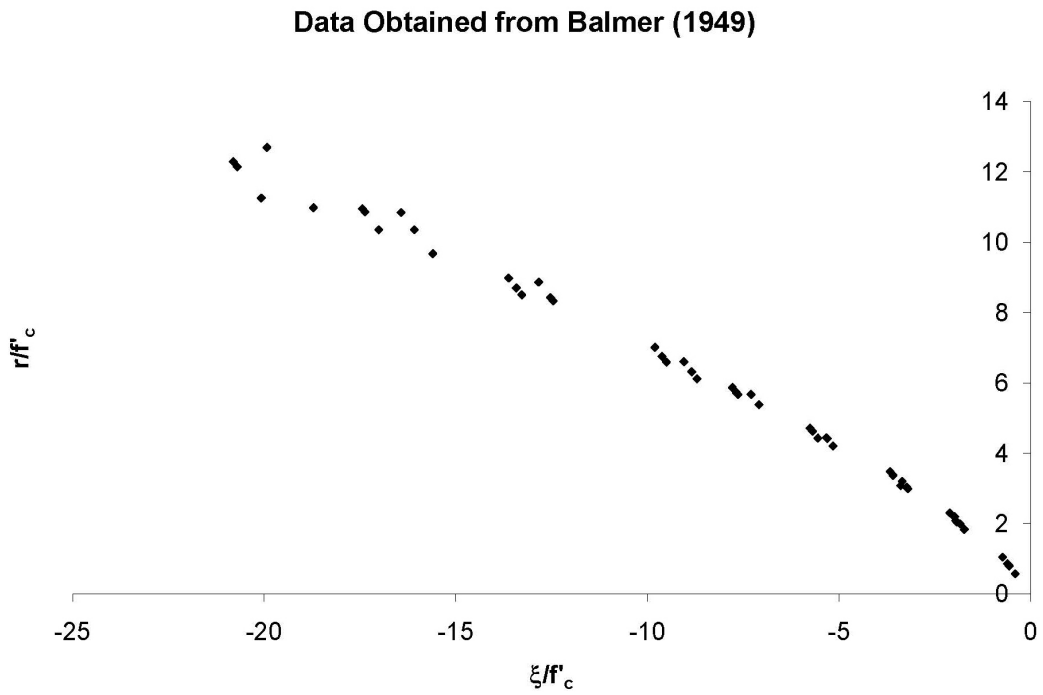

Figure C.4: Test data from Balmer (1949).

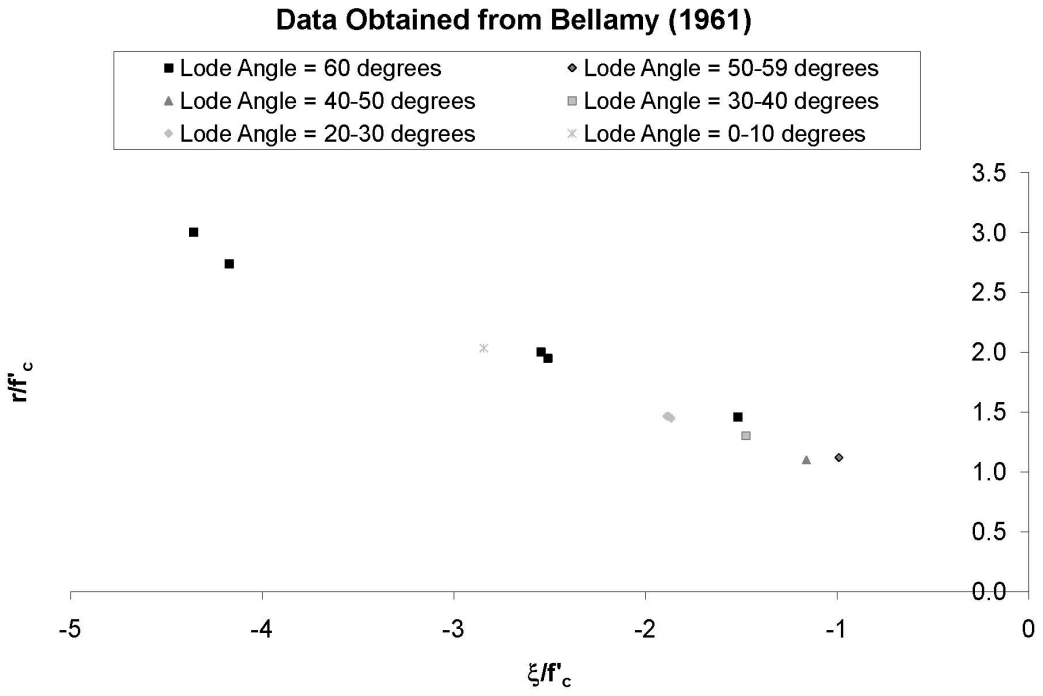

Figure C.5: Test data from Bellamy (1961).

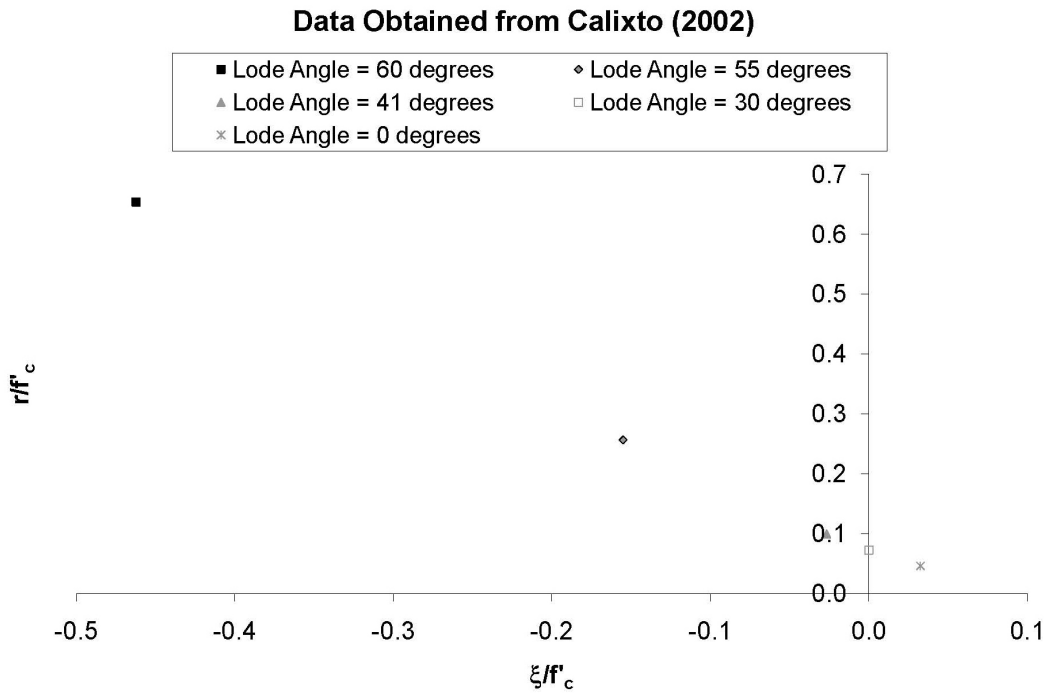

Figure C.6: Test data from Calixto (2002).

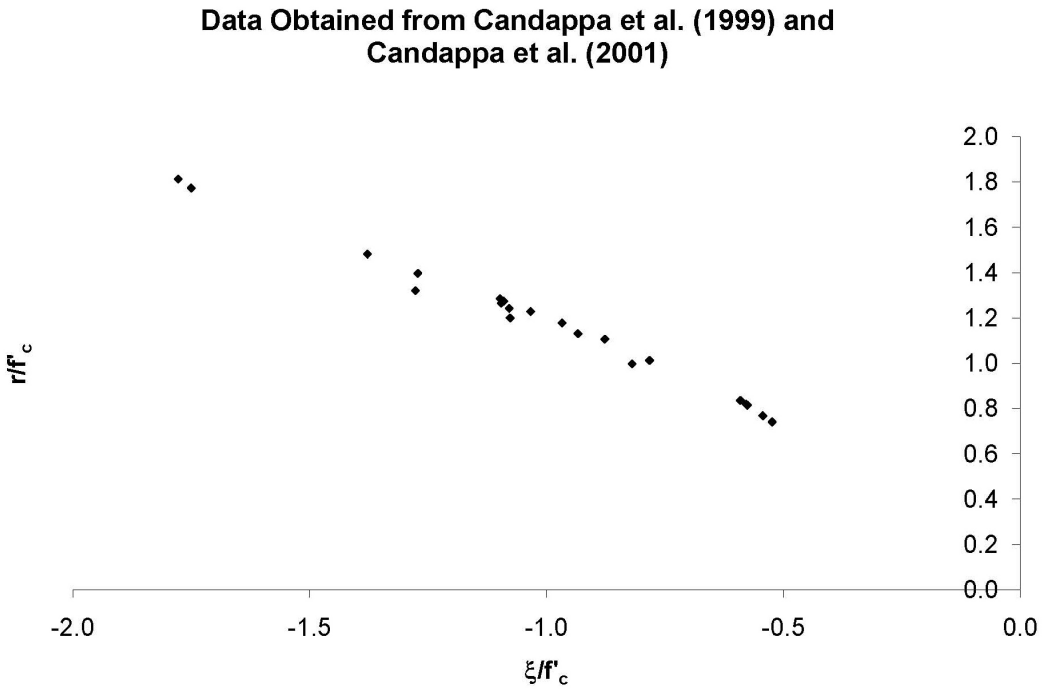

Figure C.7: Test data from Candappa et al. (1999) and Candappa et al. (2001).

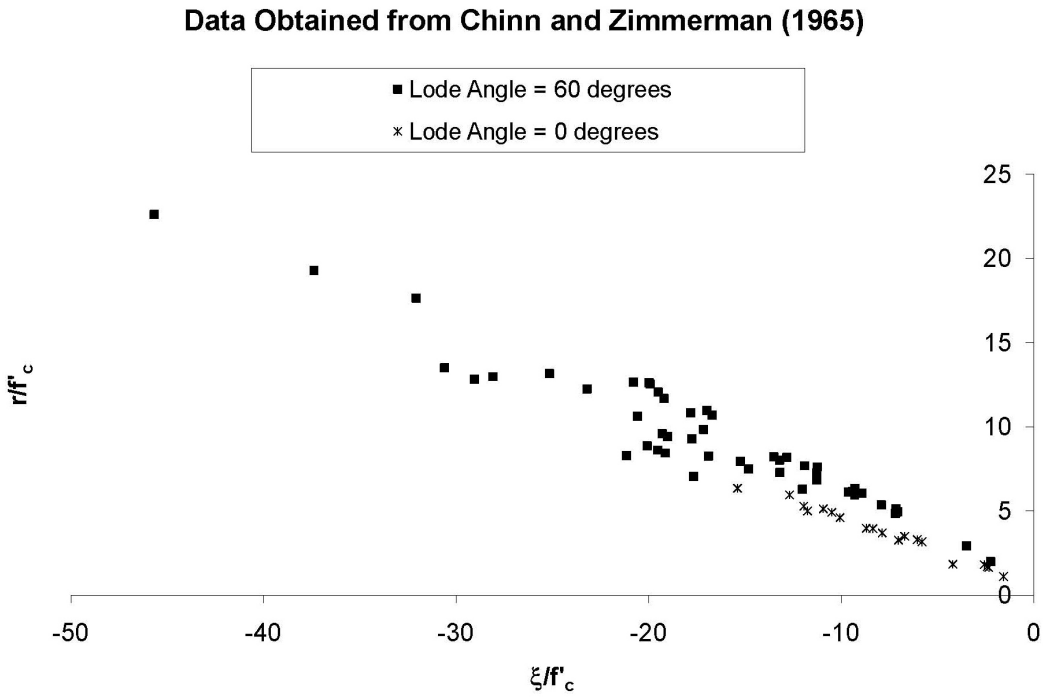

Figure C.8: Test data from Chinn and Zimmerman (1965).

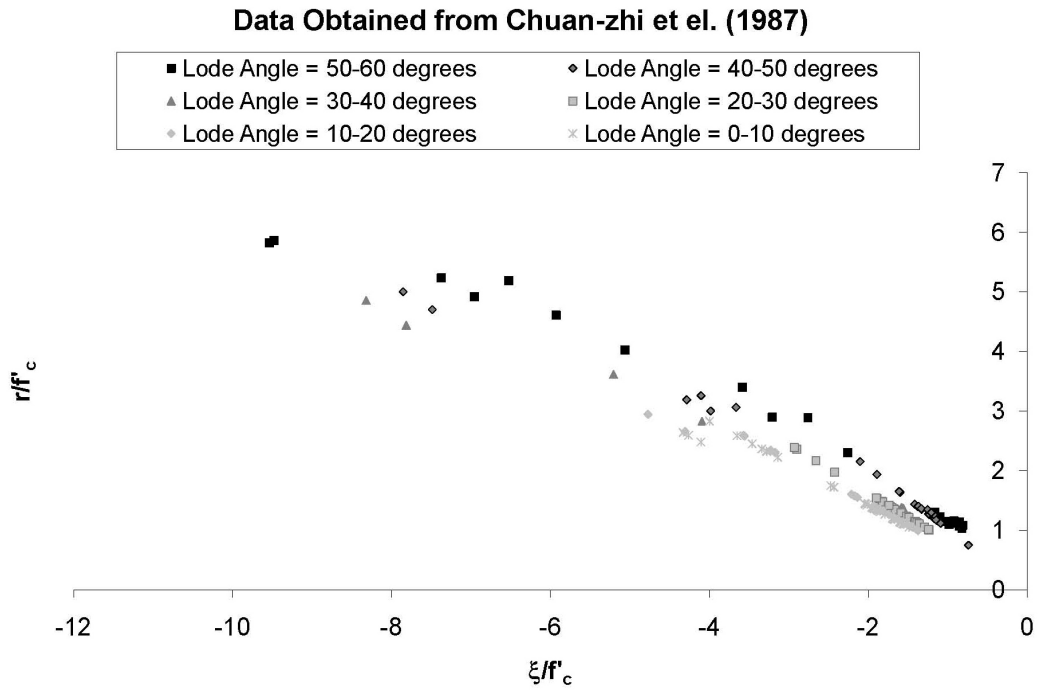

Figure C.9: Test data from Chuan-zhi et al. (1987).

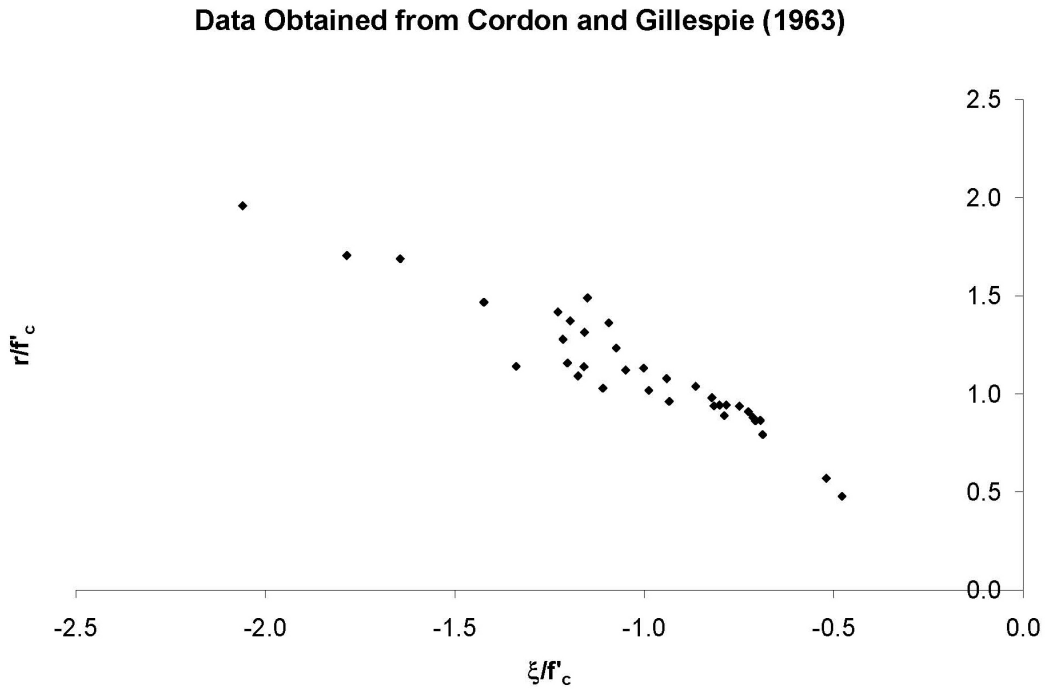

Figure C.10: Test data from Cordon and Gillespie (1963).

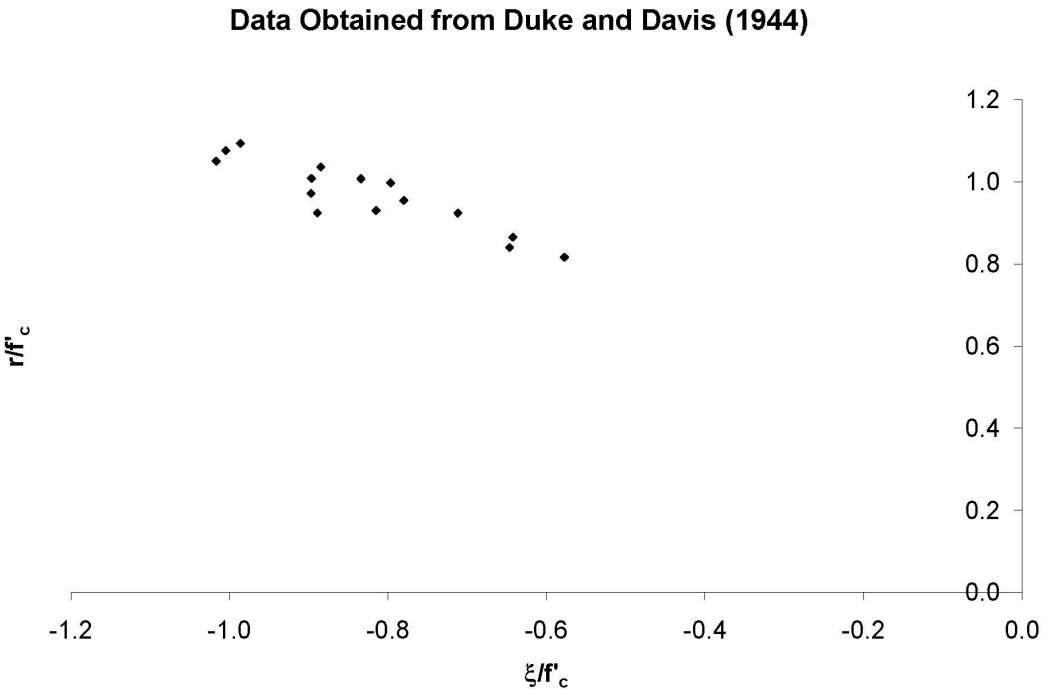

Figure C.11: Test data from Duke and Davis (1944).

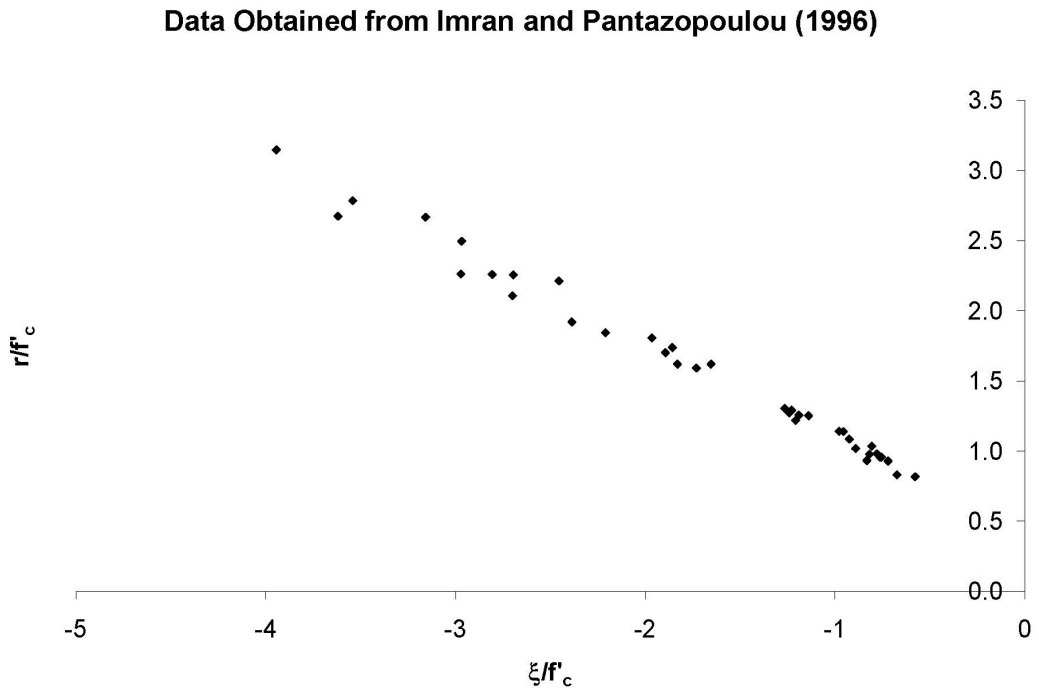

Figure C.12: Test data from Imran and Pantazopoulou (1996).

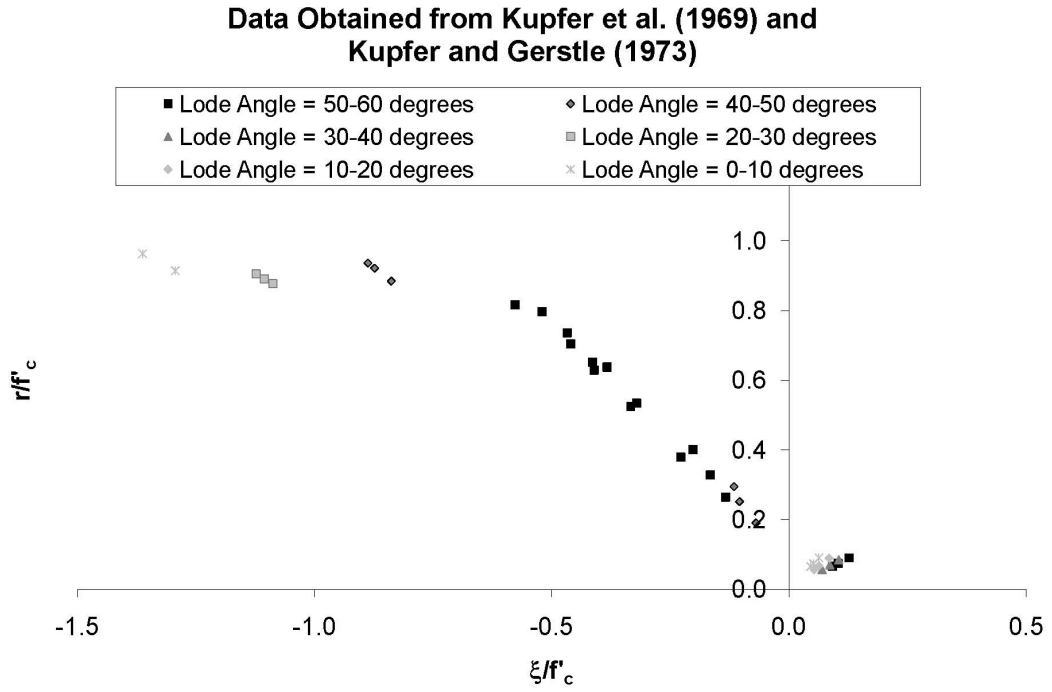

Figure C.13: Test data from Kupfer et al. (1969) and Kupfer and Gerstle (1973).

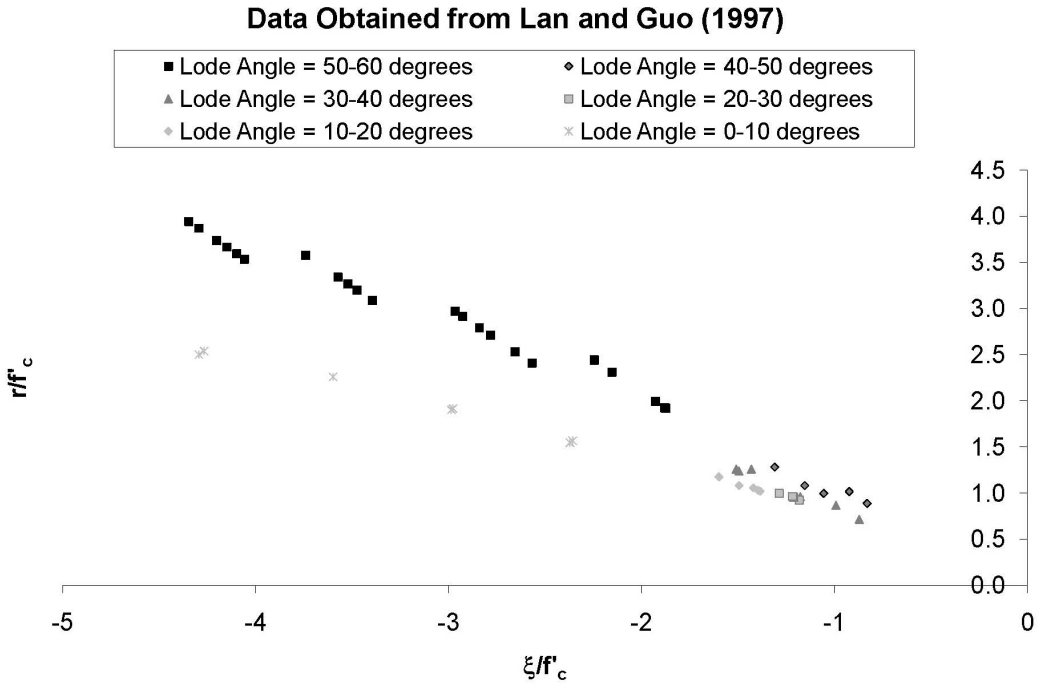

Figure C.14: Test data from Lan and Guo (1997).

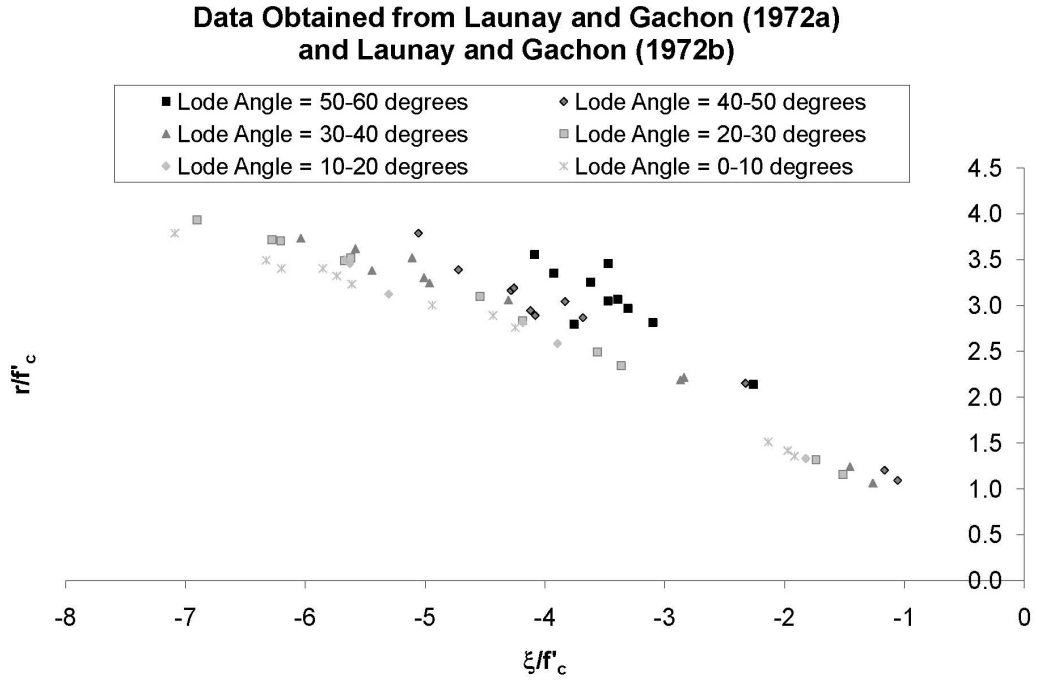

Figure C.15: Test data from Launay and Gachon (1972a) and Launay and Gachon (1972b).

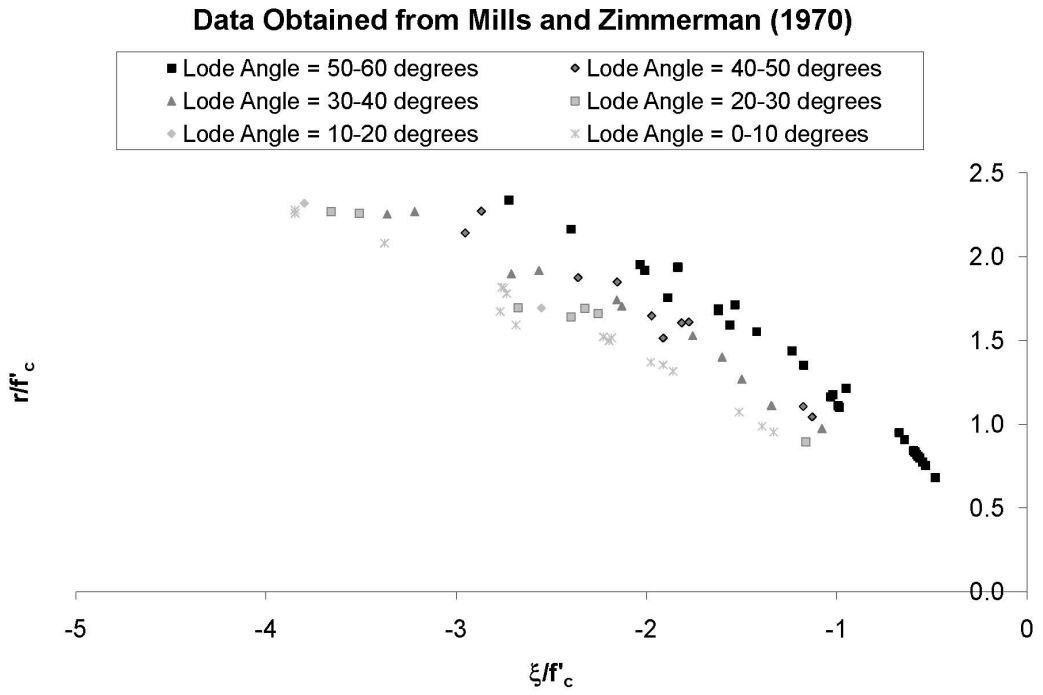

Figure C.16: Test data from Mills and Zimmerman (1970).

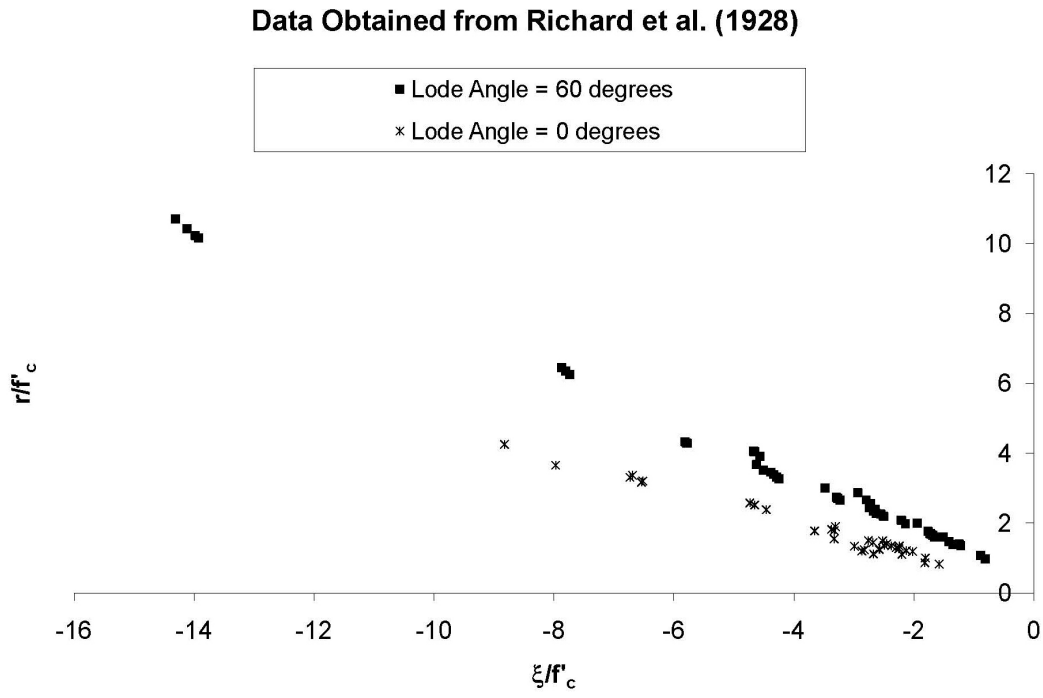

Figure C.17: Test data from Richart et al. (1928).

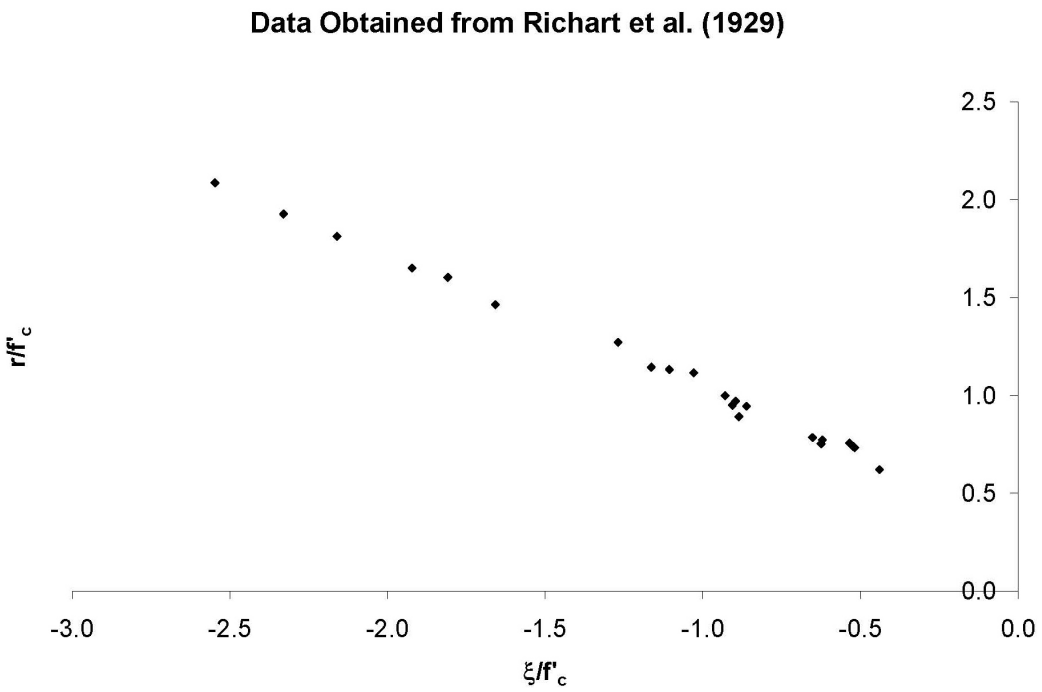

Figure C.18: Test data from Richart et al. (1929).

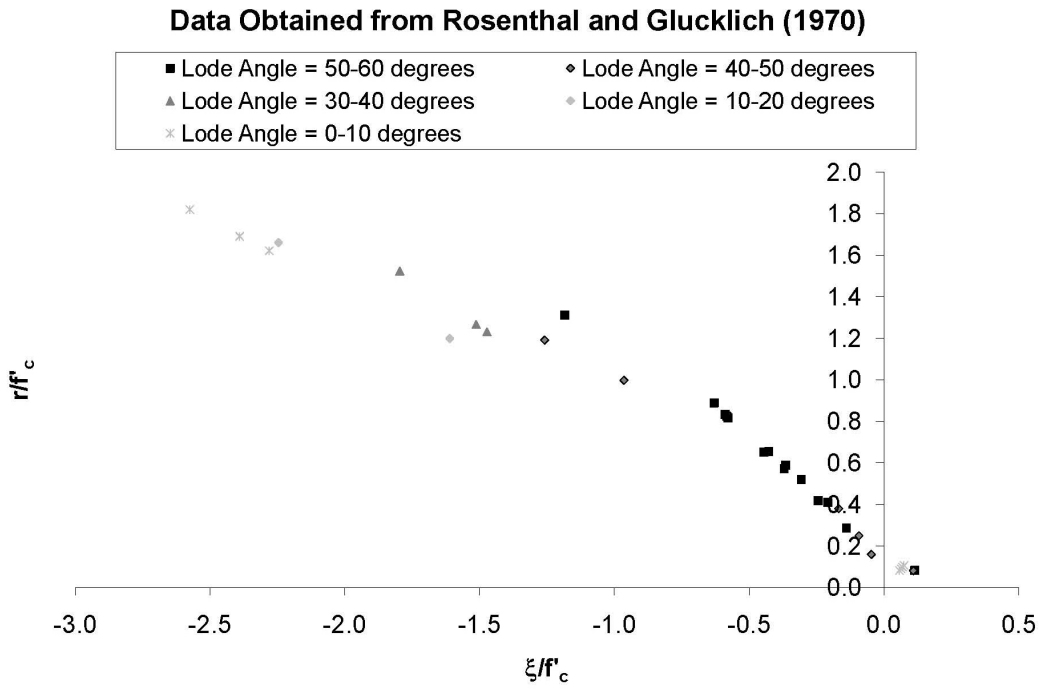

Figure C.19: Test data from Rosenthal and Glucklich (1970).

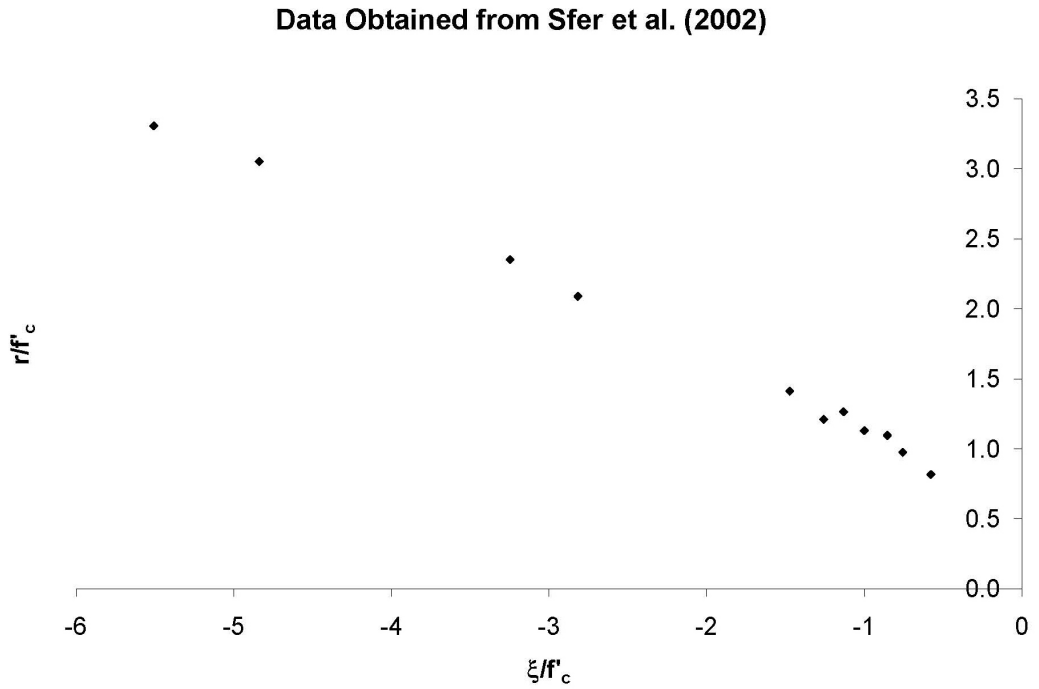

Figure C.20: Test data from Sfer et al. (2002).

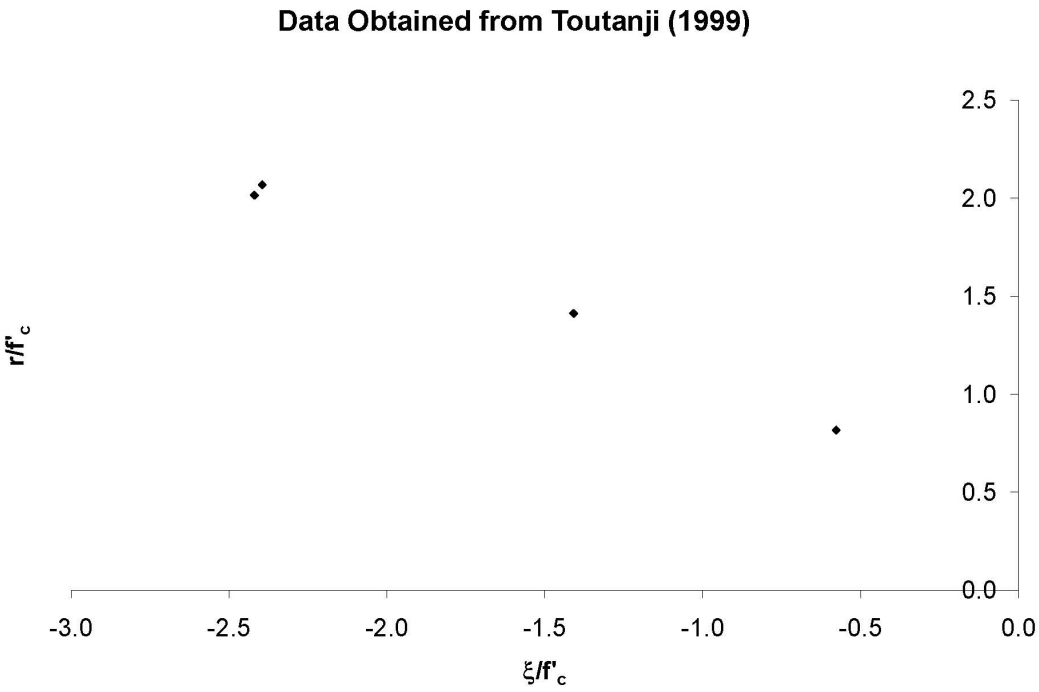

Figure C.21: Test data from Toutanji (1999).

Appendix D

Summary of Papers Used for Determining Residual Surface Parameters

Table D.1: Summary of papers used for determining residual surface parameters.

Paper	Triaxial Loading Type	Lateral Loading Magnitude (as % of f'_c)	Concrete Strength (ksi)	Specimen Shape	Specimen Size (inches)	Water-Cement Ratio	Notes
Ansari and Li (1998)	Triaxial pressure vessel	18% - 93%	6.9 - 15.6	Cylinder	4 x 8	0.26 - 0.46	included mixes: two high strength, one normal strength
Attard and Setunge (1996), Attard and Setunge (1994)	Triaxial pressure vessel	0.4% - 25%	8.4 - 19.1	Cylinder	4 x 8	0.26 - 0.45	included mixes: four high strength, one normal strength; three different coarse aggregates
Jamet et al. (1984)	Triaxial pressure vessel	10% - 86%	4.2	Cylinder	4.33 x 8.66	0.53	
van Mier (1984)	True triaxial	2.5% - 33%	5.8 - 7.4	Cubes	4 x 4 x 4	0.50	
Xie et al. (1995)	Triaxial pressure vessel	1.3% - 50.4%	8.7 - 17.3	Cylinder	2.19 x 4.33	0.22 - 0.32	included three high strength mixes

Appendix E

Fortran Code of the Finite Element Program Containing the Concrete Plasticity Model

```
!*************************************************************************
!
!  PROGRAM: Column_Plasticity
!
!  PURPOSE:  Calculate stress vs. strain and moment-curvature curves for
!            a given column cross section and given axial load range.
!
!  NOTES:  Elements must always be numbered so that the top layer nodes
!          are first and the axis of the column runs through x=y=0.
!          Present code does not allow for load reversals as the concrete
!          model does not account for crack opening/closing.
!
!  WRITTEN BY: Julie Wolf (includes sections by John Hall)
!
!*************************************************************************

      PROGRAM MAIN
      IMPLICIT REAL(KIND=16) (A-H,O-Z)
      IMPLICIT INTEGER(KIND=8) (I-N)
      DIMENSION TITLE(20)
      REAL(KIND=16), ALLOCATABLE, DIMENSION(:) :: A,B,C
      REAL(KIND=16), ALLOCATABLE, DIMENSION(:,:) :: AXLDS
C
C Array AXLDS contains the vector of axial load and moment values
C Array A contains mesh data (COOR, ID, and R)
C Array B contains element data
C Array C contains solution data (H, F, RTPT, DX, XT, XTPT, ELRT ELRTPT)
C
      INTEGER(KIND=8), ALLOCATABLE, DIMENSION(:) :: NTYPE
C
C Array NTYPE designates the plane of the node
C      0 - bottom plane
C      1 - top plane
C Used for determining degrees of freedom
C
      REAL(KIND=16) MX,MY,MSTOP,MMAX
      COMMON /INFO/ N5TEMP
      COMMON /INFO1/ NNP,NEQ,MBAND,IGO
      COMMON /INFO2/ IEG,NEG1,NEG10,NEG11,NEG100,NEG110,MAXNEL1,
     * MAXNEL10,MAXNEL11,MAXNEL100,MAXNEL110,MAXNINT
      COMMON /ELPAR/ NPAR(8)
      COMMON /POINTS/ N1,N2,N3,N4,N5,N6,N7,N8,N9,N10,N11,N1101,N1102,
     * N1103,N1104,N12,N1201,N1202,N1203,N1204,N13
      COMMON /TOL/ TOLF,TOLM,NITMAX
      COMMON /DEBUG/ IDEBUG
      OPEN (5,FILE='input.txt')
      OPEN (6,FILE='output.txt')
```

```
      OPEN (7,FILE='storage',FORM='UNFORMATTED')
      OPEN (8,FILE='MC_curves.txt')
C
C Read and print control information.
C
      READ(5,1000) TITLE
 1000 FORMAT(20A4)
      READ(5,*) NNP,NEG1,NEG10,NEG11,NEG100,NEG110,NUMAX
      ALLOCATE(NTYPE(NNP))
      ALLOCATE(AXLDS(NUMAX,2))
      AXLDS=0.Q0
      NTYPE=0
      DO 50 K=1,NUMAX
      READ(5,*) AXLDS(K,1),AXLDS(K,2)
   50 CONTINUE
      WRITE(6,1001) TITLE,NNP,NEG1,NEG10,NEG11,NEG100,NEG110,NUMAX
 1001 FORMAT(5(/),1X,20A4,4(/),1X,'NNP =',I5,/,1X,
     *    'NEG1 (Longitudinal Rebar) =',I5,(/),1X,
     *    'NEG10 (Lower Transverse Rebar) =',I5,(/),1X,
     *    'NEG11 (Upper Transverse Rebar) =',I5,(/),1X
     *    'NEG100 (Top Layer Concrete) =',I5,(/),1X,
     *    'NEG110 (Interior Concrete) =',I5,(/),1X,
     *    'NUMAX =',I5,(/),1X,'AXLDS =')
      DO 100 I=1,NUMAX
      WRITE(6,1002) AXLDS(I,1),AXLDS(I,2)
 1002 FORMAT(10X,E12.5,4X,E12.5)
  100 CONTINUE
      READ(5,*) NSSTEPS,NHSTEPS,NITMAX,ANGLE,TOLF,TOLM,MSTOP,MMAX
      WRITE(6,1003) NSSTEPS,NHSTEPS,NITMAX,ANGLE,TOLF,TOLM,MSTOP,MMAX
 1003 FORMAT(2(/),1X,'NSSTEPS =',I5,/,1X,'NHSTEPS =',I5,/,1X,
     *   'NITMAX = ',I5,/,1X,
     *   'ANGLE (IN DEGREES) OF MOMENT APPLICATION = ',E12.5,/,1X,
     *   'FORCE TOLERANCE = ',E12.5,/,1X,'MOMENT TOLERANCE = ',E12.5,/,
     *   1X,'SMALLEST MOMENT INCREMENT ATTEMPTED = ',E12.5,/,1X,
     *   'MAXIMUM MOMENT ATTEMPTED = ',E12.5)
      IF (NHSTEPS .GT. NSSTEPS .AND. NUMAX .EQ. 1
     *  .AND. AXLDS(1,2) .EQ. 0.) THEN
          WRITE(6,*) 'Number of hydrostatic steps must be less than',
     *      ' or equal to the number of static steps'
          STOP
      ENDIF
C
C Read and print nodal data.  Number equations.
      N1=1
      N2=N1+NNP*3 ! COOR
      N3=N2+NNP*3 ! ID
      N4=N3+NNP*3 ! R
      ALLOCATE(A(N4-1))
      A=0.Q0
      ZCOR=0.
C
C Generates and prints nodal coordinates.
      CALL READC(A(N1),NNP,ZCOR,NTYPE)
C
C Generates the nodal boundary conditions.  Numbers the equations and
C prints the equation numbers.  Computes NEQ.
      CALL READID(A(N2),A(N1),NNP,NEQ,NTYPE)
C
C Generates and prints nodal loads and specified displacements.
      CALL READR(A(N3),A(N2),NNP)
C
C Read and print element data.  Calculate assembly arrays.  Calculate
C and print half-bandwidth.
C
      MBAND=1
      MAXNEL1=0
      MAXNEL10=0
      MAXNEL11=0
      MAXNEL100=0
      MAXNEL110=0
      MAXNINT=1
C
      N5=1
      N6=1
      N7=1
```

```
      N8=1
      N9=1
      N10=1
      N11=1
      N1101=1
      N1102=1
      N1103=1
      N1104=1
      N12=1
      N1201=1
      N1202=1
      N1203=1
      N1204=1
      N13=NEQ*(8*6*2+1)+1
      WRITE(6,2001)
 2001 FORMAT(4(/),1X,'ELEMENT DATA')
      IGO=1
      REWIND 7
      DO 200 IEG=1,NEG1
      READ(5,*) NPAR
      IF(NPAR(1).NE.1) THEN
        WRITE(6,2002)
 2002   FORMAT(2(/),'Incorrect number of longitudinal rebar groups',
     *  ' (Type 1 elements)')
        STOP
      END IF
      CALL TRUSSA(A,B,C)
      IF(N5TEMP.GT.N5) N5=N5TEMP
  200 CONTINUE
      DO 201 IEG=1,NEG10
      READ(5,*) NPAR
      IF(NPAR(1).NE.10) THEN
        WRITE(6,2003)
 2003   FORMAT(2(/),'Incorrect number of lower transverse rebar groups',
     *      ' (Type 10 elements)')
        STOP
      ENDIF
      CALL TRUSSB(A,B,C)
      IF(N5TEMP.GT.N5) N5=N5TEMP
  201 CONTINUE
      DO 202 IEG=1,NEG11
      READ(5,*) NPAR
      IF(NPAR(1).NE.11) THEN
        WRITE(6,2004)
 2004   FORMAT(2(/),'Incorrect number of upper transverse rebar groups',
     *      ' (Type 11 elements)')
        STOP
      ENDIF
      CALL TRUSSC(A,B,C)
      IF(N5TEMP.GT.N5) N5=N5TEMP
  202 CONTINUE
      DO 203 IEG=1,NEG100
      READ(5,*) NPAR
      IF(NPAR(1).NE.100) THEN
        WRITE(6,2005)
 2005   FORMAT(2(/),'Incorrect number of solid concrete groups',
     *      ' (Type 100 elements)')
        STOP
      END IF
      CALL SOLIDA(A,B,C)
      IF(N5TEMP.GT.N5) N5=N5TEMP
  203 CONTINUE
      DO 204 IEG=1,NEG110
      READ(5,*) NPAR
      IF(NPAR(1).NE.110) THEN
        WRITE(6,2006)
 2006   FORMAT(2(/),'Incorrect number of solid concrete groups',
     *      'Type 110 elements)')
        STOP
      END IF
      CALL SOLIDB(A,B,C)
      IF(N5TEMP.GT.N5) N5=N5TEMP
  204 CONTINUE
      WRITE(6,2007) MBAND,NEQ
 2007 FORMAT(4(/),1X,'MBAND = ',I5,/,1X,'NEQ = ',I5)
```

```
C
C Assemble nodal loads.  Calculate and assemble element matrices and
C   vectors.
      N6=1+NEQ*MBAND                                          ! H
      N7=N6+NEQ                                               ! F
      N8=N7+NEQ                                               ! RTPT
      N9=N8+NEQ                                               ! DX
      N10=N9+NEQ                                              ! XT
      N11=N10+NEQ                                             ! XTPT
      N1101=N11+4*MAXNEL1*NEG1                                ! ELRT1
      N1102=N1101+4*MAXNEL10*NEG10                            ! ELRT10
      N1103=N1102+4*MAXNEL11*NEG11                            ! ELRT11
      N1104=N1103+(MAXNINT*(6*2+3)+1)*MAXNEL100*NEG100  ! ELRT100
      N12=N1104+(MAXNINT*(6*2+3)+1)*MAXNEL110*NEG110    ! ELRT110
      N1201=N12+4*MAXNEL1*NEG1                                ! ELRTPT1
      N1202=N1201+4*MAXNEL10*NEG10                            ! ELRTPT10
      N1203=N1202+4*MAXNEL11*NEG11                            ! ELRTPT11
      N1204=N1203+(MAXNINT*(6*2+3)+1)*MAXNEL100*NEG100  ! ELRTPT100
      N13=N1204+(MAXNINT*(6*2+3)+1)*MAXNEL110*NEG110    ! ELRTPT110
      ALLOCATE(B(N5-1))
      ALLOCATE(C(N13-1))
C
C
C Loop over all axial load cases
      DO 300 K=1,NUMAX
      B=0.Q0
      C=0.Q0
      MX=0.Q0
      MY=0.Q0
      DM=1000.Q0*TOLM
C
C Transfer nodal loads from R to F.
      CALL FILLF(A(N2),A(N3),C(N6),AXLDS(K,1),MX,MY,NNP,NEQ)
C
C Transfer initial element lengths to ELRTPT
      IGO=2
      REWIND 7
      DO 400 IEG=1,NEG1
      READ(7) NEND,NPAR,(B(I),I=1,NEND)
      CALL TRUSSA(A,B,C)
  400 CONTINUE
      DO 401 IEG=1,NEG10
      READ(7) NEND,NPAR,(B(I),I=1,NEND)
      CALL TRUSSB(A,B,C)
  401 CONTINUE
      DO 402 IEG=1,NEG11
      READ(7) NEND,NPAR,(B(I),I=1,NEND)
      CALL TRUSSC(A,B,C)
  402 CONTINUE
      DO 403 IEG=1,NEG100
      READ(7) NEND,NPAR,(B(I),I=1,NEND)
      CALL SOLIDA(A,B,C)
  403 CONTINUE
      DO 404 IEG=1,NEG110
      READ(7) NEND,NPAR,(B(I),I=1,NEND)
      CALL SOLIDB(A,B,C)
  404 CONTINUE
      WRITE(6,3000) AXLDS(K,1)
      WRITE(*,3000) AXLDS(K,1)
 3000 FORMAT(4(/),1X,'SOLUTION INFORMATION FOR AXIAL LOAD = ',E12.5)
      WRITE(8,3001) AXLDS(K,1)
 3001 FORMAT(/,1X,'AXIAL LOAD =',E19.12,/)
      WRITE(8,3002)
 3002 FORMAT(10x,'CURVATURE-X',18X,'MX',9X,'CURVATURE-Y',18X,'MY')
C
C Solve for axial load only
      CALL STANAL(A(N1),A(N2),A(N3),B,C(1),C(N6),C(N7),C(N8),C(N9),
     *   C(N10),C(N11),C(N12),AXLDS(K,1),NTYPE,NSSTEPS,NHSTEPS,ZCOR,
     *   NITER)
      TEMP=QSQRT(C(N11-2)*C(N11-2)+C(N11-1)*C(N11-1))
      WRITE(8,3003) C(N11-2),0.,C(N11-1),0.
 3003 FORMAT(1X,6(1X,E19.12))
c Skip moment curvature calcs if no applied moment
      IF (AXLDS(K,2) .EQ. 0.) GO TO 300
C
C Create moment-curvature curve
```

```
      WRITE(6,3004) AXLDS(K,2)
      WRITE(*,3004) AXLDS(K,2)
 3004 FORMAT(4(/),1X,'SOLUTION INFORMATION FOR MOMENT = ',E12.5)
      MX=AXLDS(K,2)*QCOSD(ANGLE)
      MY=AXLDS(K,2)*QSIND(ANGLE)
      CALL FILLF(A(N2),A(N3),C(N6),AXLDS(K,1),MX,MY,NNP,NEQ)
      CALL MCANAL(A(N1),A(N2),A(N3),B,C(1),C(N6),C(N7),C(N8),C(N9),
     *   C(N10),C(N11),C(N12),AXLDS(K,2),NTYPE,NSSTEPS,NHSTEPS,ZCOR,
     *   NITER)
  300 CONTINUE
      STOP
      END PROGRAM MAIN

C-----------------------------------------------------------------------
C-----------------------------------------------------------------------

      SUBROUTINE ASSMBL(H,F,HE,FE,IDL,NEQ,MBAND,NED,M1,M2)
C Assembles HE into H when M1.NE.0.  Assembles FE into F when M2.NE.0.
      IMPLICIT REAL(KIND=16) (A-H,O-Z)
      IMPLICIT INTEGER(KIND=8) (I-N)
      COMMON /DEBUG/ IDEBUG
      DIMENSION H(NEQ,MBAND),F(NEQ),HE(NED,NED),FE(NED*M2),IDL(NED)
      IF(M1.EQ.0) GO TO 2
C Assemble HE into H.
      DO 10 I=1,NED
      IROW=IDL(I)
      IF(IROW.EQ.0) GO TO 10
      DO 20 J=1,NED
      ICOL=IDL(J)-IROW+1
      IF(ICOL.GT.0) H(IROW,ICOL)=H(IROW,ICOL)+HE(I,J)
   20 CONTINUE
   10 CONTINUE
    2 IF(M2.EQ.0) RETURN
C Assemble FE into F.
      DO 30 I=1,NED
      IROW=IDL(I)
      IF(IROW.EQ.0) GO TO 30
      F(IROW)=F(IROW)+FE(I)
   30 CONTINUE
      RETURN
      END

      SUBROUTINE BAND(IDL,NED,NEL,MBAND)
C Computes MBAND.
      IMPLICIT REAL(KIND=16) (A-H,O-Z)
      IMPLICIT INTEGER(KIND=8) (I-N)
      COMMON /DEBUG/ IDEBUG
      DIMENSION IDL(NED,NEL)
      DO 10  N=1,NEL
      DO 20 I=1,NED
      IROW=IDL(I,N)
      IF(IROW.EQ.0) GO TO 20
      DO 30 J=1,NED
      ICOL=IDL(J,N)
      IF(ICOL.EQ.0) GO TO 30
      NDIFF=IROW-ICOL+1
      IF(NDIFF.GT.MBAND) MBAND=NDIFF
   30 CONTINUE
   20 CONTINUE
   10 CONTINUE
      RETURN
      END

      SUBROUTINE BSOLVE(A,B,N,NBD,MA,MB)
C symmetric banded equation solver for AX=B where A is N*NBD and B is N*1
      IMPLICIT REAL(KIND=16) (A-H,O-Z)
      IMPLICIT INTEGER(KIND=8) (I-N)
      COMMON /DEBUG/ IDEBUG
      DIMENSION A(N,NBD),B(N)
      IF(MA.EQ.0) GO TO 200
C forward reduction on A
      AVOD=0.Q0
      DO 100 I=1,N
      AVOD=AVOD+QABS(A(I,1))
  100 CONTINUE
      AVOD=AVOD/N
```

```
      TOL=AVOD* 1.Q-12
      DMIN=1.Q+30
      DO 110 IROW=1,N
c add below line to prevent negative stiffness
      IF(A(IROW,1).LT.DMIN) DMIN=A(IROW,1)
      IF(DMIN.LT.TOL) GO TO 300
      IF(IROW.EQ.N) GO TO 110
      MIN=KMIN0(NBD,N-IROW+1)
      DO 120 J=2,MIN
      IF (A(IROW,J).EQ.0.Q0) GO TO 120
      ST=A(IROW,J)/A(IROW,1)
      IJ1=IROW+J-1
      DO 130 K=J,MIN
      KJ1=K-J+1
      A(IJ1,KJ1)=A(IJ1,KJ1)-ST*A(IROW,K)
  130 CONTINUE
      A(IROW,J)=ST
  120 CONTINUE
  110 CONTINUE
  200 IF(MB.EQ.0) RETURN
C forward reduction and back substitution on B
      IF(N.EQ.1) B(1)=B(1)/A(1,1)
      IF(N.EQ.1) RETURN
      N1=N-1
      DO 210 I=1,N1
      MIN=KMIN0(NBD,N-I+1)
      DO 220 J=2,MIN
      JJ=I+J-1
      B(JJ)=B(JJ)-B(I)*A(I,J)
  220 CONTINUE
  210 CONTINUE
      DO 230 I=1,N
      B(I)=B(I)/A(I,1)
  230 CONTINUE
      DO 240 I=1,N1
      II=N-I+1
      MIN=KMIN0(NBD,II)
      DO 250 J=2,MIN
      JJ=II-J+1
      B(JJ)=B(JJ)-B(II)*A(JJ,J)
  250 CONTINUE
  240 CONTINUE
      RETURN
  300 WRITE(6,3000)
 3000 FORMAT(2(/),5X,'DMIN IS LESS THAN TOL; EXECUTION STOPPED.')
      WRITE(6,3001) AVOD,DMIN,TOL,IROW
 3001 FORMAT(5X,'AVOD =',1X,E12.5,4X,'DMIN =',1X,E12.5,4X,'TOL =',1X,
     * E12.5,4X,'IROW =',I5)
      STOP
      END

      SUBROUTINE CORGEN(COOR,NNP,NTYPE)
C Generates matrix COOR
      IMPLICIT REAL(KIND=16) (A-H,O-Z)
      IMPLICIT INTEGER(KIND=8) (I-N)
      COMMON /DEBUG/ IDEBUG
      DIMENSION COOR(NNP,3),COOR1(3),NTYPE(NNP)
      L=0
      LG=0
   10 READ(5,*) N,NG,(COOR1(J),J=1,3),NTYPE(N)
      IF(N.EQ.0) RETURN
      DO 20 J=1,3
      COOR(N,J)=COOR1(J)
   20 CONTINUE
      NB=L+LG
      IF((LG.LE.0).OR.(NB.GE.N)) GO TO 40
      NE=N-1
      NSPACE=(N-L-1)/LG+1
      DO 30 J=1,3
      CINC=(COOR(N,J)-COOR(L,J))/NSPACE
      DO 31 I=NB,NE,LG
      COOR(I,J)=COOR(I-LG,J)+CINC
      NTYPE(I)=NTYPE(I-LG)
   31 CONTINUE
   30 CONTINUE
   40 L=N
```

```
      LG=NG
      GO TO 10
      END

      SUBROUTINE DFCALC(DF,DQ,X,R,THETA,PSIMAX,ALPHA,GAMMA,ETA,PHI,
     *  OMEGA,PSI,BETA,DBETADPSI,YST,DFDEP,SXX,SYY,SZZ,SXY,SYZ,SXZ)
      IMPLICIT REAL(KIND=16) (A-H,O-Z)
      IMPLICIT INTEGER(KIND=8) (I-N)
      COMMON /DEBUG/ IDEBUG
      DIMENSION DF(6,1),DQ(6,1)
      REAL(KIND=16) PSIMAX,PSI,PHI,X,R,THETA,J2,J3
C
C Calculate all derivatives related to the peak loading surface
C  peak parameters
      RT = -0.5502721390459450Q0+QSQRT(-1.43439820150635Q0*X
     *          +0.0924044582071Q0*X**2.Q0+0.302799427010 2Q0)
      RC = -0.3519588917484 1Q0+QSQRT(-1.971053263759 4Q0*X
     *          +0.3102749931823 9Q0*X**2.Q0+0.1238750614807 69Q0)
      CALL RCALC(RT,RC,THETA,RPEAK)
      DRTDX = 0.5Q0/(RT+0.5502721390459450Q0)*(-1.43439820150635Q0
     *              +0.1848089164142Q0*X)
      DRCDX = 0.5Q0/(RC+0.3519588917484 1Q0)*(-1.971053263759 4Q0
     *              +0.6205499863647 8Q0*X)
      CALL DRCALC(RC,RT,DRCDX,DRTDX,THETA,DRPEAKDX,DRPEAKDTH)
      IF (X .GE. 0.) THEN
          RT = 0.Q0
          RC = 0.Q0
          RPEAK = 0.Q0
          DRTDX = 0.Q0
          DRCDX = 0.Q0
          DRPEAKDX = 0.Q0
          DRPEAKDTH = 0.Q0
      ENDIF
      DFPEAKDX = -DRPEAKDX
      DFPEAKDTH = -DRPEAKDTH
C
C Calculate all derivatives related to the yield loading surface
      IF (PSI .LT. PSIMAX) THEN
          TEMPA = QSQRT(2.Q0/3.Q0)*0.45Q0*(1.Q0+QSQRT(3.Q0)/0.45Q0)
          TEMPB = QSQRT(2.Q0/3.Q0)*0.522Q0*(1.Q0+QSQRT(3.Q0)/1.044Q0)
          TEMPC = -X/(1.Q0-X)
          RT = TEMPC*TEMPB
          RC = TEMPC*TEMPA
          CALL RCALC(RT,RC,THETA,RYIELD)
c          DRTDX = 0.5Q0/(RT+0.88222488954238 1Q0)
c     *                 *(-1.47Q0+0.262233966735318Q0*X)
c          DRCDX = 0.5Q0/(RC+1.10899432823906 0Q0)
c     *                 *(-3.61Q0+0.356609103684252Q0*X)
          TEMPC = (1.Q0-X)**2.Q0
          DRTDX = -TEMPB/TEMPC
          DRCDX = -TEMPA/TEMPC
          CALL DRCALC(RC,RT,DRCDX,DRTDX,THETA,DRYIELDDX,DRYIELDDTH)
          IF (X .GE. 0.) THEN
              RT = 0.Q0
              RC = 0.Q0
              RYIELD = 0.Q0
              DRCDX = 0.Q0
              DRTDX = 0.Q0
              DRYIELDDX = 0.Q0
              DRYIELDDTH = 0.Q0
          ENDIF
          DFYIELDDX = -DRYIELDDX
          DFYIELDDTH = -DRYIELDDTH
          DFDX = BETA*DFPEAKDX + (1.Q0-BETA)*DFYIELDDX
          DFDTH = BETA*DFPEAKDTH + (1.Q0-BETA)*DFYIELDDTH
C
C Vary Psi relationship here
C
          DPSIDEP = 1.Q0/(PHI+ALPHA*(QABS(X))**GAMMA)
          DFDEP = (RYIELD-RPEAK)*DBETADPSI*DPSIDEP
C
C Calculate all derivatives related to the residual loading surface
      ELSE IF (PSI .GT. PSIMAX) THEN
          RTT = -0.7416615013716 67Q0+QSQRT(-0.97641966644489Q0*X
     *              +0.0565121387786362Q0*X**2.Q0+0.550061782616876 0Q0)
```

```
          RCC = -0.474373208368885Q0+QSQRT(-1.34173004980343OQ0*X
     *              +0.189756033577570Q0*X**2.Q0+0.2250299408189Q0)
C Parameters to have round residual surface
c          RTT = RCC
C
          IF (X .GE. 0.) THEN
              RTT = 0.Q0
              RCC = 0.Q0
          ENDIF
          IF (RCC .GE. RC .AND. RTT .GE. RT) THEN
              DFDX = DFPEAKDX
              DFDTH = DFPEAKDTH
              RRES = RPEAK
          ELSE
              IF (RT .GT. RTT) THEN
                DRTDX = 0.5Q0/(RTT+0.74166150137166 7Q0)*
     *                    (-0.9764196664448 9Q0+0.1130242775572724Q0*X)
              ENDIF
              IF (RC .GT. RCC) THEN
                DRCDX = 0.5Q0/(RCC+0.474373208368885Q0)*
     *                    (-1.34173004980343OQ0+0.37951206715514Q0*X)
              ENDIF
C Parameters to have round residual surface
c              IF (RT .GT. RTT) THEN
c                DRTDX = DRCDX
c              ENDIF
C
              RT = QMIN1(RT,RTT)
              RC = QMIN1(RC,RCC)
              CALL RCALC(RT,RC,THETA,RRES)
              CALL DRCALC(RC,RT,DRCDX,DRTDX,THETA,DRRESDX,DRRESDTH)
              IF (X .GE. 0.) THEN
                RC = 0.Q0
                RT = 0.Q0
                RRES = 0.Q0
                DRCDX = 0.Q0
                DRTDX = 0.Q0
                DRRESDX = 0.Q0
                DRRESDTH = 0.Q0
              ENDIF
              DFRESDX = -DRRESDX
              DFRESDTH = -DRRESDTH
              DFDX = BETA*DFPEAKDX + (1.Q0-BETA)*DFRESDX
              DFDTH = BETA*DFPEAKDTH + (1.Q0-BETA)*DFRESDTH
          ENDIF
C
C Vary Psi relationship here
C
          DPSIDEP = 1.Q0/(PHI+ALPHA*(QABS(X))**GAMMA)
          DFDEP = (RRES-RPEAK)*DBETADPSI*DPSIDEP
      ELSE
          DFDX = DFPEAKDX
          DFDTH = DFPEAKDTH
          DFDEP = 0.Q0
      ENDIF
      DQDX = OMEGA*DFDX
      DQDTH = OMEGA*DFDTH
C
C Calculate all derivatives related to the invariants
      CALL PRIN(X,R,THETA,S1,S2,S3)
      X = X*YST
      R = R*YST
      J2 = R**2.Q0/2.Q0
      if (idebug .eq. 1) write(11,*) 'J2 = ',J2
      DJ2DSXX = (2.Q0*SXX-SYY-SZZ)/3.Q0
      DJ2DSYY = (-SXX+2.Q0*SYY-SZZ)/3.Q0
      DJ2DSZZ = (-SXX-SYY+2.Q0*SZZ)/3.Q0
      DJ2DSXY = 2.Q0*SXY
      DJ2DSYZ = 2.Q0*SYZ
      DJ2DSXZ = 2.Q0*SXZ

      TEMPA = X/QSQRT(3.Q0)
      J3 = (SXX-TEMPA)*(SYY-TEMPA)*(SZZ-TEMPA)-((SXX-TEMPA)*SYZ**2.Q0
     *        +SXY**2.Q0*(SZZ-TEMPA)+SXZ**2.Q0*(SYY-TEMPA))
     *        +2.Q0*SXY*SYZ*SXZ
      DJ3DSXX = (4.Q0*SYY*SZZ-2.Q0*SXX*(-SXX+SYY+SZZ)
```

```
     *          -(SYY**2.Q0+SZZ**2.Q0))/9.Q0-(2.Q0*SYZ**2.Q0
     *          -(SXY**2.Q0+SXZ**2.Q0))/3.Q0
      DJ3DSYY = (4.Q0*SXX*SZZ-2.Q0*SYY*(SXX-SYY+SZZ)
     *          -(SXX**2.Q0+SZZ**2.Q0))/9.Q0
     *          -(2.Q0*SXZ**2.Q0-(SXY**2.Q0+SYZ**2.Q0))/3.Q0
      DJ3DSZZ = (4.Q0*SXX*SYY-2.Q0*SZZ*(SXX+SYY-SZZ)
     *          -(SXX**2.Q0+SYY**2.Q0))/9.Q0
     *          -(2.Q0*SXY**2.Q0-(SXZ**2.Q0+SYZ**2.Q0))/3.Q0
      DJ3DSXY = 2.Q0*SXZ*SYZ+2.Q0/3.Q0*SXY*(SXX+SYY-2.Q0*SZZ)
      DJ3DSYZ = 2.Q0*SXY*SXZ+2.Q0/3.Q0*SYZ*(-2.Q0*SXX+SYY+SZZ)
      DJ3DSXZ = 2.Q0*SXY*SYZ+2.Q0/3.Q0*SXZ*(SXX-2.Q0*SYY+SZZ)
      TEMPA = QSIN(3.Q0*THETA)
      DTHDJ2 = 0.75Q0*QSQRT(3.Q0)*J3/(J2**2.5Q0)/TEMPA
      DTHDJ3 = -QSQRT(3.Q0)/2.Q0/(J2**1.5Q0)/TEMPA
      IF (TEMPA .LT. 1.Q-6) THEN
        DTHDJ2 = QSQRT(3.Q0)/2.Q0*J3/(J2**(2.5Q0))
        DTHDJ3 = -1.Q0/QSQRT(3.Q0)/(J2**(1.5Q0))
      ENDIF
      DTHDSXX = DTHDJ3*DJ3DSXX+DTHDJ2*DJ2DSXX
      DTHDSYY = DTHDJ3*DJ3DSYY+DTHDJ2*DJ2DSYY
      DTHDSZZ = DTHDJ3*DJ3DSZZ+DTHDJ2*DJ2DSZZ
      DTHDSXY = DTHDJ3*DJ3DSXY+DTHDJ2*DJ2DSXY
      DTHDSYZ = DTHDJ3*DJ3DSYZ+DTHDJ2*DJ2DSYZ
      DTHDSXZ = DTHDJ3*DJ3DSXZ+DTHDJ2*DJ2DSXZ

      TEMPSXX = DJ2DSXX/R/YST
      TEMPSYY = DJ2DSYY/R/YST
      TEMPSZZ = DJ2DSZZ/R/YST
      TEMPSXY = DJ2DSXY/R/YST
      TEMPSYZ = DJ2DSYZ/R/YST
      TEMPSXZ = DJ2DSXZ/R/YST
C
C Correct for case where R=0
      IF (R .EQ. 0. .OR. X .GE. 0.) THEN
          TEMPSXX = 0.Q0
          TEMPSYY = 0.Q0
          TEMPSZZ = 0.Q0
          TEMPSXY = 0.Q0
          TEMPSYZ = 0.Q0
          TEMPSXZ = 0.Q0
      ENDIF
C
C Calculated final yield and loading surface derivatives
      DF(1,1) = TEMPSXX+DFDX/QSQRT(3.Q0)/YST+DFDTH*DTHDSXX
      DF(2,1) = TEMPSYY+DFDX/QSQRT(3.Q0)/YST+DFDTH*DTHDSYY
      DF(3,1) = TEMPSZZ+DFDX/QSQRT(3.Q0)/YST+DFDTH*DTHDSZZ
      DF(4,1) = TEMPSXY+DFDTH*DTHDSXY
      DF(5,1) = TEMPSYZ+DFDTH*DTHDSYZ
      DF(6,1) = TEMPSXZ+DFDTH*DTHDSXZ
      DQ(1,1) = TEMPSXX+DQDX/QSQRT(3.Q0)/YST+DQDTH*DTHDSXX
      DQ(2,1) = TEMPSYY+DQDX/QSQRT(3.Q0)/YST+DQDTH*DTHDSYY
      DQ(3,1) = TEMPSZZ+DQDX/QSQRT(3.Q0)/YST+DQDTH*DTHDSZZ
      DQ(4,1) = TEMPSXY+DQDTH*DTHDSXY
      DQ(5,1) = TEMPSYZ+DQDTH*DTHDSYZ
      DQ(6,1) = TEMPSXZ+DQDTH*DTHDSXZ
      X = X/YST
      R = R/YST
      RETURN
      END

      SUBROUTINE DRCALC(RC,RT,DRCDX,DRTDX,THETA,DRDX,DRDTH)
      IMPLICIT REAL(KIND=16) (A-H,O-Z)
      IMPLICIT INTEGER(KIND=8) (I-N)
      COMMON /DEBUG/ IDEBUG
      REAL(KIND=16) RC,RT,DRCDX,DRTDX,THETA,TEMPA,TEMPB,DRDX,DRDTH
      TEMPA = 4.Q0*(RC**2.Q0-RT**2.Q0)*(QCOS(THETA))**2.Q0
     *          +(RC-2.Q0*RT)**2.Q0
      TEMPB = QSQRT(4.Q0*(RC**2.Q0-RT**2.Q0)*(QCOS(THETA))**2.Q0
     *          +5.Q0*RT**2.Q0-4.Q0*RT*RC)
      DRDX = (2.Q0*DRCDX*(RC**2.Q0-RT**2.Q0)*QCOS(THETA)+4.Q0*RC*
     *  (RC*DRCDX-RT*DRTDX)*QCOS(THETA)+DRCDX*(2.Q0*RT-RC)*TEMPB+RC
     *  *(2.Q0*DRTDX-DRCDX)*TEMPB+(RC*(2.Q0*RT-RC)*(8.Q0*(RC*DRCDX
     *  -RT*DRTDX)*(QCOS(THETA))**2.Q0+10.Q0*RT*DRTDX-4.Q0*DRTDX*RC
     *  -4.Q0*RT*DRCDX))/(2.Q0*TEMPB))/TEMPA-((2.Q0*RC*(RC**2.Q0
     *  -RT**2.Q0)*QCOS(THETA)+RC*(2.Q0*RT-RC)*TEMPB)*(8.Q0*(RC*DRCDX
     *  -RT*DRTDX)*(QCOS(THETA))**2.Q0+2.Q0*(RC-2.Q0*RT)*(DRCDX
```

```
     *  -2.Q0*DRTDX)))/(TEMPA**2.Q0)
      TEMPA = RC**2.Q0 - RT**2.Q0
      TEMPB = 2.Q0*RT - RC
      DRDTH = 2.Q0*QSIN(THETA)*RC*TEMPA/((4.Q0*(QCOS(THETA))**2.Q0*TEMPA
     *  +TEMPB**2.Q0)**2.Q0)/QSQRT((4.Q0*(QCOS(THETA))**2.Q0-1.Q0)*TEMPA
     *  +TEMPB**2.Q0)*((4.Q0*(QCOS(THETA))**2.Q0*TEMPA-TEMPB**2.Q0)
     *  *QSQRT((4.Q0*(QCOS(THETA))**2.Q0-1.Q0)*TEMPA+TEMPB**2.Q0)
     *  +8.Q0*(QCOS(THETA))**3.Q0*TEMPA*TEMPB+2.Q0*QCOS(THETA)
     *  *TEMPB**3.Q0-4.Q0*QCOS(THETA)*TEMPA*TEMPB)
      IF (QSIN(3.Q0*THETA) .LT. 1.Q-6) THEN
        DRDTH = 1.5Q0*RC*TEMPA/(TEMPB**2.Q0)
      ENDIF
      RETURN
      END

      SUBROUTINE FCALC(F,ELAS,SIG0,DSIG,X,R,THETA,PSI,PSIMAX,BETA,YST)
C
C Subroutine to calculate F (the loading function) given the current
C  stress state (SIG0) the stress increment (DSIG) and current hardening
C  parameter (PSI).  ELAS indicates the ratio of DSIG which is to be
C  applied.
      IMPLICIT REAL(KIND=16) (A-H,O-Z)
      IMPLICIT INTEGER(KIND=8) (I-N)
      COMMON /DEBUG/ IDEBUG
      DIMENSION SIG0(6),DSIG(6)
      REAL(KIND=16) F,ELAS,SIG0,DSIG
      REAL(KIND=16) SXX,SYY,SZZ,SXY,SYZ,SXZ,I1,I2,J2,J3,X,R,THETA
      REAL(KIND=16) RT,RC,RYIELD,RPEAK,RRES,PSIMAX,PSI,BETA,YST
      SXX = SIG0(1)+ELAS*DSIG(1)
      SYY = SIG0(2)+ELAS*DSIG(2)
      SZZ = SIG0(3)+ELAS*DSIG(3)
      SXY = SIG0(4)+ELAS*DSIG(4)
      SYZ = SIG0(5)+ELAS*DSIG(5)
      SXZ = SIG0(6)+ELAS*DSIG(6)
      I1 = SXX+SYY+SZZ
      I2 = (SXX*SYY+SYY*SZZ+SZZ*SXX)-SXY**2.Q0-SYZ**2.Q0-SXZ**2.Q0
      TEMP = I1/3.Q0
      J2 = 3.Q0*TEMP**2.Q0-I2
      J3 = (SXX-TEMP)*(SYY-TEMP)*(SZZ-TEMP)-((SXX-TEMP)*SYZ**2.Q0
     *      +SXY**2.Q0*(SZZ-TEMP)+SXZ**2.Q0*(SYY-TEMP))+2.Q0*SXY*SYZ*SXZ
      X = I1/QSQRT(3.Q0)/YST
      R = QSQRT(2.Q0*J2)/YST
      TEMP = 1.5Q0*QSQRT(3.Q0)*J3/(J2**(1.5Q0))
      IF (TEMP .LT. -1.) TEMP=-1.Q0
      IF (TEMP .GT. 1.) TEMP=1.Q0
      THETA = QACOS(TEMP)/3.Q0
      CALL PRIN(X,R,THETA,S1,S2,S3)
      IF (X .GE. 0.) THEN
            F = R
            GO TO 10
      ENDIF
C Below two expressions use fit for peak loading surface

      RT = -0.550272139045945Q0+QSQRT(-1.43439820150635Q0*X
     *          +0.0924044582071Q0*X**2.Q0+0.302799427010 2Q0)
      RC = -0.31959889174841Q0+QSQRT(-1.971053263759 4Q0*X
     *          +0.3102749931823 9Q0*X**2.Q0+0.12387506148076 9Q0)
      CALL RCALC(RT,RC,THETA,RPEAK)
      IF (PSI .LT. PSIMAX) THEN
C
C Below two expressions use fit for yield loading surface
            TEMPA = QSQRT(2.Q0/3.Q0)*0.45Q0*(1.Q0+QSQRT(3.Q0)/0.45Q0)
            TEMPB = QSQRT(2.Q0/3.Q0)*0.522Q0*(1.Q0+QSQRT(3.Q0)/1.044Q0)
            TEMPC = -X/(1.Q0-X)
            RT = TEMPC*TEMPB
            RC = TEMPC*TEMPA
            CALL RCALC(RT,RC,THETA,RYIELD)
            F = R-BETA*(RPEAK-RYIELD)-RYIELD
      ELSE IF (PSI .GT. PSIMAX) THEN
            RT = -0.741661501371667Q0+QSQRT(-0.9764196664448 9Q0*X
     *             +0.0565121387786362Q0*X**2.Q0+0.550061782616876 0Q0)
            RC = -0.474373208368885Q0+QSQRT(-1.341730049803430Q0*X
     *             +0.189756033577570Q0*X**2.Q0+0.22502994081818 9Q0)
C Parameters to have round residual surface
c            RT = RC
```

```
C
            CALL RCALC(RT,RC,THETA,RRES)
            RRES = QMIN1(RRES,RPEAK)
            F = R-BETA*(RPEAK-RRES)-RRES
      ELSE F = R-RPEAK
      ENDIF
   10 RETURN
      END

      SUBROUTINE FILLF(ID,R,F,AXLD,MX,MY,NNP,NEQ)
C Transfers nodal loads from R to F.
      IMPLICIT REAL(KIND=16) (A-H,O-Z)
      IMPLICIT INTEGER(KIND=8) (I-N)
      COMMON /DEBUG/ IDEBUG
      DIMENSION ID(NNP,3),R(NNP,3),F(NEQ)
      REAL(KIND=16) MX,MY
      DO 10 I=1,NNP
      DO 11 J=1,3
      IROW=ID(I,J)
      IF(IROW.EQ.0) GO TO 11
      F(IROW)=R(I,J)
   11 CONTINUE
   10 CONTINUE
      F(NEQ-2)=AXLD
      F(NEQ-1)=MX
      F(NEQ)=MY
      RETURN
      END

      SUBROUTINE IDGEN(ID,NNP,NTYPE)
C Generates vector ID
      IMPLICIT REAL(KIND=16) (A-H,O-Z)
      IMPLICIT INTEGER(KIND=8) (I-N)
      COMMON /DEBUG/ IDEBUG
      DIMENSION ID(NNP,3),ID1(3),NTYPE(NNP)
   10 READ(5,*) N,NE,NG,(ID1(J),J=1,3)
      IF(N.EQ.0) GO TO 40
      DO 20 J=1,3
      ID(N,J)=ID1(J)
   20 CONTINUE
      NB=N+NG
      IF((NG.LE.0).OR.(NB.GT.NE)) GO TO 10
      DO 30 I=NB,NE,NG
      DO 31 J=1,3
      ID(I,J)=ID1(J)
   31 CONTINUE
   30 CONTINUE
      GO TO 10
   40 DO 50 I=1,NNP
      IF (NTYPE(I) .EQ. 1) ID(I,3)=0
   50 CONTINUE
      END

      SUBROUTINE JACCOMP (COOR,LM,XJ,XI,P,DP,DET,NNP,NEN,IJK)
C Computes the Jacobian matrix, it's inverse, and it's determinant
      IMPLICIT REAL(KIND=16) (A-H,O-Z)
      IMPLICIT INTEGER(KIND=8) (I-N)
      COMMON /DEBUG/ IDEBUG
      DIMENSION COOR(NNP,3),LM(NEN),XJ(3,3),XI(3,3),P(4,NEN),DP(3,NEN)
C
      XJ=0.Q0
      DO 10 I=1,NEN
      J1 = LM(I)
      IF (J1.EQ.0) GO TO 10
      DO 11 J=1,3
         XJ(1,J) = XJ(1,J) + P(2,I)*COOR(J1,J)
         XJ(2,J) = XJ(2,J) + P(3,I)*COOR(J1,J)
         XJ(3,J) = XJ(3,J) + P(4,I)*COOR(J1,J)
   11 CONTINUE
   10 CONTINUE
C XJ is the Jacobian matrix at the current integration point.
C
      XI(1,1) =  XJ(2,2)*XJ(3,3) - XJ(3,2)*XJ(2,3)
      XI(2,2) =  XJ(1,1)*XJ(3,3) - XJ(3,1)*XJ(1,3)
      XI(3,3) =  XJ(1,1)*XJ(2,2) - XJ(2,1)*XJ(1,2)
      XI(1,2) = -XJ(1,2)*XJ(3,3) + XJ(3,2)*XJ(1,3)
```

```
      XI(2,1) = -XJ(2,1)*XJ(3,3) + XJ(3,1)*XJ(2,3)
      XI(1,3) =  XJ(1,2)*XJ(2,3) - XJ(2,2)*XJ(1,3)
      XI(3,1) =  XJ(2,1)*XJ(3,2) - XJ(3,1)*XJ(2,2)
      XI(2,3) = -XJ(1,1)*XJ(2,3) + XJ(2,1)*XJ(1,3)
      XI(3,2) = -XJ(1,1)*XJ(3,2) + XJ(3,1)*XJ(1,2)
      DET = XJ(1,1)*XI(1,1) + XJ(1,2)*XI(2,1) + XJ(1,3)*XI(3,1)
C DET is the determinant of XJ.
      IF (DET.LE.0.) WRITE(6,1000) IJK
      IF (DET.LE.0.) STOP
      DO 20 I=1,3
      DO 21 J=1,3
      XI(I,J) = XI(I,J)/DET
   21 CONTINUE
   20 CONTINUE
C XI is the inverse of XJ.
C
      DP = 0.Q0
      DO 30 I=1,3
      DO 31 J=1,NEN
      DP(I,J) = XI(I,1)*P(2,J) + XI(I,2)*P(3,J) + XI(I,3)*P(4,J)
   31 CONTINUE
   30 CONTINUE
C DP contains terms of the nodal displacement (pressure) to strain (pressure)
C    gradient) transformation matrix at the current integration point (X,Y,Z axes).
 1000 FORMAT (//,3X,'DETERMINANT OF JACOBIAN NON-POSITIVE IN ELEMENT ',
     1 I5,' EXECUTION STOPPED')
      RETURN
      END

      SUBROUTINE LCLCOR(COOR,LM,COORL,NNP,NEN)
C Transfers nodal coordinates for an element from COOR to COORL.
      IMPLICIT REAL(KIND=16) (A-H,O-Z)
      IMPLICIT INTEGER(KIND=8) (I-N)
      COMMON /DEBUG/ IDEBUG
      DIMENSION COOR(NNP,3),LM(NEN),COORL(NEN,3)
      DO 10 I=1,NEN
      LI=LM(I)
      DO 11 J=1,3
      IF(LI.EQ.0) COORL(I,J)=0.Q0
      IF(LI.NE.0) COORL(I,J)=COOR(LI,J)
   11 CONTINUE
   10 CONTINUE
      RETURN
      END

      SUBROUTINE LCLID(ID,LM,IDL,NEDN,NED,NEN,NEL,NEQ,NNP)
C Transfers equation numbers for all elements from ID to IDL.
C   For elements having half their nodes in the top plane
      IMPLICIT REAL(KIND=16) (A-H,O-Z)
      IMPLICIT INTEGER(KIND=8) (I-N)
      COMMON /DEBUG/ IDEBUG
      DIMENSION ID(NNP,3),LM(NEN,NEL),IDL(NED,NEL)
      DO 10 N=1,NEL
      DO 20 I=1,NEN/2
      LI=LM(I,N)
      DO 21 J=1,NEDN-1
      IF(LI.EQ.0) IDL((I-1)*(NEDN-1)+J,N)=0
      IF(LI.NE.0) IDL((I-1)*(NEDN-1)+J,N)=ID(LI,J)
   21 CONTINUE
   20 CONTINUE
      DO 30 I=NEN/2+1,NEN
      LI=LM(I,N)
      DO 31 J=1,NEDN
      IF(LI.EQ.0) IDL((I-1)*NEDN+J-NEN/2,N)=0
      IF(LI.NE.0) IDL((I-1)*NEDN+J-NEN/2,N)=ID(LI,J)
   31 CONTINUE
   30 CONTINUE
      DO 40 I=1,3
         IDL(NED-I+1,N)=NEQ-I+1
   40 CONTINUE
   10 CONTINUE
      RETURN
      END

      SUBROUTINE LCLID2(ID,LM,IDL,NNP,NEDN,NEN,NEL)
```

```
C Transfers equation numbers for all elements from ID to IDL.
C  For elements which do not lie in the top plane.
      IMPLICIT REAL(KIND=16) (A-H,O-Z)
      IMPLICIT INTEGER(KIND=8) (I-N)
      COMMON /DEBUG/ IDEBUG
      DIMENSION ID(NNP,6),LM(NEN,NEL),IDL(NEDN,NEN,NEL)
      DO 10 N=1,NEL
      DO 11 I=1,NEN
      LI=LM(I,N)
      DO 12 J=1,NEDN
      IF(LI.EQ.0) IDL(J,I,N)=0
      IF(LI.NE.0) IDL(J,I,N)=ID(LI,J)
   12 CONTINUE
   11 CONTINUE
   10 CONTINUE
      RETURN
      END

      SUBROUTINE LCLID3(ID,LM,IDL,NEDN,NED,NEN,NEL,NEQ,NNP)
C Transfers equation numbers for all elements from ID to IDL.
C   For elements having all their nodes in the top plane
      IMPLICIT REAL(KIND=16) (A-H,O-Z)
      IMPLICIT INTEGER(KIND=8) (I-N)
      COMMON /DEBUG/ IDEBUG
      DIMENSION ID(NNP,3),LM(NEN,NEL),IDL(NED,NEL)
      DO 10 N=1,NEL
      DO 20 I=1,NEN
      LI=LM(I,N)
      DO 21 J=1,NEDN-1
      IF(LI.EQ.0) IDL((I-1)*(NEDN-1)+J,N)=0
      IF(LI.NE.0) IDL((I-1)*(NEDN-1)+J,N)=ID(LI,J)
   21 CONTINUE
   20 CONTINUE
      DO 30 I=1,3
         IDL(NED-I+1,N)=NEQ-I+1
   30 CONTINUE
   10 CONTINUE
      RETURN
      END

      SUBROUTINE LCLX(X,COORL,IDL,XL,DX,NEDN,NEN,NED,NEQ,IFLAG)
C Transfers displacements for an element from X to XL.
C   For elements having half their nodes in the top plane
C   If IFLAG=0 calculates displacements assuming current coordinates
C   If IFLAG=1 calculates displacements assuming coordinates of previous time step
      IMPLICIT REAL(KIND=16) (A-H,O-Z)
      IMPLICIT INTEGER(KIND=8) (I-N)
      COMMON /DEBUG/ IDEBUG
      DIMENSION X(NEQ),COORL(NEN,3),XL(NEN,NEDN),IDL(NED),DX(NEQ)
      DO 10 I=1,NEN/2
         DO 11 J=1,NEDN-1
            IDI=IDL((I-1)*(NEDN-1)+J)
            IF(IDI.EQ.0) XL(I,J)=0.Q0
            IF(IDI.NE.0) XL(I,J)=X(IDI)
   11    CONTINUE
   10 CONTINUE
      DO 20 I=NEN/2+1,NEN
         DO 21 J=1,NEDN
            IDI=IDL((I-1)*NEDN+J-NEN/2)
            IF(IDI.EQ.0) XL(I,J)=0.Q0
            IF(IDI.NE.0) XL(I,J)=X(IDI)
   21    CONTINUE
   20 CONTINUE
      DO 30 I=1,NEN/2
         ID1=IDL((I-1)*(NEDN-1)+1)
         ID2=IDL((I-1)*(NEDN-1)+2)
         XL(I,3)=X(NEQ-2) + (COORL(I,2)-DX(ID2)*IFLAG) * X(NEQ-1)
     *      - (COORL(I,1)-DX(ID1)*IFLAG) * X(NEQ)
   30 CONTINUE
      RETURN
      END

      SUBROUTINE LCLX2(X,IDL,XL,NEDN,NEN,NED,NEQ)
C Transfers displacements for an element from X to XL.
C   For elements which do not lie in the top plane
```

```
      IMPLICIT REAL(KIND=16) (A-H,O-Z)
      IMPLICIT INTEGER(KIND=8) (I-N)
      COMMON /DEBUG/ IDEBUG
      DIMENSION X(NEQ),XL(NEN,NEDN),IDL(NEDN,NEN)
      DO 10 I=1,NEN
         DO 11 J=1,NEDN
            IDI=IDL(J,I)
            IF(IDI.EQ.0) XL(I,J)=0.Q0
            IF(IDI.NE.0) XL(I,J)=X(IDL(J,I))
   11    CONTINUE
   10 CONTINUE
      RETURN
      END

      SUBROUTINE LMGEN(LM,MAT,NEN,NEL)
C Generates vector MAT and matrix LM
      IMPLICIT REAL(KIND=16) (A-H,O-Z)
      IMPLICIT INTEGER(KIND=8) (I-N)
      COMMON /DEBUG/ IDEBUG
      DIMENSION LM(NEN,NEL),MAT(NEL),LM1(NEN)
   10 READ(5,*) N,NE,NG,MAT1,(LM1(I),I=1,NEN),LMG
      IF(N.EQ.0) RETURN
      MAT(N)=MAT1
      DO 20 I=1,NEN
      LM(I,N)=LM1(I)
   20 CONTINUE
      NB=N+NG
      IF((NG.LE.0).OR.(NB.GT.NE)) GO TO 10
      DO 30 J=NB,NE,NG
      MAT(J)=MAT1
      DO 31 I=1,NEN
      IF(LM1(I).EQ.0) LM(I,J)=0
      IF(LM1(I).NE.0) LM(I,J)=LM(I,J-NG)+LMG
   31 CONTINUE
   30 CONTINUE
      GO TO 10
      END

      SUBROUTINE MCANAL(COOR,ID,R,B,H,F,RTPT,DX,XT,XTPT,ELRT,ELRTPT,
     *   MOMENT,NTYPE,NSSTEPS,NHSTEPS,ZCOR,NITER)
      IMPLICIT REAL(KIND=16) (A-H,O-Z)
      IMPLICIT INTEGER(KIND=8) (I-N)
      COMMON /INFO1/ NNP,NEQ,MBAND,IGO
      COMMON /INFO2/ IEG,NEG1,NEG10,NEG11,NEG100,NEG110,MAXNEL1,
     * MAXNEL10,MAXNEL11,MAXNEL100,MAXNEL110,MAXNINT
      COMMON /ELPAR/ NPAR(8)
      COMMON /POINTS/ N1,N2,N3,N4,N5,N6,N7,N8,N9,N10,N11,N1101,N1102,
     * N1103,N1104,N12,N1201,N1202,N1203,N1204,N13
      COMMON /TOL/ TOLF,TOLM,NITMAX
      COMMON /DEBUG/ IDEBUG
      COMMON /MISC/ PSIMAX,KAPPA
      DIMENSION COOR(NNP,3),ID(NNP,3),R(NNP,3),B(N5-1),H(NEQ,MBAND),
     *   F(NEQ),RTPT(NEQ),DX(NEQ),XT(NEQ),XTPT(NEQ),
     *   ELRT(N12-N11),ELRTPT(N13-N12),NTYPE(NNP)
      REAL(KIND=16) MOMENT,KAPPA
      TIME=0.Q0
      DT=QABS(MOMENT/NHSTEPS)
C Calculate elastic stiffness matrix and factor
C Remove below code to iterate with tangent stiffness
C
      IGO=3
      H=0.Q0
      REWIND 7
      DO 10 IEG=1,NEG1
      READ(7) NEND,NPAR,(B(I),I=1,NEND)
      CALL TRUSSA(COOR,B,H)
   10 CONTINUE
      DO 20 IEG=1,NEG10
      READ(7) NEND,NPAR,(B(I),I=1,NEND)
      CALL TRUSSB(COOR,B,H)
   20 CONTINUE
      DO 30 IEG=1,NEG11
      READ(7) NEND,NPAR,(B(I),I=1,NEND)
      CALL TRUSSC(COOR,B,H)
   30 CONTINUE
      DO 40 IEG=1,NEG100
```

```
      READ(7) NEND,NPAR,(B(I),I=1,NEND)
      CALL SOLIDA(COOR,B,H)
   40 CONTINUE
      DO 50 IEG=1,NEG110
      READ(7) NEND,NPAR,(B(I),I=1,NEND)
      CALL SOLIDB(COOR,B,H)
   50 CONTINUE
c add large stiffness in two rotational DOFs
      H(NEQ-1,1)=H(NEQ-1,1)+1.0Q17
c      H(NEQ,1)=H(NEQ,1)+1.0Q17
c
      CALL BSOLVE(H,DX,NEQ,MBAND,1,0)
      DO 100 N=1,NHSTEPS
      TIME=TIME+DT
      FRAC=QABS(TIME/MOMENT)
C  Set previous time step displacement and element responses equal
C     to current time step values
C
      XT = XTPT
      ELRT = ELRTPT
      NITER=0
      DO 200 K=1,NITMAX
      DO 205 I=1,NEQ-2
         DX(I)=F(I)-RTPT(I)
  205 CONTINUE
      DO 206 I=NEQ-1,NEQ
         DX(I)=F(I)*FRAC-RTPT(I)
  206 CONTINUE
      DO 210 I=1,NNP
         DO 211 J=1,3
            IDI=ID(I,J)
            IF(IDI.EQ.0) GO TO 211
            IF(QABS(DX(IDI)).GT.TOLF) GO TO 1
  211    CONTINUE
  210 CONTINUE
      IF(QABS(DX(NEQ-2)).GT.TOLF) GO TO 1
      IF(QABS(DX(NEQ-1)).GT.TOLM) GO TO 1
      IF(QABS(DX(NEQ)).GT.TOLM) GO TO 1
      GO TO 2
    1 CALL BSOLVE(H,DX,NEQ,MBAND,0,1)
      DO 230 I=1,NNP
         DO 231 J=1,3
            IDI=ID(I,J)
            IF (IDI.EQ.0) GO TO 231
            COOR(I,J)=COOR(I,J) + DX(IDI)
  231    CONTINUE
  230 CONTINUE
      DO 240 I=1,NEQ
         XTPT(I) = XTPT(I) + DX(I)
         DX(I) = XTPT(I)- XT(I)
  240 CONTINUE
      DO 250 I=1,NNP
         IF (NTYPE(I).EQ.1) COOR(I,3)=ZCOR+XTPT(NEQ-2)
     *      +COOR(I,2)*XTPT(NEQ-1)-COOR(I,1)*XTPT(NEQ)
  250 CONTINUE
      RTPT=0.Q0
      IGO=4
      REWIND 7
      DO 260 IEG=1,NEG1
      READ(7) NEND,NPAR,(B(I),I=1,NEND)
      CALL TRUSSA(COOR,B,H)
  260 CONTINUE
      DO 261 IEG=1,NEG10
      READ(7) NEND,NPAR,(B(I),I=1,NEND)
      CALL TRUSSB(COOR,B,H)
  261 CONTINUE
      DO 262 IEG=1,NEG11
      READ(7) NEND,NPAR,(B(I),I=1,NEND)
      CALL TRUSSC(COOR,B,H)
  262 CONTINUE
      DO 263 IEG=1,NEG100
      READ(7) NEND,NPAR,(B(I),I=1,NEND)
      CALL SOLIDA(COOR,B,H)
  263 CONTINUE
      DO 264 IEG=1,NEG110
      READ(7) NEND,NPAR,(B(I),I=1,NEND)
```

```
      CALL SOLIDB(COOR,B,H)
  264 CONTINUE
c add large FORCE in two rotational DOFs
      RTPT(NEQ-1)=RTPT(NEQ-1)+1.0Q17*DX(NEQ-1)
      RTPT(NEQ)=RTPT(NEQ)+1.0Q17*DX(NEQ)
c
      NITER=K
  200 CONTINUE

    2 WRITE(6,2000) TIME,NITER
      WRITE(*,2000) TIME,NITER
 2000 FORMAT(1X,'MOMENT =',E12.5,5X,'NITER =',I5)
      IF (NITER .EQ. NITMAX) WRITE(6,2001) F(NEQ-1)*FRAC-RTPT(NEQ-1)
 2001 FORMAT(6X, 'MOMENT IMBALANCE = ',E12.5)
      WRITE(8,2005) XTPT(NEQ-1),F(NEQ-1)*FRAC-mrotx,XTPT(NEQ),
     *  F(NEQ)*FRAC-mroty
 2005 FORMAT(1X,6(1X,E19.12))
  100 CONTINUE
      WRITE(6,2003)
 2003 FORMAT(2(/),25X,'POST MOMENT ELEMENT RESPONSES',/)
      CALL PPICT(COOR,ID,B,H,XTPT,2,NTYPE,TIME)
      RETURN
      END

      SUBROUTINE PPICT(COOR,ID,B,C,XTPT,ND,NTYPE,TIME)
      IMPLICIT REAL(KIND=16) (A-H,O-Z)
      IMPLICIT INTEGER(KIND=8) (I-N)
      COMMON /INFO1/ NNP,NEQ,MBAND,IGO
      COMMON /INFO2/ IEG,NEG1,NEG10,NEG11,NEG100,NEG110,MAXNEL1,
     * MAXNEL10,MAXNEL11,MAXNEL100,MAXNEL110,MAXNINT
      COMMON /ELPAR/ NPAR(8)
      COMMON /POINTS/ N1,N2,N3,N4,N5,N6,N7,N8,N9,N10,N11,N1101,N1102,
     * N1103,N1104,N12,N1201,N1202,N1203,N1204,N13
      COMMON /DEBUG/ IDEBUG
      DIMENSION COOR(NNP,3),ID(NNP,3),B(N5-1),XTPT(NEQ),NTYPE(NNP)
      IGO=5
      REWIND 7
      DO 100 IEG=1,NEG1
      READ(7) NEND,NPAR,(B(I),I=1,NEND)
      CALL TRUSSA(COOR,B,C)
  100 CONTINUE
      DO 101 IEG=1,NEG10
      READ(7) NEND,NPAR,(B(I),I=1,NEND)
      CALL TRUSSB(COOR,B,C)
  101 CONTINUE
      DO 102 IEG=1,NEG11
      READ(7) NEND,NPAR,(B(I),I=1,NEND)
      CALL TRUSSC(COOR,B,C)
  102 CONTINUE
      DO 103 IEG=1,NEG100
      READ(7) NEND,NPAR,(B(I),I=1,NEND)
      CALL SOLIDA(COOR,B,C)
  103 CONTINUE
      DO 104 IEG=1,NEG110
      READ(7) NEND,NPAR,(B(I),I=1,NEND)
      CALL SOLIDB(COOR,B,C)
  104 CONTINUE
      IF (ND.EQ.1) RETURN
      WRITE(6,1000)
 1000 FORMAT(/,3X,'NODE',8X,'XDISP',8X,'YDISP',8X,'ZDISP')
      DO 200 I=1,NNP
      XDISP=0.Q0
      YDISP=0.Q0
      ZDISP=0.Q0
      ID1=ID(I,1)
      ID2=ID(I,2)
      ID3=ID(I,3)
      IF(ID1.NE.0) XDISP=XTPT(ID1)
      IF(ID2.NE.0) YDISP=XTPT(ID2)
      IF(ID3.NE.0 .AND. NTYPE(I).EQ.0) ZDISP=XTPT(ID3)
      IF(NTYPE(I).EQ.1) THEN
         ZDISP=XTPT(NEQ-2)+COOR(I,2)*XTPT(NEQ-1)-COOR(I,1)*XTPT(NEQ)
      ENDIF
      WRITE(6,2000) I,XDISP,YDISP,ZDISP
 2000 FORMAT(3X,I4,3(1X,E12.5))
  200 CONTINUE
```

```
      WRITE(6,2001)
 2001 FORMAT(/,3X,'TOP PLANE',/,9X,'ZDISP',2X,'CURVATURE-X',
     *  2X,'CURVATURE-Y')
      WRITE(6,2002) XTPT(NEQ-2),XTPT(NEQ-1),XTPT(NEQ)
 2002 FORMAT(1X,3(1X,E12.5),4(/))
      RETURN
      END

      SUBROUTINE PRIN(X,R,THETA,S1,S2,S3)
      IMPLICIT REAL(KIND=16) (A-H,O-Z)
      IMPLICIT INTEGER(KIND=8) (I-N)
      COMMON /DEBUG/ IDEBUG
      REAL(KIND=16) X,R,THETA,PI
C SIGM = sigma_mean = mean stress
C SQJ2 = square root of the invariant J2
C S1,S2,S3 = principal stresses with S1>S2>S3
      PI = 3.14159265358979323846264338327950
      SIGM = X/QSQRT(3.Q0)
      SQJ2 = R/QSQRT(2.Q0)
      TEMP = 2.Q0/QSQRT(3.Q0)*SQJ2
      TEMP2 = 2.Q0/3.Q0*PI
      S1 = SIGM + TEMP*QCOS(THETA)
      S2 = SIGM + TEMP*QCOS(THETA - TEMP2)
      S3 = SIGM + TEMP*QCOS(THETA + TEMP2)
      RETURN
      END

      SUBROUTINE RCALC(RT,RC,THETA,R)
      IMPLICIT REAL(KIND=16) (A-H,O-Z)
      IMPLICIT INTEGER(KIND=8) (I-N)
      COMMON /DEBUG/ IDEBUG
      REAL(KIND=16) R,RT,RC,THETA
      R=(2.Q0*RC*(RC**2.Q0-RT**2.Q0)*QCOS(THETA)+RC*(2.Q0*RT-RC)
     *      *QSQRT(4.Q0*(RC**2.Q0-RT**2.Q0)*(QCOS(THETA))**2.Q0
     *      +5.Q0*RT**2.Q0-4.Q0*RT*RC))/(4.Q0*(RC**2.Q0-RT**2.Q0)
     *      *(QCOS(THETA))**2.Q0+(RC-2.Q0*RT)**2.Q0)
      RETURN
      END

      SUBROUTINE READC(COOR,NNP,ZCOR,NTYPE)
C Generates and prints nodal coordinates.
      IMPLICIT REAL(KIND=16) (A-H,O-Z)
      IMPLICIT INTEGER(KIND=8) (I-N)
      COMMON /DEBUG/ IDEBUG
      DIMENSION COOR(NNP,3),NTYPE(NNP)
      CALL CORGEN(COOR,NNP,NTYPE)
      WRITE(6,1000)
 1000 FORMAT(4(/),1X,'NODAL COORDINATES',/,6X,'NODE',14X,'X',12X,'Y',
     * 12X,'Z',4X,'TYPE')
      DO 10 I=1,NNP
      WRITE(6,1001) I,(COOR(I,J),J=1,3),NTYPE(I)
      IF (COOR(I,3).GT.ZCOR) ZCOR=COOR(I,3)
   10 CONTINUE
 1001 FORMAT(6X,I4,2X,3(1X,E12.5),7X,I1)
      RETURN
      END


      SUBROUTINE READID(ID,COOR,NNP,NEQ,NTYPE)
C Generates the nodal boundary conditions.  Numbers the equations and
C prints the equation numbers.  Computes NEQ.
      IMPLICIT REAL(KIND=16) (A-H,O-Z)
      IMPLICIT INTEGER(KIND=8) (I-N)
      COMMON /DEBUG/ IDEBUG
      DIMENSION ID(NNP,3), COOR(NNP,3),NTYPE(NNP)
      ID=1
      CALL IDGEN(ID,NNP,NTYPE)
C Number the nonzero terms of ID from 1 to NEQ.  Set NEQ.
      NEQ=0
      DO 20 I=1,NNP
      DO 21 J=1,3
      IF(ID(I,J).EQ.0) GO TO 21
      NEQ=NEQ+1
      ID(I,J)=NEQ
   21 CONTINUE
   20 CONTINUE
```

```
C Add final 3 DOF's to account for top plane vertical displacement
C  and two rotations
      NEQ=NEQ+3
      WRITE(6,2000)
 2000 FORMAT(4(/),1X,'EQUATION NUMBERS',/,6X,'NODE',4X,'DOF 1',2X,
     * 'DOF 2',2X,'DOF 3')
      DO 30 I=1,NNP
      WRITE(6,3000) I,(ID(I,J),J=1,3)
   30 CONTINUE
 3000 FORMAT(6X,I4,2X,6(3X,I4))
      RETURN
      END

      SUBROUTINE READR(R,ID,NNP)
C Generates and prints nodal loads and specified displacements.
      IMPLICIT REAL(KIND=16) (A-H,O-Z)
      IMPLICIT INTEGER(KIND=8) (I-N)
      COMMON /DEBUG/ IDEBUG
      DIMENSION R(NNP,3)
      R=0.Q0
      CALL RGEN(R,ID,NNP)
      WRITE(6,1000)
 1000 FORMAT(4(/),1X,'SPECIFIED NODAL LOADS',/,6X,
     * 'NODE',10X,'DOF 1',8X,'DOF 2',8X,'DOF 3')
      DO 10 I=1,NNP
      WRITE(6,1001) I,(R(I,J),J=1,3)
 1001 FORMAT(6X,I4,2X,6(1X,E12.5))
   10 CONTINUE
      RETURN
      END

      SUBROUTINE RECT (P,R,S,T)
C RECT COMPUTES SHAPE FUNCTION VALUES AND DERIVATIVES FOR AN 8 NODE ELEMENT
C AT THE LOCAL COORDINATE LOCATION R,S,T.
      IMPLICIT REAL(KIND=16) (A-H,O-Z)
      IMPLICIT INTEGER(KIND=8) (I-N)
      COMMON /DEBUG/ IDEBUG
      DIMENSION P(4,8)
C
      DO 10 I=1,4
C I=1 FOR SHAPE FUNCTION VALUES; =2 FOR R DERIVATIVES; =3 FOR S DERIVATIVES;
C =4 FOR T DERIVATIVES.
      IF (I.EQ.1) GO TO 4
      IF (I.EQ.2) GO TO 5
      IF (I.EQ.3) GO TO 6
      IF (I.EQ.4) GO TO 7
    4 AR = 1.Q0 + R
      SR = 1.Q0 - R
      AS = 1.Q0 + S
      SS = 1.Q0 - S
      AT = 1.Q0 + T
      ST = 1.Q0 - T
      GO TO 8
    5 AR = 1.Q0
      SR = -1.Q0
      GO TO 8
    6 AR = 1.Q0 + R
      SR = 1.Q0 - R
      AS = 1.Q0
      SS = -1.Q0
      GO TO 8
    7 AS = 1.Q0 + S
      SS = 1.Q0 - S
      AT = 1.Q0
      ST = -1.Q0
    8 P(I,1) = 0.125Q0*SR*AS*AT
      P(I,2) = 0.125Q0*SR*SS*AT
      P(I,3) = 0.125Q0*AR*SS*AT
      P(I,4) = 0.125Q0*AR*AS*AT
      P(I,5) = 0.125Q0*SR*AS*ST
      P(I,6) = 0.125Q0*SR*SS*ST
      P(I,7) = 0.125Q0*AR*SS*ST
      P(I,8) = 0.125Q0*AR*AS*ST
   10 CONTINUE
      RETURN
      END
```

```
      SUBROUTINE RGEN(R,ID,NNP)
C Generates vector R
      IMPLICIT REAL(KIND=16) (A-H,O-Z)
      IMPLICIT INTEGER(KIND=8) (I-N)
      COMMON /DEBUG/ IDEBUG
      DIMENSION R(NNP,3),ID(NNP,3),R1(3)
   10 READ(5,*) N,NE,NG,(R1(J),J=1,3)
      IF(N.EQ.0) RETURN
      DO 20 J=1,3
      R(N,J)=R1(J)
C      IF(R1(J).NE.0 .AND. ID(N,J).EQ.1) THEN
C         WRITE(6,1000) N,J
C 1000    FORMAT(/,1X,'NODAL LOADS ARE IGNORED IN THIS PROGRAM.',/,
C     *      'NODE = ',I4,5X,'DOF = ',I1,/)
C         R(N,J)=0
C      ENDIF
   20 CONTINUE
      NB=N+NG
      IF((NG.LE.0).OR.(NB.GT.NE)) GO TO 10
      DO 30 I=NB,NE,NG
      DO 31 J=1,3
      R(I,J)=R1(J)
   31 CONTINUE
   30 CONTINUE
      GO TO 10
      END

      SUBROUTINE SOLIDA(A,B,C)
C Sets up storage for subroutine SOLID1
      IMPLICIT REAL(KIND=16) (A-H,O-Z)
      IMPLICIT INTEGER(KIND=8) (I-N)
      COMMON /DEBUG/ IDEBUG
      COMMON /INFO/ N5TEMP
      COMMON /INFO1/ NNP,NEQ,MBAND,IGO
      COMMON /INFO2/ IEG,NEG1,NEG10,NEG11,NEG100,NEG110,MAXNEL1,
     * MAXNEL10,MAXNEL11,MAXNEL100,MAXNEL110,MAXNINT
      COMMON /ELPAR/ NELTYP,NEL,NUMAT,NEN,NINT,NDUM(3)
      COMMON /POINTS/ N1,N2,N3,N4,N5,N6,N7,N8,N9,N10,N11,N1101,N1102,
     * N1103,N1104,N12,N1201,N1202,N1203,N1204,N13
      REAL(KIND=16), ALLOCATABLE, DIMENSION(:) :: BSUB
      DIMENSION A(N4-1),B(N5-1),C(N13-1)
C
      IF (MAXNEL100.LT.NEL) MAXNEL100=NEL
      IF (NINT.EQ.2) MAXNINT=8
      IF (NINT.EQ.3) MAXNINT=4
      N401=1   +NUMAT                     ! E
      N402=N401+NUMAT                     ! POISSON'S RATIO
      N403=N402+NUMAT                     ! f'c
      N404=N403+NEL                       ! MAT
      N405=N404+NEN*NEL                   ! LM
      N5TEMP=N405+(NEN*3-NEN/2+3)*NEL     ! IDL
      NEND=N5TEMP-1
      IF (IGO.EQ.1) THEN
         ALLOCATE(BSUB(NEND))
         BSUB=0.Q0
         CALL SOLID1(A(N1),A(N2),A(N3),BSUB(1),BSUB(N401),BSUB(N402),
     *      BSUB(N403),BSUB(N404),BSUB(N405),C(1),C(N6),C(N7),C(N8),
     *      C(N9),C(N10),C(N1103),C(N1203))
         WRITE(7) NEND,NELTYP,NEL,NUMAT,NEN,NINT,(NDUM(I),I=1,3),
     *      (BSUB(I),I=1,NEND)
         DEALLOCATE(BSUB)
      ELSE
         CALL SOLID1(A(N1),A(N2),A(N3),B(1),B(N401),B(N402),B(N403),
     *      B(N404),B(N405),C(1),C(N6),C(N7),C(N8),C(N9),C(N10),
     *      C(N1103),C(N1203))
      ENDIF
      RETURN
      END

      SUBROUTINE SOLID1(COOR,ID,R,E,PR,YST,MAT,LM,IDL,H,F,RTPT,DX,XT,
     *    XTPT,ELRT,ELRTPT)
C Performs computations for 6 or 8 node solid elements.
      IMPLICIT REAL(KIND=16) (A-H,O-Z)
      IMPLICIT INTEGER(KIND=8) (I-N)
      COMMON /INFO1/ NNP,NEQ,MBAND,IGO
```

```
      COMMON /INFO2/ IEG,NEG1,NEG10,NEG11,NEG100,NEG110,MAXNEL1,
     * MAXNEL10,MAXNEL11,MAXNEL100,MAXNEL110,MAXNINT
      COMMON /ELPAR/ NELTYP,NEL,NUMAT,NEN,NINT,NDUM(3)
      COMMON /DEBUG/ IDEBUG
      DIMENSION COOR(NNP,3),ID(NNP,3),R(NNP,3),E(NUMAT),PR(NUMAT),
     *   YST(NUMAT),MAT(NEL),LM(NEN,NEL),H(NEQ,MBAND),F(NEQ),RTPT(NEQ),
     *   IDL(NEN*3-NEN/2+3,NEL),DX(NEQ),XT(NEQ),XTPT(NEQ),
     *   ELRT(MAXNINT*(6*2+3)+1,MAXNEL100,NEG100),
     *   ELRTPT(MAXNINT*(6*2+3)+1,MAXNEL100,NEG100)
      DIMENSION HE(NEN*3-NEN/2+3,NEN*3-NEN/2+3),RE(NEN*3-NEN/2+3),
     *   COORL(NEN,3),XP(NEN*3),T(NEN*3,NEN*3-NEN/2+3),
     *   TT(NEN*3-NEN/2+3,NEN*3),TEMP(NEN*3,NEN*3-NEN/2+3),
     *   HEP(NEN*3,NEN*3),REP(NEN*3),XTL(NEN,3),XTPTL(NEN,3),
     *   DXL(NEN*3),DEPS(6),DSIG(6),DTT(6,6,MAXNINT,MAXNEL100,NEG100)
C
      NEDN=3
      NLED=NEN*NEDN
      NGED=NLED-NEN/2+3
C
      IF (NEN.NE.6 .AND. NEN.NE.8) THEN
         WRITE(6,1000)
 1000    FORMAT('Invalid number of nodes for solid element. ',
     *      'Program terminated.')
         STOP
      ENDIF
      IF (IGO.EQ.1) GOTO 1 ! Input element data
      IF (IGO.EQ.2) GOTO 2 ! Determine initial element volumes
      IF (IGO.EQ.3) GOTO 3 ! calculate the tangent stiffness, H
      IF (IGO.EQ.4) GOTO 4 ! calculate RTPT and ELRTPT
      IF (IGO.EQ.5) GOTO 5 ! Print the system picture
      WRITE(6,1001)
 1001 FORMAT('Fatal error in subroutine SOLID1. Invalid value for IGO.')
      STOP
C
C Read and print element data.  Calculate assembly arrays and half-
C    bandwidth
C
    1 WRITE(6,1002) IEG
 1002 FORMAT(//,2X,'TOP LAYER SOLID ELEMENT GROUP NUMBER',I4,10X)
      WRITE(6,1003) NEL,NUMAT,NEN,NINT
 1003 FORMAT(/,4X,'NEL =',I5,4X,'NUMAT =',I3,4X,'NEN = ',I2,
     *   4X,'NINT = ',I2)
      WRITE(6,1004)
 1004 FORMAT(/,4X,'MATERIAL/GEOMETRIC SETS',/,9X,'SET',14X,'E',
     *   4X,'POISSONS RATIO',10X,'YST')
      DO 100 I=1,NUMAT
      READ(5,*) E(I),PR(I),YST(I)
      WRITE(6,1005) I,E(I),PR(I),YST(I)
 1005 FORMAT(8X,I4,3X,E12.5,6X,E12.5,1X,E12.5)
  100 CONTINUE
C
C Generates vector MAT and matrix LM
      CALL LMGEN(LM,MAT,NEN,NEL)
      WRITE(6,1006)
 1006 FORMAT(/,4X,'MATERIAL SET NUMBERS AND CONNECTIVITY VECTORS',/,
     *   9X,'ELE',3X,'SET',5X,'NODE NUMBERS')
      DO 110 N=1,NEL
C
C Transfers nodal coordinates for an element from COOR to COORL.
      WRITE(6,1007) N,MAT(N),(LM(I,N),I=1,NEN)
 1007 FORMAT(8X,I4,2X,I4,5X,8(2X,I4))
  110 CONTINUE
C
C Transfers equation numbers for all elements from ID to IDL.
C   For elements having half their nodes in the top plane
      CALL LCLID(ID,LM,IDL,NEDN,NGED,NEN,NEL,NEQ,NNP)
C
C Calculate MBAND
      CALL BAND(IDL,NGED,NEL,MBAND)
      RETURN
C
C Set initial volumes for elements, initialize YFLAG, and
C    initialize DTT to the elastic stiffness matrix
C
    2 DTT = 0.Q0
```

```
C Add line below to iterate with the tangent stiffness
c      WRITE(9) DTT
       DO 200 N=1,NEL
       CALL SOLSTF(HEP,ELRT,ELRTPT,DXL,REP,COOR,LM(1,N),E(MAT(N)),
     *  PR(MAT(N)),YST(MAT(N)),NINT,N,NEN,0,MAXNEL100,NEG100)
 200   CONTINUE
       RETURN
C
C Calculate and assemble element matrices and vectors
C
    3  DO 300 N=1,NEL
c       if (idebug .eq. 1) write(11,3100) n,nel
c 3100 format('Calculating stiffness for solid element ',i5,' of ',i5)
       M=MAT(N)
       CALL SOLSTF(HEP,ELRT,ELRTPT,DXL,REP,COOR,LM(1,N),E(M),PR(M),
     *   YST(M),NINT,N,NEN,1,MAXNEL100,NEG100)
C
C Transfers nodal coordinates for an element from COOR to COORL.
       CALL LCLCOR(COOR,LM(1,N),COORL,NNP,NEN)
C
C Define transformation matrix
C
       T=0.Q0
       TT=0.Q0
       TEMP=0.Q0
          T(1,1)=1.Q0
          T(2,2)=1.Q0
          T(4,3)=1.Q0
          T(5,4)=1.Q0
          T(7,5)=1.Q0
          T(8,6)=1.Q0
          T(10,7)=1.Q0
          T(11,8)=1.Q0
       IF (NEN.EQ.6) THEN
          T(12,9)=1.Q0
          T(13,10)=1.Q0
          T(14,11)=1.Q0
          T(15,12)=1.Q0
          T(16,13)=1.Q0
          T(17,14)=1.Q0
          T(18,15)=1.Q0
          T(3,16)=1.Q0
          T(3,17)=COORL(1,2)
          T(3,18)=-COORL(1,1)
          T(6,16)=1.Q0
          T(6,17)=COORL(2,2)
          T(6,18)=-COORL(2,1)
          T(9,16)=1.Q0
          T(9,17)=COORL(3,2)
          T(9,18)=-COORL(3,1)
       ENDIF
       IF (NEN.EQ.8) THEN
          T(13,9)=1.Q0
          T(14,10)=1.Q0
          T(15,11)=1.Q0
          T(16,12)=1.Q0
          T(17,13)=1.Q0
          T(18,14)=1.Q0
          T(19,15)=1.Q0
          T(20,16)=1.Q0
          T(21,17)=1.Q0
          T(22,18)=1.Q0
          T(23,19)=1.Q0
          T(24,20)=1.Q0
          T(3,21)=1.Q0
          T(3,22)=COORL(1,2)
          T(3,23)=-COORL(1,1)
          T(6,21)=1.Q0
          T(6,22)=COORL(2,2)
          T(6,23)=-COORL(2,1)
          T(9,21)=1.Q0
          T(9,22)=COORL(3,2)
          T(9,23)=-COORL(3,1)
          T(12,21)=1.Q0
          T(12,22)=COORL(4,2)
```

```
         T(12,23)=-COORL(4,1)
      ENDIF
      DO 310 I=1,NEN*3
         DO 320 J=1,NEN*3-NEN/2+3
            TT(J,I)=T(I,J)
  320    CONTINUE
  310 CONTINUE
C
C Transform to global coordinates
C
      TEMP=MATMUL(HEP,T)
      HE=MATMUL(TT,TEMP)
      CALL ASSMBL(H,F,HE,RE,IDL(1,N),NEQ,MBAND,NGED,1,0)
  300 CONTINUE
      RETURN
C
    4 DO 400 N=1,NEL
      M=MAT(N)
C
C Transfers nodal coordinates for an element from COOR to COORL.
      CALL LCLCOR(COOR,LM(1,N),COORL,NNP,NEN)
C
C Transfer displacements for an element from X to XL.
C   For elements having half their nodes in the top plane
      CALL LCLX(XT,COORL,IDL(1,N),XTL,DX,NEDN,NEN,NGED,NEQ,1)
      CALL LCLX(XTPT,COORL,IDL(1,N),XTPTL,DX,NEDN,NEN,NGED,NEQ,0)
      DO 410 I=1,NEN
         DXL(I*3-2) = XTPTL(I,1)-XTL(I,1)
         DXL(I*3-1) = XTPTL(I,2)-XTL(I,2)
         DXL(I*3)   = XTPTL(I,3)-XTL(I,3)
  410 CONTINUE
      CALL SOLSTF(HEP,ELRT,ELRTPT,DXL,REP,COOR,LM(1,N),E(M),PR(M),
     *   YST(M),NINT,N,NEN,2,MAXNEL100,NEG100)
C
C Define transformation matrix
C
      T=0.Q0
      TT=0.Q0
      TEMP=0.Q0
         T(1,1)=1.Q0
         T(2,2)=1.Q0
         T(4,3)=1.Q0
         T(5,4)=1.Q0
         T(7,5)=1.Q0
         T(8,6)=1.Q0
         T(10,7)=1.Q0
         T(11,8)=1.Q0
      IF (NEN.EQ.6) THEN
         T(12,9)=1.Q0
         T(13,10)=1.Q0
         T(14,11)=1.Q0
         T(15,12)=1.Q0
         T(16,13)=1.Q0
         T(17,14)=1.Q0
         T(18,15)=1.Q0
         T(3,16)=1.Q0
         T(3,17)=COORL(1,2)
         T(3,18)=-COORL(1,1)
         T(6,16)=1.Q0
         T(6,17)=COORL(2,2)
         T(6,18)=-COORL(2,1)
         T(9,16)=1.Q0
         T(9,17)=COORL(3,2)
         T(9,18)=-COORL(3,1)
      ENDIF
      IF (NEN.EQ.8) THEN
         T(13,9)=1.Q0
         T(14,10)=1.Q0
         T(15,11)=1.Q0
         T(16,12)=1.Q0
         T(17,13)=1.Q0
         T(18,14)=1.Q0
         T(19,15)=1.Q0
         T(20,16)=1.Q0
         T(21,17)=1.Q0
         T(22,18)=1.Q0
```

```
         T(23,19)=1.Q0
         T(24,20)=1.Q0
         T(3,21)=1.Q0
         T(3,22)=COORL(1,2)
         T(3,23)=-COORL(1,1)
         T(6,21)=1.Q0
         T(6,22)=COORL(2,2)
         T(6,23)=-COORL(2,1)
         T(9,21)=1.Q0
         T(9,22)=COORL(3,2)
         T(9,23)=-COORL(3,1)
         T(12,21)=1.Q0
         T(12,22)=COORL(4,2)
         T(12,23)=-COORL(4,1)
      ENDIF
      DO 420 I=1,NEN*3
         DO 430 J=1,NEN*3-NEN/2+3
            TT(J,I)=T(I,J)
  430    CONTINUE
  420 CONTINUE
C
C Transform to global coordinates
C
      RE=MATMUL(TT,REP)
      CALL ASSMBL(H,RTPT,HE,RE,IDL(1,N),NEQ,MBAND,NGED,0,1)
  400 CONTINUE
      RETURN
C
    5 WRITE(6,5000) IEG
 5000 FORMAT(//,2X,'SOLID CONCRETE ELEMENT GROUP NUMBER ',I4)
      DO 500 N=1,NEL
      M=MAT(N)
      WRITE(6,5001) N,NEN,ELRTPT(MAXNINT*(6*2+3)+1,N,IEG)
 5001 FORMAT(/,4X,'ELEMENT NUMBER',I4,/,'NEN =',I2,/,'VOLUME = ',
     *   E12.5,//)
      IF (MAXNINT.EQ.1) THEN
         WRITE(6,5002)
 5002    FORMAT(2X,'STRESS VECTOR',4X,'STRAIN VECTOR')
         DO 510 I=1,6
         WRITE(6,5003) ELRTPT(I,N,IEG),ELRTPT(6+I,N,IEG)
 5003    FORMAT(3X,E12.5,5X,E12.5,5X,E12.5)
  510    CONTINUE
         WRITE(6,5004) ELRTPT(13,N,IEG)
 5004    FORMAT(/,2X,'PSI = ',E12.5)
      ENDIF
      IF (MAXNINT.EQ.4) THEN
         WRITE(6,5005)
 5005    FORMAT(4X,'STRESS VECTORS',/,6X,'INT PT 1',6X,'INT PT 2',6X,
     *      'INT PT 3',6X,'INT PT 4')
         DO 520 I=1,6
         WRITE(6,5006) ELRTPT(I,N,IEG),ELRTPT(6+I,N,IEG),
     *      ELRTPT(2*6+I,N,IEG),ELRTPT(3*6+I,N,IEG)
 5006    FORMAT(8(2X,E12.5))
  520    CONTINUE
         WRITE(6,5007)
 5007    FORMAT(//,4X,'STRAIN VECTORS',/,6X,'INT PT 1',6X,'INT PT 2',6X,
     *      'INT PT 3',6X,'INT PT 4')
         DO 530 I=1,6
         WRITE(6,5006) ELRTPT(4*6+I,N,IEG),ELRTPT(5*6+I,N,IEG),
     *      ELRTPT(6*6+I,N,IEG),ELRTPT(7*6+I,N,IEG)
  530    CONTINUE
        WRITE(6,5008)
 5008   FORMAT(//,4X,'FINAL VALUE OF PSI',/,6X,'INT PT 1',6X,'INT PT 2',
     *      6X,'INT PT 3',6X,'INT PT 4')
        WRITE(6,5006) ELRTPT(8*6+1,N,IEG),ELRTPT(8*6+2,N,IEG),
     *      ELRTPT(8*6+3,N,IEG),ELRTPT(8*6+4,N,IEG)
      ENDIF
      IF (MAXNINT.EQ.8) THEN
         WRITE(6,5009)
 5009    FORMAT(4X,'STRESS VECTORS',/,6X,'INT PT 1',6X,'INT PT 2',6X,
     *      'INT PT 3',6X,'INT PT 4',6X,'INT PT 5',6X,'INT PT 6',6X,
     *      'INT PT 7',6X,'INT PT 8')
         DO 540 I=1,6
         WRITE(6,5006) ELRTPT(I,N,IEG),ELRTPT(6+I,N,IEG),
     *      ELRTPT(2*6+I,N,IEG),ELRTPT(3*6+I,N,IEG),ELRTPT(4*6+I,N,IEG),
     *      ELRTPT(5*6+I,N,IEG),ELRTPT(6*6+I,N,IEG),ELRTPT(7*6+I,N,IEG)
```

```
  540    CONTINUE
         WRITE(6,5010)
 5010    FORMAT(//,4X,'STRAIN VECTORS',/,6X,'INT PT 1',6X,'INT PT 2',6X,
     *      'INT PT 3',6X,'INT PT 4',6X,'INT PT 5',6X,'INT PT 6',6X,
     *      'INT PT 7',6X,'INT PT 8')
         DO 550 I=1,6
         WRITE(6,5006) ELRTPT(8*6+I,N,IEG),ELRTPT(9*6+I,N,IEG),
     *      ELRTPT(10*6+I,N,IEG),ELRTPT(11*6+I,N,IEG),
     *      ELRTPT(12*6+I,N,IEG),ELRTPT(13*6+I,N,IEG),
     *      ELRTPT(14*6+I,N,IEG),ELRTPT(15*6+I,N,IEG)
  550    CONTINUE
        WRITE(6,5011)
 5011   FORMAT(//,4X,'FINAL VALUE OF PSI',/,6X,'INT PT 1',6X,'INT PT 2',
     *      6X,'INT PT 3',6X,'INT PT 4',6X,'INT PT 5',6X,'INT PT 6',6X,
     *      'INT PT 7',6X,'INT PT 8')
        WRITE(6,5006) ELRTPT(16*6+1,N,IEG),ELRTPT(16*6+2,N,IEG),
     *      ELRTPT(16*6+3,N,IEG),ELRTPT(16*6+4,N,IEG),
     *      ELRTPT(16*6+5,N,IEG),ELRTPT(16*6+6,N,IEG),
     *      ELRTPT(16*6+7,N,IEG),ELRTPT(16*6+8,N,IEG)
      ENDIF
  500 CONTINUE
      RETURN
      END

      SUBROUTINE SOLIDB(A,B,C)
C Sets up storage for subroutine SOLID10
      IMPLICIT REAL(KIND=16) (A-H,O-Z)
      IMPLICIT INTEGER(KIND=8) (I-N)
      COMMON /DEBUG/ IDEBUG
      COMMON /INFO/ N5TEMP
      COMMON /INFO1/ NNP,NEQ,MBAND,IGO
      COMMON /INFO2/ IEG,NEG1,NEG10,NEG11,NEG100,NEG110,MAXNEL1,
     * MAXNEL10,MAXNEL11,MAXNEL100,MAXNEL110,MAXNINT
      COMMON /ELPAR/ NELTYP,NEL,NUMAT,NEN,NINT,NDUM(3)
      COMMON /POINTS/ N1,N2,N3,N4,N5,N6,N7,N8,N9,N10,N11,N1101,N1102,
     * N1103,N1104,N12,N1201,N1202,N1203,N1204,N13
      REAL(KIND=16), ALLOCATABLE, DIMENSION(:) :: BSUB
      DIMENSION A(N4-1),B(N5-1),C(N13-1)
C
      IF (MAXNEL110.LT.NEL) MAXNEL110=NEL
      IF (NINT.EQ.2) MAXNINT=8
      IF (NINT.EQ.3) MAXNINT=4
      N401=1   +NUMAT                    ! E
      N402=N401+NUMAT                    ! POISSON'S RATIO
      N403=N402+NUMAT                    ! f'c
      N404=N403+NEL                      ! MAT
      N405=N404+NEN*NEL                  ! LM
      N5TEMP=N405+NEN*3*NEL              ! IDL
      NEND=N5TEMP-1
      IF (IGO.EQ.1) THEN
         ALLOCATE(BSUB(NEND))
         BSUB=0.Q0
         CALL SOLID10(A(N1),A(N2),A(N3),BSUB(1),BSUB(N401),BSUB(N402),
     *      BSUB(N403),BSUB(N404),BSUB(N405),C(1),C(N6),C(N7),C(N8),
     *      C(N9),C(N10),C(N1104),C(N1204))
         WRITE(7) NEND,NELTYP,NEL,NUMAT,NEN,NINT,(NDUM(I),I=1,3),
     *      (BSUB(I),I=1,NEND)
         DEALLOCATE(BSUB)
      ELSE
         CALL SOLID10(A(N1),A(N2),A(N3),B(1),B(N401),B(N402),B(N403),
     *      B(N404),B(N405),C(1),C(N6),C(N7),C(N8),C(N9),C(N10),
     *      C(N1104),C(N1204))
      ENDIF
      RETURN
      END

      SUBROUTINE SOLID10(COOR,ID,R,E,PR,YST,MAT,LM,IDL,H,F,RTPT,DX,XT,
     *    XTPT,ELRT,ELRTPT)
C Performs computations for 6 or 8 node interior solid elements.
      IMPLICIT REAL(KIND=16) (A-H,O-Z)
      IMPLICIT INTEGER(KIND=8) (I-N)
      COMMON /INFO1/ NNP,NEQ,MBAND,IGO
      COMMON /INFO2/ IEG,NEG1,NEG10,NEG11,NEG100,NEG110,MAXNEL1,
     * MAXNEL10,MAXNEL11,MAXNEL100,MAXNEL110,MAXNINT
      COMMON /ELPAR/ NELTYP,NEL,NUMAT,NEN,NINT,NDUM(3)
      COMMON /DEBUG/ IDEBUG
```

```
      DIMENSION COOR(NNP,3),ID(NNP,3),R(NNP,3),E(NUMAT),PR(NUMAT),
     *   YST(NUMAT),MAT(NEL),LM(NEN,NEL),H(NEQ,MBAND),F(NEQ),RTPT(NEQ),
     *   IDL(3,NEN,NEL),DX(NEQ),XT(NEQ),XTPT(NEQ),
     *   ELRT(MAXNINT*(6*2+3)+1,MAXNEL110,NEG110),
     *   ELRTPT(MAXNINT*(6*2+3)+1,MAXNEL110,NEG110)
      DIMENSION HE(NEN*3,NEN*3),RE(NEN*3),COORL(NEN,3),XP(NEN*3),
     *   XTL(NEN,3),XTPTL(NEN,3),DXL(NEN*3),DEPS(6),DSIG(6),
     *   DTT(6,6,MAXNINT,MAXNEL110,NEG110)
C
      NEDN=3
      NED=NEN*NEDN
C
      IF (NEN.NE.6 .AND. NEN.NE.8) THEN
         WRITE(6,1000)
 1000    FORMAT('Invalid number of nodes for interior solid element. ',
     *      'Program terminated.')
         STOP
      ENDIF
      IF (IGO.EQ.1) GOTO 1 ! Input element data
      IF (IGO.EQ.2) GOTO 2 ! Determine initial element volumes
      IF (IGO.EQ.3) GOTO 3 ! calculate the tangent stiffness, H
      IF (IGO.EQ.4) GOTO 4 ! calculate RTPT and ELRTPT
      IF (IGO.EQ.5) GOTO 5 ! Print the system picture
      WRITE(6,1001)
 1001 FORMAT('Fatal error in subroutine SOLID10. '
     *   'Invalid value for IGO.')
      STOP
C
C Read and print element data.  Calculate assembly arrays and half-
C    bandwidth
C
    1 WRITE(6,1002) IEG
 1002 FORMAT(//,2X,'INTERIOR SOLID ELEMENT GROUP NUMBER',I4,10X)
      WRITE(6,1003) NEL,NUMAT,NEN,NINT
 1003 FORMAT(/,4X,'NEL =',I5,4X,'NUMAT =',I3,4X,'NEN = ',I2,
     *   4X,'NINT = ',I2)
      WRITE(6,1004)
 1004 FORMAT(/,4X,'MATERIAL/GEOMETRIC SETS',/,9X,'SET',14X,'E',
     *   4X,'POISSONS RATIO',10X,'YST')
      DO 100 I=1,NUMAT
      READ(5,*) E(I),PR(I),YST(I)
      WRITE(6,1005) I,E(I),PR(I),YST(I)
 1005 FORMAT(8X,I4,3X,E12.5,6X,E12.5,1X,E12.5)
  100 CONTINUE
C
C Generates vector MAT and matrix LM
      CALL LMGEN(LM,MAT,NEN,NEL)
      WRITE(6,1006)
 1006 FORMAT(/,4X,'MATERIAL SET NUMBERS AND CONNECTIVITY VECTORS',/,
     *   9X,'ELE',3X,'SET',5X,'NODE NUMBERS')
      DO 110 N=1,NEL
C
C Transfers nodal coordinates for an element from COOR to COORL.
      WRITE(6,1007) N,MAT(N),(LM(I,N),I=1,NEN)
 1007 FORMAT(8X,I4,2X,I4,5X,8(2X,I4))
  110 CONTINUE
C
C Transfers equation numbers for all elements from ID to IDL.
C   For elements which do not lie in the top plane
      CALL LCLID2(ID,LM,IDL,NNP,NEDN,NEN,NEL)
C
C Calculate MBAND
      CALL BAND(IDL,NED,NEL,MBAND)
      RETURN
C
C Set initial volumes for elements, initialize YFLAG, and
C    initialize DTT to the elastic stiffness matrix
C
    2 DTT = 0.Q0
C Add line below to iterate with the tangent stiffness
c      WRITE(9) DTT
      DO 200 N=1,NEL
      CALL SOLSTF(HE,ELRT,ELRTPT,DXL,RE,COOR,LM(1,N),E(MAT(N)),
     *  PR(MAT(N)),YST(MAT(N)),NINT,N,NEN,0,MAXNEL110,NEG110)
 200  CONTINUE
```

```
      RETURN
C
C Calculate and assemble element matrices and vectors
C
    3 DO 300 N=1,NEL
c      if (idebug .eq. 1) write(11,3100) n,nel
c 3100 format('Calculating stiffness for solid element ',i5,' of ',i5)
      M=MAT(N)
      CALL SOLSTF(HE,ELRT,ELRTPT,DXL,RE,COOR,LM(1,N),E(M),PR(M),
     *   YST(M),NINT,N,NEN,1,MAXNEL110,NEG110)
      CALL ASSMBL(H,F,HE,RE,IDL(1,1,N),NEQ,MBAND,NED,1,0)
  300 CONTINUE
      RETURN
C
    4 DO 400 N=1,NEL
c      if (idebug .eq. 1) write(11,4100) n,nel
c 4100 format('Calculating forces for interior solid element ',i5,
c     *  ' of ',i5)
      M=MAT(N)
C
C Transfers nodal coordinates for an element from COOR to COORL.
      CALL LCLCOR(COOR,LM(1,N),COORL,NNP,NEN)
C
C Transfer displacements for an element from X to XL.
C   For elements which do not lie in the top plane
      CALL LCLX2(XT,IDL(1,1,N),XTL,NEDN,NEN,NED,NEQ)
      CALL LCLX2(XTPT,IDL(1,1,N),XTPTL,NEDN,NEN,NED,NEQ)
      DO 410 I=1,NEN
         DXL(I*3-2) = XTPTL(I,1)-XTL(I,1)
         DXL(I*3-1) = XTPTL(I,2)-XTL(I,2)
         DXL(I*3)   = XTPTL(I,3)-XTL(I,3)
  410 CONTINUE
      CALL SOLSTF(HE,ELRT,ELRTPT,DXL,RE,COOR,LM(1,N),E(M),PR(M),
     *   YST(M),NINT,N,NEN,2,MAXNEL110,NEG110)
      CALL ASSMBL(H,RTPT,HE,RE,IDL(1,1,N),NEQ,MBAND,NED,0,1)
  400 CONTINUE
      RETURN
C
    5 WRITE(6,5000) IEG
 5000 FORMAT(//,2X,'INTERIOR SOLID CONCRETE ELEMENT GROUP NUMBER ',I4)
      DO 500 N=1,NEL
      M=MAT(N)
      WRITE(6,5001) N,NEN,ELRTPT(MAXNINT*(6*2+3)+1,N,IEG)
 5001 FORMAT(/,4X,'ELEMENT NUMBER',I4,/,'NEN =',I2,/,'VOLUME = ',
     *   E12.5,//)
      IF (MAXNINT.EQ.1) THEN
         WRITE(6,5002)
 5002    FORMAT(2X,'STRESS VECTOR',4X,'STRAIN VECTOR')
         DO 510 I=1,6
         WRITE(6,5003) ELRTPT(I,N,IEG),ELRTPT(6+I,N,IEG)
 5003    FORMAT(3X,E12.5,5X,E12.5,5X,E12.5)
  510    CONTINUE
         WRITE(6,5004) ELRTPT(13,N,IEG)
 5004    FORMAT(/,2X,'PSI = ',E12.5)
      ENDIF
      IF (MAXNINT.EQ.4) THEN
         WRITE(6,5005)
 5005    FORMAT(4X,'STRESS VECTORS',/,6X,'INT PT 1',6X,'INT PT 2',6X,
     *      'INT PT 3',6X,'INT PT 4')
         DO 520 I=1,6
         WRITE(6,5006) ELRTPT(I,N,IEG),ELRTPT(6+I,N,IEG),
     *      ELRTPT(2*6+I,N,IEG),ELRTPT(3*6+I,N,IEG)
 5006    FORMAT(8(2X,E12.5))
  520    CONTINUE
         WRITE(6,5007)
 5007    FORMAT(//,4X,'STRAIN VECTORS',/,6X,'INT PT 1',6X,'INT PT 2',6X,
     *      'INT PT 3',6X,'INT PT 4')
         DO 530 I=1,6
         WRITE(6,5006) ELRTPT(4*6+I,N,IEG),ELRTPT(5*6+I,N,IEG),
     *      ELRTPT(6*6+I,N,IEG),ELRTPT(7*6+I,N,IEG)
  530    CONTINUE
        WRITE(6,5008)
 5008   FORMAT(//,4X,'FINAL VALUE OF PSI',/,6X,'INT PT 1',6X,'INT PT 2',
     *      6X,'INT PT 3',6X,'INT PT 4')
        WRITE(6,5006) ELRTPT(8*6+1,N,IEG),ELRTPT(8*6+2,N,IEG),
```

```
     *      ELRTPT(8*6+3,N,IEG),ELRTPT(8*6+4,N,IEG)
            ENDIF
            IF (MAXNINT.EQ.8) THEN
               WRITE(6,5009)
 5009       FORMAT(4X,'STRESS VECTORS',/,6X,'INT PT 1',6X,'INT PT 2',6X,
     *      'INT PT 3',6X,'INT PT 4',6X,'INT PT 5',6X,'INT PT 6',6X,
     *      'INT PT 7',6X,'INT PT 8')
               DO 540 I=1,6
               WRITE(6,5006) ELRTPT(I,N,IEG),ELRTPT(6+I,N,IEG),
     *      ELRTPT(2*6+I,N,IEG),ELRTPT(3*6+I,N,IEG),ELRTPT(4*6+I,N,IEG),
     *      ELRTPT(5*6+I,N,IEG),ELRTPT(6*6+I,N,IEG),ELRTPT(7*6+I,N,IEG)
  540       CONTINUE
               WRITE(6,5010)
 5010       FORMAT(//,4X,'STRAIN VECTORS',/,6X,'INT PT 1',6X,'INT PT 2',6X,
     *      'INT PT 3',6X,'INT PT 4',6X,'INT PT 5',6X,'INT PT 6',6X,
     *      'INT PT 7',6X,'INT PT 8')
               DO 550 I=1,6
               WRITE(6,5006) ELRTPT(8*6+I,N,IEG),ELRTPT(9*6+I,N,IEG),
     *      ELRTPT(10*6+I,N,IEG),ELRTPT(11*6+I,N,IEG),
     *      ELRTPT(12*6+I,N,IEG),ELRTPT(13*6+I,N,IEG),
     *      ELRTPT(14*6+I,N,IEG),ELRTPT(15*6+I,N,IEG)
  550       CONTINUE
              WRITE(6,5011)
 5011       FORMAT(//,4X,'FINAL VALUE OF PSI',/,6X,'INT PT 1',6X,'INT PT 2',
     *      6X,'INT PT 3',6X,'INT PT 4',6X,'INT PT 5',6X,'INT PT 6',6X,
     *      'INT PT 7',6X,'INT PT 8')
              WRITE(6,5006) ELRTPT(16*6+1,N,IEG),ELRTPT(16*6+2,N,IEG),
     *      ELRTPT(16*6+3,N,IEG),ELRTPT(16*6+4,N,IEG),
     *      ELRTPT(16*6+5,N,IEG),ELRTPT(16*6+6,N,IEG),
     *      ELRTPT(16*6+7,N,IEG),ELRTPT(16*6+8,N,IEG)
            ENDIF
  500 CONTINUE
            RETURN
            END

            SUBROUTINE SOLSTF(STF,ELRT,ELRTPT,DXL,REP,COOR,LM,EE,PR,YST,
     *   NINT,IJK,NEN,IFLAG,MAXNEL,NEG)
            IMPLICIT REAL(KIND=16) (A-H,O-Z)
            IMPLICIT INTEGER(KIND=8) (I-N)
            COMMON /INFO1/ NNP,NEQ,MBAND,IGO
            COMMON /INFO2/ IEG,NEG1,NEG10,NEG11,NEG100,NEG110,MAXNEL1,
     * MAXNEL10,MAXNEL11,MAXNEL100,MAXNEL110,MAXNINT
            COMMON /DEBUG/ IDEBUG
            COMMON /TOL/ TOLF,TOLM,NITMAX
            COMMON /MISC/ PSIMAX,KAPPA
            DIMENSION STF(NEN*3,NEN*3),DXL(NEN*3),REP(NEN*3),COOR(NNP,3),
     * ELRT(MAXNINT*(6*2+3)+1,MAXNEL,NEG),LM(NEN),
     * ELRTPT(MAXNINT*(6*2+3)+1,MAXNEL,NEG)
            DIMENSION RI(25),SI(25),TI(25),WI(25),BT(NEN*3,6),B(6,NEN*3),
     * P(4,NEN),DP(3,NEN),XJ(3,3),XI(3,3),D(6,6),DT(6,6),DINV(6,6),
     * DEPS(6),DSIG(6),DF(6,1),DQ(6,1),DFT(1,6),TEMP(6,1),DEPSP(6),
     * DTT(6,6,MAXNINT,MAXNEL,NEG)
            REAL(KIND=16) PSIMAX,KAPPA,PSI,PHI,F,ELAS,DEN,X,R,THETA,J2,J3,
     * NDEPSP,TEMPPSI,D1,DET,VOL,PF
            INTEGER(KIND=8) FINT

C
C If IFLAG = 0 -> Calculate the element volume and initialize YFLAG.
C If IFLAG = 1 -> Calculate the stiffness matrix
C If IFLAG = 2 -> Calculate the stress, strain, and force vector
C
C RI,SI,TI AND WI CONTAIN THE R,S,T COORDINATES AND WEIGHTS, RESPECTIVELY, OF
C THE INTEGRATION POINTS FOR THE TRIANGULAR PRISM AND RECTANGULAR PRISM
C ELEMENTS IN THE FOLLOWING ORDER:  1 POINT (TRIANGULAR PRISM, NINT=1),
C 1 POINT (RECTANGULAR PRISM, NINT=1), 8 PTS (TP,4x2), 8 PTS (RP,2x2x2),
C 3 PTS (TP,3x1), 4 PTS (RP,2x2x1)
C
            RI(1) = 1.Q0/3.Q0
            RI(2) = 0.Q0
            RI(3) = RI(1)
            RI(4) = RI(1)
            RI(5) = 0.6Q0
            RI(6) = 0.2Q0
            RI(7) = 0.2Q0
            RI(8) = 0.6Q0
            RI(9) = 0.2Q0
```

```
      RI(10) = 0.2Q0
      RI(11) = -1.Q0/QSQRT(3.Q0)
      RI(12) = RI(11)
      RI(13) = 1.Q0/QSQRT(3.Q0)
      RI(14) = RI(13)
      RI(15) = RI(11)
      RI(16) = RI(11)
      RI(17) = RI(13)
      RI(18) = RI(13)
      RI(19) = 0.5Q0
      RI(20) = 0.Q0
      RI(21) = RI(19)
      RI(22) = RI(11)
      RI(23) = RI(11)
      RI(24) = RI(13)
      RI(25) = RI(13)
C
      SI(1) = RI(1)
      SI(2) = 0.Q0
      SI(3) = RI(1)
      SI(4) = RI(1)
      SI(5) = 0.2Q0
      SI(6) = 0.6Q0
      SI(7) = 0.2Q0
      SI(8) = 0.2Q0
      SI(9) = 0.6Q0
      SI(10) = 0.2Q0
      SI(11) = RI(13)
      SI(12) = RI(11)
      SI(13) = RI(11)
      SI(14) = RI(13)
      SI(15) = RI(13)
      SI(16) = RI(11)
      SI(17) = RI(11)
      SI(18) = RI(13)
      SI(19) = RI(19)
      SI(20) = RI(19)
      SI(21) = 0.Q0
      SI(22) = RI(13)
      SI(23) = RI(11)
      SI(24) = RI(11)
      SI(25) = RI(13)
C
      TI = 0.Q0
      TI(3) = RI(13)
      TI(4) = RI(11)
      TI(5) = RI(13)
      TI(6) = RI(13)
      TI(7) = RI(13)
      TI(8) = RI(11)
      TI(9) = RI(11)
      TI(10) = RI(11)
      TI(11) = RI(13)
      TI(12) = RI(13)
      TI(13) = RI(13)
      TI(14) = RI(13)
      TI(15) = RI(11)
      TI(16) = RI(11)
      TI(17) = RI(11)
      TI(18) = RI(11)
C
      WI = 1.Q0
      WI(2) = 8.Q0
      WI(3) = -9.Q0/32.Q0
      WI(4) = WI(3)
      WI(5) = 25.Q0/96.Q0
      WI(6) = WI(5)
      WI(7) = WI(5)
      WI(8) = WI(5)
      WI(9) = WI(5)
      WI(10) = WI(5)
      WI(19) = RI(1)
      WI(20) = RI(1)
      WI(21) = RI(1)
      WI(22) = 2.Q0
      WI(23) = WI(22)
```

```
      WI(24) = WI(22)
      WI(25) = WI(22)
C
C D is the elastic stiffness matrix
C
      C11 = EE*(1.Q0-PR)/((1.Q0+PR)*(1.Q0-2.Q0*PR))
      C22 = EE*PR/((1.Q0+PR)*(1.Q0-2.Q0*PR))
      C33 = EE/(2.Q0*(1.Q0+PR))
      D = 0.Q0
      D(1,1) = C11
      D(1,2) = C22
      D(1,3) = C22
      D(2,1) = C22
      D(2,2) = C11
      D(2,3) = C22
      D(3,1) = C22
      D(3,2) = C22
      D(3,3) = C11
      D(4,4) = C33
      D(5,5) = C33
      D(6,6) = C33
C
C Calculate the inverse of the elastic material matrix
      C4 = (C11**2.Q0+C11*C22-2.Q0*C22**2.Q0)
      C1 = (C11+C22)/C4
      C2 = -C22/C4
      C3 = 1.Q0/C33
      DINV = 0.Q0
      DINV(1,1) = C1
      DINV(1,2) = C2
      DINV(1,3) = C2
      DINV(2,1) = C2
      DINV(2,2) = C1
      DINV(2,3) = C2
      DINV(3,1) = C2
      DINV(3,2) = C2
      DINV(3,3) = C1
      DINV(4,4) = C3
      DINV(5,5) = C3
      DINV(6,6) = C3
C
C
      IF (IFLAG.EQ.0) VOL = 0.Q0
      IF (IFLAG.EQ.1) STF = 0.Q0
      IF (IFLAG.EQ.2) REP = 0.Q0
C
C  NINT=INTEGRATION SCHEME: 1 OR 2 POINT.
      IF ((NEN.EQ.6).AND.(NINT.EQ.1)) L1=1
      IF ((NEN.EQ.6).AND.(NINT.EQ.1)) L2=1
      IF ((NEN.EQ.8).AND.(NINT.EQ.1)) L1=2
      IF ((NEN.EQ.8).AND.(NINT.EQ.1)) L2=2
      IF ((NEN.EQ.6).AND.(NINT.EQ.2)) L1=3
      IF ((NEN.EQ.6).AND.(NINT.EQ.2)) L2=10
      IF ((NEN.EQ.8).AND.(NINT.EQ.2)) L1=11
      IF ((NEN.EQ.8).AND.(NINT.EQ.2)) L2=18
      IF ((NEN.EQ.6).AND.(NINT.EQ.3)) L1=19
      IF ((NEN.EQ.6).AND.(NINT.EQ.3)) L2=21
      IF ((NEN.EQ.8).AND.(NINT.EQ.3)) L1=22
      IF ((NEN.EQ.8).AND.(NINT.EQ.3)) L2=25
C  L1 TO L2 ARE THE GAUSS QUADRATURE POINT LOCATIONS.
C
      DO 100 L=L1,L2
C  L LOOPS OVER THE INTEGRATION POINTS
      P = 0.Q0
      IF (NEN.EQ.6) CALL TRI (P,RI(L),SI(L),TI(L))
      IF (NEN.EQ.8) CALL RECT (P,RI(L),SI(L),TI(L))
      CALL JACCOMP(COOR,LM,XJ,XI,P,DP,DET,NNP,NEN,IJK)
      D1 = WI(L)*DET
      ELRTPT(MAXNINT*(6*2+2)+L-L1+1,IJK,IEG) = D1
      IF (IFLAG.EQ.0) THEN
            VOL = VOL + D1
            GO TO 100
      ENDIF
      B = 0.Q0
      DO 130 J=1,NEN
      J1 = 3*(J-1) + 1
```

```
      J2 = J1 + 1
      J3 = J1 + 2
      B(1,J1) = DP(1,J)
      B(2,J2) = DP(2,J)
      B(3,J3) = DP(3,J)
      B(4,J1) = DP(2,J)
      B(4,J2) = DP(1,J)
      B(5,J2) = DP(3,J)
      B(5,J3) = DP(2,J)
      B(6,J1) = DP(3,J)
      B(6,J3) = DP(1,J)
  130 CONTINUE
C B IS THE NODAL DISPLACEMENT TO STRAIN (X,Y,Z AXES) TRANSFORMATION MATRIX AT
C THE CURRENT INTEGRATION POINT.
C
      BT = 0.Q0
      DO 140 I=1,6
         DO 150 J=1,NEN*3
            BT(J,I)=B(I,J)
  150    CONTINUE
  140 CONTINUE
C BT IS THE TRANSPOSE OF B AT THE CURRENT INTEGRATION POINT.
C
      IF (IFLAG.EQ.1) THEN
         B = MATMUL(D,B)
         STF = STF + D1*MATMUL(BT,B)
         GO TO 100
      ENDIF
C THE CONTRIBUTION TO THE PORTIONS OF THE ROWS OF THE STIFFNESS MATRIX
C AT THE CURRENT INTEGRATION POINT HAS BEEN ADDED INTO STF.
C
C Define constants here
      OMEGA = 0.5Q0
      PHI = 0.5Q0
      ALPHA = 10.0Q0 !0.6Q1*5.Q3/YST
      GAMMA = 1.72Q0
      PSIMAX = 0.6Q-3
      FINT = 10
      TOLLS = 0.000001Q0
      KAPPA=0.6q0
      PSI = ELRT(MAXNINT*12+L-L1+1,IJK,IEG)
C
C Below two lines require beta as a function of psi
      BETA = ((PSI/PSIMAX)**KAPPA)
     *      *QEXP(1.Q0-((PSI/PSIMAX)**KAPPA))
      DBETADPSI = KAPPA*QEXP(1.Q0-((PSI/PSIMAX)**KAPPA))
     *  * (1.Q0 - ((PSI/PSIMAX)**KAPPA))
     *  / (PSIMAX*((PSI/PSIMAX)**(1.q0-KAPPA)))
C
C CE 108 pg. 9-19 step a. Calculate strain increment
      DEPS = MATMUL(B,DXL)
C
C CE 108 pg. 9-19 step b. Calculate stress increment assuming elastic behavior
      DSIG = MATMUL(D,DEPS)
C
C CE 108 pg. 9-19 step c. Compute current stress/strain state
      DO 200 I=1,6
         NSIG = (L-L1+1)*6-6+I
         NEPS = MAXNINT*6+(L-L1+1)*6-6+I
         ELRTPT(NSIG,IJK,IEG) = ELRT(NSIG,IJK,IEG)+DSIG(I)
         ELRTPT(NEPS,IJK,IEG) = ELRT(NEPS,IJK,IEG)+DEPS(I)
  200 CONTINUE
C
C Add this line to remove plasticity
c      GO TO 1
C
C CE 108 pg. 9-19 step d. Compute F and determine stress state
      CALL FCALC(F,1.Q0,ELRT((L-L1+1)*6-5,IJK,IEG),DSIG,
     *      X,R,THETA,PSI,PSIMAX,BETA,YST)
C
C If the current stress is below the loading surface and was not previously cracked/crushed
C  set loading type to elastic and tangent matrix to the elastic matrix
      IF (F .LT. 0.Q0 .AND.
     *     ELRT(MAXNINT*13+L-L1+1,IJK,IEG) .GE. -5.Q0) THEN
          ELRTPT(MAXNINT*13+L-L1+1,IJK,IEG) = 0.Q0
```

```
C            IF (F .GT. -TOLLS) ELRTPT(MAXNINT*13+L-L1+1,IJK,IEG) = 10.Q0
             DT = D
             GO TO 1
      ENDIF
C
C If in axial tension or previously in axial tension, apply plane stress
       IF (ELRTPT((L-L1+1)*6-3,IJK,IEG) .GT. 0.Q0 .OR.
     *  (ELRT(MAXNINT*13+L-L1+1,IJK,IEG) .LE. -5.Q0 .AND.
     *  ELRT(MAXNINT*13+L-L1+1,IJK,IEG) .GE. -15.Q0)) THEN
             ELRTPT((L-L1+1)*6-3,IJK,IEG) = 0.Q0
             ELRTPT((L-L1+1)*6-1,IJK,IEG) = 0.Q0
             ELRTPT((L-L1+1)*6,IJK,IEG) = 0.Q0
             ELRTPT(MAXNINT*13+L-L1+1,IJK,IEG) = -10.Q0
             C11 = EE/(1.Q0-PR**2.Q0)
             C22 = C22*PR
             C33 = C11*(1.Q0-PR)/2.Q0
             DT = 0.Q0
             DT(1,1) = C11
             DT(1,2) = C22
             DT(2,1) = C22
             DT(2,2) = C11
             DT(4,4) = C33
             DSIG = MATMUL(DT,DEPS)
             ELRTPT((L-L1+1)*6-5,IJK,IEG) = ELRT((L-L1+1)*6-5,IJK,IEG)
     *           +DSIG(1)
             ELRTPT((L-L1+1)*6-4,IJK,IEG) = ELRT((L-L1+1)*6-4,IJK,IEG)
     *           +DSIG(2)
             ELRTPT((L-L1+1)*6-2,IJK,IEG) = ELRT((L-L1+1)*6-2,IJK,IEG)
     *           +DSIG(4)
             GO TO 1
         ENDIF
C
C If concrete was previously in net tension => completely cracked so zero out stress
         IF (ELRT(MAXNINT*13+L-L1+1,IJK,IEG) .LT. -15.Q0) THEN
             DO 205 J=1,6
                NSIG = (L-L1+1)*6-6+J
                ELRTPT(NSIG,IJK,IEG) = 0.Q0
  205        CONTINUE
             ELRTPT(MAXNINT*13+L-L1+1,IJK,IEG) = -20.Q0
             DT=0.Q0
             GO TO 1
         ENDIF
C
C If you are at the origin and have not previously loaded the specimen at all,
C   assign elastic loading and skip plasticity.
       IF (F .EQ. 0.Q0 .AND.
      *  ELRT(MAXNINT*13+L-L1+1,IJK,IEG) .GE. -1.Q0) THEN
             IF (X .EQ. 0.Q0 .AND.
     *         ELRT(MAXNINT*13+L-L1+1,IJK,IEG) .LT. 5.Q0
     *           .AND. ELRT(MAXNINT*12+L-L1+1,IJK,IEG) .EQ. 0.Q0) THEN
                ELRTPT(MAXNINT*13+L-L1+1,IJK,IEG) = 0.Q0
                DT = D
                GO TO 1
             ENDIF
       ENDIF
C
C CE 108 pg. 9-19 step e.  Determine ELAS based on previous stress state
       IF (ELRT(MAXNINT*13+L-L1+1,IJK,IEG) .GT. 5.Q0 .OR.
     *       ELRT(MAXNINT*13+L-L1+1,IJK,IEG) .LT. -5.Q0) THEN
             ELAS = 0.Q0
       ELSE
             CALL ZBRENT(0.Q0,1.Q0,ELAS,TOLLS,
     *           ELRT((L-L1+1)*6-5,IJK,IEG),DSIG,X,R,THETA,PSI,
     *           PSIMAX,BETA,YST)
             ELRTPT(MAXNINT*13+L-L1+1,IJK,IEG) = 10.Q0
             IF (ELAS .EQ. 0.Q0 .AND.
     *         ELRT(MAXNINT*12+L-L1+1,IJK,IEG) .EQ. 0.Q0) THEN
                CALL FCALC(PF,0.Q0,ELRT((L-L1+1)*6-5,IJK,IEG),DSIG,
     *               X,R,THETA,PSI,PSIMAX,BETA,YST)
                IF (PF .LE. 0.Q0) THEN
                    ELAS = 1.Q0
                    ELRTPT(MAXNINT*13+L-L1+1,IJK,IEG) = 0.Q0
                ENDIF
             ENDIF
       ENDIF
```

```
C
C CE 108 pg. 9-19 step f.  Push current stress state to current loading surface
      DO 210 I=1,6
         NSIG = (L-L1+1)*6-6+I
         ELRTPT(NSIG,IJK,IEG) = ELRT(NSIG,IJK,IEG)+ELAS*DSIG(I)
  210 CONTINUE
      IF (ELAS .EQ. 1.) THEN
        ELRTPT(MAXNINT*13+L-L1+1,IJK,IEG) = 10.Q0
        GO TO 1
      ENDIF
      DEPS = DEPS*(1.Q0-ELAS)
      DEPS = DEPS/FINT
C
C CE 108 pg. 9-19 step g. Calculate elastic and plastic stress
      DO 220 I=1,FINT
            CALL FCALC(F,0.Q0,ELRTPT((L-L1+1)*6-5,IJK,IEG),DSIG,
     *          X,R,THETA,PSI,PSIMAX,BETA,YST)
C If in tension, zero out stresses and set flag
            IF (X .GT. 0.) THEN
                DO 230 J=1,6
                    NSIG = (L-L1+1)*6-6+J
                    ELRTPT(NSIG,IJK,IEG) = 0.Q0
  230           CONTINUE
                    ELRTPT(MAXNINT*13+L-L1+1,IJK,IEG)= -20.Q0
                GO TO 1
            ENDIF
            NSIG = (L-L1+1)*6-6
            SXX = ELRTPT(NSIG+1,IJK,IEG)
            SYY = ELRTPT(NSIG+2,IJK,IEG)
            SZZ = ELRTPT(NSIG+3,IJK,IEG)
            SXY = ELRTPT(NSIG+4,IJK,IEG)
            SYZ = ELRTPT(NSIG+5,IJK,IEG)
            SXZ = ELRTPT(NSIG+6,IJK,IEG)
            CALL DFCALC(DF,DQ,X,R,THETA,PSIMAX,ALPHA,GAMMA,ETA,PHI,
     *          OMEGA,PSI,BETA,DBETADPSI,YST,DFDEP,SXX,SYY,SZZ,SXY,SYZ,
     *          SXZ)
            DO 240 J=1,6
                DFT(1,J) = DF(J,1)
  240       CONTINUE
C
C Calculate DT = the tangent material matrix
C   DEN is the denominator (scalar) of the DT expression
            TEMP = 0.Q0
            TEMP(4,1) = DQ(4,1)
            TEMP(5,1) = DQ(5,1)
            TEMP(6,1) = DQ(6,1)
            DEN = 0.Q0
            DO 250 J=1,6
                DEN = DEN + (TEMP(J,1)+DQ(J,1))*DQ(J,1)
  250       CONTINUE
            DEN = 2.Q0/3.Q0*DEN
            DEN = QSQRT(DEN)
            DEN = -DFDEP*DEN
            TEMP = 0.Q0
            TEMP = MATMUL(D,DQ)
            DO 260 J=1,6
                DEN = DEN + DF(J,1)*TEMP(J,1)
  260       CONTINUE
            DFT = MATMUL(DFT,D)
            DT = MATMUL(DQ,DFT)
            DT = MATMUL(D,DT)
            DT = DT/DEN
            DT = D - DT
            IF (DEN .EQ. 0.) THEN
                IF (X .EQ. 0. .AND.
     *            ELRT(MAXNINT*12+L-L1+1,IJK,IEG) .EQ. 0.Q0) THEN
                    DT = D
                    ELRTPT(MAXNINT*13+L-L1+1,IJK,IEG)=0.Q0
                ELSE
                    DT = 0.Q0
                    ELRTPT(MAXNINT*13+L-L1+1,IJK,IEG)=10.Q0
                END IF
            END IF
C  Compute the new stress for the given DT and increment in strain
            DSIG = MATMUL(DT,DEPS)
```

```
            DO 280 K = 1,6
                TEMP(K,1) = DSIG(K)
  280       CONTINUE
            IF (DEN .EQ. 0. .AND. X .EQ. 0.) THEN
                DSIG = FINT*DSIG
                DO 290 J=1,6
                    NSIG = (L-L1+1)*6-6+J
                    ELRTPT(NSIG,IJK,IEG) = ELRTPT(NSIG,IJK,IEG)+DSIG(J)
  290           CONTINUE
                GO TO 1
            ENDIF
C
C Set up iteration to return stress state to yield surface
            DO 300 J=1,NITMAX
                DEPSP = DEPS - MATMUL(DINV,DSIG)
                NDEPSP = 0.Q0
                DO 320 K=1,3
                    NDEPSP = NDEPSP + DEPSP(K)*DEPSP(K)
  320           CONTINUE
                DO 330 K=4,6
                    NDEPSP = NDEPSP + 2.Q0 * DEPSP(K)*DEPSP(K)
  330           CONTINUE
                NDEPSP = QSQRT(2.Q0/3.Q0*NDEPSP)
                AVEX = X/2.Q0 + (ELRTPT((L-L1+1)*6-5,IJK,IEG)
     *              + ELRTPT((L-L1+1)*6-4,IJK,IEG) + DSIG(1)
     *              + ELRTPT((L-L1+1)*6-3,IJK,IEG) + DSIG(2)
     *              + DSIG(3))/QSQRT(3.Q0)/YST/2.Q0
C
C Vary Psi relationship here
C
               IF (PSI .GE. PSIMAX) THEN
                    TEMPPSI = PSI + NDEPSP/
     *                  (PHI + ALPHA * (QABS(AVEX))**GAMMA)
               ELSE
                    TEMPPSI = PSI + NDEPSP/
     *                  (PHI + ALPHA * (QABS(AVEX))**GAMMA)
               ENDIF
C
C Below two lines require beta as a function of psi
                BETA = ((TEMPPSI/PSIMAX)**KAPPA)
     *              *QEXP(1.Q0-((TEMPPSI/PSIMAX)**KAPPA))
                DBETADPSI = KAPPA*QEXP(1.Q0-((TEMPPSI/PSIMAX)**KAPPA))
     *              * (1.Q0 - ((TEMPPSI/PSIMAX)**KAPPA))
     *              / (PSIMAX*((TEMPPSI/PSIMAX)**(1.q0-KAPPA)))
                IF (ELRT(MAXNINT*13+L-L1+1,IJK,IEG) .EQ. 0.) GO TO 2
                IF (PSI .LT. 1Q-5) GO TO 2
                CALL FCALC(F,1.Q0,ELRTPT((L-L1+1)*6-5,IJK,IEG),
     *              DSIG,X,R,THETA,TEMPPSI,PSIMAX,BETA,YST)
C If in axial compression but still net tension the concrete
C   must be cracked/crushed so zero out stresses
                IF (X .GT. 0.Q0) THEN
                    if (elrtpt((l-l1+1)*6-3,ijk,ieg) .le. 0.q0) then
                        DO 340 K=1,6
                            NSIG = (L-L1+1)*6-6+K
                            ELRTPT(NSIG,IJK,IEG) = 0.Q0
  340                   CONTINUE
                        ELRTPT(MAXNINT*13+L-L1+1,IJK,IEG) = -20.Q0
                        DT=0.Q0
                       GO TO 1
                    ELSE IF (ELRT(MAXNINT*13+L-L1+1,IJK,IEG)
     *                  .EQ. -10.Q0
     *             .OR. ELRTPT((L-L1+1)*6-3,IJK,IEG) .GT. 0.Q0) THEN
                        ELRTPT((L-L1+1)*6-3,IJK,IEG) = 0.Q0
                        ELRTPT((L-L1+1)*6-1,IJK,IEG) = 0.Q0
                        ELRTPT((L-L1+1)*6,IJK,IEG) = 0.Q0
                        ELRTPT(MAXNINT*13+L-L1+1,IJK,IEG) = -10.Q0
                        C11 = EE/(1.Q0-PR**2.Q0)
                        C22 = C22*PR
                        C33 = C11*(1.Q0-PR)/2.Q0
                        DT = 0.Q0
                        DT(1,1) = C11
                        DT(1,2) = C22
                        DT(2,1) = C22
                        DT(2,2) = C11
                        DT(4,4) = C33
```

```
                        DSIG = MATMUL(DT,DEPS)
                        ELRTPT((L-L1+1)*6-5,IJK,IEG) =
     *                      ELRT((L-L1+1)*6-5,IJK,IEG)+DSIG(1)
                        ELRTPT((L-L1+1)*6-4,IJK,IEG) =
     *                      ELRT((L-L1+1)*6-4,IJK,IEG)+DSIG(2)
                        ELRTPT((L-L1+1)*6-2,IJK,IEG) =
     *                      ELRT((L-L1+1)*6-2,IJK,IEG)+DSIG(4)
                        GO TO 1
                    ENDIF
                 ENDIF
                IF (J .EQ. NITMAX .AND. QABS(F) .GT. QABS(TEMPF)) THEN
                    DO 310 K = 1,6
                        DSIG(K) = TEMP(K,1)
  310               CONTINUE
                ENDIF
                IF (QABS(F) .LT. TOLLS) GO TO 2
                IF (J .EQ. NITMAX) GO TO 2
                IF (J .EQ. 1) TEMPF = F
                CALL DFCALC(DF,DQ,X,R,THETA,PSIMAX,ALPHA,GAMMA,ETA,PHI,
     *              OMEGA,TEMPPSI,BETA,DBETADPSI,YST,DFDEP,SXX,SYY,SZZ,
     *              SXY,SYZ,SXZ)
c                CALL DFCALC2(DF,ELRTPT((L-L1+1)*6-5,IJK,IEG),
c     *              TEMPPSI,PSIMAX,BETA,YST)
                DEN = 0.Q0
                DO 350 K = 1,6
                    DEN = DEN + DF(K,1)*DF(K,1)
  350           CONTINUE
                IF (DEN .EQ. 0.) GO TO 2
                DO 360 K = 1,6
                    DSIG(K) = DSIG(K) - DF(K,1)*F/DEN
  360           CONTINUE
  300       CONTINUE
    2       PSI = TEMPPSI
            DO 390 J=1,6
                NSIG = (L-L1+1)*6-6+J
                ELRTPT(NSIG,IJK,IEG) = ELRTPT(NSIG,IJK,IEG)+DSIG(J)
  390       CONTINUE
  220 CONTINUE
      ELRTPT(MAXNINT*12+L-L1+1,IJK,IEG) = PSI
      ELRTPT(MAXNINT*13+L-L1+1,IJK,IEG) = 10.Q0
C
C CE 108 pg. 9-19 step h. Add contribution to force vector
    1 DO 400 I=1,6
         DO 410 J=1,NEN*3
            NSIG=(L-L1+1)*6-6+I
            REP(J) = REP(J)+D1*BT(J,I)*ELRTPT(NSIG,IJK,IEG)
  410    CONTINUE
  400 CONTINUE
  100 CONTINUE
      IF (IFLAG.EQ.0) ELRTPT(MAXNINT*(6*2+3)+1,IJK,IEG)=VOL
      RETURN
      END


      SUBROUTINE STANAL(COOR,ID,R,B,H,F,RTPT,DX,XT,XTPT,ELRT,ELRTPT,
     *   AXLD,NTYPE,NSSTEPS,NHSTEPS,ZCOR,NITER)
      IMPLICIT REAL(KIND=16) (A-H,O-Z)
      IMPLICIT INTEGER(KIND=8) (I-N)
      COMMON /INFO1/ NNP,NEQ,MBAND,IGO
      COMMON /INFO2/ IEG,NEG1,NEG10,NEG11,NEG100,NEG110,MAXNEL1,
     * MAXNEL10,MAXNEL11,MAXNEL100,MAXNEL110,MAXNINT
      COMMON /ELPAR/ NPAR(8)
      COMMON /POINTS/ N1,N2,N3,N4,N5,N6,N7,N8,N9,N10,N11,N1101,N1102,
     * N1103,N1104,N12,N1201,N1202,N1203,N1204,N13
      COMMON /TOL/ TOLF,TOLM,NITMAX
      COMMON /DEBUG/ IDEBUG
      COMMON /MISC/ PSIMAX,KAPPA
      DIMENSION COOR(NNP,3),ID(NNP,3),R(NNP,3),B(N5-1),H(NEQ,MBAND),
     *   F(NEQ),RTPT(NEQ),DX(NEQ),XT(NEQ),XTPT(NEQ),
     *   ELRT(N12-N11),ELRTPT(N13-N12),NTYPE(NNP)
      REAL(KIND=16) KAPPA
      TIME=0.Q0
      DT=QABS(AXLD/NSSTEPS)
C Calculate elastic stiffness matrix and factor
C Remove below code to iterate with tangent stiffness
C
```

```
      IGO=3
      H=0.Q0
      REWIND 7
      DO 10 IEG=1,NEG1
      READ(7) NEND,NPAR,(B(I),I=1,NEND)
      CALL TRUSSA(COOR,B,H)
   10 CONTINUE
      DO 20 IEG=1,NEG10
      READ(7) NEND,NPAR,(B(I),I=1,NEND)
      CALL TRUSSB(COOR,B,H)
   20 CONTINUE
      DO 30 IEG=1,NEG11
      READ(7) NEND,NPAR,(B(I),I=1,NEND)
      CALL TRUSSC(COOR,B,H)
   30 CONTINUE
      DO 40 IEG=1,NEG100
      READ(7) NEND,NPAR,(B(I),I=1,NEND)
      CALL SOLIDA(COOR,B,H)
   40 CONTINUE
      DO 50 IEG=1,NEG110
      READ(7) NEND,NPAR,(B(I),I=1,NEND)
      CALL SOLIDB(COOR,B,H)
   50 CONTINUE
c add large stiffness in two rotational DOFs
      H(NEQ-1,1)=H(NEQ-1,1)+1.0Q17
      H(NEQ,1)=H(NEQ,1)+1.0Q17
c
      CALL BSOLVE(H,DX,NEQ,MBAND,1,0)
      DO 100 N=1,NSSTEPS
      TIME=TIME+DT
      FRAC=QABS(TIME/AXLD)
      IF (N .LT. NHSTEPS) THEN
        FRAC2=(N*1.Q0)/(NHSTEPS*1.Q0)
      ELSE
        FRAC2 = 1.Q0
      ENDIF
      IF(AXLD.EQ.0.) FRAC=1.Q0
C  Set previous time step displacement and element responses equal
C     to current time step values
C
      XT = XTPT
      ELRT = ELRTPT
      NITER=0
      DO 200 K=1,NITMAX
      DO 205 I=1,NEQ-3
         DX(I)=F(I)*FRAC2-RTPT(I)
  205 CONTINUE
c removed P-delta moment (should be to NEQ, not to NEQ-2)
      DO 210 I=NEQ-2,NEQ-1
         DX(I)=F(I)*FRAC-RTPT(I)
  210 CONTINUE
        DO 220 I=1,NNP
         DO 221 J=1,3
            IDI=ID(I,J)
            IF(IDI.EQ.0) GO TO 221
            IF(QABS(DX(IDI)).GT.TOLF) GO TO 1
  221    CONTINUE
  220 CONTINUE
      IF(QABS(DX(NEQ-2)).GT.TOLF) GO TO 1
      IF(QABS(DX(NEQ-1)).GT.TOLM) GO TO 1
      IF(QABS(DX(NEQ)).GT.TOLM) GO TO 1
      GO TO 2
    1 CALL BSOLVE(H,DX,NEQ,MBAND,0,1)
      DO 240 I=1,NNP
         DO 241 J=1,3
            IDI=ID(I,J)
            IF (IDI.EQ.0) GO TO 241
            COOR(I,J)=COOR(I,J) + DX(IDI)
  241    CONTINUE
  240 CONTINUE
      DO 250 I=1,NEQ
         XTPT(I) = XTPT(I) + DX(I)
         DX(I) = XTPT(I)- XT(I)
  250 CONTINUE
      DO 260 I=1,NNP
         IF (NTYPE(I).EQ.1) COOR(I,3)=ZCOR+XTPT(NEQ-2)
```

```
     *      +COOR(I,2)*XTPT(NEQ-1)-COOR(I,1)*XTPT(NEQ)
  260 CONTINUE
      RTPT=0.Q0
      IGO=4
      REWIND 7
      DO 270 IEG=1,NEG1
      READ(7) NEND,NPAR,(B(I),I=1,NEND)
      CALL TRUSSA(COOR,B,H)
  270 CONTINUE
      DO 271 IEG=1,NEG10
      READ(7) NEND,NPAR,(B(I),I=1,NEND)
      CALL TRUSSB(COOR,B,H)
  271 CONTINUE
      DO 272 IEG=1,NEG11
      READ(7) NEND,NPAR,(B(I),I=1,NEND)
      CALL TRUSSC(COOR,B,H)
  272 CONTINUE
      DO 273 IEG=1,NEG100
      READ(7) NEND,NPAR,(B(I),I=1,NEND)
      CALL SOLIDA(COOR,B,H)
  273 CONTINUE
      DO 274 IEG=1,NEG110
      READ(7) NEND,NPAR,(B(I),I=1,NEND)
      CALL SOLIDB(COOR,B,H)
  274 CONTINUE
c add large FORCE in two rotational DOFs
      RTPT(NEQ-1)=RTPT(NEQ-1)+1.0Q17*DX(NEQ-1)
      RTPT(NEQ)=RTPT(NEQ)+1.0Q17*DX(NEQ)
      NITER=K
  200 CONTINUE
    2 WRITE(6,2000) TIME,NITER
      WRITE(*,2000) TIME,NITER
 2000 FORMAT(1X,'LOAD =',E12.5,5X,'NITER =',I5)
      IF (NITER .EQ. NITMAX) WRITE(6,2001) F(NEQ-2)*FRAC-RTPT(NEQ-2)
 2001 FORMAT(6X, 'AXIAL LOAD IMBALANCE = ',E12.5)
  100 CONTINUE
      WRITE(6,2003)
 2003 FORMAT(2(/),25X,'POST AXIAL LOAD ELEMENT RESPONSES',/)
      CALL PPICT(COOR,ID,B,H,XTPT,2,NTYPE,TIME)
      RETURN
      END

      SUBROUTINE TOP(NTYPE,LM,NEN,NEL,NNP)
C Create array NTYPE which denotes top/bottom plane for each node
C  **Only call from element subroutines which have nodes in the top plane**
      IMPLICIT REAL(KIND=16) (A-H,O-Z)
      IMPLICIT INTEGER(KIND=8) (I-N)
      COMMON /DEBUG/ IDEBUG
      DIMENSION NTYPE(NNP),LM(NEN,NEL)
      DO 10 I=1,NEL
         DO 20 J=1,NEN/2
            NODE=LM(J,I)
            NTYPE(NODE)=1
   20    CONTINUE
   10 CONTINUE
      RETURN
      END

      SUBROUTINE TRI (P,CX,CY,T)
C TRI COMPUTES SHAPE FUNCTION VALUES AND DERIVATIVES FOR A 6 NODE ELEMENT
C AT THE LOCAL COORDINATE LOCATION CX,CY,T.
      IMPLICIT REAL(KIND=16) (A-H,O-Z)
      IMPLICIT INTEGER(KIND=8) (I-N)
      COMMON /DEBUG/ IDEBUG
      DIMENSION P(4,8)
C
      DO 10 I=1,4
C I=1 FOR SHAPE FUNCTION VALUES; =2 FOR CX DERIVATIVES; =3 FOR CY DERIVATIVES;
C =4 FOR T DERIVATIVES.
      IF (I.EQ.1) GO TO 4
      IF (I.EQ.2) GO TO 5
      IF (I.EQ.3) GO TO 6
      IF (I.EQ.4) GO TO 7
    4 R = CX
      S = CY
      V = 1.Q0 - R - S
```

```
      AT = 1.Q0 + T
      ST = 1.Q0 - T
      GO TO 8
    5 R = 1.Q0
      S = 0.Q0
      V = -1.Q0
      GO TO 8
    6 R = 0.Q0
      S = 1.Q0
      GO TO 8
    7 R = CX
      S = CY
      V = 1.Q0 - R - S
      AT = 1.Q0
      ST = -1.Q0
    8 P(I,1) = 0.5Q0*R*AT
      P(I,2) = 0.5Q0*S*AT
      P(I,3) = 0.5Q0*V*AT
      P(I,4) = 0.5Q0*R*ST
      P(I,5) = 0.5Q0*S*ST
      P(I,6) = 0.5Q0*V*ST
   10 CONTINUE
      RETURN
      END


      SUBROUTINE TRUSSA(A,B,C)
C Sets up storage for subroutine TRUSS1.
      IMPLICIT REAL(KIND=16) (A-H,O-Z)
      IMPLICIT INTEGER(KIND=8) (I-N)
      REAL(KIND=16), ALLOCATABLE, DIMENSION(:) :: BSUB
      COMMON /INFO/ N5TEMP
      COMMON /INFO1/ NNP,NEQ,MBAND,IGO
      COMMON /INFO2/ IEG,NEG1,NEG10,NEG11,NEG100,NEG110,MAXNEL1,
     * MAXNEL10,MAXNEL11,MAXNEL100,MAXNEL110,MAXNINT
      COMMON /ELPAR/ NELTYP,NEL,NUMAT,NDUM(5)
      COMMON /POINTS/ N1,N2,N3,N4,N5,N6,N7,N8,N9,N10,N11,N1101,N1102,
     * N1103,N1104,N12,N1201,N1202,N1203,N1204,N13
      COMMON /DEBUG/ IDEBUG
      DIMENSION A(N4-1),B(N5-1),C(N13-1)
C
      IF (MAXNEL1.LT.NEL) MAXNEL1=NEL
      N401=1   +NUMAT    ! E
      N402=N401+NUMAT    ! AREA
      N403=N402+NUMAT    ! YST
      N404=N403+NUMAT    ! YRT
      N405=N404+NEL      ! MAT
      N406=N405+2*NEL    ! LM
      N407=N406+8*NEL    ! IDL
      N5TEMP=N407+NEL    ! ALEN
      NEND=N5TEMP-1
      IF (IGO.EQ.1) THEN
          ALLOCATE(BSUB(NEND))
          BSUB=0.Q0
          CALL TRUSS1(A(N1),A(N2),A(N3),BSUB(1),BSUB(N401),BSUB(N402),
     *       BSUB(N403),BSUB(N404),BSUB(N405),BSUB(N406),BSUB(N407),
     *       C(1),C(N6),C(N7),C(N8),C(N9),C(N10),C(N11),C(N12))
          WRITE(7) NEND,NELTYP,NEL,NUMAT,(NDUM(I),I=1,5),
     *       (BSUB(I),I=1,NEND)
          DEALLOCATE(BSUB)
      ELSE
          CALL TRUSS1(A(N1),A(N2),A(N3),B(1),B(N401),B(N402),B(N403),
     *      B(N404),B(N405),B(N406),B(N407),C(1),C(N6),C(N7),
     *      C(N8),C(N9),C(N10),C(N11),C(N12))
      ENDIF
      RETURN
      END

      SUBROUTINE TRUSS1(COOR,ID,R,E,AREA,YST,YRT,MAT,LM,IDL,ALEN,
     *     H,F,RTPT,DX,XT,XTPT,ELRT,ELRTPT)
C Performs computations for longitudinal truss elements.
      IMPLICIT REAL(KIND=16) (A-H,O-Z)
      IMPLICIT INTEGER(KIND=8) (I-N)
      COMMON /INFO1/ NNP,NEQ,MBAND,IGO
      COMMON /INFO2/ IEG,NEG1,NEG10,NEG11,NEG100,NEG110,MAXNEL1,
     * MAXNEL10,MAXNEL11,MAXNEL100,MAXNEL110,MAXNINT
```

```
      COMMON /ELPAR/ NELTYP,NEL,NUMAT,NDUM(5)
      COMMON /DEBUG/ IDEBUG
      DIMENSION COOR(NNP,3),ID(NNP,3),R(NNP,3),E(NUMAT),
     * AREA(NUMAT),YST(NUMAT),YRT(NUMAT),MAT(NEL),LM(2,NEL),
     * IDL(8,NEL),ALEN(NEL),ELRT(4,MAXNEL1,NEG1),ELRTPT(4,MAXNEL1,NEG1),
     * H(NEQ,MBAND),F(NEQ),RTPT(NEQ),DX(NEQ),XT(NEQ),XTPT(NEQ)
      DIMENSION HEP(6,6),REP(6),COORL(2,3),XP(6),T(6,8),TT(8,6),
     * TEMP(6,8),HE(8,8),RE(8)
C
      NEN=2             ! Number of nodes per element
      NEDN=3            ! Number of degrees of freedom per node
      NLED=6            ! Number of local degrees of freedom per element
      NGED=NLED-NEN/2+3 !Number of global degrees of freedom per element
C
C NGED reflects removing the vertical degrees of freedom from the nodes
C   in the upper plane then adding back in the 3 top plane DOFs
C
      IF (IGO.EQ.1) GOTO 1 ! Input element data
      IF (IGO.EQ.2) GOTO 2 ! Transfer initial lengths to ELRT
      IF (IGO.EQ.3) GOTO 3 ! calculate the tangent stiffness, H
      IF (IGO.EQ.4) GOTO 4 ! calculate RTPT and ELRTPT
      IF (IGO.EQ.5) GOTO 5 ! Print the system picture
      WRITE(6,1000)
 1000 FORMAT('Fatal error in subroutine TRUSS1. Invalid value for IGO.')
      STOP
C
C Read and print element data.  Calculate assembly arrays and half-
C bandwidth.
    1 WRITE(6,1001) IEG
 1001 FORMAT(//,2X,'LONGITUDINAL REBAR ELEMENT GROUP NUMBER',I4,10X)
      WRITE(6,1002) NEL,NUMAT
 1002 FORMAT(/,4X,'NEL =',I4,4X,'NUMAT =',I3)
      WRITE(6,1003)
 1003 FORMAT(/,4X,'MATERIAL/GEOMETRIC SETS',/,9X,'SET',14X,'E',
     * 9X,'AREA',10X,'YST',10X,'YRT')
      DO 100 I=1,NUMAT
      READ(5,*) E(I),AREA(I),YST(I),YRT(I)
      WRITE(6,1004) I,E(I),AREA(I),YST(I),YRT(I)
 1004 FORMAT(8X,I4,2X,4(1X,E12.5))
  100 CONTINUE
C
C Generates vector MAT and matrix LM
      CALL LMGEN(LM,MAT,NEN,NEL)
      WRITE(6,1005)
 1005 FORMAT(/,4X,'MATERIAL SET NUMBERS AND CONNECTIVITY VECTORS',/,
     * 9X,'ELE',8X,'LENGTH',3X,'SET',5X,'NODE NUMBERS')
      DO 120 N=1,NEL
C
C Transfers nodal coordinates for an element from COOR to COORL.
      CALL LCLCOR(COOR,LM(1,N),COORL,NNP,NEN)
      ALEN(N)=0.Q0
      DO 110 I=1,3
      XP(I)=COORL(1,I)-COORL(2,I)
      ALEN(N)=ALEN(N)+XP(I)*XP(I)
  110 CONTINUE
      ALEN(N)=QSQRT(ALEN(N))
      WRITE(6,1006) N,ALEN(N),MAT(N),(LM(I,N),I=1,NEN)
 1006 FORMAT(8X,I4,2X,E12.5,2X,I4,5X,2(2X,I4))
  120 CONTINUE
C
C Transfers equation numbers for all elements from ID to IDL.
C   For elements having half their nodes in the top plane
      CALL LCLID(ID,LM,IDL,NEDN,NGED,NEN,NEL,NEQ,NNP)
      CALL BAND(IDL,NGED,NEL,MBAND)
      RETURN
C
C Transfer initial element lengths to ELRTPT
    2 DO 200 N=1,NEL
        ELRTPT(4,N,IEG)=ALEN(N)
  200 CONTINUE
      RETURN
C
C Calculate and assemble element matrices and vectors
    3 DO 300 N=1,NEL
      M=MAT(N)
```

```
C
C Transfers nodal coordinates for an element from COOR to COORL.
      CALL LCLCOR(COOR,LM(1,N),COORL,NNP,NEN)
      CLEN=0.Q0
      DO 310 I=1,3
      XP(I)=COORL(1,I)-COORL(2,I)
      CLEN=CLEN+XP(I)*XP(I)
  310 CONTINUE
      CLEN=QSQRT(CLEN)
      DO 320 I=1,3
      XP(I)=XP(I)/CLEN
      XP(I+3)=-XP(I)
  320 CONTINUE
C Define transformation matrix from local to global DOFs
C
      T=0.Q0
      T(1,1)=1.Q0
      T(2,2)=1.Q0
      T(4,3)=1.Q0
      T(5,4)=1.Q0
      T(6,5)=1.Q0
      T(3,6)=1.Q0
      T(3,7)=COORL(1,2)
      T(3,8)=-COORL(1,1)
      DO 330 I=1,8
         DO 331 J=1,6
            TT(I,J)=T(J,I)
  331 CONTINUE
  330 CONTINUE
      EAA=E(M)*AREA(M)/ALEN(N)
      ELS=QABS(E(M)*ELRTPT(2,N,IEG)) ! ELRTPT(2)=elastic strain
      IF(ELS.GE.YST(M)) EAA=EAA*YRT(M)
      DO 340 I=1,6
      DO 341 J=1,6
      HEP(I,J)=XP(I)*XP(J)*EAA
  341 CONTINUE
  340 CONTINUE
C Transform to global DOFs
C
      TEMP=MATMUL(HEP,T)
      HE=MATMUL(TT,TEMP)
      CALL ASSMBL(H,F,HE,RE,IDL(1,N),NEQ,MBAND,NGED,1,0)
  300 CONTINUE
      RETURN
C
C Compute and print stresses, strains, forces and displacements.
    4 DO 400 N=1,NEL
      M=MAT(N)
      PLEN=ELRT(4,N,IEG)        ! Length at previous time step
      EPSET=ELRT(2,N,IEG)       ! Elastic strain at previous time step
      EPSETPT=ELRTPT(2,N,IEG)   ! Elastic strain at current time step
      YEPS=YST(M)/E(M)          ! Yield strain
C
C Transfers nodal coordinates for an element from COOR to COORL.
      CALL LCLCOR(COOR,LM(1,N),COORL,NNP,NEN)
      CLEN=0.Q0
      DO 410 I=1,3
         XP(I)=COORL(1,I)-COORL(2,I)
         CLEN=CLEN+XP(I)*XP(I)
  410 CONTINUE
      CLEN=QSQRT(CLEN)
      DO 420 I=1,3
         XP(I)=XP(I)/CLEN
         XP(I+3)=-XP(I)
  420 CONTINUE
C Determine if loading plastically (1), loading elastically (2),
C    loading transition (3), or unloading elastically (4)
      EPST=(PLEN-ALEN(N))/ALEN(N)   ! Previous total strain
      EPSTPT=(CLEN-ALEN(N))/ALEN(N) ! Current total strain
      DEPS=EPSTPT-EPST              ! Change in total strain
C Assume elastic then check assumption
      EPSETPT=EPSET+DEPS
      IF (QABS(EPSTPT).LT.QABS(EPST) .AND. QABS(EPSETPT).LE.YEPS) THEN
         IFLAG=4        ! Elastic unloading
      ELSEIF (QABS(EPSETPT).LE.YEPS) THEN
```

```
         IFLAG=2        ! Elastic loading
       ELSEIF (QABS(EPSET).LT.YEPS) THEN
         IFLAG=3        ! Transition loading
       ELSEIF (QABS(EPSET).GE.YEPS) THEN
         IFLAG=1        ! Plastic loading
       ELSE
         WRITE(6,4000) N,IEG
 4000    FORMAT(2(/),5X,'NO CASE FOUND FOR ELEMENT ',I4,
     *      ' OF LONGITUDINAL REBAR GROUP ',I4)
         STOP
       ENDIF
       IF (IFLAG.EQ.2 .OR. IFLAG.EQ.4) THEN
         ELRTPT(2,N,IEG)=ELRT(2,N,IEG)+DEPS
         ELRTPT(3,N,IEG)=ELRT(3,N,IEG)
       ENDIF
       IF (IFLAG.EQ.3 .OR. IFLAG.EQ.1) THEN
         IF (DEPS.GT.0) ELRTPT(2,N,IEG)=YEPS
         IF (DEPS.LT.0) ELRTPT(2,N,IEG)=-YEPS
         IF (DEPS.EQ.0) ELRTPT(2,N,IEG)=ELRT(2,N,IEG)
         ELRTPT(3,N,IEG)=ELRT(3,N,IEG)+DEPS
     *      -(ELRTPT(2,N,IEG)-ELRT(2,N,IEG))
       ENDIF
       ELRTPT(1,N,IEG)=ELRTPT(2,N,IEG)*E(M)+ELRTPT(3,N,IEG)*YRT(M)*E(M)
       ELRTPT(4,N,IEG)=CLEN
C Define transformation matrix from local to global DOFs
C
       TT=0.Q0
       TT(1,1)=1.Q0
       TT(2,2)=1.Q0
       TT(3,4)=1.Q0
       TT(4,5)=1.Q0
       TT(5,6)=1.Q0
       TT(6,3)=1.Q0
       TT(7,3)=COORL(1,2)
       TT(8,3)=-COORL(1,1)
       REP=0.Q0
       RE=0.Q0
       DO 430 I=1,6
         REP(I)=ELRTPT(1,N,IEG)*XP(I)*AREA(M)
  430  CONTINUE
       DO 440 I=1,8
         DO 450 J=1,6
           RE(I)=RE(I)+TT(I,J)*REP(J)
  450    CONTINUE
  440  CONTINUE
       CALL ASSMBL(H,RTPT,HE,RE,IDL(1,N),NEQ,MBAND,NGED,0,1)
  400  CONTINUE
       RETURN

    5  WRITE(6,5000) IEG
 5000  FORMAT(//,2X,'LONGITUDINAL REBAR ELEMENT GROUP NUMBER',I4,10X)
       DO 500 N=1,NEL
       M=MAT(N)
       WRITE(6,5001) N
 5001  FORMAT(/,4X,'ELEMENT NUMBER',I4,/,7X,'YIELD STRESS',10X,'STRESS',
     *    11X,'FORCE',6X,'YIELD STRAIN',6X,'ELASTIC STRAIN',6X,
     *    'PLASTIC STRAIN')
       FORCE=ELRTPT(1,N,IEG)*AREA(M)
       YEPS=YST(M)/E(M)
       WRITE(6,5002) YST(M),ELRTPT(1,N,IEG),FORCE,
     *    YEPS,ELRTPT(2,N,IEG),ELRTPT(3,N,IEG)
 5002  FORMAT(3X,3(4X,E12.5),6X,E12.5,2(8X,E12.5))
  500  CONTINUE
       RETURN
       END

       SUBROUTINE TRUSSB(A,B,C)
C Sets up storage for subroutine TRUSS10.
       IMPLICIT REAL(KIND=16) (A-H,O-Z)
       IMPLICIT INTEGER(KIND=8) (I-N)
       REAL(KIND=16), ALLOCATABLE, DIMENSION(:) :: BSUB
       COMMON /INFO/ N5TEMP
       COMMON /INFO1/ NNP,NEQ,MBAND,IGO
       COMMON /INFO2/ IEG,NEG1,NEG10,NEG11,NEG100,NEG110,MAXNEL1,
     * MAXNEL10,MAXNEL11,MAXNEL100,MAXNEL110,MAXNINT
```

```
      COMMON /ELPAR/ NELTYP,NEL,NUMAT,NDUM(5)
      COMMON /POINTS/ N1,N2,N3,N4,N5,N6,N7,N8,N9,N10,N11,N1101,N1102,
     * N1103,N1104,N12,N1201,N1202,N1203,N1204,N13
      COMMON /DEBUG/ IDEBUG
      DIMENSION A(N4-1),B(N5-1),C(N13-1)
C
      IF (MAXNEL10.LT.NEL) MAXNEL10=NEL
      N401=1   +NUMAT    ! E
      N402=N401+NUMAT    ! AREA
      N403=N402+NUMAT    ! YST
      N404=N403+NUMAT    ! YRT
      N405=N404+NEL      ! MAT
      N406=N405+2*NEL    ! LM
      N407=N406+6*NEL    ! IDL
      N5TEMP=N407+NEL    ! ALEN
      NEND=N5TEMP-1
      IF (IGO.EQ.1) THEN
          ALLOCATE(BSUB(NEND))
          BSUB=0.Q0
          CALL TRUSS10(A(N1),A(N2),A(N3),BSUB(1),BSUB(N401),BSUB(N402),
     *       BSUB(N403),BSUB(N404),BSUB(N405),BSUB(N406),BSUB(N407),
     *       C(1),C(N6),C(N7),C(N8),C(N9),C(N10),C(N1101),C(N1201))
          WRITE(7) NEND,NELTYP,NEL,NUMAT,(NDUM(I),I=1,5),
     *       (BSUB(I),I=1,NEND)
          DEALLOCATE(BSUB)
      ELSE
          CALL TRUSS10(A(N1),A(N2),A(N3),B(1),B(N401),B(N402),B(N403),
     *      B(N404),B(N405),B(N406),B(N407),C(1),C(N6),C(N7),
     *      C(N8),C(N9),C(N10),C(N1101),C(N1201))
      ENDIF
      RETURN
      END

      SUBROUTINE TRUSS10(COOR,ID,R,E,AREA,YST,YRT,MAT,LM,IDL,ALEN,
     *     H,F,RTPT,DX,XT,XTPT,ELRT,ELRTPT)
C Performs computations for lower transverse truss elements.
      IMPLICIT REAL(KIND=16) (A-H,O-Z)
      IMPLICIT INTEGER(KIND=8) (I-N)
      COMMON /INFO1/ NNP,NEQ,MBAND,IGO
      COMMON /INFO2/ IEG,NEG1,NEG10,NEG11,NEG100,NEG110,MAXNEL1,
     * MAXNEL10,MAXNEL11,MAXNEL100,MAXNEL110,MAXNINT
      COMMON /ELPAR/ NELTYP,NEL,NUMAT,NDUM(5)
      COMMON /DEBUG/ IDEBUG
      DIMENSION COOR(NNP,3),ID(NNP,3),R(NNP,3),E(NUMAT),
     * AREA(NUMAT),YST(NUMAT),YRT(NUMAT),MAT(NEL),LM(2,NEL),
     * IDL(3,2,NEL),ALEN(NEL),ELRT(4,MAXNEL10,NEG10),
     * ELRTPT(4,MAXNEL10,NEG10),H(NEQ,MBAND),F(NEQ),RTPT(NEQ),DX(NEQ),
     * XT(NEQ),XTPT(NEQ)
      DIMENSION HE(6,6),RE(6),COORL(2,3),XP(6)
C
      NEN=2    ! Number of nodes per element
      NEDN=3   ! Number of degrees of freedom per node
      NED=6    ! Number of degrees of freedom per element
C
      IF (IGO.EQ.1) GOTO 1 ! Input element data
      IF (IGO.EQ.2) GOTO 2 ! Transfer initial lengths to ELRT
      IF (IGO.EQ.3) GOTO 3 ! calculate the tangent stiffness, H
      IF (IGO.EQ.4) GOTO 4 ! calculate RTPT and ELRTPT
      IF (IGO.EQ.5) GOTO 5 ! Print the system picture
      WRITE(6,1000)
 1000 FORMAT('Fatal error in subroutine TRUSS10. ',
     *   'Invalid value for IGO.')
      STOP
C
C Read and print element data.  Calculate assembly arrays and half-
C bandwidth.
    1 WRITE(6,1001) IEG
 1001 FORMAT(//,2X,'LOWER TRANSVERSE REBAR ELEMENT GROUP NUMBER',I4,10X)
      WRITE(6,1002) NEL,NUMAT
 1002 FORMAT(/,4X,'NEL =',I4,4X,'NUMAT =',I3)
      WRITE(6,1003)
 1003 FORMAT(/,4X,'MATERIAL/GEOMETRIC SETS',/,9X,'SET',14X,'E',
     * 9X,'AREA',10X,'YST',10X,'YRT')
      DO 100 I=1,NUMAT
      READ(5,*) E(I),AREA(I),YST(I),YRT(I)
```

```
      WRITE(6,1004) I,E(I),AREA(I),YST(I),YRT(I)
 1004 FORMAT(8X,I4,2X,4(1X,E12.5))
  100 CONTINUE
C
C Generates vector MAT and matrix LM
      CALL LMGEN(LM,MAT,NEN,NEL)
      WRITE(6,1005)
 1005 FORMAT(/,4X,'MATERIAL SET NUMBERS AND CONNECTIVITY VECTORS',/,
     * 9X,'ELE',8X,'LENGTH',3X,'SET',5X,'NODE NUMBERS')
      DO 120 N=1,NEL
C
C Transfers nodal coordinates for an element from COOR to COORL.
      CALL LCLCOR(COOR,LM(1,N),COORL,NNP,NEN)
      ALEN(N)=0.QO
      DO 110 I=1,3
      XP(I)=COORL(1,I)-COORL(2,I)
      ALEN(N)=ALEN(N)+XP(I)*XP(I)
  110 CONTINUE
      ALEN(N)=QSQRT(ALEN(N))
      WRITE(6,1006) N,ALEN(N),MAT(N),(LM(I,N),I=1,NEN)
 1006 FORMAT(8X,I4,2X,E12.5,2X,I4,5X,2(2X,I4))
  120 CONTINUE
C
C Transfers equation numbers for all elements from ID to IDL.
C  For elements which do not lie in the top plane.
      CALL LCLID2(ID,LM,IDL,NNP,NEDN,NEN,NEL)
      CALL BAND(IDL,NED,NEL,MBAND)
      RETURN
C
C Transfer initial element lengths to ELRTPT
    2 DO 200 N=1,NEL
         ELRTPT(4,N,IEG)=ALEN(N)
  200 CONTINUE
      RETURN
C
C Calculate and assemble element matrices and vectors
    3 DO 300 N=1,NEL
      M=MAT(N)
C
C Transfers nodal coordinates for an element from COOR to COORL.
      CALL LCLCOR(COOR,LM(1,N),COORL,NNP,NEN)
      CLEN=0.QO
      DO 310 I=1,3
      XP(I)=COORL(1,I)-COORL(2,I)
      CLEN=CLEN+XP(I)*XP(I)
  310 CONTINUE
      CLEN=QSQRT(CLEN)
      DO 320 I=1,3
      XP(I)=XP(I)/CLEN
      XP(I+3)=-XP(I)
  320 CONTINUE
      EAA=E(M)*AREA(M)/ALEN(N)
      ELS=QABS(E(M)*ELRTPT(2,N,IEG)) ! ELRTPT(2)=elastic strain
      IF(ELS.GE.YST(M)) EAA=EAA*YRT(M)
      DO 340 I=1,6
      DO 341 J=1,6
      HE(I,J)=XP(I)*XP(J)*EAA
  341 CONTINUE
  340 CONTINUE
      CALL ASSMBL(H,F,HE,RE,IDL(1,1,N),NEQ,MBAND,NED,1,0)
  300 CONTINUE
      RETURN
C
C Compute and print stresses, strains, forces and displacements.
    4 DO 400 N=1,NEL
      M=MAT(N)
      PLEN=ELRT(4,N,IEG)        ! Length at previous time step
      EPSET=ELRT(2,N,IEG)       ! Elastic strain at previous time step
      EPSETPT=ELRTPT(2,N,IEG)   ! Elastic strain at current time step
      YEPS=YST(M)/E(M)          ! Yield strain
C
C Transfers nodal coordinates for an element from COOR to COORL.
      CALL LCLCOR(COOR,LM(1,N),COORL,NNP,NEN)
      CLEN=0.QO
      DO 410 I=1,3
```

```
         XP(I)=COORL(1,I)-COORL(2,I)
         CLEN=CLEN+XP(I)*XP(I)
  410 CONTINUE
      CLEN=QSQRT(CLEN)
      DO 420 I=1,3
         XP(I)=XP(I)/CLEN
         XP(I+3)=-XP(I)
  420 CONTINUE
C Determine if loading plastically (1), loading elastically (2),
C    loading transition (3), or unloading elastically (4)
      EPST=(PLEN-ALEN(N))/ALEN(N)    ! Previous total strain
      EPSTPT=(CLEN-ALEN(N))/ALEN(N) ! Current total strain
      DEPS=EPSTPT-EPST               ! Change in total strain
C Assume elastic then check assumption
      EPSETPT=EPSET+DEPS
      IF (QABS(EPSTPT).LT.QABS(EPST) .AND. QABS(EPSETPT).LE.YEPS) THEN
         IFLAG=4         ! Elastic unloading
      ELSEIF (QABS(EPSETPT).LE.YEPS) THEN
         IFLAG=2         ! Elastic loading
      ELSEIF (QABS(EPSET).LT.YEPS) THEN
         IFLAG=3         ! Transition loading
      ELSEIF (QABS(EPSET).GE.YEPS) THEN
         IFLAG=1         ! Plastic loading
      ELSE
         WRITE(6,4000) N,IEG
 4000    FORMAT(2(/),5X,'NO CASE FOUND FOR ELEMENT ',I4,
     *      ' OF LOWER TRANSVERSE REBAR GROUP ',I4)
         STOP
      ENDIF
      IF (IFLAG.EQ.2 .OR. IFLAG.EQ.4) THEN
         ELRTPT(2,N,IEG)=ELRT(2,N,IEG)+DEPS
         ELRTPT(3,N,IEG)=ELRT(3,N,IEG)
      ENDIF
      IF (IFLAG.EQ.3 .OR. IFLAG.EQ.1) THEN
         IF (DEPS.GT.0) ELRTPT(2,N,IEG)=YEPS
         IF (DEPS.LT.0) ELRTPT(2,N,IEG)=-YEPS
         IF (DEPS.EQ.0) ELRTPT(2,N,IEG)=ELRT(2,N,IEG)
         ELRTPT(3,N,IEG)=ELRT(3,N,IEG)+DEPS
     *      -(ELRTPT(2,N,IEG)-ELRT(2,N,IEG))
      ENDIF
      ELRTPT(1,N,IEG)=ELRTPT(2,N,IEG)*E(M)+ELRTPT(3,N,IEG)*YRT(M)*E(M)
      ELRTPT(4,N,IEG)=CLEN
      RE=0.QO
      DO 430 I=1,6
         RE(I)=ELRTPT(1,N,IEG)*XP(I)*AREA(M)
  430 CONTINUE
      CALL ASSMBL(H,RTPT,HE,RE,IDL(1,1,N),NEQ,MBAND,NED,0,1)
  400 CONTINUE
      RETURN

    5 WRITE(6,5000) IEG
 5000 FORMAT(//,2X,'LOWER TRANSVERSE REBAR ELEMENT GROUP NUMBER',I4,10X)
      DO 500 N=1,NEL
      M=MAT(N)
      WRITE(6,5001) N
 5001 FORMAT(/,4X,'ELEMENT NUMBER',I4,/,7X,'YIELD STRESS',10X,'STRESS',
     *   11X,'FORCE',6X,'YIELD STRAIN',6X,'ELASTIC STRAIN',6X,
     *   'PLASTIC STRAIN')
      FORCE=ELRTPT(1,N,IEG)*AREA(M)
      YEPS=YST(M)/E(M)
      WRITE(6,5002) YST(M),ELRTPT(1,N,IEG),FORCE,
     *   YEPS,ELRTPT(2,N,IEG),ELRTPT(3,N,IEG)
 5002 FORMAT(3X,3(4X,E12.5),6X,E12.5,2(8X,E12.5))
  500 CONTINUE
      RETURN
      END

      SUBROUTINE TRUSSC(A,B,C)
C Sets up storage for subroutine TRUSS11.
      IMPLICIT REAL(KIND=16) (A-H,O-Z)
      IMPLICIT INTEGER(KIND=8) (I-N)
      REAL(KIND=16), ALLOCATABLE, DIMENSION(:) :: BSUB
      COMMON /INFO/ N5TEMP
      COMMON /INFO1/ NNP,NEQ,MBAND,IGO
      COMMON /INFO2/ IEG,NEG1,NEG10,NEG11,NEG100,NEG110,MAXNEL1,
```

```
     * MAXNEL10,MAXNEL11,MAXNEL100,MAXNEL110,MAXNINT
      COMMON /ELPAR/ NELTYP,NEL,NUMAT,NDUM(5)
      COMMON /POINTS/ N1,N2,N3,N4,N5,N6,N7,N8,N9,N10,N11,N1101,N1102,
     * N1103,N1104,N12,N1201,N1202,N1203,N1204,N13
      COMMON /DEBUG/ IDEBUG
      DIMENSION A(N4-1),B(N5-1),C(N13-1)
C
      IF (MAXNEL11.LT.NEL) MAXNEL11=NEL
      N401=1   +NUMAT    ! E
      N402=N401+NUMAT    ! AREA
      N403=N402+NUMAT    ! YST
      N404=N403+NUMAT    ! YRT
      N405=N404+NEL      ! MAT
      N406=N405+2*NEL    ! LM
      N407=N406+7*NEL    ! IDL
      N5TEMP=N407+NEL    ! ALEN
      NEND=N5TEMP-1
      IF (IGO.EQ.1) THEN
          ALLOCATE(BSUB(NEND))
          BSUB=0.Q0
          CALL TRUSS11(A(N1),A(N2),A(N3),BSUB(1),BSUB(N401),BSUB(N402),
     *       BSUB(N403),BSUB(N404),BSUB(N405),BSUB(N406),BSUB(N407),
     *       C(1),C(N6),C(N7),C(N8),C(N9),C(N10),C(N1102),C(N1202))
          WRITE(7) NEND,NELTYP,NEL,NUMAT,(NDUM(I),I=1,5),
     *       (BSUB(I),I=1,NEND)
          DEALLOCATE(BSUB)
      ELSE
          CALL TRUSS11(A(N1),A(N2),A(N3),B(1),B(N401),B(N402),B(N403),
     *      B(N404),B(N405),B(N406),B(N407),C(1),C(N6),C(N7),
     *      C(N8),C(N9),C(N10),C(N1102),C(N1202))
      ENDIF
      RETURN
      END

      SUBROUTINE TRUSS11(COOR,ID,R,E,AREA,YST,YRT,MAT,LM,IDL,ALEN,
     *     H,F,RTPT,DX,XT,XTPT,ELRT,ELRTPT)
C Performs computations for upper transverse truss elements.
      IMPLICIT REAL(KIND=16) (A-H,O-Z)
      IMPLICIT INTEGER(KIND=8) (I-N)
      COMMON /INFO1/ NNP,NEQ,MBAND,IGO
      COMMON /INFO2/ IEG,NEG1,NEG10,NEG11,NEG100,NEG110,MAXNEL1,
     * MAXNEL10,MAXNEL11,MAXNEL100,MAXNEL110,MAXNINT
      COMMON /ELPAR/ NELTYP,NEL,NUMAT,NDUM(5)
      COMMON /DEBUG/ IDEBUG
      DIMENSION COOR(NNP,3),ID(NNP,3),R(NNP,3),E(NUMAT),
     * AREA(NUMAT),YST(NUMAT),YRT(NUMAT),MAT(NEL),LM(2,NEL),
     * IDL(7,NEL),ALEN(NEL),ELRT(4,MAXNEL11,NEG11),
     * ELRTPT(4,MAXNEL11,NEG11),H(NEQ,MBAND),F(NEQ),RTPT(NEQ),DX(NEQ),
     * XT(NEQ),XTPT(NEQ)
      DIMENSION HEP(6,6),REP(6),COORL(2,3),XP(6),T(6,7),TT(7,6),
     * TEMP(6,7),HE(7,7),RE(7)
C
      NEN=2    ! Number of nodes per element
      NEDN=3   ! Number of degrees of freedom per node
      NLED=6   ! Number of local degrees of freedom per element
      NGED=NLED-NEN+3  ! Number of global degrees of freedom per element
C
C NGED reflects removing the vertical degrees of freedom from both nodes
C   then adding back in the 3 top plane DOFs in place of each
C
      IF (IGO.EQ.1) GOTO 1 ! Input element data
      IF (IGO.EQ.2) GOTO 2 ! Transfer initial lengths to ELRT
      IF (IGO.EQ.3) GOTO 3 ! calculate the tangent stiffness, H
      IF (IGO.EQ.4) GOTO 4 ! calculate RTPT and ELRTPT
      IF (IGO.EQ.5) GOTO 5 ! Print the system picture
      WRITE(6,1000)
 1000 FORMAT('Fatal error in subroutine TRUSS11. ',
     *   'Invalid value for IGO.')
      STOP
C
C Read and print element data.  Calculate assembly arrays and half-
C bandwidth.
    1 WRITE(6,1001) IEG
 1001 FORMAT(//,2X,'UPPER TRANSVERSE REBAR ELEMENT GROUP NUMBER',I4,10X)
      WRITE(6,1002) NEL,NUMAT
```

```
 1002 FORMAT(/,4X,'NEL =',I4,4X,'NUMAT =',I3)
      WRITE(6,1003)
 1003 FORMAT(/,4X,'MATERIAL/GEOMETRIC SETS',/,9X,'SET',14X,'E',
     * 9X,'AREA',10X,'YST',10X,'YRT')
      DO 100 I=1,NUMAT
      READ(5,*) E(I),AREA(I),YST(I),YRT(I)
      WRITE(6,1004) I,E(I),AREA(I),YST(I),YRT(I)
 1004 FORMAT(8X,I4,2X,4(1X,E12.5))
  100 CONTINUE
C
C Generates vector MAT and matrix LM
      CALL LMGEN(LM,MAT,NEN,NEL)
      WRITE(6,1005)
 1005 FORMAT(/,4X,'MATERIAL SET NUMBERS AND CONNECTIVITY VECTORS',/,
     * 9X,'ELE',8X,'LENGTH',3X,'SET',5X,'NODE NUMBERS')
      DO 120 N=1,NEL
C
C Transfers nodal coordinates for an element from COOR to COORL.
      CALL LCLCOR(COOR,LM(1,N),COORL,NNP,NEN)
      ALEN(N)=0.Q0
      DO 110 I=1,3
      XP(I)=COORL(1,I)-COORL(2,I)
      ALEN(N)=ALEN(N)+XP(I)*XP(I)
  110 CONTINUE
      ALEN(N)=QSQRT(ALEN(N))
      WRITE(6,1006) N,ALEN(N),MAT(N),(LM(I,N),I=1,NEN)
 1006 FORMAT(8X,I4,2X,E12.5,2X,I4,5X,2(2X,I4))
  120 CONTINUE
C
C Transfers equation numbers for all elements from ID to IDL.
C  For elements having all their nodes in the top plane.
      CALL LCLID3(ID,LM,IDL,NEDN,NGED,NEN,NEL,NEQ,NNP)
      CALL BAND(IDL,NGED,NEL,MBAND)
      RETURN
C
C Transfer initial element lengths to ELRTPT
    2 DO 200 N=1,NEL
         ELRTPT(4,N,IEG)=ALEN(N)
  200 CONTINUE
      RETURN
C
C Calculate and assemble element matrices and vectors
    3 DO 300 N=1,NEL
      M=MAT(N)
C
C Transfers nodal coordinates for an element from COOR to COORL.
      CALL LCLCOR(COOR,LM(1,N),COORL,NNP,NEN)
      CLEN=0.Q0
      DO 310 I=1,3
      XP(I)=COORL(1,I)-COORL(2,I)
      CLEN=CLEN+XP(I)*XP(I)
  310 CONTINUE
      CLEN=QSQRT(CLEN)
      DO 320 I=1,3
      XP(I)=XP(I)/CLEN
      XP(I+3)=-XP(I)
  320 CONTINUE
C Define transformation matrix from local to global DOFs
C
      T=0.Q0
      T(1,1)=1.Q0
      T(2,2)=1.Q0
      T(4,3)=1.Q0
      T(5,4)=1.Q0
      T(3,5)=1.Q0
      T(3,6)=COORL(1,2)
      T(3,7)=-COORL(1,1)
      T(6,5)=1.Q0
      T(6,6)=COORL(2,2)
      T(6,7)=-COORL(2,1)
      DO 330 I=1,7
         DO 331 J=1,6
            TT(I,J)=T(J,I)
  331 CONTINUE
  330 CONTINUE
      EAA=E(M)*AREA(M)/ALEN(N)
```

```
      ELS=QABS(E(M)*ELRTPT(2,N,IEG)) ! ELRTPT(2)=elastic strain
      IF(ELS.GE.YST(M)) EAA=EAA*YRT(M)
      DO 340 I=1,6
      DO 341 J=1,6
      HEP(I,J)=XP(I)*XP(J)*EAA
  341 CONTINUE
  340 CONTINUE
C Transform to global DOFs
C
      TEMP=MATMUL(HEP,T)
      HE=MATMUL(TT,TEMP)
      CALL ASSMBL(H,F,HE,RE,IDL(1,N),NEQ,MBAND,NGED,1,0)
  300 CONTINUE
      RETURN
C
C Compute and print stresses, strains, forces and displacements.
    4 DO 400 N=1,NEL
      M=MAT(N)
      PLEN=ELRT(4,N,IEG)        ! Length at previous time step
      EPSET=ELRT(2,N,IEG)       ! Elastic strain at previous time step
      EPSETPT=ELRTPT(2,N,IEG)   ! Elastic strain at current time step
      YEPS=YST(M)/E(M)          ! Yield strain
C
C Transfers nodal coordinates for an element from COOR to COORL.
      CALL LCLCOR(COOR,LM(1,N),COORL,NNP,NEN)
      CLEN=0.Q0
      DO 410 I=1,3
         XP(I)=COORL(1,I)-COORL(2,I)
         CLEN=CLEN+XP(I)*XP(I)
  410 CONTINUE
      CLEN=QSQRT(CLEN)
      DO 420 I=1,3
         XP(I)=XP(I)/CLEN
         XP(I+3)=-XP(I)
  420 CONTINUE
C Determine if loading plastically (1), loading elastically (2),
C    loading transition (3), or unloading elastically (4)
      EPST=(PLEN-ALEN(N))/ALEN(N)   ! Previous total strain
      EPSTPT=(CLEN-ALEN(N))/ALEN(N) ! Current total strain
      DEPS=EPSTPT-EPST              ! Change in total strain
C Assume elastic then check assumption
      EPSETPT=EPSET+DEPS
      IF (QABS(EPSTPT).LT.QABS(EPST) .AND. QABS(EPSETPT).LE.YEPS) THEN
         IFLAG=4        ! Elastic unloading
      ELSEIF (QABS(EPSETPT).LE.YEPS) THEN
         IFLAG=2        ! Elastic loading
      ELSEIF (QABS(EPSET).LT.YEPS) THEN
         IFLAG=3        ! Transition loading
      ELSEIF (QABS(EPSET).GE.YEPS) THEN
         IFLAG=1        ! Plastic loading
      ELSE
         WRITE(6,4000) N,IEG
 4000    FORMAT(2(/),5X,'NO CASE FOUND FOR ELEMENT ',I4,
     *      ' OF UPPER TRANSVERSE REBAR GROUP ',I4)
         STOP
      ENDIF
      IF (IFLAG.EQ.2 .OR. IFLAG.EQ.4) THEN
         ELRTPT(2,N,IEG)=ELRT(2,N,IEG)+DEPS
         ELRTPT(3,N,IEG)=ELRT(3,N,IEG)
      ENDIF
      IF (IFLAG.EQ.3 .OR. IFLAG.EQ.1) THEN
         IF (DEPS.GT.0) ELRTPT(2,N,IEG)=YEPS
         IF (DEPS.LT.0) ELRTPT(2,N,IEG)=-YEPS
         IF (DEPS.EQ.0) ELRTPT(2,N,IEG)=ELRT(2,N,IEG)
         ELRTPT(3,N,IEG)=ELRT(3,N,IEG)+DEPS
     *      -(ELRTPT(2,N,IEG)-ELRT(2,N,IEG))
      ENDIF
      ELRTPT(1,N,IEG)=ELRTPT(2,N,IEG)*E(M)+ELRTPT(3,N,IEG)*YRT(M)*E(M)
      ELRTPT(4,N,IEG)=CLEN
C Define transformation matrix from local to global DOFs
C
      T=0.Q0
      TT(1,1)=1.Q0
      TT(2,2)=1.Q0
```

```
      TT(3,4)=1.Q0
      TT(4,5)=1.Q0
      TT(5,3)=1.Q0
      TT(6,3)=COORL(1,2)
      TT(7,3)=-COORL(1,1)
      TT(5,6)=1.Q0
      TT(6,6)=COORL(2,2)
      TT(7,6)=-COORL(2,1)
      REP=0.Q0
      RE=0.Q0
      DO 430 I=1,6
         REP(I)=ELRTPT(1,N,IEG)*XP(I)*AREA(M)
  430 CONTINUE
      DO 440 I=1,7
         DO 450 J=1,6
            RE(I)=RE(I)+TT(I,J)*REP(J)
  450    CONTINUE
  440 CONTINUE
      CALL ASSMBL(H,RTPT,HE,RE,IDL(1,N),NEQ,MBAND,NGED,0,1)
  400 CONTINUE
      RETURN

    5 WRITE(6,5000) IEG
 5000 FORMAT(//,2X,'UPPER TRANSVERSE REBAR ELEMENT GROUP NUMBER',I4,10X)
      DO 500 N=1,NEL
      M=MAT(N)
      WRITE(6,5001) N
 5001 FORMAT(/,4X,'ELEMENT NUMBER',I4,/,7X,'YIELD STRESS',10X,'STRESS',
     *   11X,'FORCE',6X,'YIELD STRAIN',6X,'ELASTIC STRAIN',6X,
     *   'PLASTIC STRAIN')
      FORCE=ELRTPT(1,N,IEG)*AREA(M)
      YEPS=YST(M)/E(M)
      WRITE(6,5002) YST(M),ELRTPT(1,N,IEG),FORCE,
     *   YEPS,ELRTPT(2,N,IEG),ELRTPT(3,N,IEG)
 5002 FORMAT(3X,3(4X,E12.5),6X,E12.5,2(8X,E12.5))
  500 CONTINUE
      RETURN
      END

      SUBROUTINE zbrent(x1,x2,ELAS,tol,SIG0,DSIG,X,R,THETA,PSI,
     *  PSIMAX,BETA,YST)
      IMPLICIT REAL(KIND=16) (A-H,O-Z)
      IMPLICIT INTEGER(KIND=8) (I-N)
      INTEGER(KIND=8) ITMAX
      REAL(KIND=16) tol,x1,x2,EPS
      PARAMETER (ITMAX=1000,EPS=1.q-16)
C  Using Brents method, find the root of a function func known to lie between x1 and x2.
C  The root, returned as zbrent, will be refined until its accuracy is tol.
C  Parameters: Maximum allowed number of iterations, and machine floating-point precision.
      INTEGER(KIND=8) iter
      REAL(KIND=16) a,b,c,d,e,fa,fb,fc,p,q,r,s,tol1,xm
      a=x1
      b=x2
      CALL FCALC(fa,a,SIG0,DSIG,X,R,THETA,PSI,PSIMAX,BETA,YST)
      CALL FCALC(fb,b,SIG0,DSIG,X,R,THETA,PSI,PSIMAX,BETA,YST)
      if((fa.gt.0..and.fb.gt.0.).or.(fa.lt.0..and.fb.lt.0.)) then
            write(6,*) 'root must be bracketed for zbrent'
            write(6,*) 'fcalc(a) = ',fa
            write(6,*) 'fcalc(b) = ',fb
            write(6,*) 'psi = ', psi
            write(6,*) 'program terminated by subroutine zbrent'
            if (fa .gt. 0.q0) elas = 0.q0
            if (fb .lt. 0.q0) elas = 1.q0
            stop
      endif
      c=b
      fc=fb
      do 11 iter=1,ITMAX
        if((fb.gt.0..and.fc.gt.0.).or.(fb.lt.0..and.fc.lt.0.))then
            c=a     !Rename a, b, c and adjust bounding interval d.
            fc=fa
            d=b-a
            e=d
        endif
        if(abs(fc).lt.abs(fb)) then
```

```
          a=b
          b=c
          c=a
          fa=fb
          fb=fc
          fc=fa
      endif
      tol1=2.Q0*EPS*abs(b)+0.5Q0*tol   !Convergence check.
      xm=.5Q0*(c-b)
      if(abs(xm).le.tol1 .or. fb.eq.0.)then
          ELAS=b
          return
      endif
      if(abs(e).ge.tol1 .and. abs(fa).gt.abs(fb)) then
          s=fb/fa   !Attempt inverse quadratic interpolation.
          if(a.eq.c) then
              p=2.Q0*xm*s
              q=1.Q0-s
          else
              q=fa/fc
              r=fb/fc
              p=s*(2.Q0*xm*q*(q-r)-(b-a)*(r-1.Q0))
              q=(q-1.Q0)*(r-1.Q0)*(s-1.Q0)
          endif
          if(p.gt.0.) q=-q   !Check whether in bounds.
          p=abs(p)
          if(2.Q0*p .lt. min(3.Q0*xm*q-abs(tol1*q),abs(e*q))) then
              e=d   !Accept interpolation.
              d=p/q
          else
              d=xm    !Interpolation failed, use bisection.
              e=d
          endif
      else    !Bounds decreasing too slowly, use bisection.
          d=xm
          e=d
      endif
      a=b    !Move last best guess to a.
      fa=fb
      if(abs(d) .gt. tol1) then    !Evaluate new trial root.
          b=b+d
      else
          b=b+sign(tol1,xm)
      endif
      CALL FCALC(fb,b,SIG0,DSIG,X,R,THETA,PSI,PSIMAX,BETA,YST)
   11 enddo
      pause 'zbrent exceeding maximum iterations'
      ELAS=b
      return
      END
```

Appendix F

Summary of Papers Used for Model Identification

Table F.1: Summary of papers used for validating the model.

Paper	Loading Type	Confinement Type	Confinement Details	Concrete Strength (ksi)	Cross Section Shape	Specimen Size (inches)
Chaallal and Shahawy (2000)	Combined Axial and Flexural	Steel hoops	#3 bars at 4″	3.7	Rectangular	8 x 14 x 84
Harries and Carey (2003)	Axial	E-Glass FRP	3 and 9 plies, bonded and unbonded	4.1 - 4.7	Circular and Square	6 x 12 (circular); 6 x 6 x 12 (square)
Harries and Kharel (2003)	Axial	E-Glass and Carbon FRP	E-Glass 1, 2, 3, 6, 9, 12, and 15 plies; Carbon 1, 2, and 3 plies	4.7	Circular	6 x 12
Mander et al. (1988a)	Axial	Steel spirals and hoops	0.39″ - 0.47″ diameter bars at 1.6″-4.0″ pitch (spirals); 0.23″ diameter bars at 1.0″-2.0″ spacing (hoops)	3.8 - 4.1	Circular and Rectangular	19.7 x 59.1 (circular); 5.9 x 27.6 x 47.2 (rectangular)
Scott et al. (1982)	Axial	Steel hoops	0.39″ diameter bars at 2.8″	3.2	Square	17.7 x 17.7 x 47.2

Appendix G

Finite Element Meshes Used for Comparisons to Tests on Reinforced Concrete Members

Black dots are shown at the location of all nodes. Thin lines indicate the outlines of the solid concrete elements. Thick lines indicate the presence of spring elements. Spring elements are used to represent longitudinal rebar, hoop bars, or fiber reinforced polymer (FRP) confinement.

G.1 Chaallal and Shahawy (2000)

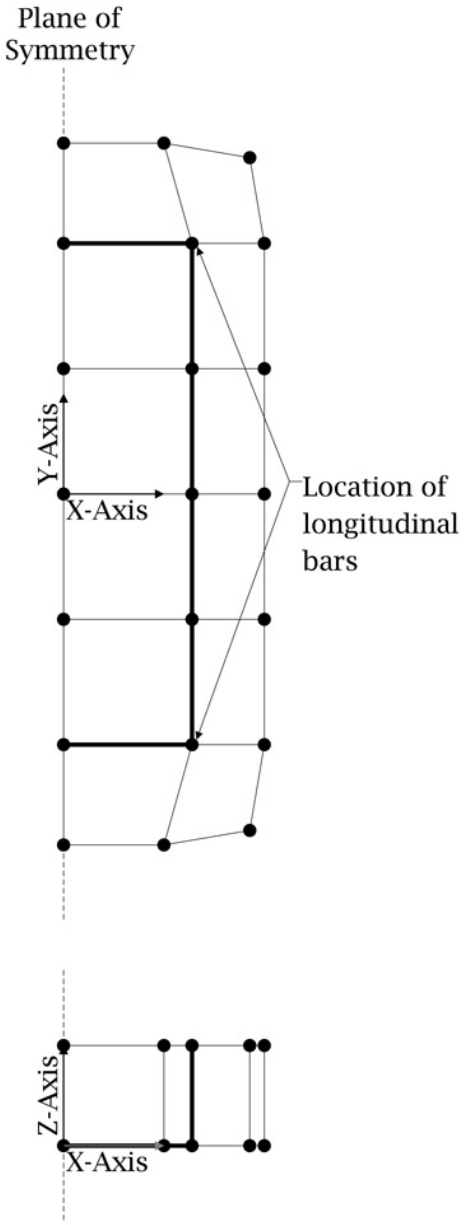

Figure G.1: Finite element representation of member tested in Chaallal and Shahawy (2000).

G.2 Harries and Carey (2003)

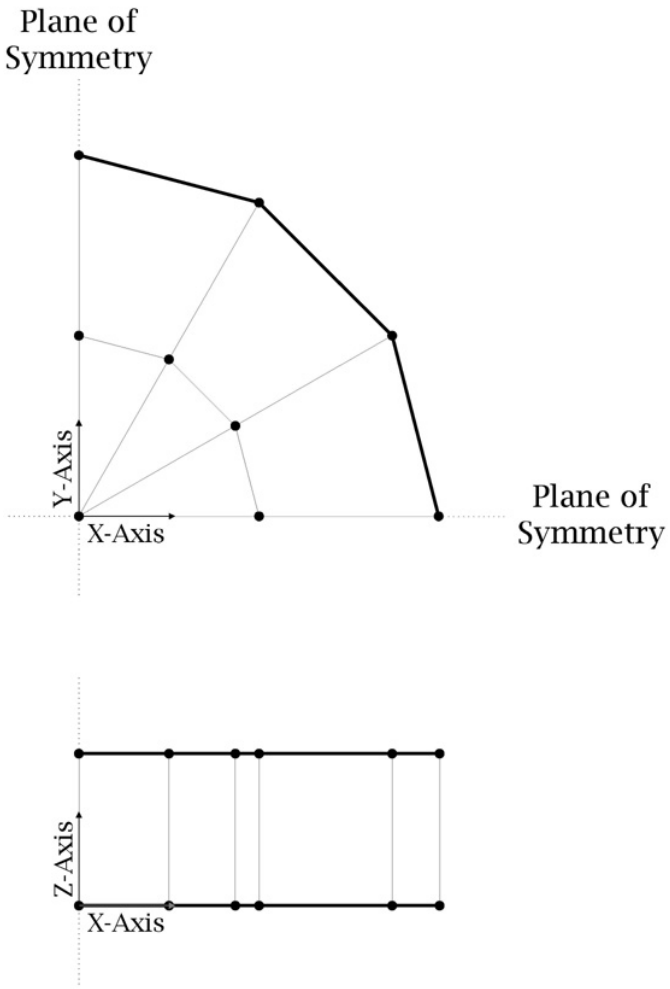

Figure G.2: Finite element representation of member with circular cross section tested in Harries and Carey (2003).

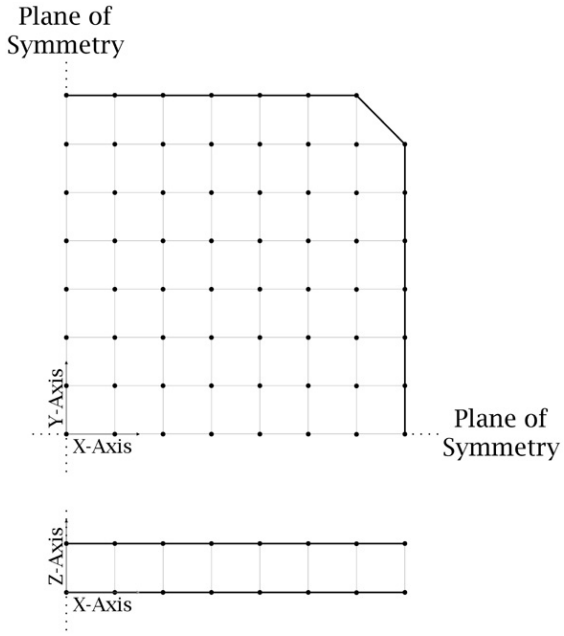

Figure G.3: Finite element representation of member with square cross section and 0.43 inch (11 mm) corner radius tested in Harries and Carey (2003).

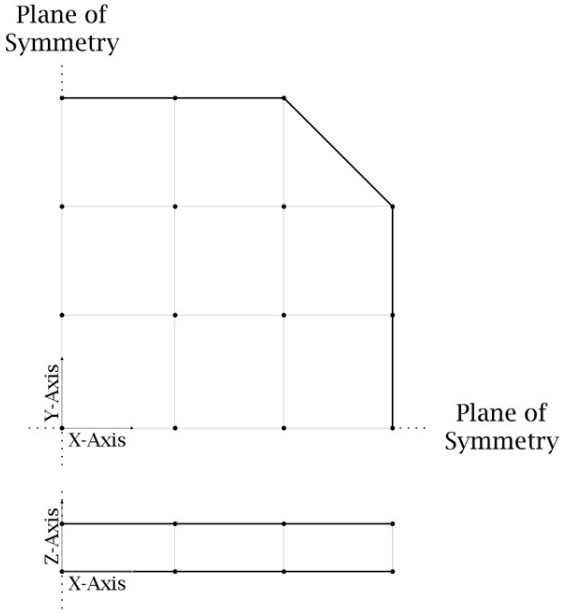

Figure G.4: Finite element representation of member with square cross section and 0.98 inch (25 mm) corner radius tested in Harries and Carey (2003).

G.3 Harries and Kharel (2003)

The mesh used for the members tested in Harries and Kharel (2003) is identical to the mesh depicted in Figure G.2.

G.4 Mander et al. (1988a)

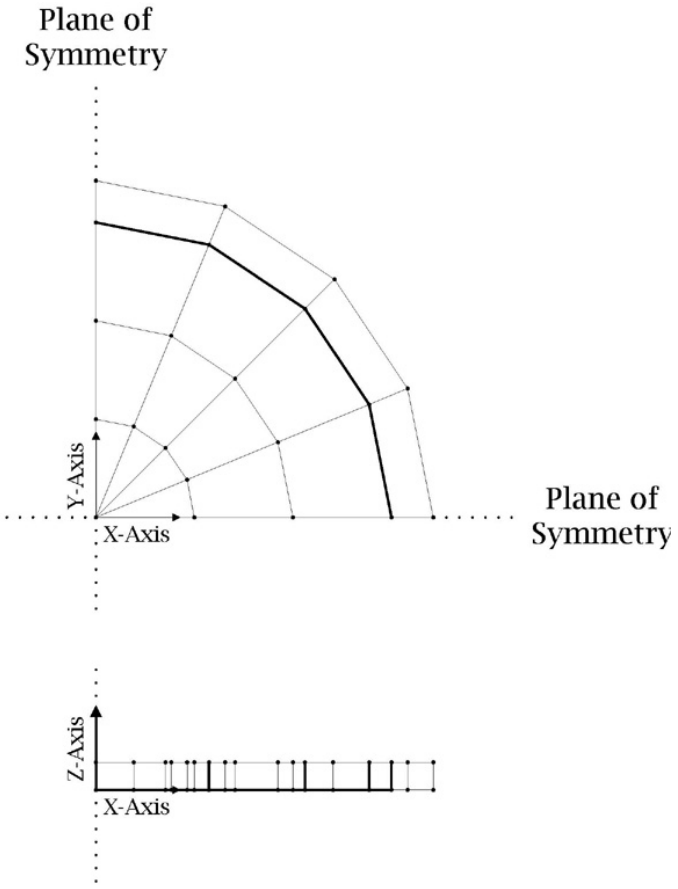

Figure G.5: Finite element representation of column 1 tested in Mander et al. (1988a).

Note that the longitudinal bars are redistributed for the mesh in column 1. Mesh refinement is necessary to preserve element quality. Thus, five longitudinal bars are in the mesh to represent the four that are actually in the column. The longitudinal bar area is defined to be equivalent and, therefore, the bars in the mesh are each smaller than the actual longitudinal bars in the column. However, this does not

affect performance of the column under pure axial load, which is the only load case considered for this column.

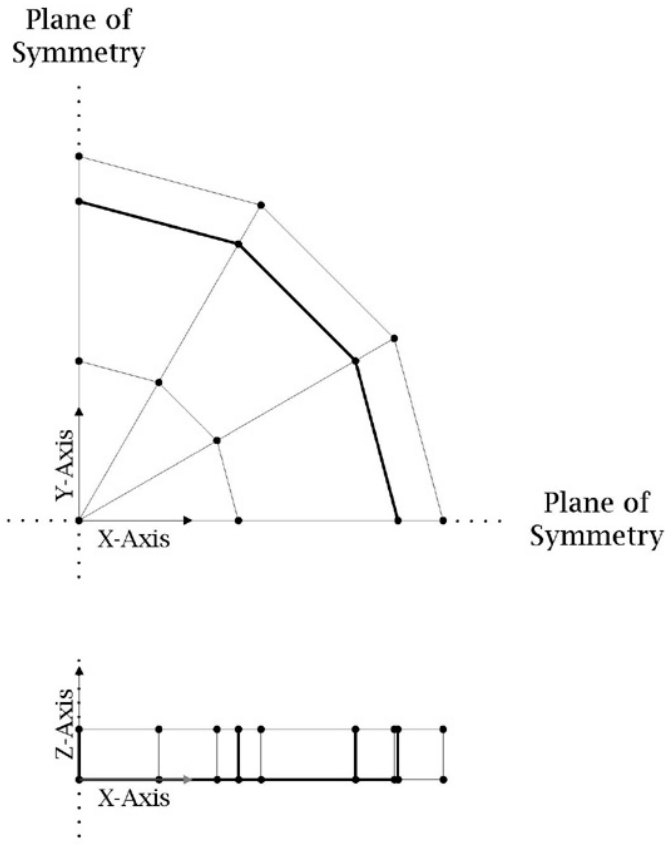

Figure G.6: Finite element representation of columns 2-4 tested in Mander et al. (1988a).

For each column, the height of the mesh in the z direction is defined as half of the hoop spacing. Thus, meshes representing columns 2 through 4 each have a different value for the height. Figure G.6 depicts the height for column 2. The mesh shown in Figure G.6 is also used to represent the unconfined column with the same height as column 4. The longitudinal rebar and hoop elements are removed for that case.

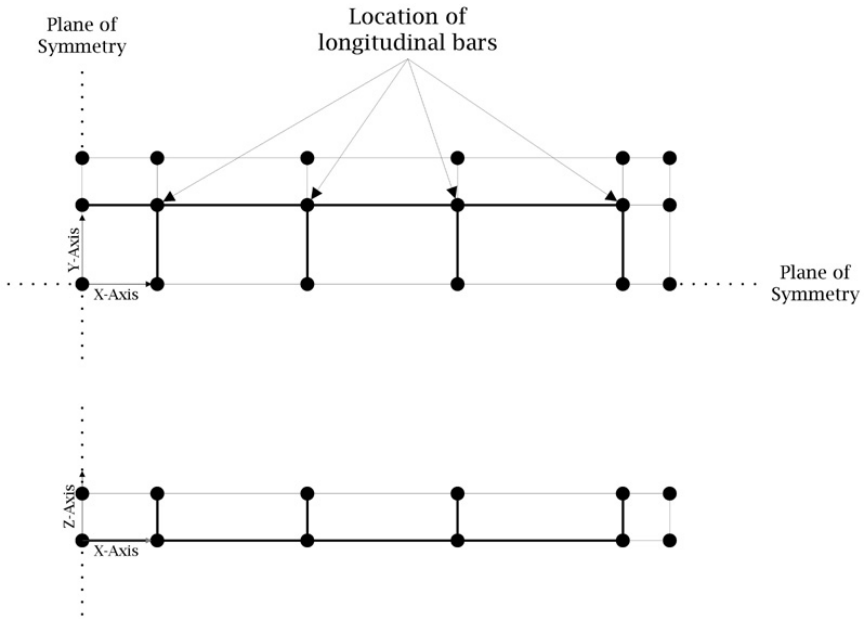

Figure G.7: Finite element representation of walls 1, 3, and 4 tested in Mander et al. (1988a).

Wall 3 has a hoop spacing equal to twice that of walls 1 and 4. The correct height of the mesh in the z direction (equal to half the hoop spacing) is used for each individual mesh. The height depicted in Figure G.7 is representative of the height for walls 1 and 4. The mesh shown in Figure G.7 is also used to represent the unconfined wall with the same height value as walls 1 and 4. The longitudinal rebar and hoop elements are removed for that case.

G.5 Scott et al. (1982)

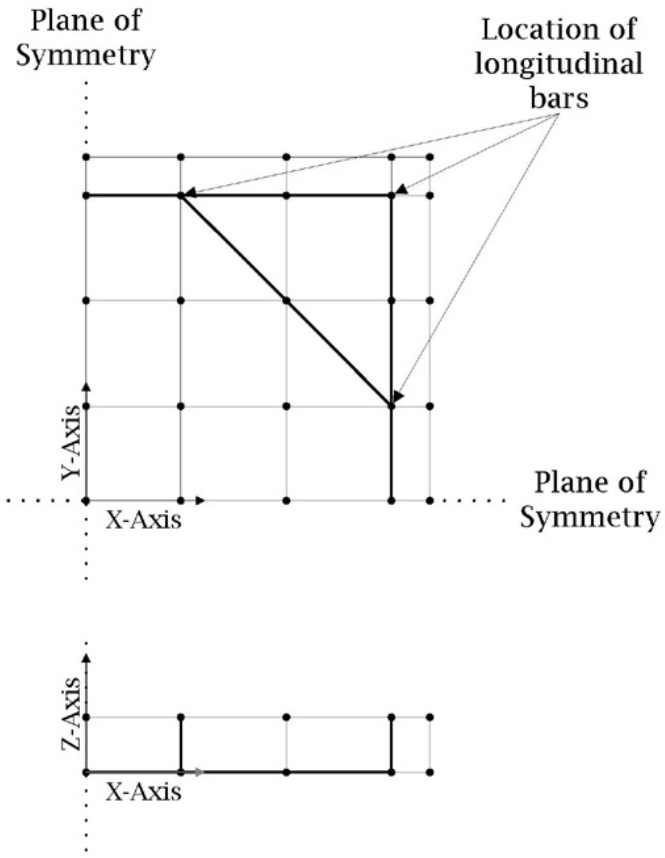

Figure G.8: Finite element representation of column 2 tested in Scott et al. (1982).

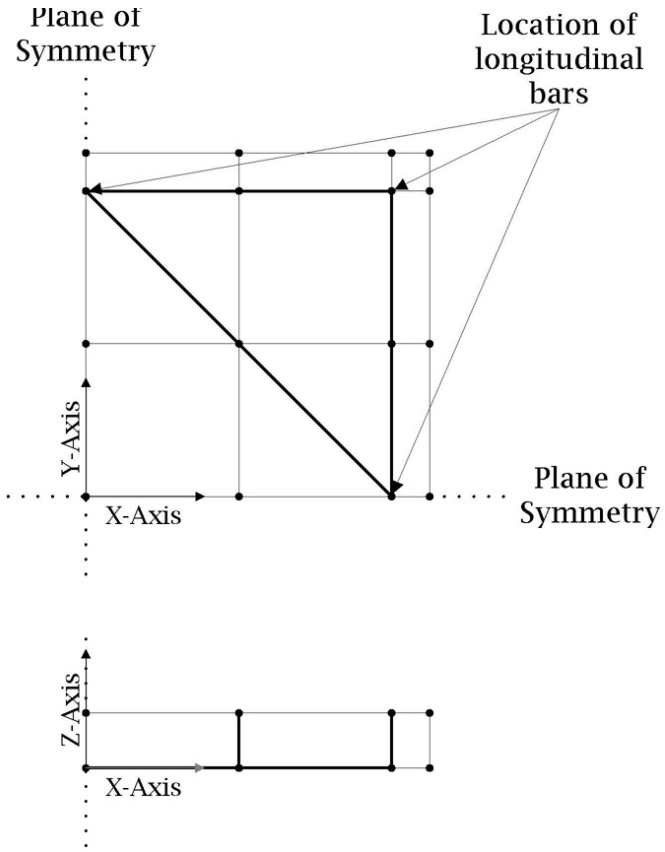

Figure G.9: Finite element representation of column 6 tested in Scott et al. (1982).

The mesh shown in Figure G.9 is also used to represent the unconfined column. The longitudinal rebar and hoop elements are removed for that case.

Appendix H

Finite Element Meshes Used for Effects of Cross Sectional Shape and Confining Material

Meshes are shown in this chapter in the same method as Appendix G. Black dots are shown at the location of all nodes. Thin lines indicate the outlines of the solid concrete elements. Thick lines indicate the presence of spring elements. Spring elements are used to represent longitudinal rebar, hoop bars, or FRP confinement.

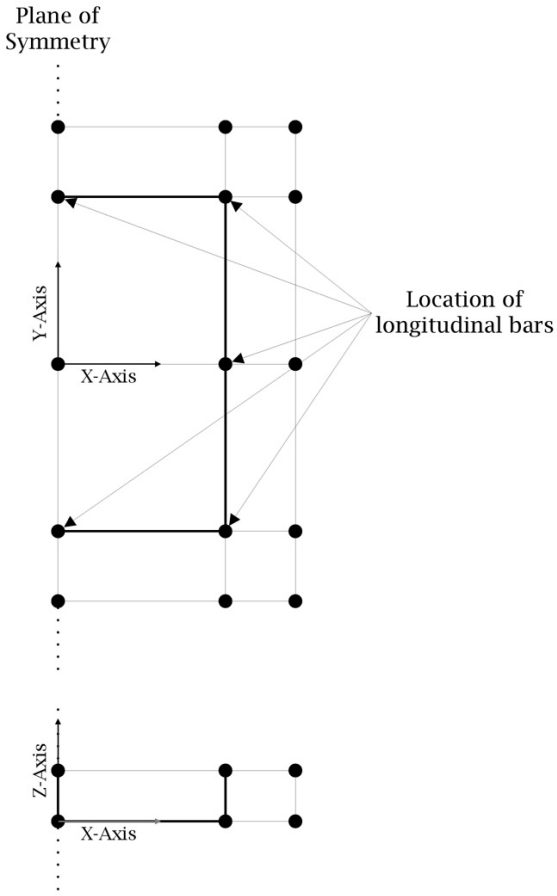

Figure H.1: Finite element representation of square column confined by steel hoops, used for comparison in Chapter 7.

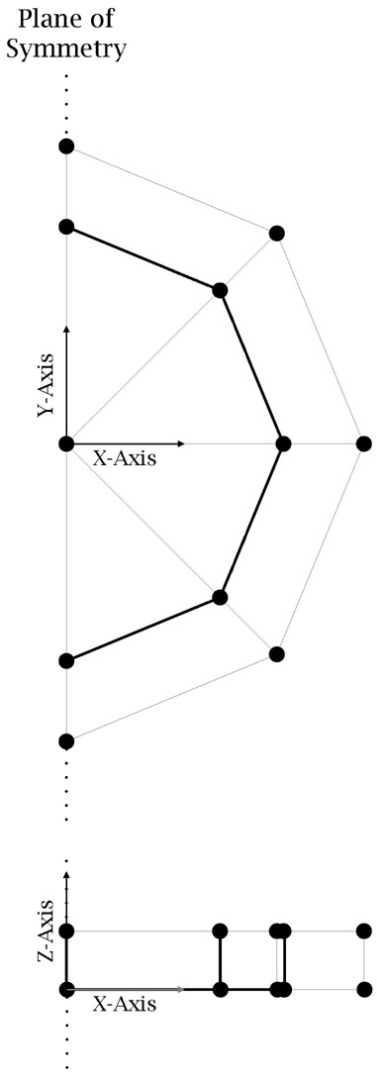

Figure H.2: Finite element representation of circular column confined by steel hoops, used for comparison in Chapter 7.

Four different hoop spacings are analyzed for each of the meshes shown in Figures H.1 and H.2. The figures depict the three inch hoop spacing. For each individual hoop spacing considered, the height of the mesh in the z direction is equal to half of the hoop spacing.

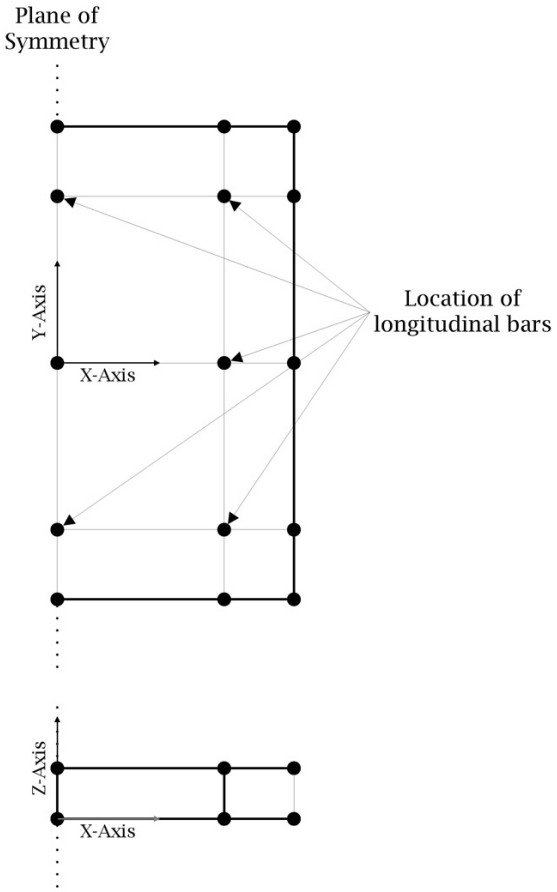

Figure H.3: Finite element representation of square column confined by FRP, used for comparison in Chapter 7.

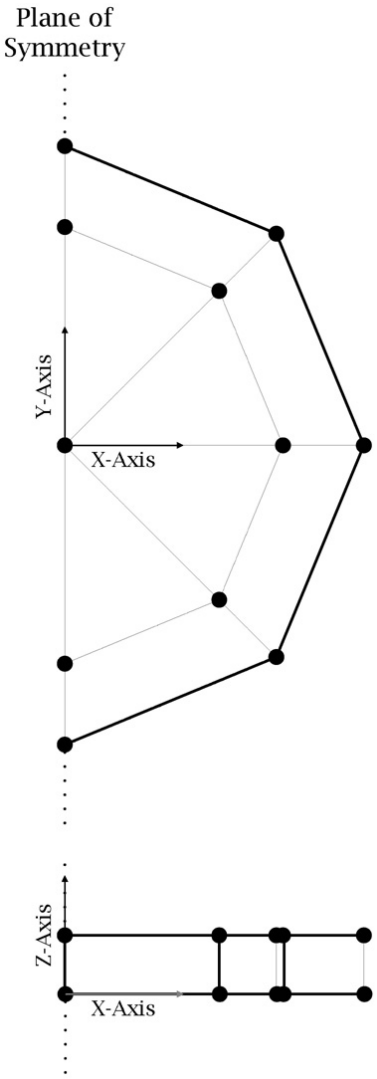

Figure H.4: Finite element representation of circular column confined by FRP, used for comparison in Chapter 7.

Mesh refinement is necessary when the neutral axis crosses the integration points at the edge of the compression side of the section. For the axial load-moment combined loading case with axial loads of 0, 140, 280, and 420 kips (0, 623, 1246, and 1868 kN) applied to the square cross section confined by FRP, the mesh shown in Figure H.5 is used to correctly capture the location of the neutral axis. This fine of a mesh is not necessary for any other section or load case.

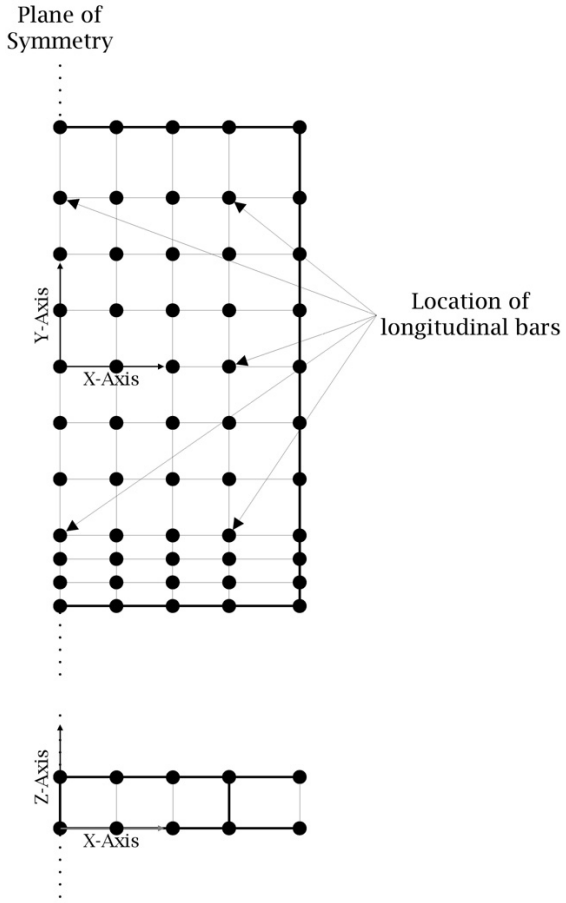

Figure H.5: Finite element representation of square column confined by FRP, used for special load cases of comparison in Chapter 7.